

Surface Engineered Titanium for Improved Tribological, Electrochemical and Tribo-electrochemical Performance

Richard Bailey

A thesis submitted in partial fulfilment of

the requirements for the degree of

Doctor of Philosophy

at

De Montfort University

2015

Preamble

This thesis is submitted for the degree of Doctor of Philosophy (Ph.D) in the School of Engineering and Sustainable Development, Faculty of Technology, De Montfort University (DMU) of Leicester under the supervision of **Dr. Yong Sun**. No part of this thesis has been submitted for any degree or diploma at any other university or institution. To the best of the author's knowledge, all work in this thesis is original unless reference is made to other work. Part of this thesis has been published or under review for publications listed below:

List of Journal Publications:

1. BAILEY, R. and SUN, Y. (2015) Corrosion and Tribocorrosion Performance of Thermally Oxidised Commercially Pure Titanium in a 0.9% NaCl Solution. *Journal of Materials Engineering and Performance*, 24 (4), pp. 1669-1678.
2. BAILEY, R. and SUN, Y. (2015) Pack carburisation of commercially pure titanium with limited oxygen diffusion for improved tribological properties. *Surface and Coatings Technology*, 261 (0), pp. 28-34.
3. SUN, Y. and BAILEY, R. (2014) Improvement in tribocorrosion behaviour of 304 stainless steel by surface mechanical attrition treatment. *Surface and Coatings Technology*, 253 (0), pp. 284-291
4. BAILEY, R. and SUN, Y. (2013) Unlubricated sliding friction and wear characteristics of thermally oxidised commercially pure titanium. *Wear*, 308 (12), pp. 61-70.

Acknowledgements

Firstly, I would like to offer my sincerest gratitude to my supervisor, Dr. Yong Sun, who has supported me throughout this project with his patience and knowledge, whilst allowing me the room to work in my own way. I could not ask for a better or friendlier supervisor.

I would like to thank the University for granting me access to all available facilities and Mr. Paul Taylor for his time and expertise in the operation of the scanning electron microscope. Also, a big thank you to all the mechanical work shop technicians, who were always on hand and willing to help at every opportunity.

I would also like to thank Dr. X.Y. Li of the University of Birmingham for making available both XRD and GDOS for structural characterisation.

I would like to thank De Montfort University for their financial support of my studentship. Special thanks are also due to the Alderman Newton's Educational Foundation, The Sidney Perry Foundation and the Wyvernian Fondation for providing additional financial support during the course of this work.

I would like to thank my family for providing both emotional and financial support throughout my studies, without which, this project would have been impossible.

Finally, a special thank you is required for Miss Faith Robinson, who has not only provided technical support in proof reading this work, but also offered a level of emotional support of which I will be eternally grateful.

Abstract

In the present study, efforts have been made to produce protective surface layers in order to improve the tribological, electrochemical and tribo-electrochemical response of titanium. In order to achieve this, two different techniques were employed: 1) thermal oxidation (TO) and 2) pack carburisation with oxygen diffusion (PC).

Thermal oxidation of commercially pure titanium (CP-Ti) was undertaken at a temperature of 625 °C for durations of 5, 20 and 72 h. This results in a multi-layered structure comprising a titanium dioxide layer (rutile) atop of an α -titanium oxygen diffusion zone (α -Ti(O)). Initial attempts have also been made to improve the frictional behaviour of the oxide layer, using a prior surface mechanical attrition treatment (SMAT) and controlled slow cooling after oxidation. The results demonstrate that these prior and post treatments have a positive effect on the tribological performance of the oxide layer.

Electrochemical and tribo-electrochemical characterisation was also carried out in a 0.9% NaCl solution. Electrochemical tests provided evidence that oxygen content in the upper part of the oxygen diffusion zone (depths < 5 μ m from the surface) helps to accelerate passive film formation and thus improve the corrosion resistance of CP-Ti. Tribo-electrochemical testing of TO-Ti was carried out against an alumina counter face under various anodic and cathodic potentials. It is shown that the rutile oxide layer offers low friction and improved wear resistance. An unusual anodic protection behaviour for the oxide film has also been observed. When the TO-Ti is polarised anodically during sliding, the durability of the oxide layer is prolonged, resulting in low friction and much reduced material loss.

In the present work a new pack carburising surface treatment method has been

developed, whereby oxygen diffusion and carburisation of CP-Ti were undertaken concurrently. Optimisation of the process showed that a temperature of 925 °C for 20 h resulted in a multilayer structure comprising of a titanium carbide (TiC) network layer atop of a relatively thick α -Ti(O) diffusion zone.

Tribological testing demonstrated that the new surface treatment can significantly enhance the tribological properties of titanium, in terms of much reduced friction ($\mu \approx 0.2$), improved wear resistance and enhanced load bearing capacity. Electrochemical corrosion testing also showed the PC-Ti retained the favourable corrosion characteristics of CP-Ti. Tribocorrosive testing revealed an improved tribological response when compared with that of untreated CP-Ti.

Contents

Contents	ix
List of Figures	xv
List of Tables	xvi
1 Introduction	1
1.1 Background and Motivation	1
1.2 Objectives	3
1.3 Thesis Organisation	3
Abbreviations	1
2 Literature Survey	5
2.1 Tribology	5
2.1.1 Friction	5
2.1.2 Wear	8
2.1.3 Surface Roughness	11
2.1.4 Surface Contact	12
2.1.5 Lubrication	14
2.2 Corrosion	17
2.2.1 Electrochemical Corrosion	17
2.2.2 Electrochemical Techniques for Corrosion Study	20
2.2.3 Corrosion Mechanisms	26

2.3	Tribocorrosion	29
2.3.1	The Synergistic Approach	30
2.3.2	The Mechanistic Approach	30
2.3.3	The Third-Body Approach	31
2.3.4	Electrochemical Techniques for Tribocorrosion Study	33
2.4	Titanium	37
2.4.1	General Properties	37
2.4.2	Titanium Crystal Structure	38
2.4.3	Alloys	40
2.4.4	Tribology of Ti	41
2.4.5	Corrosion	42
2.5	Titanium Dioxide (TiO ₂)	44
2.5.1	General Properties	44
2.5.2	Crystal Structure	46
2.5.3	Rutile TiO ₂	47
2.6	Titanium Carbide	48
2.6.1	General Properties	48
2.6.2	Crystal Structure	48
2.7	Titanium Surface Modification	49
2.7.1	Boronising	51
2.7.2	Nitriding	52
2.7.3	Oxidation	54
2.7.4	Thermal Oxidation	54
2.7.5	Carburising	62
3	Experimental Methods and Surface Analysis Techniques	67
3.1	Substrate Material and Preparation	67
3.2	Surface Engineering Techniques	68
3.2.1	Thermal Oxidation	68

3.2.2	Pack Carburisation	70
3.3	Chemical and Surface Analysis Techniques	72
3.3.1	X-Ray Diffraction (XRD)	72
3.3.2	Glow Discharge Optical Spectroscopy (GDOS)	74
3.3.3	Metallographic Examination	74
3.3.4	Light Microscope Analysis	75
3.3.5	Scanning Electron Microscopy (SEM)	75
3.3.6	Ball Cratering	78
3.3.7	Micro-Hardness Test	79
3.4	Tribological Measurements	80
3.4.1	Tribology Test	80
3.4.2	Wear Rate Measurements	81
3.5	Electrochemical Measurements	83
3.5.1	Free Corrosion Potential Measurements	84
3.5.2	Potentiodynamic (PD) Measurements	84
3.5.3	Potentiostatic (PS) Measurements	84
3.5.4	Mott-Stocky (M-S) Analysis	85
3.6	Tribocorrosion Testing	85
3.6.1	Open Circuit Potential	86
3.6.2	Potentiostatic Testing	86

4 Results and Discussion: Tribological, Corrosion and Tribocorrosion Behaviour of Thermally Oxidised CP Titanium 87

4.1	Microstructural Characterisation	88
4.1.1	Layer Morphology	88
4.1.2	Chemical Composition Analysis by GDOS	90
4.1.3	Diffusion Layer Thickness	91
4.1.4	X-Ray Diffraction	92
4.1.5	Surface Hardness	94

4.2	Unlubricated Sliding Friction and Wear Characteristics	95
4.2.1	Sliding Friction Behaviour	95
4.2.2	Wear Rate	100
4.2.3	Initial Attempts to Improve Oxide Layer Performance	102
4.2.4	Identification of Four Frictional Zones	107
4.2.5	The Role of Rutile in Reducing Friction	111
4.3	Electrochemical Behaviour as a Function of Depth from the Oxidised Surface	113
4.3.1	Potentiodynamic Behaviour	114
4.3.2	Current Transient Behaviour	116
4.3.3	Mott-Stocky Behaviour	118
4.4	Tribocorrosion Behaviour	120
4.4.1	Open Circuit Tribocorrosion Behaviour	120
4.4.2	Effect of Applied Potential on Tribocorrosion Behaviour	124
4.4.3	Total Material Loss Rate	129

**5 Results and Discussion: Optimisation of Pack Carburised CP-Ti with
Oxygen Diffusion for Improved Tribological Performance 132**

5.1	The Effect of Temperature on the Carburisation Process	133
5.1.1	Layer Morphology	133
5.1.2	Glow Discharge Optical Spectroscopy (GDOS)	134
5.1.3	X-ray Diffraction (XRD)	135
5.1.4	Tribological Response	136
5.1.5	Mechanisms Involved in Producing Optimal Film Performance	139
5.2	The Effect of Pack Composition on Film Growth	142
5.2.1	Structural Investigation	142
5.2.2	Tribological Response	144
5.2.3	Optimal Pack Composition	148
5.3	The Effect of Carburisation Time on Film Growth	148

5.3.1	Structural Characterisation	149
5.3.2	Tribological Response	157
5.3.3	Duration Optimisation	160
6	Results and Discussion: Tribological, Corrosion and Tribocorrosion Behaviour of Pack Carburised CP-Ti with Limited Oxygen Diffusion	161
6.1	Tribological Response	162
6.1.1	Unlubricated Sliding friction	162
6.1.2	Lubricated Sliding Friction	166
6.1.3	Tribological Comparison Between Pack Carburised Ti, Thermally Oxidised Ti and AISIS 440C Stainless Steel	167
6.2	Electrochemical Behaviour as a Function of Depth from the Carburised Surface	170
6.2.1	Potentiodynamic Behaviour	170
6.2.2	Current Transient Behaviour	172
6.3	Tribocorrosion Behaviour	175
6.3.1	Open Circuit Tribocorrosion Behaviour	175
6.3.2	Effect of Applied Potential on Tribocorrosion Behaviour	177
6.3.3	Total Material Loss Rate	183
7	Conclusions and Recommendations	186
7.1	Conclusions	186
7.2	Recommendations	191
	References	193

List of Figures

2.1	The impact of roughness on friction	7
2.2	Schematic figures of four types of wear	11
2.3	Surface profile	12
2.4	The effect of contact load on the number of contact points	13
2.5	The Stribeck curve	16
2.6	Anodic and cathodic polarisation of a passive metal	23
2.7	The Tafel Plot	24
2.8	Eleven types of corrosion	28
2.9	The tribocorrosion system	33
2.10	The unit cell crystal structure of α -Ti and β -Ti	38
2.11	Slip systems of hexagonal crystal lattices	39
2.12	Schematic diagrams showing the effect of alloying elements on equilibrium phase diagrams of Ti-alloys	41
2.13	Pourbaix diagram for titanium	43
2.14	The current-potential relationship for Ti in an acidic solution	44
2.15	The crystal phases of titanium dioxide	47
2.16	Crystal structure of titanium carbide	50
2.17	Titanium-boron phase diagram	51
2.18	Titanium-nitrogen phase diagram	53
2.19	Titanium-oxygen phase diagram	56
2.20	The variation of Titaniums lattice parameters with oxygen content	57

2.21	Titanium-carbon phase diagram	63
2.22	The variation of lattice parameters with carbon content	63
3.1	The cooling rates employed during this study	68
3.2	Schematic diagram of the surface mechanical attrition treatment (SMAT) setup	69
3.3	Schematic diagram of the pack carburisation vessel	70
3.4	The derivation of Bragg's law	73
3.5	Schematic diagram of the XRD apparatus	73
3.6	Schematic diagram of the Scanning electron microscope	76
3.7	Interactive volume of a material at the point of electron beam bombardment during SEM analysis	77
3.8	The ball cratering technique	78
3.9	Pin on disk tribometer	80
3.10	Wear track cross sectional area calculation using numerical integration	82
3.11	The three-electrode cell	84
3.12	Tribocorrosion test cell	86
4.1	Ball craters made on the surface of thermally oxidised Ti (TO-Ti)	89
4.2	SEM image showing the cross sectional profile of TO-Ti at 625 °C for, 20 h	89
4.3	GDOS profiles for TO-Ti	90
4.4	Theoretical oxygen concentration profiles at 625 °C for 5 h, 20 h and 72 h	91
4.5	XRD patterns for both untreated and TO-Ti	92
4.6	Hardness profiles for TO-Ti	94
4.7	Coefficient of friction (COF) curves recorded for the untreated and TO-Ti under a 1 N load	96
4.8	Wear track morphology for TO-Ti produced under a 1 N load	97
4.9	SEM image showing wear track morphology of the 625 °C/20 h sample under a 1 N load	98

4.10	COF curves recorded for the untreated and TO-Ti under a 2 N load	99
4.11	Wear track morphology of TO-Ti, produced under a 2 N load	100
4.12	COF curves recorded for the untreated and TO-Ti under a 5 N load	101
4.13	Morphology of wear track produced at 5 N load on 625 °C/20 h oxidised sample	101
4.14	Measured wear rate as a function of applied load for various samples	102
4.15	COF curves showing the effects of, the prior SMAT treatment and the controlled slow cooling	105
4.16	Wear track images displayed for TO-Ti treated with, furnace cooling, SMAT before TO and slow furnace cooling	106
4.17	Frictional characteristics of TO-Ti	109
4.18	Wear track morphology produced on the 625 °C/5 h oxidised sample, under a contact load of 2 N after various durations	110
4.19	Anodic polarisation curves for TO-Ti	115
4.20	Current transient curves measuring film formation at various depths from the surface of TO-Ti	117
4.21	M-S plots generated for the passive film at the surface and at various depths from the surface of the TO-Ti	118
4.22	Charge carrier density relative to the depth of the TO surface	119
4.23	Open circuit potential (OCP) and COF curves recorded for a contact load of 2 N in a 0.9% NaCl solution for TO-Ti	122
4.24	SEM images showing wear track morphology of the OCP tribocorrosion tests after various sliding durations	123
4.25	COF and current density against time for tribocorrosion testing at various potentials	125
4.26	SEM images showing the wear track morphology produced on the TO-Ti, after tribocorrosion testing at various potentials	128

4.27	Contribution of mechanical wear and corrosion to total material loss rate (TMLR) of TO-Ti and untreated Ti	131
5.1	SEM images showing the cross sectional structure after pack carburisation (PC) for 20 h at various temperatures	134
5.2	GDOS profiles produced after carburisation at various temperatures for a duration of 20 h	135
5.3	XRD patterns generated from samples carburised at various temperatures	136
5.4	COF curves recorded for samples pack carburised at various temperatures	137
5.5	Wear rate of pack carburised titanium (PC-Ti) produced at various temperatures	139
5.6	Optical micrographs showing cross sectional profiles and surface ball craters for PC-Ti with various pack composition	143
5.7	Layer thickness of TiC network and ODZ with regard to the carbonate concentration	144
5.8	COF curves for the response of PC-Ti produced under loads of 20 N and 40 N for various pack compositions	145
5.9	Optical images showing wear track morphology of Ti carburised at 925 °C for a duration of 20 h with various carbonate percentages	146
5.10	Wear rate of PC-Ti, produced under various loads with various pack compositions	147
5.11	Ball craters made on the surface of PC-Ti at 925 °C for durations of 10 h, 20 h and 40 h	149
5.12	Optical and SEM micrographs showing the cross sectional morphology of PC-Ti treated at 925 °C for durations of 10 h, 20 h and 40 h	150
5.13	EDX maps showing element composition of carburised Ti	152
5.14	GDOS profiles produced after carburisation at 925 °C for durations of 10 h, 20 h and 40 h	153

5.15	XRD patterns generated from the carburised samples produced at 925 °C for durations of 10 h, 20 h and 40 h	154
5.16	Cross sectional hardness profiles for the carburised samples produced at 925 °C for 10 h, 20 h and 40 h	156
5.17	Wear volume data for PC-Ti produced at 925 °C for 10 h, 20 h and 40 h under various loads	157
5.18	COF curves for PC-Ti produced at 925 °C for 10 h, 20 h and 40 h under a contact load of 40 N	158
5.19	Optical micrographs showing wear track morphology of Ti carburised at 925 °C for durations of 10 h 20 h and 40 h	159
6.1	Typical friction curve of PC-Ti	162
6.2	SEM images showing morphology of the wear track produced on the 925 °C/20 h carburised sample, under a contact load of 20 N for various durations	164
6.3	COF curves recorded at a contact load of 20 N for the PC-Ti in lubricated and un-lubricated conditions	166
6.4	Ball crater and wear track morphology produced at a load of 20 N for 30 h under lubricated conditions on PC-Ti	167
6.5	COF curves recorded at a contact load of 20 N for: Untreated Ti, TO-Ti, PC-Ti and AISI 440C stainless steel	168
6.6	Measured wear rate as a function of applied load for: Untreated Ti, TO-Ti, PC-Ti and AISI 440C stainless steel	169
6.7	Anodic polarisation curves measured for PC-Ti at various depths for the treated surface, in a 0.9% NaCl solution	171
6.8	Pourbaix diagram for TiC	172
6.9	Current transient curves in the log (I) vs. log(t) scale measured during film formation at various depths from the surface of PC-Ti	174

6.10	OCP and COF curves recorded for a contact load of 20 N in a 0.9%NaCl solution for PC-Ti	175
6.11	PC-Ti friction coefficient (μ) and current density (I) against time for tribocorrosion testing at various potentials	178
6.12	SEM images showing the wear track morphology produced on the PC-Ti, after tribocorrosion testing at various potentials	182
6.13	TMLR of PC-Ti, TO-Ti and untreated Ti	183

List of Tables

2.1	Properties of commercially pure titanium	37
2.2	Slip system of HCP crystal lattice	40
2.3	Properties of titanium dioxide (Rutile)	45
2.4	Properties titanium carbide	49
2.5	Titanium carbide structural properties.	49
2.6	The pre-exponential constants and activation energies for diffusion of oxygen in titanium	58
2.7	The pre-exponential constants and activation energies for diffusion of carbon in titanium	65
3.1	Chemical composition of CP-Ti samples	67
3.2	Summary of thermal oxidation (TO) conditions used in this study	70
3.3	Summary of the pack carburising (PC) conditions used in this study	71
3.4	Vickers hardness geometry	79
3.5	Tribometer test parameters	81
4.1	Structural summary of TO-Ti	88
4.2	Calculated lattice constants of α -Ti(O) and rutile (TiO ₂)	93
5.1	Variation in carbon and carbonate percentage used within the pack	142
5.2	Summary of the layer thickness developed during pack carburisation	151
5.3	Calculated lattice constants of α -Ti(O) and TiC	155

Chapter 1

Introduction

1.1 Background and Motivation

Titanium possesses a unique combination of light weight, high strength, excellent corrosion resistance and biocompatibility, making it a desirable engineering material. However, the uses of titanium have been restricted to mostly non-tribological applications, due to the severe galling problem encountered in sliding contacts, producing large wear rates and the possibility of seizure [1, 2]. Such a poor tribological response of titanium has long been the subject of investigations, with many factors being identified as contributing towards its high and unstable friction and severe adhesive wear. Dong and Bell [2] suggested a compound effect of electron configuration, crystal structure and lubrication ineffectiveness, that results in a high level of adhesive wear associated with a large amount of material transfer when subjected to tribological conditions. As the poor tribological response of titanium is a manifestation of its surface traits, surface modification can be an effective approach to overcome such issues [3].

There have been numerous works focused on improving the tribological characteristics of titanium, and the following surface treatments have been demonstrated by various authors: boronising [4, 5], nitriding [6, 7], thermal oxidation [8–10], carburising [11, 12] and laser surface treatments [13, 14].

Of these methods thermal oxidation (TO) offers a simple and cost effective way to improve the friction/wear characteristics of titanium. It has been established that thermal oxidation produces a layered structure comprising of an oxide layer at the surface and a hardened oxygen diffusion zone in the subsurface of titanium [2]. The oxide layer can have low friction and low wear rates [15], while the oxygen diffusion zone can be beneficial in enhancing the load bearing capacity, the lubrication ability and abrasive wear resistance of titanium [16, 17]. However, the oxide layer generated has a tendency to delaminate from the substrate, causing sudden failure and removal of the layer, even at relatively low loads. This is especially true when thicker layers are generated during high temperature oxidation or prolonged oxidation [2, 10]. Numerous studies have focused on the optimising of the thermal oxidation process in order to create a sufficiently thick but tightly adherent TiO_2 (rutile) layer [2, 10, 18]. However, there is still much work to do in order to create a thick but tightly adherent film.

Titanium Carbide (TiC) has attracted considerable attention due to its high melting point, low density, high hardness (2500-3000HV), superior chemical and thermal stability, and outstanding wear resistance [19]. Carburising can be used to produce a TiC layer on titanium and its alloys for improved tribological properties [11, 20, 21]. One of the main issues associated with titanium carburisation is the high affinity between titanium and oxygen, which results in the formation of titanium dioxide (TiO_2) at elevated temperatures. Therefore, carburisation is normally undertaken within a vacuum or in an oxygen-depleted environment to allow carbon absorption to occur rather than oxidation [21]. Another issue relates to the maximum solubility of carbon in titanium. Due to the low solubility there will be a limited subsurface hardening effect of the diffusion zone. This diffusion zone is often necessary for increasing load bearing capacity [16]. Therefore, carburised titanium is expected to have limited load bearing capacity.

In order to withstand the high stresses associated with many practical applications, such as in gears and bearings, deep case hardening is required along with a low wearing, hard surface. None of the above methods are able to successfully achieve the relevant

level of protection [16].

1.2 Objectives

The main aim of the research was to develop new methods/techniques that could be used to improve the wear, corrosion and tribocorrosive characteristics of commercially pure titanium, through surface modification. In order to achieve this, the following tasks must be completed:

- To understand the thermal oxidation mechanisms and kinetics of titanium.
- To optimise the thermal oxidation process for improved film-substrate adhesion.
- To investigate the effect of oxygen diffusion on the tribological and electrochemical response of titanium.
- To develop a new carburising technique to improve the tribological, electrochemical and tribo-electrochemical performance of titanium.

1.3 Thesis Organisation

This thesis contains seven chapters. Chapter Two presents an extensive literature review. The review covers some basic theories of tribology and corrosion while focusing on the tribological and electrochemical properties of titanium. This section also gives an overview of some currently employed methods of surface engineering titanium.

In Chapter Three, the sample preparation, experimental procedures and equipment used were described.

Chapter Four covers all work regarding the thermal oxidation of titanium. Material characterisation of thermally oxidised titanium was carried out with the tribological, electrochemical and tribo-electrochemical behaviour described.

Chapter Five covers all work regarding a new pack carburisation technique for titanium. All material optimisation and characterisation results are discussed.

Chapter Six covers the testing of the optimised material characterised in Chapter Five. Tribological, electrochemical and tribo-electrochemical behaviour of the pack carburised titanium was investigated.

The main conclusions from this study and the possible future work which could be carried out as a result of the main findings are given in Chapter Seven.

Chapter 2

Literature Survey

2.1 Tribology

Tribology is an all encompassing and multi-disciplined area of study. Tribology is defined as the science and technology of interacting surfaces in relative motion and of all related subjects and practices [22]. This implies that tribology is the study of friction, wear and lubrication. The word tribology in itself is relatively new, with its use seen in only the more recent of publications, first dating from around 1966 [23]. However, that being said, the topics that are covered by the term tribology have been studied for hundreds, if not thousands of years.

Modern day research into tribology is focused around the reduction in material loss in order to improve material longevity and durability. This is achieved through the improvement of material characteristics or through the control of friction. In order to carry out such improvements, knowledge as to the contact mechanics and structural chemistry of materials surfaces and interfaces are required [24].

2.1.1 Friction

Friction is a resistive force that is brought about when two bodies in contact are moved relative to each other [22]. Friction is often associated with wear and this can be greatly

affected by a materials surface structure and any lubricating environment. Friction between two surfaces usually manifests itself in the form of heat. However, there are other modes of energy dissipation, which will be discussed at a later stage. This energy dissipation is often an unwanted side effect and can create inefficiency within mechanical systems, such as bearings and gears. There are, however, cases where friction is required, such as in brakes and clutches. The need to control the level of friction between two surfaces is of great importance and relevance [22, 24–26].

2.1.1.1 The Coefficient of Friction

When two bodies are forced to move relative to each other, a tangential force (F_t) is required. This force allows the moving body to overcome the normal load (F_n) of the desired moving body. There is also a frictional constant, which is unique between the two contacting bodies. This frictional constant is known as the coefficient of friction (μ) and can be seen expressed in Eq. 2.1 [25]. The coefficient of friction (COF) allows for a quantitative value to be associated with the friction experienced between the surfaces of the contacting bodies. The coefficient of friction can be affected by: chemical, topological and structural changes during sliding contact [22, 25, 27].

$$\mu = \frac{F_t}{F_n} \quad (2.1)$$

2.1.1.2 Components of Friction

No surface is completely flat and when two surfaces are brought together, they touch at asperity interfaces. At these points, the contact pressure may be close to the yield strength of the material, as discussed later by Eq. 2.9 (page 13) and 2.10 (page 14). When sliding is initiated, it can be seen that these asperities will be deformed along the points of surface contact. The friction force experienced in this instance is known as the deformation of asperities (F_d) and is associated with the ploughing that can be observed when a harder material is in contact with a softer material. Adhesive friction is another component of

friction that can be observed. Under the combined conditions of an applied load and perpendicular sliding, a large amount of heat energy is produced. This can lead to the growth of junctions between the two surfaces. These junctions must then be sheared for the sliding movement to continue, this is known as adhesive friction (F_a). During sliding there is a combination of both F_d and F_a friction. This allows us to show that the total frictional force (F_t) can be described via Eq. 2.2.

$$F_t = F_d + F_a \quad (2.2)$$

In order to control friction to the required levels, it is important to understand the type of friction occurring. When there is high surface roughness invoked through spiky asperities and an undulating surface, the dominating friction component is that of plastic deformation. Conversely, it can be seen that low surface roughness and flat surfaces generate large amounts of adhesion. This can be seen graphically in Fig. 2.1 [25–27]. This curve shows, an optimum surface roughness range that gives the lowest friction. Below this optimum roughness, friction increases due to increased adhesion between very smooth surfaces. Above the optimal roughness, friction also increases due to increases asperity deformation.

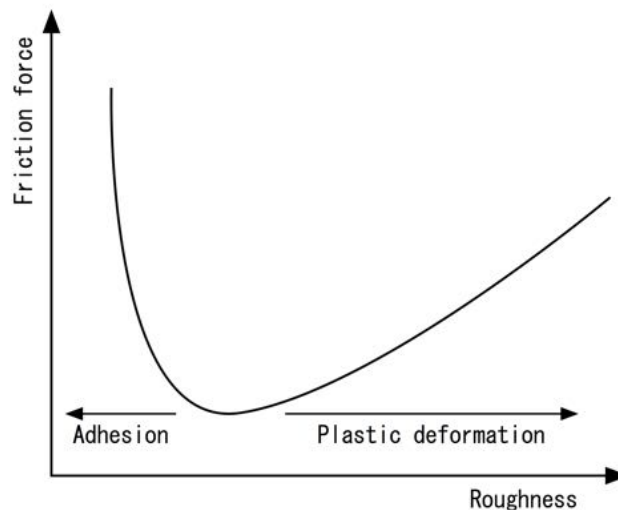


Fig. 2.1: The impact of roughness on friction [25]

2.1.2 Wear

Wear is one of the main modes of material degradation and is generally observed where friction occurs. This type of degradation is achieved through the physical contact of materials in motion. Wear in most cases results in some form of gradual material loss which can lead to failure. The effects of wear are mostly related to the surface condition of materials [24–26, 28].

When two materials are placed in sliding contact, material degradation will occur. The material lost by such movement (wear volume) can be expressed mathematically by Eq. 2.3. This equation allows the abrasive wear rate of the softer material in sliding contact to be evaluated.

$$\frac{V}{L} = K \frac{F_n}{H} \quad (2.3)$$

where: V is the volume of the material lost, L is the total sliding distance, F_n is the normal applied load, H is the softer materials hardness and K is the wear coefficient. Eq. 2.3 [25] is usually rearranged by creating a new quantity K/H and is known as the dimensional wear coefficient (k') with units of $\text{mm}^3 \text{N}^{-1} \text{m}^{-1}$. This new quantity represents the volume of material removed, per unit distance, per unit load (see Eq. 2.4) [25].

$$k' = \frac{V}{LF_n} \quad (2.4)$$

2.1.2.1 Mechanisms of Wear

Wear can be classified in a number of ways, a simple classification would be that between non-lubricated wear (dry wear) and lubricated wear. It is, however, common practice to classify wear through the mechanisms responsible for its generation. Wear consists of multiple mechanisms, making it difficult to distinguish between types of wear. It has, however, been achieved and one of the most common methods widely used is that suggested by Budinski. In this approach, four classifications of wear are created: Adhesive wear, abrasive wear, corrosive wear and surface fatigue wear [26], depicted

schematically in Fig. 2.2.

Adhesive Wear

Adhesive wear is the transfer of material as generated when cold welded junctions are created between two surfaces and then sheared through a sliding motion. This removed material may stay attached to the harder material or become detached and involved in the wear process, or be observed as wear debris. Severe damage of this type can result in the tearing and removal of large chunks of material. When observed on a large scale, this type of adhesive wear is known as galling and is a particular issue when both contacting surfaces are made from the same material or when there is poor lubrication, high speed sliding and high temperatures. The ratio of surface hardness and elasticity modulus (E/H) is the most important properties that allows for suppressed adhesive wear [26, 28].

Abrasive Wear

Abrasive wear is observed when hard particles or hard rough surfaces are forced to move against a solid surface. This type of wear is identified by the creation of grooves/scratches in the softer material, as the harder material moves over it and is known as two body wear. The formation of wear particles can also, in some cases, be observed. Due to the creation of wear particles, this generates a second mode of wear that can occur during abrasive contact that is known as three body wear. Abrasive wear can be categorised according to the type of contact occurring and is generally separated into four categories [26, 28]:

- **Low stress abrasion;** low contact stresses that do not induce plastic deformation, results in little, if any, plastic deformation/strain hardening within the contact area. Wear appears as surface scratches and a ploughing effect can be observed.
- **High stress abrasion;** high contact stress induces plastic deformation and thus strain hardening of the material occurs. Large scratches and indentation (pitting) from particles can be observed.

- **Gouging abrasion;** this is a high stress abrasion that can be seen as large grooves or gouges. Plastic deformation is a leading factor in the creation of such surface markings.
- **Polishing wear;** very low stresses are used and material surfaces show no visible sign of scratching, fracture and plastic generation leads to the smoothing (reduction in roughness) and brightening of surface material.

Corrosive Wear

When sliding contact takes place in a corrosive environment, chemical degradation can add to the physical effects of wear [28]. While there can be some lubricating effect from the fluid, substantial wear is inevitable. If a passive metal is subjected to sliding contact in a corrosive environment there are three possible outcomes:

- The formation of a lubricating film within the contact zone, which can inhibit both corrosion and wear.
- A weak film is produced which is then removed over and over resulting in an increased rate of wear.
- A protective surface film may form but then through subsequent surface contact pitting can develop. Galvanic coupling between the film and underlying substrate could cause rapid corrosion [30].

Surface Fatigue Wear

Repeated sliding and rolling of a surface can result in subsurface micro cracking from subsurface stresses. Subsurface stresses can create areas of high plastic deformation and low deformation. This change in material structure, can eventually lead to crack growth and surface fracture resulting in visible pits and spalls [26, 28].

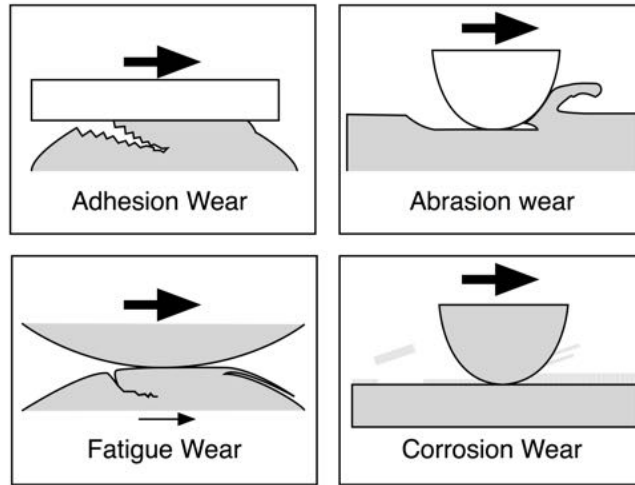


Fig. 2.2: Schematic figures of four types of wear [31]

2.1.3 Surface Roughness

When a solid surface is investigated on a microscopic level, it can be seen that no surface is truly flat. Surface irregularities can be seen on the most finely polished samples. These irregularities are defined as the surface roughness. The surface roughness of a material is defined by Eq. 2.5. This uses a centre line average approach and the height (y) above this line to calculate the average surface roughness (R_a) over a given length (L), as shown in Fig. 2.3 [25]. Using the average surface roughness fails to show the difference between a gently undulating surface and ones that have much spikier peaks. The root mean square (RMS) roughness (R_q) gives a greater significance to the surface variations, as shown in Eq. 2.6 [22, 25].

$$R_a = \frac{1}{L} \int |y(x)| dx \quad (2.5)$$

$$R_q = \sqrt{\frac{1}{L} \int y^2(x) dx} \quad (2.6)$$

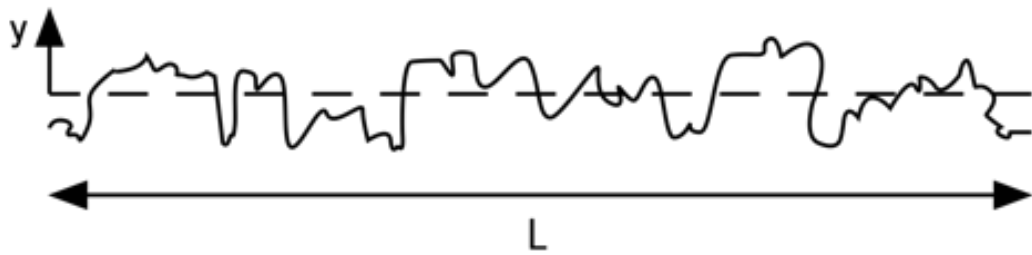


Fig. 2.3: Surface profile showing surface height relative to the average centre line [25]

2.1.4 Surface Contact

When two surfaces are brought together, it can be seen that there will initially be only a few points of contact between each surface. When two surfaces meet, it is possible to calculate the pressure experienced at the interface using Hertz contact theory. A simple example of point contact would be that of a sphere pushing on a plate, assuming only one large asperity is present for each surface. Eq. 2.7 describes the maximum pressure exerted at the point of contact [32].

$$P_0 = 0.5784 \times \sqrt[3]{\frac{wE_r^2}{r^2}} \quad (2.7)$$

Eq. 2.7 shows the maximum contact pressure (P_0) generated using a sphere of radius (r) and an applied load (w). The term denoted by E_r is known as the contact modulus and is calculated by using the Young's modulus (E) and the Poisson's ratio (ν) for each of the contacting surface materials, as shown in Eq. 2.8 [32].

$$\frac{1}{E_r} = \frac{1 - \nu_1^2}{E_1} + \frac{1 - \nu_2^2}{E_2} \quad (2.8)$$

When studying surface contact, it is true to say that almost all surfaces will not be in contact via a single asperity but rather multiple asperities will be in contact at any one

time. The number of peak asperities in contact at any one time, increases with increasing contact load. Fig. 2.4 gives a graphical representation of the effect load has on the number of contact points between surfaces. This figure also shows how the actual contact area is substantially smaller than the apparent contact area for two surfaces.

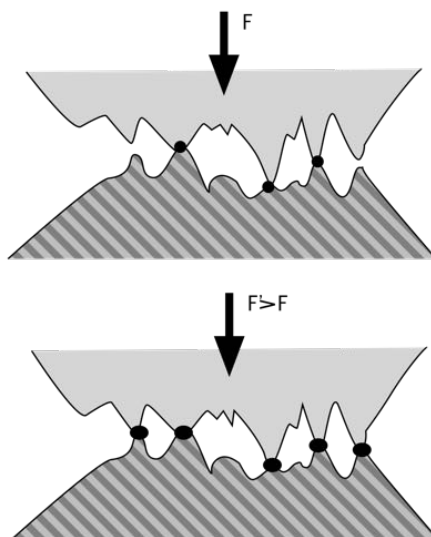


Fig. 2.4: Diagram showing how increasing contact load from F to F' increases the number of contact points [24]

The mathematical expression denoted by Eq. 2.7 is said to be true when there is a single asperity contact. This is helpful in determining a rough estimate as to the type of deformation that may be experienced under a given contact load. However, there are methods that can help to deduce the type of asperity deformation that is likely to be experienced during loaded contact. This method requires that all asperity tips be considered spherical. For this case, the contact pressure can be expressed using Eq. 2.9 [24].

$$P = 0.3 \left[\frac{E}{1 - \nu^2} \right] \sqrt{\frac{\sigma}{\beta}} \quad (2.9)$$

Where β is the mean radius of curvature assumed for the spherical asperities and σ is the standard deviation of the height distribution. This equation can be modified to introduce a new parameter known as the plasticity index (ψ). This allows the threshold

between plastic and elastic deformation to be calculated [24].

$$\psi = \left[\frac{E}{H(1 - \nu^2)} \right] \sqrt{\frac{\sigma}{\beta}} \quad (2.10)$$

Where E , H and ν are the Young's modulus, hardness and Poisson's ratio of the softest material. The plasticity index shows the nature of asperity deformation using the following classification:

- $\psi \geq 1$: Plastic contact
- $1 > \psi \geq 0.6$: Elasto-plastic contact
- $\psi < 0.6$: Elastic contact

These equations allow for the basic analysis of surface contact to be generated and provide a starting block for suggesting how a material will react under differing contact conditions [22, 24–26]. When surface engineering, the E/H ratio is of great importance. Increasing the surface hardness of a material will decrease the plasticity index and promote elastic contact. Increasing the plasticity index can change the mode of surface contact, thus surface hardening techniques can be an effective method for reducing adhesive wear. A surface coating with high hardness and low Young's modulus is also beneficial in reducing plasticity index.

2.1.5 Lubrication

Lubrication is a method that is commonly employed to reduce friction between sliding surfaces. Lubricants can be either in solid or liquid form and work by reducing or removing the conditions for adhesive and abrasive wear to occur. The most common form of lubrication is that using oils or greases. These allow for a great reduction in friction and wear but also help to control the dissipation of heat [24–26].

Liquid lubricants separate opposing surfaces through pressure within the fluid film. This can be caused by the shape of the opposite surfaces or by an external force. The

reduction in friction observed can be related directly to the lubricating liquids flow properties.

When dealing with lubrication, the value of Lambda (λ) provides a measure as to how likely and how severe asperity interactions will be during lubricated sliding. The lambda ratio is described by Eq. 2.11 [33].

$$\lambda = \frac{h_{min}}{\sigma^*} \quad (2.11)$$

where h_{min} is the minimum film thickness and σ^* is the root mean square surface roughness of the two surfaces defined by Eq. 2.12 [33].

$$\sigma^{*2} = R_{q1}^2 + R_{q2}^2 \quad (2.12)$$

where R_{q1} and R_{q2} are the root mean square surface roughness values for each surface. The lambda value can be associated with differing boundary conditions between lubricant and surfaces:

Hydrodynamic Lubrication; when $\lambda > 3$ there is a full fluid film separating both surfaces. This complete separation allows for low friction and low wear to be achieved.

Mixed Elastohydrodynamic Lubrication; when $1 < \lambda < 3$ this is when there is a film between two surfaces but there is still contact between asperities on each surface. The overall result is still a reduction in friction and wear. This is a more real life representation of lubrication.

Boundary Lubrication; when $\lambda < 1$ it is often due to extremely high loads or low sliding speeds. This type of lubrication generates pockets of high pressure lubricant trapped between surfaces. This can lead to severe surface damage of the materials.

The differing boundary conditions have also been associated with the coefficient of friction (μ) by Stribeck. It was demonstrated that the friction coefficient is directly

proportional to the lubricant viscosity (η), the relative speed of the two surfaces (ω) and the inverse of the contact pressure (P).

$$\mu = \frac{\eta\omega}{P} \quad (2.13)$$

This is often shown graphically through the use of a Stribeck diagram as shown in Fig. 2.5. This can be related to the lambda ratio, in a sense that the three lubricating regimes identified are also fully present in the diagram. The diagram shows the initial boundary lubrication having little effect on the frictional response due to the large amounts surface contact occurring. As the speed is increased mixed lubrication occurs. Whereby, the film is starting to generate between the surfaces, reducing the amount of surface contact. There is a point when the two surfaces are no longer in contact and are separated by a very small film. At this point the optimal lubrication conditions are observed with the lowest coefficient of friction achieved. Increasing the velocity of the surfaces further results in an increased coefficient of friction. This is due to fluid drag, as the surfaces separated further friction is produced within the lubricant itself [24–26].

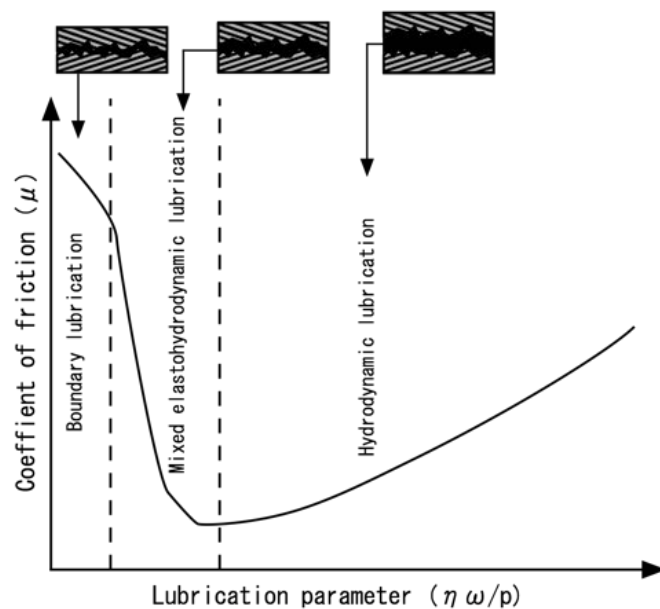


Fig. 2.5: The Stribeck curve [25]

2.2 Corrosion

Corrosion is a natural process and is, in essence, a result of the conservation of energy and the need for high energy systems to move to lower, more stable systems in accordance to the second law of thermodynamics [27]. When defining corrosion in metals, the most common and understood description is that of a process in which the interaction of metal and the environment leads to a detrimental effect on the material properties, which is undesirable deterioration of a material [34]. When a metal is placed in a corrosive environment, there are three ways in which the metal can respond: The first case is that it could act in an immune state (no corrosion); the second case is that it could act in an active manner (corrosion causing material loss) and the third case is that the material could exhibit passive behaviour. When a material acts passively, this is down to the creation of a passive oxide film on the metal surface. This greatly reduces the corrosion rate of the material by providing an enhanced corrosion resistant film [26]. This deterioration of an active state metal is an electrochemical process, which can result in a loss of material or accumulation of deposits [23].

2.2.1 Electrochemical Corrosion

When a metal is in an active state, corrosion involves the transfer of electrons, thus an electric current is produced during the corrosion process. This loss of electrons happens when an active metal is in some form of electrolytic solution. This creates metal ions which are soluble in the solution. As a result, metal is lost from the surface structure and therefore, corrosion takes place. When metal atoms undergo corrosion reactions, they are converted into ions due to the loss of electrons to the corrosive medium described by Eq. 2.14.



where M is a metal, e is an electron and n is the valence. This electron producing reaction is formally known as an anodic reaction, resulting in oxidation of the metal as electrons are transmitted. This movement of electrons is coupled by a cathodic reaction which consumes these electrons and is termed reduction. The cathode is an essential couple to the anode and when connected electrically in an electrolyte, they produce what is known as a basic wet corrosion cell. It is possible for the anode and cathode to exist on the same piece of metal. If any of the four parts of the wet corrosion cell are removed, then corrosion will not occur. All aqueous corrosion can be thought of in this way, even if they do not resemble this model directly [26, 27, 34].

The electrical nature of corrosion can be described through changes in electrical potential and current flow and thus, can be described as a change in the free energy of the material. Therefore, electrical measurements can be used to measure corrosion. Faradays Law (Eq. 2.15) describes the relationship between free energy (ΔG) and electrochemical potential (E).

$$\Delta G = (-nF)E \quad (2.15)$$

Where F is Faradays constant ($96.494 \text{ C mol}^{-1}$) and n is the number of electrons in the reaction. A negative value for the free energy shows that the metal will react to form corrosion products. Although a negative value for ΔG means a reaction will occur, there is no telling the rate of the reaction. However, it can be shown that the greater the negative, the greater the reactivity of the metal. A positive value shows that a reaction will not occur.

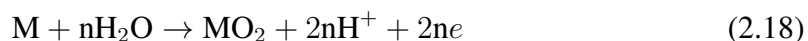
When considering aqueous corrosion, the concentration of ions can have a huge effect on the corrosion rate of materials. By using Faradays law, entropy and Gibbs energy, a relationship between potential and species concentration can be generated. This is known as the Nernst equation (Eq. 2.16) and is of great use for determining the effect of ionic concentration on the electrode potential [26, 27].

$$E = E^o - \frac{RT}{zF} \ln \frac{[\text{products}]}{[\text{reactants}]} = E^o - \frac{0.059}{z} \ln \frac{[\text{products}]}{[\text{reactants}]} \quad (2.16)$$

E is the half-cell reduction potential at the temperature of interest, E° is the standard half-cell reduction potential, R is the universal gas constant ($8.314472(15)\text{J K}^{-1}\text{mol}^{-1}$), T is the absolute temperature, F is the Faraday constant, z is the number of moles of electrons transferred in the cell reaction or half-reaction. Eq. 2.16 can be used to show a relationship between potential and pH [27], as described by Eq. 2.17.

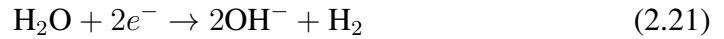
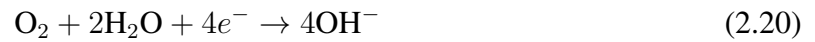
$$E = E^\circ - 0.59\text{pH} \quad (2.17)$$

E is the half-cell reduction potential at the temperature of interest, E° is the standard half-cell reduction potential, $\text{pH} = -\log[\text{H}^+]$ for the solution. Using Eq. 2.17, Pourbaix diagrams can be created. These can be used to show how a material will respond to a given combination of Potential and pH. These diagrams predict what will occur on a metal surface in contact with an aqueous solution [27, 35, 36]. Fig.2.13 shows the Pourbaix diagram for titanium at 25°C which will be discussed in detail in section 2.4.5. E/pH diagrams are excellent for showing how concentration of ions can affect the corrosion potential of a metal and how potential and pH are directly linked. These diagrams also help to show why, under certain conditions, some materials show lower corrosion rates than their reactivity suggests. It can be seen that Eq. 2.14 is true for active metals but is not the case for passive metals. Eq. 2.18 is a description of the reactions that occur on the surface of a passive metal when oxidation forms a passive film on the metals surface [37].



The transferred electrons are consumed by the reactions of oxidising agents such as protons (acidic solutions), dissolved oxygen (aerated solutions) and water according to

the following reactions:



These reactions show why some materials that show passive behaviour are much better at resisting corrosion than their corrosion potential would suggest [37].

When considering the corrosion of metals, there are other contributing factors affecting corrosion. The first of these is the metallurgical characteristics of the material. The differing metal crystal structures and the location of grain boundaries can have an effect on the corrosion potential of a material. When working with metals, there are few circumstances where single crystal structures are used. Most materials exhibit areas of different crystal structure and grain boundaries. It is also important to remember a materials inherent tendency to corrode and its reactivity; the more reactive a metal, the more willing it is to corrode and to form corrosive products.

2.2.2 Electrochemical Techniques for Corrosion Study

There are many methods to measure the corrosion rate of materials, each giving its own unique view as to the kinematics of corrosion taking place. These tests include: field tests, simulated service tests and laboratory accelerated tests. Field and service tests involve the visual monitoring of specific parts or samples over long durations of time to see how they react to a particular environment. This is beneficial to know precisely how a material will react to a given condition. However, for a more general view and a snapshot of material characteristics in a particular environment, it is important to run laboratory tests. Of these tests, in particular electrochemical tests offer an insight into the kinematic mechanisms of corrosion in real time and provide data that no other methods can offer.

In the study of electrochemistry, the three-electrode cell is the standard laboratory

apparatus used for the data acquisition and the investigation of the corrosion properties of materials. In this three-electrode setup, the working electrode is the sample to be tested. The auxiliary electrode is there to carry the current created in the circuit and is not needed when measuring potential. The reference electrode is there to measure the potential of the working electrode. In order to minimise IR drop, the reference electrode should be placed as close to, but not touching the working electrode. These three electrodes are connected to a source of e.m.f, a galvanometer and a voltmeter in an electrolyte solution. The data is usually collected on a computer using a data logger. The setup described above allows for readings of both potential and current. It also allows for the current to be measured at set potentials to analyse the effects of potential on the corrosion behaviour of the sample [27].

When carrying out electrochemical tests, it is important to use a combination of techniques to understand fully the surface state and the corrosion potential of the given material. A number of recent publications ([37–39] to name but a few) have used the three electrode setup and the following techniques when characterising the corrosion of materials.

2.2.2.1 Open Circuit Potential (OCP)

Open circuit potential (OCP) also known as free corrosion potential (E_{corr}), is when the anodic reaction rate is equal to the cathodic reaction rate. Therefore, there is no net current flow to or from the electrode (no external current or voltage). The value of E_{corr} is often used to give an indication of surface state, be that passive or active, allowing changes in a materials surface condition to be monitored. OCP measurements can also be used to determine whether a protective film has been removed and at what point the film loses integrity.

The actual relevance of the potentials measured is negligible and interpretation of the results is of greater importance. If the sample has a relatively high OCP, this shows the sample is in a passive state. Reversely, if the OCP is low, the sample is activated and

corrosion is more likely to occur. This is beneficial for demonstrating the changing state of a material as time goes on and any sudden shifts in potential shows a change in the materials active state. If there is a shift from a high value of OCP to a low value of OCP, this is known as a cathodic shift and is usually associated with the activation of a metal's surface. Reversely, if the materials OCP changes from a low to a high value this can be signalling the onset of passivation. Open circuit potential is a good way of determining the state of a material in real time and allows for characterisation of the material's reaction to a particular corrosive environment [40].

It is important to mention the shortcomings in the measurement of OCP readings. The potential generated during this type of reading is an average of the whole material surface and does not identify areas of anodic and cathodic potential in the sample, just the overall average. This means that some areas of the sample could be corroding faster than the OCP suggests. There is also an issue in the fact that OCP does not represent any definitive answer as to the amount of corrosion occurring, it only provides a visual map of the surface condition over time. This data can be compared to other samples to give an insight into the effective corrosive resistance of one material to another [35].

2.2.2.2 Potentiodynamic Polarisation (PD)

In this type of measurement, the potential of the sample is changed from being cathodic to anodic during a potential sweep. This type of measurement is one of the most widely used examples of electrochemical corrosion testing. This potential sweep allows the relationship between the current and the potential to be established dynamically, which is called a polarisation curve. Changing the potential, is in effect, changing the corrosive nature of the solution [40]. The changing current density shows the change in corrosion rate. This type of measurement is useful in determining the active passive behaviour of the test sample, over a range of potentials.

In Fig. 2.6, a typical polarisation curve is shown for a passive material. A good corrosion resistant material should display the following characteristics: a low current

density in the passive region, a wide passive potential range and a high corrosion potential. These types of corrosion tests are very effective means of studying the surface condition of a sample in real time. The larger the current density, the more active the material surface is and susceptible to corrosive attack [41].

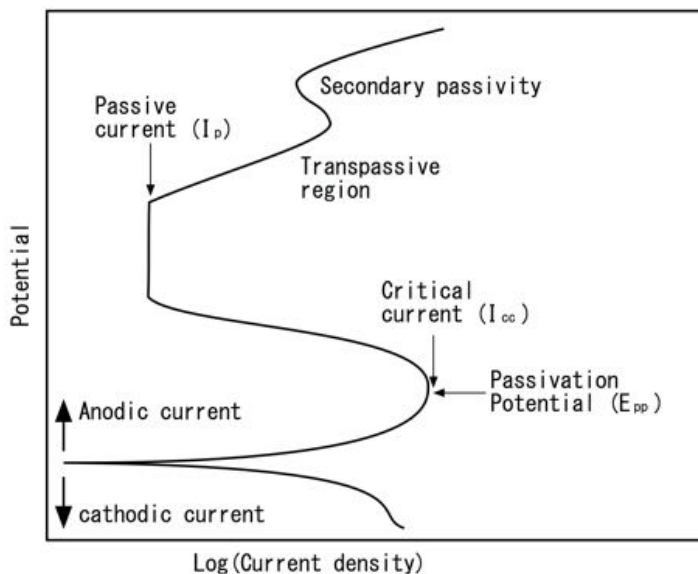


Fig. 2.6: A hypothetical polarisation sweep showing both anodic and cathodic potentials of a passive metal [42]

Using potentiodynamic polarisation, it is sometimes possible to determine the free corrosion potential (E_{corr}) of the material and thus, determine the corrosion current density (i_{corr}) using a technique called the Tafel Plot. Using the anodic and cathodic branches, the tangential lines to these slopes can be used to extrapolate the free corrosion potential, which is equivalent to the open circuit potential. At this locality, the current density can then be observed. This is one of the simplest way to calculate the corrosion rate under freely corroding conditions [27, 42]. Fig. 2.7 shows how this is done on a hypothetical plot.

Polarisation curves are a good method used to understand the reaction kinetics at a materials surface; they also give a quantitative result for corrosion rates when the data is ideal. However, there can be occasions when the Tafel Plot is not reliable and the

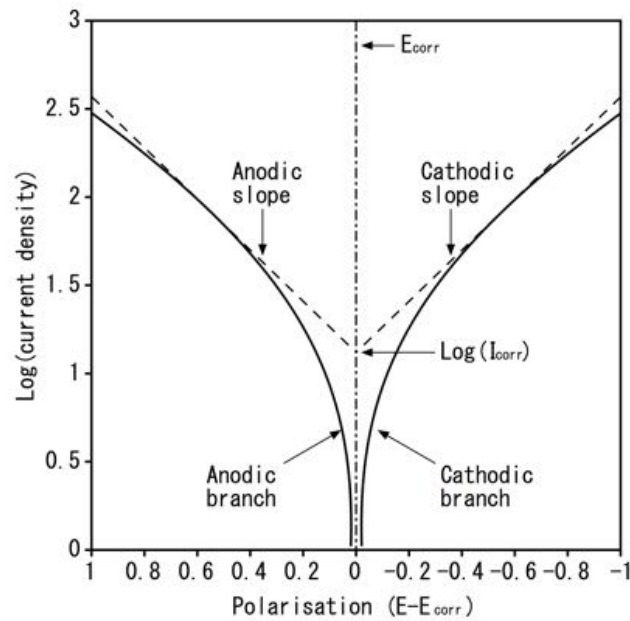


Fig. 2.7: Tafel Plot that can be used to calculate the corrosion rate under no applied potential [41]

corrosion rate at open potential is incorrect. Therefore, experience and knowledge of polarisation curves are required to fully understand the data obtained and the relative kinetics of a material under different conditions [41]. Polarisation is of great significance in showing the active and passive states of a material at different potentials. There is however, the issue that most real world situations are not under any polarisation and just at OCP. The polarisation results show how a material will react under several environmental conditions, that are not necessarily going to be experienced.

2.2.2.3 Potentiostatic Polarisation (PS)

During potentiostatic polarisation, the potential (E) of a test sample is held constant either anodically or cathodically. The current (I) is then measured against time (t). Plotting current against time for the polarised sample can give insight into the evolution of electrochemical kinetics involved during corrosion. Using fixed potentials, it is possible to simulate different corroding conditions using just one basic electrolyte [37]. Potentiostatic measurements are of great importance in the study of passive materials, as

the growth/decay of passive films can be measured. The Point Defect Model (PDM) and the High Field Theory (HFT) are well used models to describe the change in ion flux at the samples surface [43–45]. As the passive film thickens, the ion flux is reduced, leading to lower conduction and therefore, lower current densities. The decay of current over time has been expressed mathematically using the following formula [44–46]:

$$I = 10^{[-A+K \log t]} \quad (2.22)$$

Therefore, if the current transient curve is plotted using a logarithmic scale ($\log I$ against $\log t$), the K value will describe the slope. It has been suggested that the value of K can be an indication as to the surface condition and structure of the passive film. If the value of $K = -1$, a highly compact protective film is present. However, if $K = -0.5$, this can be an indication of a porous or broken film. Using this value of K , protective films can be analysed for susceptibility to corrosive attack. The closer the value K is to -1 , the greater the protection offered by such film [44, 45].

2.2.2.4 Mott-Stocky (M-S) Measurements

Passivity in metals is due to the formation of a thin protective film at the metals surface and most passive films formed this way show semiconductor characteristics [47–50]. The stability and effective corrosion resistance of a passive film can be correlated to the amount of dopant. Higher levels of dopant indicate a film with lower corrosion resistance due to larger quantities of charge carriers.

Mott-Schottky (M-S) plots can be used to determine the dopant density for both n-type (N_D) and p-type (N_P) semiconductors. Eq. 2.23 [45, 49, 51] shows the relationship between space charge layer Capacitance (C) and dopant density.

$$N_{D/P} = \frac{2C^2}{\epsilon_0 \epsilon e} \left(E - E_{fb} - \frac{kT}{e} \right) \quad (2.23)$$

Where ϵ_0 is the vacuum permittivity ($8.85 \times 10^{-14} \text{ F cm}^{-1}$), ϵ is the dielectric

constant of an oxide, e is electron charge (1.602×10^{-19} C), this is negative for P-type semiconductors, E_{fb} is the flat band potential, k is the Boltzmann constant (1.38×10^{-23} m² kg s⁻² K⁻¹) and T is the temperature in K. By measuring film impedance (Z'') at various potentials under a given frequency (f), the capacitance (C) can be calculated using Eq. 2.24 [45].

$$C = \frac{1}{-2\pi f Z''} \quad (2.24)$$

Using a plot of $1/C^2$ against E , a linear region should exist with a positive slope for an n-type semiconductor and a negative slope for p-type semiconductors. Using the absolute value of such slope (S) the dopant density ($N_{D/P}$) can be calculated via Eq. 2.25 [45].

$$N_{D/P} = \frac{2}{\epsilon_0 \epsilon e |S|} \quad (2.25)$$

2.2.3 Corrosion Mechanisms

When investigating the corrosion behaviour of metals, it is important to understand the mechanisms and the corrosion types encountered. In the classification of corrosion, there are three determining factors in identifying the corrosion type: the nature of the corrodent, the mechanism of corrosion and the appearance of the corroded substance. Visual identification is also of great use in analysing corrosion. Through visual inspection, it is possible to identify eight forms of corrosion, giving a great insight into the corrosion mechanisms taking place on the specimens surface:

Uniform or General Corrosion; this is when uniform corrosion occurs across an entire surface of the metal. Uniform corrosion is not of great concern, as it can be estimated and monitored with no sudden or abrupt failures likely.

Pitting Corrosion; this is a highly localised form of corrosion and produces defined holes. Pitting corrosion is common in engineering metals and is attributed to the formation of localised anodic area on the metal, relative to the rest of the surface. Some of the main

causes of pitting are due to local loss of passivity or rupture of protective coatings (oxide films).

Crevice Corrosion; this includes corrosion under tubercles of deposits, filiform corrosion and poulitice corrosion. This corrosion generally forms at narrow openings or gaps between metal-to-metal or non-metal-to-metal interfaces. These types of corrosion can be formed by design crevices (bolt holes) or by accident (metallurgical defects). Crevice corrosion is propagated through the dissolution of a metal and hydrolysis of that metal to create an acidic medium within the crevice, leading to accelerated corrosion.

Galvanic Corrosion; galvanic corrosion occurs when a metal or alloy is electrically coupled to another metal or conducting non-metal in the same electrolyte. During galvanic coupling, corrosion of the less anodic metal increases. The reactivity of metals is dependent on its position in the galvanic series. The difference in relative reactivity allows for a potential to be generated and electron flow to occur.

Erosion Corrosion; this includes cavitation corrosion and fretting corrosion. When abrasion and mechanical wear are combined with corrosive conditions, a more severe attack may be prominent.

Inter-granular Corrosion; this is the corrosion of grain boundaries and closely adjacent regions, with negligible attack to the grain itself. This is caused by potential differences between and precipitates and impurities that form at the grain boundary.

Dealloying; this is a corrosion process where a more active element is selectively removed from the alloy. This leaves a porous weak structure of the less reactive metal.

Environmentally Assisted Cracking; this includes stress corrosion cracking, corrosion fatigue and hydrogen damage. This type of corrosion is induced when metals are subjected to both a corrosive environment and a mechanical use. Stress corrosion cracking is the combination of tensile stress in corrosive conditions whilst, corrosion fatigue is the result of the fluctuating or cyclic stress in corrosive conditions. These mechanical

systems in a corrosive environment lead to accelerated crack propagation within the metal. Another environmental factor is hydrogen damage. This can cause problems such as hydrogen embrittlement, which can weaken the mechanical properties of the metal.

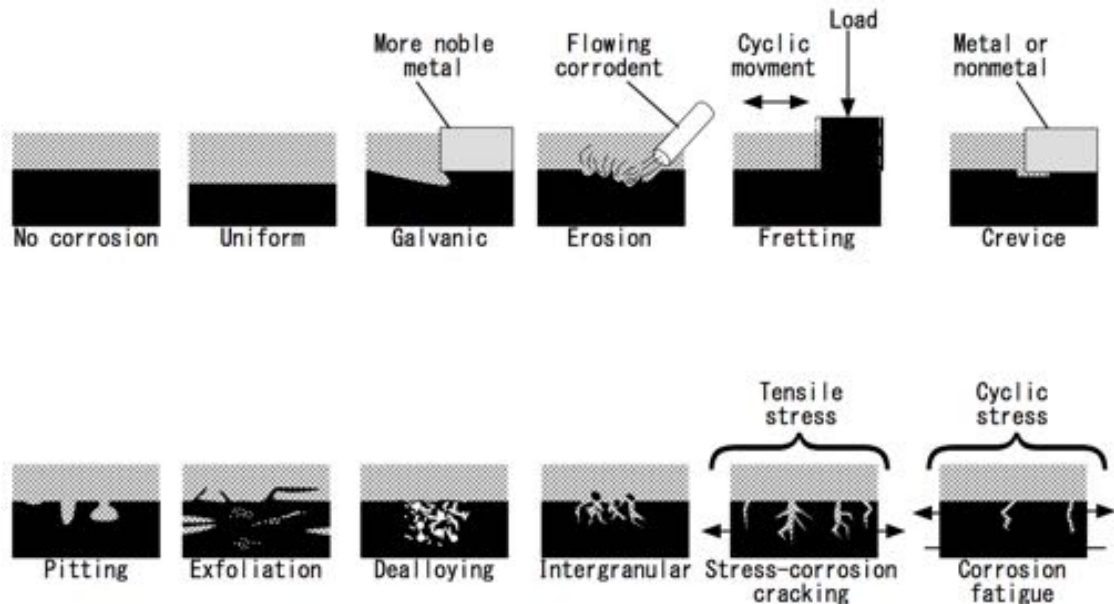


Fig. 2.8: Graphical representation of the types of corrosion that can be visually observed [35]

All these forms of corrosion are inherently distinct. However, there are many occasions where two or more forms of corrosion can be present at any one time. Working experience and knowledge of the types of corrosion expected can have an overwhelming impact on the ability to diagnose corrosion type from visual inspection [35]. Fig. 2.8 can be of great help for classifying simple corrosion types.

Corrosion is also affected by the environment in which a metal is subjected. Corrosive behaviour of metals can be dramatically affected by pH, temperature, velocity and the presence of biological organisms. Thus, corrosion can be encountered in all manner of situations. Corrosive environments can be generally classified as: atmospheric, underground/soil, water, acidic and alkaline. However, it can be noted that combinations of these environments are usually observed [34, 35].

2.3 Tribocorrosion

Tribocorrosion covers the interaction of mechanical loading and chemical reactions that occur when exposed to corrosive environments. Wear is a mechanical process which occurs through the rubbing or impacting of surfaces, whilst corrosion is an electrochemical reaction of a material. When a material is tested under tribocorrosion conditions, it may be seen that corrosion may accelerate wear or wear may accelerate corrosion. Material degradation due to the combined effect of corrosion and wear can occur under a wide range of conditions. These conditions can range from two body to three body surface contacts. Also, the surface contact geometry itself can have an effect on the wear rate observed during this degradation process. Tribocorrosion is often used in a more rigid sense to describe sliding contact in a corrosive environment. This scenario can be witnessed in a number of real life applications under differing corrosive environments:

- Moving engine parts
- Mining equipment
- Waste incinerator
- Plumbing and Pumps
- Joint Prosthesis (Hips, Knee...etc.)

When investigating tribocorrosion during the applications listed, it is important to control the effect of combined wear and corrosion to prolong component life. However, there are occasions when tribocorrosion has been used in a positive perspective. There is a process known as chemo-mechanical polishing (CMP) and this helps in the manufacture of advanced integrated circuit device technology.

During tribocorrosion, the contribution of both mechanical wear and corrosion in the overall material degradation process is of great value and importance. By studying the effect of both corrosion and wear, it is possible to determine whether wear has accelerated corrosion or corrosion has accelerated mechanical wear in the material degradation process. By understanding how a material is behaving in a combined environment of wear

and corrosion, it is possible to modify the material to allow for improved wear resistance and longer lasting components in the given medium. There have been several attempts at the quantification of tribocorrosion and its effect on wear rates. Through quantitative analysis, the data generated will give information regarding the major factors attributing towards materials degradation in combined conditions. These approaches will now be discussed.

2.3.1 The Synergistic Approach

Under tribocorrosion conditions, the wear rate of the material cannot simply be assumed to be the sum mechanical wear and corrosion. Both corrosion and mechanical wear are not independent of each other and are very much a part of a synergistic effect. This combined effect was first proposed by Watson [52] and can be displayed mathematically by Eq. 2.26.

$$V_t = V_w + V_c + V_s \quad (2.26)$$

Where V_t is the total volume of material removed, V_w and V_c are the respective volumes of material lost due to mechanical and chemical wear and V_s is the volume of wear from the combined synergistic effect between both the wear and corrosion. Although, it is possible to quantify the effect of tribocorrosion (see Eq. 2.26), this quantification is just a number generated and cannot be monitored during the testing of a materials tribological and corrosive properties. This value gives very little indication as to the underlying mechanisms involved in the tribocorrosion process and is a convenient way of describing any additional wear encountered in the combined conditions.

2.3.2 The Mechanistic Approach

The mechanistic approach has been used in many recent publications [6, 37, 41, 53–57] to name but a few. In this approach, material degradation is combined with sliding and corroding conditions as a result of two mechanisms:

Mechanical Wear (V_{mech}); In this process the metal is worn through mechanical contact, exposing fresh metal.

Wear Accelerated Corrosion (V_{chem}); This is when corrosion is accelerated due to exposure of fresh metal, that may be more reactive than that at the surface.

From these two mechanisms, we obtain an expression detailing the total volume lost (V_{tot}) during the tribocorrosion process (as shown in Eq. 2.27 [37])

$$V_{tot} = V_{mech} + V_{chem} \quad (2.27)$$

When investigating chemical wear, it is important to note that there are actually two contributing factors to this mechanism. The corrosion of a material in the worn and non worn areas can be substantially different, especially for passive materials. For highly passive materials, the unworn corrosion could be seen as negligible and the (V_{chem}) can be attributed solely to the corrosion in the worn areas of the material.

(V_{mech}) and (V_{chem}) are very much independent mechanisms in their own right but are intrinsically linked and highly dependent on each other. Using this mechanistic approach, it is possible to compare how different factors (contact: load, speed, area...etc) affect the rate at which each mechanism contributes towards the total wear volume. The main downside to this approach is the amount of simplification used to describe the contact area. There is no information generated as to differing chemical conditions throughout the test and only a volume for the whole test. There is also a concern in using this model to discuss wear when third bodies are generated in the contact area; this can lead to reduced friction and wear that is non-conforming with this model [37].

2.3.3 The Third-Body Approach

When discussing the effects of tribocorrosion, it can be argued that quantitative data provides a great insight into the contribution of either corrosion or wear on a system. However, this leaves little evidence as to the processes involved during tribocorrosion.

The third-body approach provides no quantitative data but is a method that can explain particular phenomena observed during tribocorrosion.

When discussing the third-body approach, it is important to understand that this method involves the consideration of the wear particles generated in the contact zone and their reaction/flow depending on environment. Wear particles have a considerable effect on the wear mechanics between two surfaces and play a vital part in the total wear volume of a material. Depending on corrosive environment and mechanical loading, there will be different manifestations of wear particles developed in the wear tracks. This wear debris then interacts with both surfaces and the electrolyte until a critical size when it will be ejected from the contact zone.

Fig. 2.9 created by Mischler [37], shows to great effect the interactions at the different stages of the wear particles and how they might interact with the contact zone. The arrows indicate the probable material movement. The counter face material will remove wear particles from the substrate metal (1), these can then be removed directly from the contact zone (2) or can become trapped within the contact zone, forming third-bodies (3). The third-body particles can become attached to the counter face (4), the original substrate (6) or fragment further into smaller particles (5). Once small enough, the third-bodies could be ejected from the contact zone (7). Corrosion can occur at two locations: on third-body (8) and on the substrate material (9) after detachment.

The build up of wear particles and the subsequent removal from the contact area can be affected by numerous factors from both a mechanical and chemical aspect. By using the three body approach to analyse tribocorrosion, this allows for a systematic qualitative review of the contact area. This links visual topography with the materials environment and the total wear rates observed, thus generating information on the effect that differing conditions have on the build up of third-bodies [37, 41].

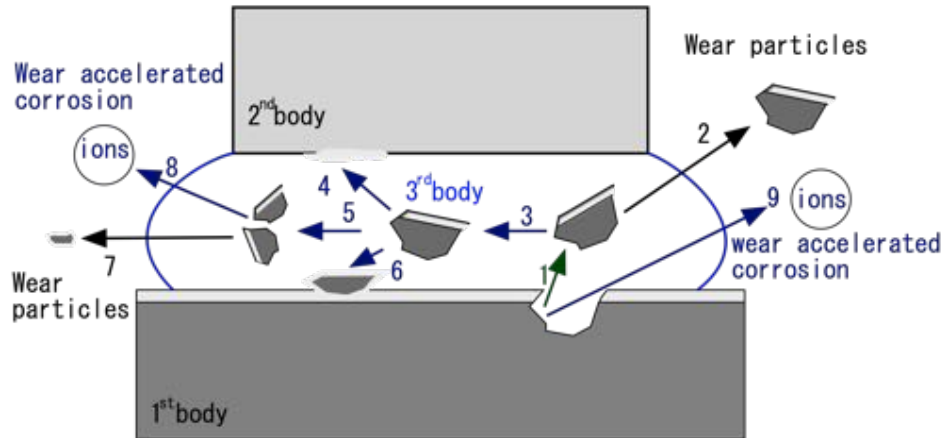


Fig. 2.9: Schematic diagram of possible material reactions in a tribocorrosion system [37]

2.3.4 Electrochemical Techniques for Tribocorrosion Study

During the study of tribocorrosion electrochemical methods can be used in conjunction with classical wear tests. These combined tests allow for both the mechanical and chemical characteristics to be analysed. This allows materials to be profiled under numerous loading and environmental conditions. Tribo-electrochemical techniques are very effective at investigating the combined effect of corrosion and wear. Using a modified pin on disc tribometer various electrochemical reading can be taken.

2.3.4.1 Open Circuit Potential (OCP)

Open circuit potential testing combined with friction testing, gives a real time representation of a materials electrochemical state along with the frictional response of the sample in real time. When both tests are run in tandem, it is possible to show when a materials state changes from passive to active, due to the mechanical wear of any surface films present on a passive material. This transition can be affected by the mechanical wear exerted onto the metal. It is important to note that the measured potential is a reflection of a galvanic couple generated between the worn wear track and the unworn test area. The actual values are of less significance than the overall trend of the data [58].

When conducting open circuit testing, it is customary to allow the sample to reach steady state conditions (conditions whereby the voltage measured deviates by just ± 1 mV) before engaging the contact load. This allows the response of the contacting material to be correctly analysed. Sudden cathodic shifts in the OCP equate to a material that has become more electrochemically active and more susceptible to corrosion [40].

The nature of the open circuit response for a material varies depending on its intrinsic electrochemical characteristics. For an active metal subjected to sliding contact, it has been observed that there is very little change to the potentials measured, compared with that under non sliding conditions [57, 59]. This is due to there being no structural/chemical differences throughout the active metals construction. However, the same cannot be said for passive metals or surface treated materials. During sliding, there can often be a cathodic shift observed, due to the exposure of the underlying active metal caused by mechanical wear [54, 60, 61]. A usually passive metal is then susceptible to corrosive attack.

2.3.4.2 Potentiodynamic (PD)

Potentiodynamic polarisation testing (potentiodynamic sweeps) can be used in conjunction with sliding wear testing. This type of testing allows the dependence of anodic or cathodic current to be determined for the tested sample. Using this method, the active/passive nature of a material can be monitored through the application of different potentials, while under sliding wear conditions. This method allows for the effect of wear on the corrosion potential of a sample to be evaluated [41].

When a material is subjected to sliding wear, a materials passive region can be shifted to a much more active state, with larger current densities recorded. Corrosion potential E_{corr} will also be shifted to a more cathodic location. This is as expected, once a passive material is rubbed, there is a cathodic shift due to the more reactive state of the material.

Potentiodynamic testing can generate a quantitative result for the corrosion current of a sample undergoing sliding wear. The results obtained are highly dependent on the

sliding properties imposed by the tribometer [40]. The current measured during the test is directly related to the sliding frequency and the applied normal load. Both effects can be explained by the active/passive ratio in the sample. The higher the ratio, the larger the currents that will be measured from the sample. This is exactly the same process by which OCP is governed.

Potentiodynamic testing not only allows the electrochemical aspects of the material to be monitored at different potentials, but also the friction encountered during sliding contact can be affected by the changing potential [41]. The friction encountered can also be used as evidence in the attainment of the chemical state of the sample. Sudden drops or increases in friction can be associated with different chemical states of the sample and changing of the wear mechanisms encountered. One example of this is when the material is polarised with a large cathodic potential. This can result in hydrogen embrittlement, increasing surface hardness. This increase in surface hardness will manifest itself as higher friction, when measured by the tribometer [38, 40].

2.3.4.3 Potentiostatic Testing

During potentiostatic testing, a single fixed potential is applied to the test sample, with the resulting friction and current density measured with respect to time.

The measuring of current allows for the observation of the electrochemical kinematics of the sample, during real time, under sliding wear. By holding the potential of the sample it is possible to perform an in-depth investigation into material characteristics observed during the potential dynamic sweep. At different potentials, the material may react differently to the applied sliding contact. Active or passive regions can be investigated in order to understand the influence of sliding/corrosion on the wear rate [41].

The total material loss (TML) in volume (V_{total}) is a sum of both mechanical (V_{mech}) and chemical (V_{chem}) volume loss as shown in Eq. 2.27 on page 31.

Faradays' law (Eq. 2.28) can be used to estimate the contribution of chemical wear in the tribocorrosion process. The anodic current detected during tribocorrosion testing is

related to the amount of material lost due to anodic oxidation and/or dissolution through Faraday's law [41, 55, 56].

$$V_{chem} = \frac{IMt}{nF\rho} \quad (2.28)$$

Where I is the current (A) developed during sliding contact, t is the time (s) of sliding contact, F is Faradays constant (964 858.34 A s mol⁻¹), M is the atomic mass of the metal (47.767 g mol⁻¹ for Ti), n is the charge number for the oxidation valence (valence =+4 for Ti [62]) and ρ is the density of the metal (4.11 g cm⁻³) . Using Faraday's law can become difficult when a material is known to exhibit numerous valances, in particular for passive metals. This quantitative analysis method is a key benefit of using potentiostatic measurements, when it is possible to determine the lost metals valance.

2.4 Titanium

2.4.1 General Properties

Titanium is the 4th most abundant metal on earth and was discovered by Gregor in 1791. However, production proved to be difficult as titanium is found most commonly in ores of titanium dioxide (TiO₂) and ilmenite (FeTiO₃). Commercial production of titanium involves the chlorination of titanium containing mineral, this produces titanium tetrachloride (TiCl₄), which is then reduced with magnesium (Mg) (the Kroll process) or Sodium (Na) (the Hunter process). These processes produce a porous metal structure known as a sponge which must then be melted in a chemically inert atmosphere (usually argon) to create titanium ingots [63].

Titanium sponge production was estimated to be 222 000 t (excluding U.S. production) in 2013. This is a 10% increase over the 2012 production figure, and was in response to increased demand from aerospace applications. Titanium has found many industrial uses due to its low density, high strength and excellent corrosion resistance (see Table 2.1). Currently, the aerospace industry accounts for 73% of all titanium metal used, with the remaining 27% from the following industries: armour, chemical processing, marine, medical, power generation and sporting goods [64].

Table 2.1: Properties of commercially pure titanium

Property	Value
Liner thermal expansion coefficient	$8.36 \times 10^{-10} \text{ K}^{-1}$
Thermal conductivity	$14.99 \text{ W m}^{-1} \text{ K}$
Specific heat capacity	$523 \text{ J kg}^{-1} \text{ K}$
Electrical resistivity	$5.6 \times 10^{-7} \Omega \text{ m}$
Young's modulus	115 GPa
Poisson's Ratio	0.33
Offset yield strength	275 MPa
Ultimate tensile strength	345 MPa
Density	4.51 g cm^{-3}

2.4.2 Titanium Crystal Structure

Titanium and its alloys are able to exist in a wide range of microstructures. There are three polymorphic forms of titanium: alpha titanium (α -Ti), beta titanium (β -Ti) and alpha beta titanium (α - β -Ti) [36]. Depending on both thermal and thermochemical processes, the microstructure can be controlled for differing applications. The allotropic transformation of commercially pure titanium occurs at 882.5 °C, where the structure changes from the α hexagonal closed pack (HCP) phase to the β body centred cubic (BCC) phase. The HCP structure of the α -Ti phase has lattice parameters of $a = 2.95 \text{ \AA}$ and $c = 4.686 \text{ \AA}$, resulting in a c/a of 1.587. This can be seen schematically in Fig. 2.10a, with the most densely packed lattice planes highlighted. When transformed to the β -Ti phase the crystal structure changes to that of BCC, with lattice parameter of $a = 2.95 \text{ \AA}$. The unit cell of this phase can be observed in Fig. 2.10b and the densely packed $\{110\}$ plane identified. This transition temperature is very much dependant on the composition of the titanium. By carefully selecting alloying elements, it is possible to stabilise the β phase titanium so that it is present at room temperature.

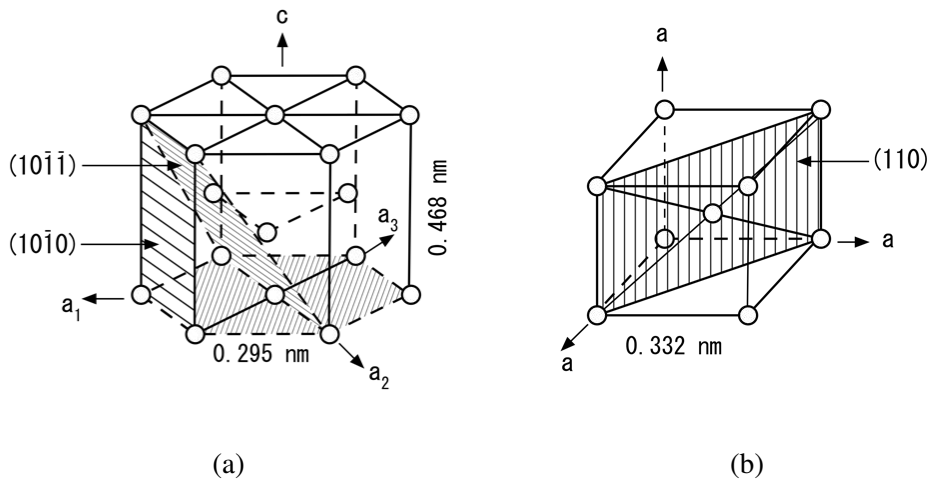


Fig. 2.10: The unit cell crystal structure of (a) α -Ti and (b) β -Ti [63]

The ideal c/a ratio for a HCP crystal structure is $c/a = 1.633$. In HCP metals, slip primarily occurs in the $\langle 11\bar{2}0 \rangle$ (or burgers vector \vec{a}) direction (see Fig. 2.11). The slip

planes are either the basal (0002) with two independent planes of slip or, prism ($10\bar{1}0$), with two independent slip planes. There could also be some pyramidal $\langle 10\bar{1}1 \rangle$ slip planes but these are the result of both prism and basal slip and therefore, do not contribute to the total number of slip planes. These result in just four independent slip systems [65]. The c/a ratio for titanium is smaller than this ideal value. This reduced c/a ratio of α -Ti leads to larger spacing between prism planes, thus causing the packing density of the planes to increase relative to the basal plane (0002). This favours slip on the prism planes rather than the basal planes [63, 66, 67] .

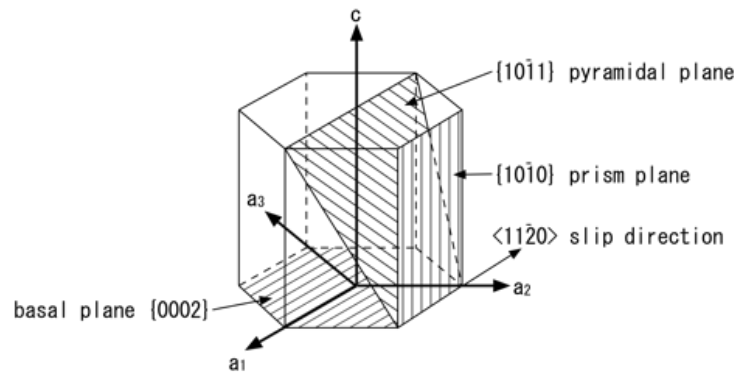


Fig. 2.11: Slip systems of hexagonal crystal lattices [68]

The Von Mises criterion requires at least five independent slip systems for homogenous plastic deformation to take place [69]. Therefore, for HCP systems to exhibit good ductility, an additional deformation mode is required. It has been shown that for homogenous deformation to occur strain in the \vec{c} direction is required along with \vec{a} . This is known as $\langle \bar{1}123 \rangle$ (or $\vec{a} + \vec{c}$) slip [68]. This type of slip results in five independent slip systems, as shown in Table 2.2. When in the β -phase, titanium slip systems are predominately $\{110\}$, $\{112\}$ and $\{123\}$ in the $\langle 111 \rangle$ direction. This is a contributing factor to the increased ductility of β -Ti alloys over α -Ti alloys [67].

Table 2.2: Slip system of HCP crystal lattice

Slip system	Bergers Vector type	Slip direction	Slip plane	N ^o of slip systems	
				Total	Independent
1	\vec{a}	$\langle 11\bar{2}0 \rangle$	(0002)	3	2
2	\vec{a}	$\langle 11\bar{2}0 \rangle$	$\{10\bar{1}0\}$	3	2
3	\vec{a}	$\langle 11\bar{2}0 \rangle$	$\{10\bar{1}1\}$	6	4
4	$\vec{a} + \vec{c}$	$\langle 11\bar{2}3 \rangle$	$\{10\bar{1}1\}$	12	5

2.4.3 Alloys

Using alloying elements in Ti can have substantial effect on the alpha/beta transus temperature. Through the use of alloying elements, the beta phase can be sufficiently stabilised to coexist with alpha at room temperature (see Fig. 2.12). There are three structural types of titanium alloys: Alpha, alpha-beta and metastable beta depending on the composition of alloying elements.

Elements having extensive solubility in alpha phase titanium, generally raise the allotropic transformation temperature, and these are known as alpha-stabilisers. Common alpha stabilising elements include: Al, O, N and C. It is important to note that O, N and C form interstitial solid solutions and fill interstitial within the titanium atoms. Whereas, almost all other alloying elements form solid solutions where solute atoms replace or substitute Ti atoms in both alpha and beta titanium. This alpha phase can also be strengthened using tin or zirconium. These materials are soluble in both alpha and beta phase titanium and the addition of these elements has little effect on the transus temperature and are known as neutral additions [63].

Beta stabilisers reduce the transformation temperature and allow for beta titanium to be present at lower temperatures depending on concentration. Beta stabilisers can be separated into two categories: beta-isomorphous elements or beta-eutectoid elements. Isomorphous elements are V, Mo, Nb and Ta and show complete mutual solubility with the BCC titanium crystal structure. Mn, Fe, Cr, Co, Ni, Cu, Si and H are all eutectoid elements and have restricted beta solubility. These elements can form inter-metallic

compounds through eutectoid decomposition [67].

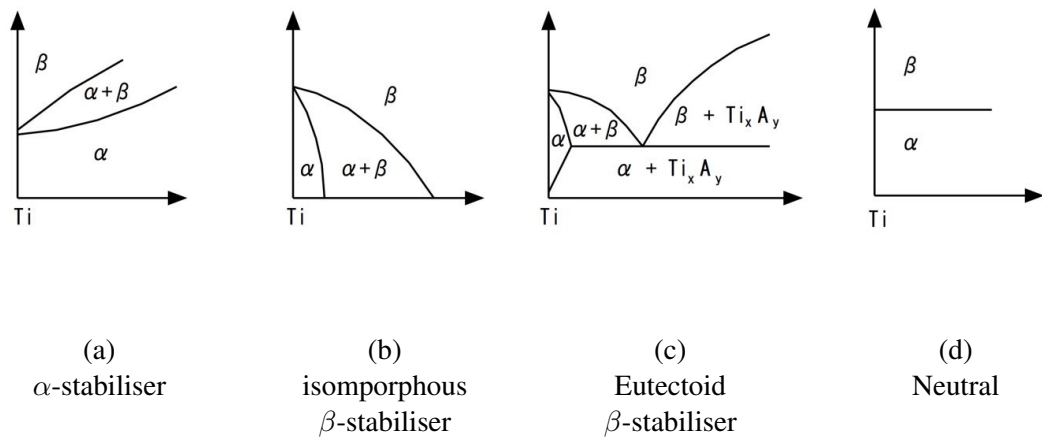


Fig. 2.12: Schematic diagrams showing the effect of alloying elements on equilibrium phase diagrams of Ti-alloys [63]

2.4.4 Tribology of Ti

The unique combination of lightweight, high strength, excellent corrosion resistance and biocompatibility make titanium a desirable engineering material. However, the uses of titanium have been heavily restricted to mostly non-tribological applications, due to the severe galling problem encountered in sliding contact, resulting in large wear rates and the possibility of seizure [2, 70]. Such poor tribological response of titanium has been investigated by Dong and Bell [2]. They suggested a compound effect of electron configuration, crystal structure and lubrication ineffectiveness as being the major contributing factors giving rise to the high unstable friction. This results in the severe adhesive wear, which can be observed during sliding contact [1, 2].

2.4.4.1 Electron configuration

Both the chemical activity and the frictional response of a metal are directly linked. The higher the coefficient of friction, the more reactive the metal. This phenomenon has been linked to the D-bond character of metals. The more inter-metallic bonding there is within a metal, the less bonding that can occur across the sliding interface. Therefore, the higher

the D-bond character, the lower the COF [71]. Titanium has a D-Bond character of 27%, resulting in a high COF ($\mu = 0.6$) [2].

2.4.4.2 Crystal Structure

Crystal structure Hexagonal crystal structures with an ideal c/a ratio of 1.633 exhibits more favourable tribological properties than that of cubic crystal structure [72]. However, Ti has a c/a ratio of 1.588. which is less than ideal and favours slip in the prismatic $\{10\bar{1}0\}$ and pyramidal $\{10\bar{1}1\}$ slip planes. This results in an increased number of slip systems and promotes continuous junction growth [2].

2.4.4.3 Lubrication Ineffectiveness

Conventional lubricants (minerals oils and greases) are generally ineffective when applied to titanium and its alloys [73]. The low heat conductance of Ti, is thought to add to the overall ineffectiveness of lubrication [2, 25].

2.4.5 Corrosion

Titanium exhibits excellent corrosion resistance in most environments, which is a result of a protective titanium oxide surface film. Ti is chemically very active, and when exposed to oxygen will instantaneously form a thin passive film at the base metals surface. As long as this chemically passive oxide film retains its integrity and remains tightly bound to the metal, titanium is able to withstand most oxidising environments, for example in salt solutions, including chlorides, hypochlorides, sulphates, sulphides and in nitric acid solutions. However, titanium is not corrosion resistant under reducing agents, very powerful oxidising agents or in the presence of fluoride ions (F^-). These environments are able to breakdown the integrity of the oxide film. The Pourbaix diagram for titanium (Fig. 2.13) shows the electrochemical response of titanium in various pH and potential.

Titanium can also be susceptible to hydrogen embrittlement or stress corrosion cracking when simultaneously subjected to mechanical stress and aggressive corrosive

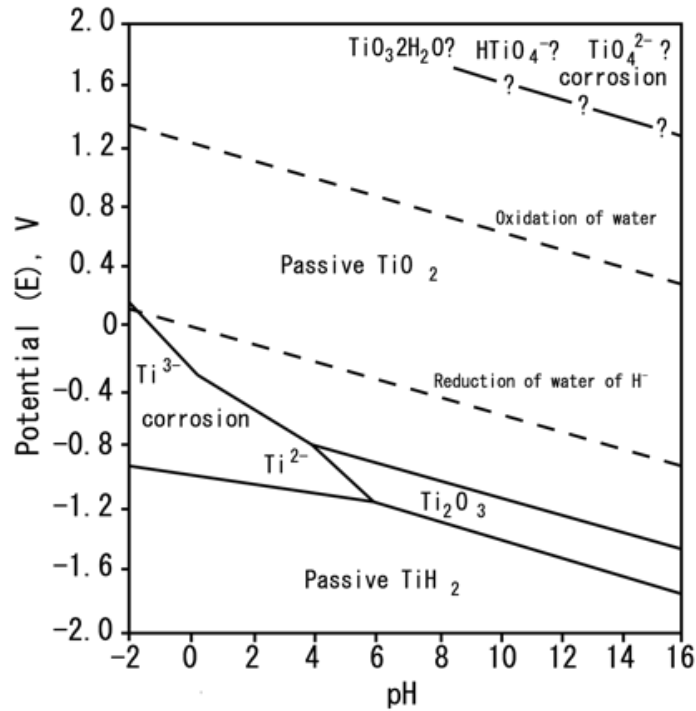


Fig. 2.13: Pourbaix diagram for titanium (E/pH) [36]

environments. The HCP phase has a low hydrogen solubility and small amounts of hydrogen diffusion can result in brittle fracture, mainly along the basal planes [67, 74, 75].

The electrochemical response of Ti in aqueous solutions has been extensively investigated by Kelly [38] and found to exhibit four different types of behaviour:

Active: In this state the metal can be oxidised at a relatively high rate, forming Ti(III) ions.

Passive: In this state the metal is covered by a titanium oxide film. This film prevents vast amounts of further oxidation occurring. However, over time, Ti(IV) ions can be formed. The Ti(IV) ions will either enter the solution or enhance the passive film.

Active-Passive: This is a transitional phase where total film thickness/coverage is incomplete, impeding the passivation of Ti.

Hydrogen Evolution: When Ti is polarised to a sufficiently negative potential (via

external application or galvanic couple), hydrogen evolution can actively corrode titanium.

The behaviours highlighted depend on various environmental parameters. These include: pH, temperature and exposure time. The standard current - potential response of titanium in an acidic solution can be observed in Fig. 2.14. The four regions described by Kelly [38] have been highlighted. The low current densities during the passive region correlate to a very low corrosion rate.

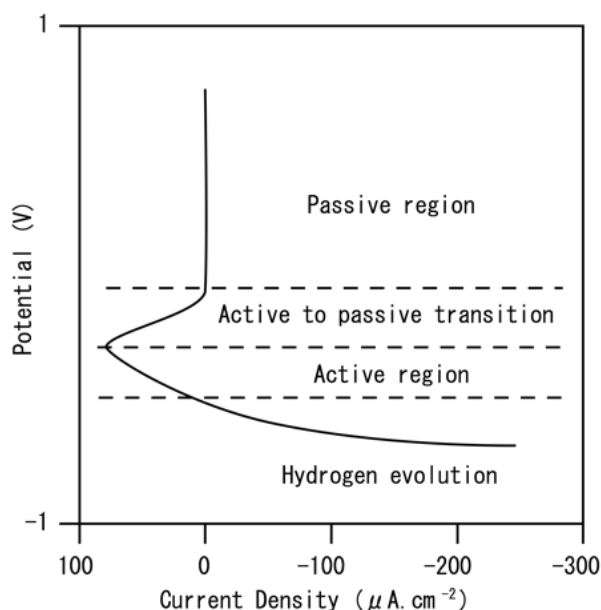


Fig. 2.14: Schematic illustration of the current-potential relationship for Ti in an acidic solution. Units indicated are for perspective and are not an accurate representation [38]

2.5 Titanium Dioxide (TiO₂)

2.5.1 General Properties

Titanium dioxide can be found naturally in the earth's crust however, it is most commonly processed from ilmenite. TiO₂ is produced from titanium mineral concentrates, by either the chloride process or the sulphate process. The chloride process involves, natural rutile,

ilmenite or sag, this is converted to TiCl₄. This is then oxidised at approximately 1000 °C and the resulting TiO₂ is then cleansed of any residual chloride and hydrochloric acid that may have formed during the reaction. In the sulphate process, ilmenite or titanium slag is reacted with sulphuric acid. Titanium hydroxide (TiO(OH)₂) is then formed through hydrolysis, this is then filtered and cleaned. Either process may be used to produce TiO₂. To finish, the crude TiO₂ is then milled to produce a controlled particle size and then the surface treated or coated to improve its functional behaviour in various media.

Titanium dioxide has found a wide and varied portfolio of use, with it most commonly use as a white pigment in paints and cosmetic products. TiO₂ is also commonly used by the clean energy industries in solar cells and for the production of hydrogen. Other common uses include: Catalysis, gas sensors, corrosion resistant coating, and optical coating. It also plays a role in biocompatibility of bone implants. Lately it is also being used in Li-based batteries and electrochemical devices [76]. Titanium oxide has been the subject of numerous studies with regard to wear resistant coatings [8, 70, 77]. These coatings are formed via deposition techniques [15, 78] or in site oxidation of bulk titanium [10, 70]. Titanium dioxide has some very good mechanical, thermal and electrochemical characteristics, some of which are highlighted in Table. 2.3.

Table 2.3: Properties of titanium dioxide (Rutile)

Property	Value
Liner thermal expansion coefficient	10.1 K ⁻¹
Thermal conductivity	7 W m ⁻¹ K
Specific heat capacity	690 J kg ⁻¹ K
Electrical resistivity	5 × 10 ¹⁵ Ω m
Young's modulus	282 GPa
Shear modulus	110.5 GPa
Poisson's Ratio	0.28
Offset yield strength	350.5 MPa
Ultimate tensile strength	350.5 MPa
Density	4 4.01 × 10 ³ kg m ⁻³
Hardness - Vickers	1011.5HV

2.5.2 Crystal Structure

There are three crystallographic forms of titanium dioxide; rutile, anatase and brookite. Rutile and anatase (see Fig. 2.15) both possess a tetragonal crystal structure with rutile containing six atoms per unit cell and anatase containing twelve. In both of these structures, each Ti atom is coordinated to six O atoms and each O is coordinated to three Ti atoms. Rutile and anatase are often described as being chains of TiO₆ octahedrons with common edges. In rutile, there are two common edges with neighbouring octahedra sharing one corner along the $\langle 110 \rangle$ type directions, and are stacked by their long axis alternating by 90° (see Fig. 2.15a). In anatase, there are four common edges with the corner sharing octahedra forming (001) planes. They are connected by their edges with the plane of the octahedral below (see Fig. 2.15b). The TiO₆ octahedron is slightly distorted in both rutile and anatase with two of the Ti-O bonds being slightly longer than the other four, this causes the O-Ti-O bond angle to deviate from 90°. This bond distortion is much greater in the anatase form when compared with the rutile form. Brookite has a much more complicated structure. It has eight formula units in its orthorhombic cell. The interatomic distances and the O-Ti-O bond angles are similar to those of rutile and anatase. The difference is that there are now six different Ti-O bonds lengths ranging from 1.87 to 2.04 Å, with twelve different O-Ti-O bond angles, ranging from 77° to 105°. In contrast, rutile and anatase only possess two different Ti-O bond lengths and O-Ti-O bond angles. Brookite can also be described as a distorted TiO₆ octahedra sharing three edges (Fig. 2.15c) [79]. Of these forms, rutile is the most common as it is the most thermodynamically stable form. Both anatase and brookite can be converted into the rutile form through heating at temperatures above 400 °C [80].

Titanium dioxide deformation is always by slip in the $\{101\} \langle 101 \rangle$ and $\{110\} \langle 001 \rangle$ systems, with the $\{101\} \langle 101 \rangle$ slip system being by far the more active. It is suggested that the Burgers vector of a dislocation gliding on a $\{101\} \langle 101 \rangle$ system is $\frac{1}{2} \langle aOc \rangle$, and that pairs of partial dislocations are separated by stacking faults [81].

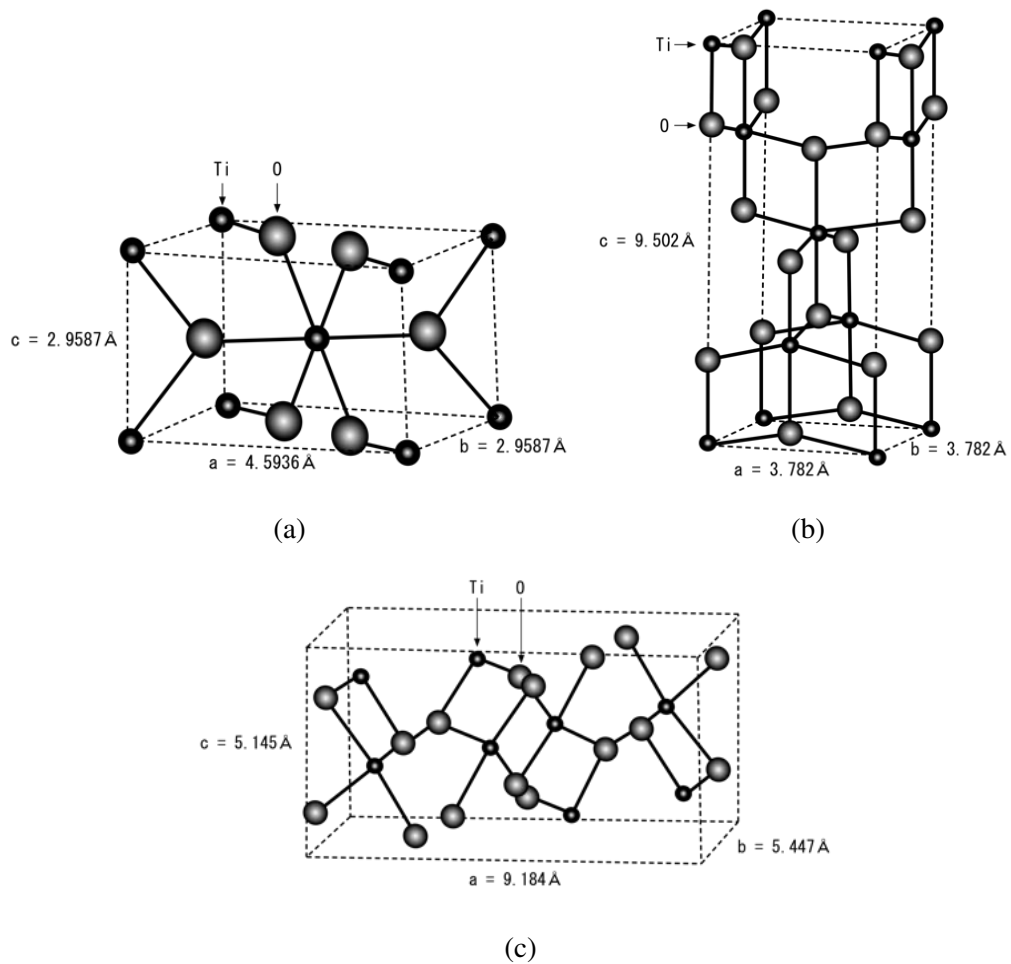


Fig. 2.15: The crystal phases of titanium dioxide; (a) Rutile, (b) Anatase and (c) Brookite [82]

2.5.3 Rutile TiO₂

During this study only the rutile phase of titanium dioxide was observed. Rutile is also the technologically preferred form. This is due to the increased index of refraction and higher dielectric constant [80]. It is also known to have the best tribological characteristics of the three phases. Rutile has been shown to have a low friction coefficient which is much lower than the anatase form [83]. In recent years rutile has also been widely investigated in the biomedical implant sector due to its excellent biocompatibility [84]. Rutile has been shown to have a much lower rate of Ti-ion dissolution, when compared with the anatase phase [85]. The properties highlighted make rutile the most relevant phase of titanium dioxide when investigating: tribology, corrosion and tribocorrosion.

2.6 Titanium Carbide

2.6.1 General Properties

Titanium carbide can be found naturally occurring on earth in the form of a very rare mineral known as khamrabaevite (Ti,V,Fe)C. However, for industrial applications, TiC is produced through the reduction of TiO₂ into its sub-oxides (Ti₆O₁₁, Ti₅O₉, Ti₄O₇ and Ti₃O₅), an inter-metallic oxycarbide (Ti₂OC) phase is then observed and finally, the formation of TiC [86].

Titanium carbide has become a very important non-oxide ceramic, widely used in the fields where high wear resistance is essential. There is also increasing interest in biomedical applications [87]. Titanium carbide has attracted considerable attention due to its extremely high melting point, low density, high hardness (2500-3000 HV), chemical and thermal stability, along with outstanding wear resistance [19] as highlighted in Table. 2.4. The high hardness value is of particular interest when looking at wear resistance.

The chemical resistance is very good and it is resistant to most acidic mediums. However, TiC is susceptible to attack by nitric acid (HNO₃) and hydrofluoric acid (HF). TiC can also be heated in hydrogen with no form of decomposition. TiC can be oxidised in air at temperatures above 800 °C.

2.6.2 Crystal Structure

TiC has a rock salt (B1) face centred cubic (FCC) crystal structure. The crystal structure parameters can be observed in Table 2.5 and represented graphically in Fig. 2.16.

TiC exhibits a ductile brittle transition (DBT). Although the melting point of TiC is 3150 °C, the DBT can occur at temperatures as low as 800 °C [88]. This BDT temperature has an effect on the type of crystal slip observed. When below the BDT titanium carbide (as most transition carbides show) slip is dominated by $\{111\} \langle 1\bar{1}0 \rangle$ and $\{110\} \langle 1\bar{1}0 \rangle$. With slip occurring in the $\{111\}$ planes, this gives rise to twelve planes of slip.

Table 2.4: Properties titanium carbide

Property	Value
Liner thermal expansion coefficient	7 K^{-1}
Thermal conductivity	$21.5 \text{ W m}^{-1} \text{ K}$
Specific heat capacity	$556.5 \text{ J kg}^{-1} \text{ K}$
Electrical resistivity	$2.145 \times 10^{-6} \Omega \text{ m}$
Young's modulus	$4.35 \times 10^2 \text{ GPa}$
Shear modulus	$1.76 \times 10^2 \text{ GPa}$
Poisson's Ratio	0.235
Offset yield strength	$2.95 \times 10^2 \text{ MPa}$
Ultimate tensile strength	$2.95 \times 10^2 \text{ MPa}$
Density	$4.91 \times 10^3 \text{ kg m}^{-3}$
Hardness - Vickers	2850HV

When the temperatures are above the DBT temperature, $\{111\} < \bar{1}10 >$ slip occurs [86].

It is interesting to note that TiC shows isomorphism with both titanium nitride (TiN) and titanium oxide (TiO). Oxygen or nitrogen can substitute for carbon to form any number of binary and ternary solid solutions with a wide range of homogeneity. These solid solutions can be considered as Ti(C,N,O) mixed crystals [89].

Table 2.5: Titanium carbide structural properties.

Property	Value
Crystal structure	Cubic, cF8
Space group	$Fm\bar{3}m$
Co ordinate geometry	Octahedral
Lattice parameters	4.328 \AA

2.7 Titanium Surface Modification

Surface engineering techniques can be applied with varying degrees of success to titanium alloys. Surface modification is attractive for use on titanium as these techniques allow for the preservation of the excellent bulk properties while modifying the surface properties to combat the wear and galling problems associated with titanium. The surface engineering

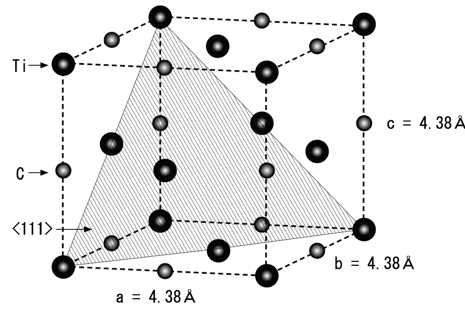


Fig. 2.16: Crystal structure of titanium carbide [88]

of titanium and titanium alloys are often designated by three broad categories: heat treatment, coatings and thermochemical treatments [7, 90, 91].

Heat Treatment: The heat treatment of titanium allows for the optimisation of some important properties such as fracture toughness, fatigue strength and tensile strength. Heat treatments can produce an optimum combination of ductility, machinability and structural stability through micro structural refinements [67]. The response of titanium and titanium alloys to the various heat treatments depends on the composition of the metal alloy. Thermal hardening processes are generally ineffective at producing tribological improvements without any changing of the surface composition [7].

Coatings: There are numerous types of surface coatings that can be applied to titanium and its alloys. Some of the most common coatings include: chemical conversion coatings, plating, physical vapour deposition (PVD) and sprayed coatings [90, 92] Using surface coatings allows for improvements in: lubricity, corrosion resistance, heat resistance and wear characteristics of titanium. Surface coating techniques require good adhesion and any benefit gained from coatings will only remain as long as the coating remains intact.

Thermochemical Treatments: Titanium and titanium alloys are chemically very active and react readily with most interstitial elements. This gives a wide range of possibilities with regard to diffusion-based surface treatments [90]. Various mechanical properties of titanium and titanium alloys, can be modified depending on the thermochemical

treatments used. The processes of boronising, nitriding, oxidation and carburising are among the most popular thermochemical treatments used. These all improve the surface properties of titanium and its alloys. The aforementioned treatments can decrease wear and improve corrosion resistance, while decreasing friction and greatly increase surface hardness of the material.

2.7.1 Boronising

Boronising can be used to increase the surface hardness of titanium (Ti). Boron (B) has an extremely low solubility in Ti ($\leq 1.5at\%$) in both α -Ti and β -Ti phases, as depicted in the phase diagram (Fig. 2.17a [93]). Diffusion of boron in titanium leads to the formation of both titanium diboride (TiB_2) and titanium boride (TiB) phases. The low solubility of B in Ti results in clearly defined compound structure with a continuous monolithic TiB_2 layer and an inner TiB whiskered structure [5] depicted graphically in Fig. 2.17b. The TiB_2 surface layer offers the most benefit in terms of increased hardness, with values reaching 3000 HV and TiB able to show hardness up to 2000 HV. This is a significant improvement over the 320 HV associated with commercially pure titanium [5, 93].

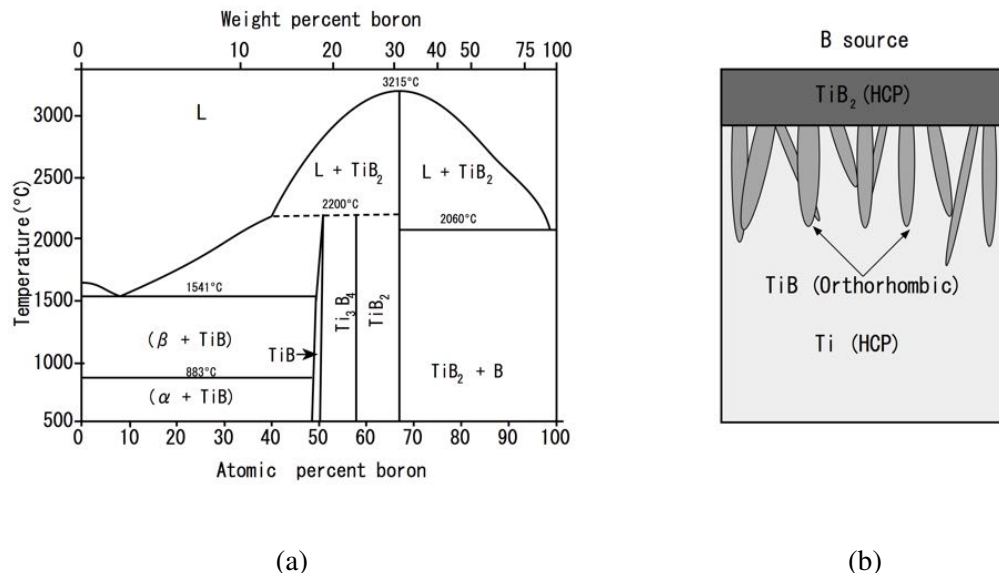


Fig. 2.17: Titanium-boron phase diagram [93] (a) with a schematic diagram of phase formation after the boriding treatment (b)

Boronising of titanium can be performed by using the following techniques: Fluidised bed reactor [94], laser boriding [95], pack boriding [96] and plasma assisted boriding [97]. However, solid source boriding through the use of pack compounds is the most commonly used, due to it being most cost effective and least hazardous [98]. In order for film growth to occur using pack carburisation methods, temperatures between 800 – 1100°C and durations up to 24 h are used [99]. The whiskers thickness and length are dependent on the crystal structure of the titanium, the α -Ti phase results in thinner whiskers, while the β -Ti phase generate thicker whiskers [96].

The tribological advantages of boronised titanium has been investigated by numerous authors [4, 93, 95, 97]. It is clearly observable that boronised titanium offers an exceptional improvement in both the frictional response of Ti and reduced material loss during wear. During sliding against an alumina contact, borided titanium exhibited a friction coefficient of $\mu = 0.11$ [4], which is a vast improvement from $\mu = 0.6$ for untreated titanium [100]. During sliding contact, the mechanisms of wear change from adhesive wear for untreated Ti to abrasive polishing for the boronised titanium [93]. The TiB whiskers are believed to benefit the adhesion of the TiB₂ structure, by acting as an anchor to the subsurface bulk Ti [98]. One of the limiting factors in the boronising of titanium is the low diffusivity of boron into TiB₂ [101]. As the TiB₂ phase builds up, it acts as a barrier preventing deep case hardening. It is only possible to obtain depths from 25-100 μ m using conventional boronising methods [98].

2.7.2 Nitriding

Over the years, nitriding has become a frequently used surface hardening technique for titanium and its alloys. Nitriding has been shown to effectively reduce the wear rate of titanium. Nitrogen (N) has a high solubility in α -Ti (8 wt%, at 1000 °C), as depicted in Fig. 2.18a [7]. During the nitriding process, the high solubility of titanium results in the formation of a multilayered structure with TiN (titanium nitride) and Ti₂N compound layer formed atop of an alpha (N)-Ti diffusion zone (see Fig. 2.18b) [102]. The surface

hardness generated from the nitriding process is between 1500-3000 HV [7].

When titanium is heated in an active nitrogen rich atmosphere that is purged of oxygen, nitrogen absorption into the solid occurs. Once absorbed, nitrogen diffusion occurs, filling interstitial sites within the HCP crystal structure of the titanium. Once the concentration of the nitrogen exceeds the solubility limit, new phase formation will occur. Ti_2N phase will be produced, changing the crystal structure from HCP to a tetragonal structure. Nitrogen absorption continues until at a sufficient level that the cubic TiN phase is formed. During the nitriding process a multilayered structure is produced, as depicted by Fig. 2.18b.

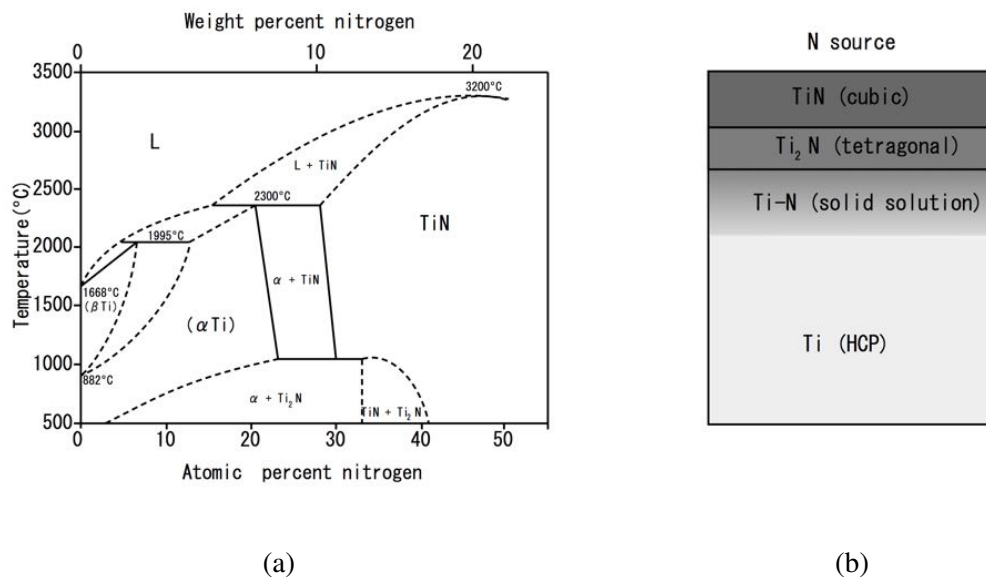


Fig. 2.18: Titanium-nitrogen phase diagram [102] (a) with a schematic diagram of phase formation after the nitriding treatment (b)

There are various methods of titanium nitriding that can be used to induce the multilayer structure depicted in Fig. 2.17b. These include: plasma nitriding [103, 104], ion beam nitriding [105], laser nitriding [106] and gas nitriding [7, 102, 107]. Of these methods, gas nitriding is one of the most common methods due to its ability to simply and cost effectively form hardened surface layers. According to literature gas nitriding can be performed at temperatures ranging from 650 to 1050 °C and durations of 1 to 100 hours [7]. The temperature and time can be controlled depending on the required film thickness.

Tribological characteristics of nitrided titanium have been investigated by numerous authors, in both dry and lubricated sliding contact. Most investigations have shown that nitriding treatment is effective at reducing the wear rate of titanium [104, 108, 109]. However, the frictional response of nitrided titanium is very dependent on surface treatment technique. Various studies have shown that nitrided titanium does little to the coefficient of friction (μ) of titanium and thus, still experiences a high unstable friction coefficient of $\mu = 0.6$ when in contact with an alumina (Al_2O_3) ball [104, 108, 110].

2.7.3 Oxidation

Oxidation offers a way to increase both the corrosion resistance and the surface hardness of titanium. This is achieved through the expansion of the naturally occurring titanium dioxide film (1.5-10 nm thick) at the surface of titanium [111]. Oxygen has a high solubility in α -Ti and numerous methods have been developed to produce an oxide layer of relevant thickness or, an oxygen hardened layer to improve the tribological/electrochemical response of titanium. These include anodising [112], oxygen diffusion [16, 113], ion implantation [114], plasma electrolytic oxidation [115], palladium treated thermal oxidation [70], and thermal oxidation (TO) [2, 77, 116, 117]. Of these methods, thermal oxidation offers a simple and cost effective way to improve the friction/wear characteristics of titanium.

2.7.4 Thermal Oxidation

Previous studies have demonstrated that thermal oxidation produces a multi-layered structure atop of the bulk titanium [118]. This structure is formed initially by solid solution hardening through oxygen absorption and diffusion. This process creates what is known as a hardened oxygen diffusion zone (ODZ or alpha case). Once the oxygen concentration reaches a sufficient level, a titanium dioxide (rutile) layer (TiO_2) will form at the surface of the titanium [9, 100, 119]. The titanium dioxide film formed has various properties that are of interest from both a tribological and corrosion resistance point of

view.

2.7.4.1 Microstructure of the Oxide Layer

The composition of this naturally occurring oxide film varies with various titanium sub oxides being identified: Ti_3O , Ti_2O , Ti_3O_2 , TiO , Ti_2O_3 , Ti_3O_5 and TiO_2 , which are known as the Magneli phases (Ti_nO_{2n-1}) [82], as shown in Fig. 2.19.

Theoretically, rutile titanium dioxide with TiO_2 stoichiometry has a primitive tetragonal unit cell and does not have easy shear planes to offer low friction [120, 121]. However, according to [122], rutile-like oxides slightly deficient in oxygen, known as Magneli phases, should have lower friction than titanium dioxide and behave as a lubricious material. Magneli phase exhibits contact mechanics different from that of rutile phase, explained to be due to the lamellar crystal structure arising from the lamellar organisation of oxygen vacancies to form easy shear crystallographic planes [121, 122].

This wide variety of titanium oxides is a result of the variable oxidation state of titanium (+IV, +III and +I). However, the preferred oxidation state of titanium is +IV and therefore, TiO_2 is the most thermodynamically stable with a very negative Gibbs energy of $-888.8 \text{ kJ kmol}^{-1}$ [123] making it very stable. TiO_2 (titanium dioxide) is the most predominant stoichiometry found at the metal oxide interface [123].

2.7.4.2 Dissolution of Oxygen in Ti

Oxygen has a maximum solubility of 33 at% in the α -phase Ti. Oxygen occupies the octehdral interstitial sites within the HCP crystal structure, which can occur randomly or in an ordered pattern, along alternate (0002) planes [125]. The effects of oxygen dissolution in Ti is an expansion of the lattice in the 'c' direction. The 'a' direction is only very slightly distorted and can be considered constant. The lattice parameters are very much dependent on the amount of oxygen present within the structure as demonstrated by Fig. 2.20. From 0% to 7% Oat%, the c perimeter will expand linearly from 4.68 Å to 4.73 Å. From 7 - 15% the expansion of the c parameter is reduced. Slowing of the c

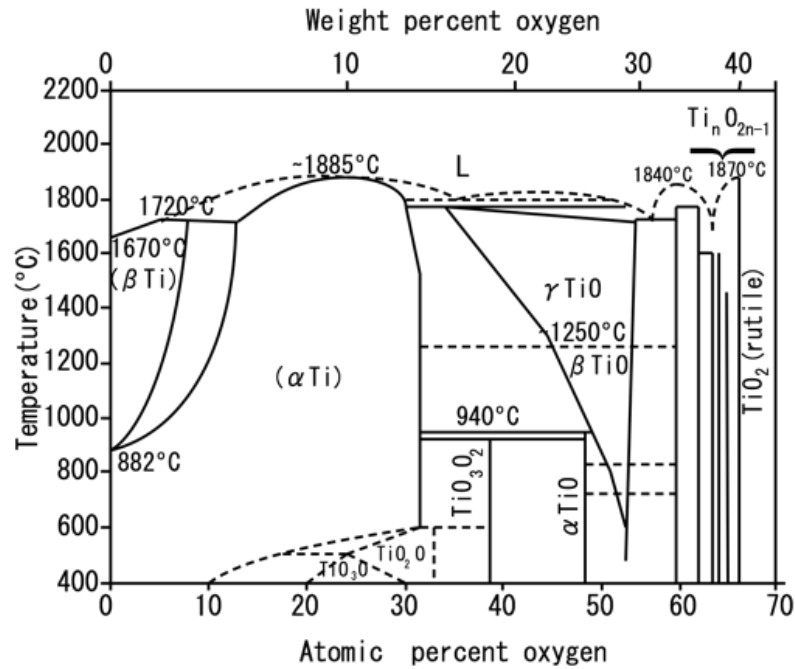


Fig. 2.19: Titanium-oxygen phase diagram [124]

axis expansion has been attributed to the degree of order shown by the interstitial oxygen. Between 7-15% it is proposed the formation of Ti_6O ordering helps to reduce the rate of expansion. Once the oxygen concentration surpasses, 15% linear expansion in the c direction occurs at a much faster rate [126].

2.7.4.3 Kinetics of Oxidation

The rate of film growth during the thermal oxidation of titanium has been the subject of many studies [8, 9, 118, 128]. Many of these studies demonstrate that between $500\text{ }^\circ\text{C} \rightarrow 1000\text{ }^\circ\text{C}$ the rate of growth of the oxide film follows the parabolic rate law (Eq. 2.29) [129]. Where x is the scale thickness and k is the proportionality constant. The proportionality constant is a direct function of the diffusion coefficient (D), oxygen pressure (P) and temperature (T). Eq. 2.29 holds true for most metals that develop fully dense non porous scales [130].

$$x = k\sqrt{t} \quad (2.29)$$

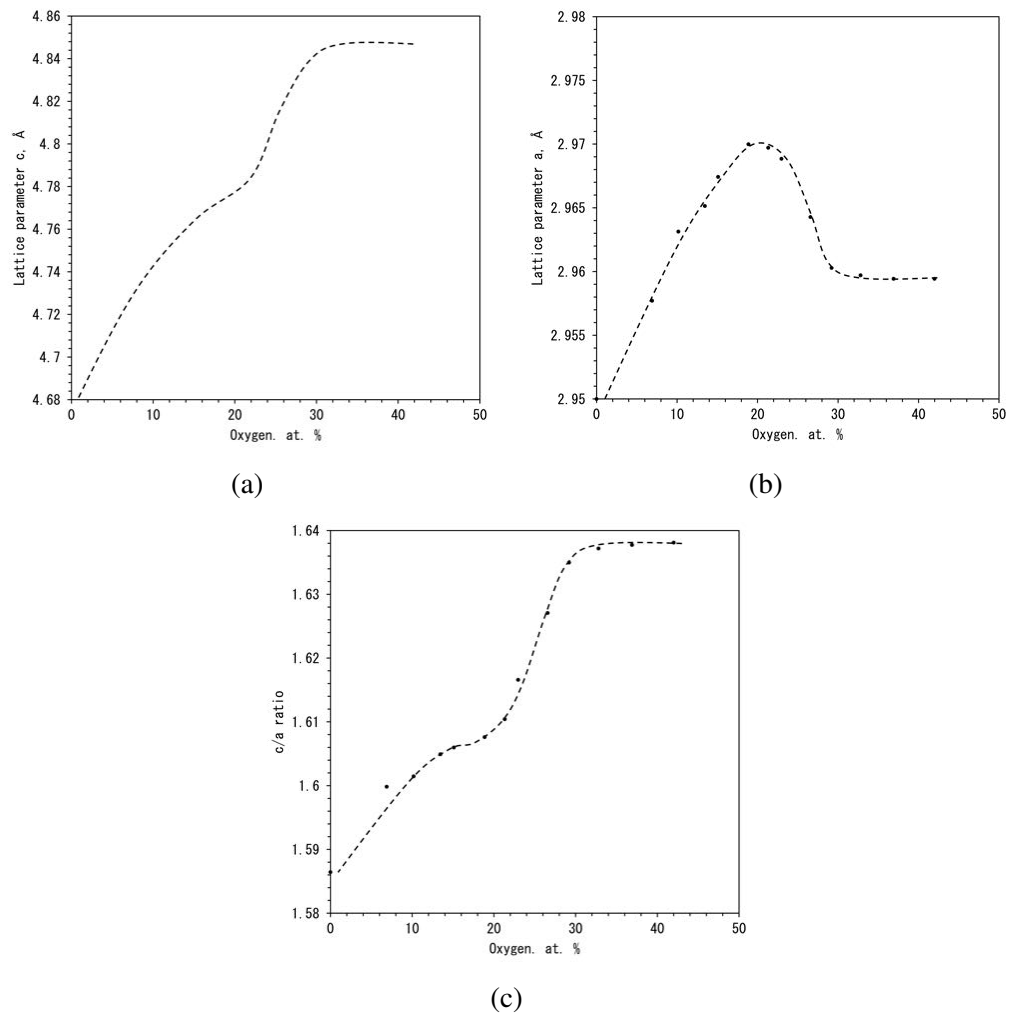


Fig. 2.20: The variation of lattice parameters with oxygen content: a) c direction, b) a direction and c) c/a ratio [127]

The rate law is valid throughout the entire aforementioned temperature range, and also describes both oxygen dissolution and oxide scale formation. The allotropic transformation of titanium from HCP (α -Ti) to BCC (β -Ti) at 883 °C has very little effect on the oxidation mechanisms of Ti. Using the Arrhenius equation (Eq. 2.30 [130]), the diffusion coefficient (D) of oxygen in titanium can be calculated. Where D_0 is the pre exponential frequency factor, Q is the activation energy, R is the universal gas constant ($8.314\,462\,1\text{ J mol}^{-1}\text{ K}^{-1}$) and T is the temperature.

$$D = D_0 e^{-Q/RT} \quad (2.30)$$

There is a small variation in the diffusion coefficients of alpha phase and beta phase titanium. This is highlighted by the pre exponential constants and activation energy displayed in Table. 2.6 [131].

Table 2.6: The pre-exponential constants and activation energies for diffusion of oxygen in alpha and beta titanium

	Alpha titanium	Beta titanium
D_0 (m s^{-2})	4.08×10^{-5}	4.5×10^{-5}
Q (kJ mol^{-1})	197	151

Although it has been shown that titanium dioxide film growth obeys the parabolic rate law, this is only true for the initial stages of film growth. Initial film growth consists of a compact and tightly adherent film. However, after extended oxidation, there is a critical film thickness at which delamination will occur. Stresses between the oxide scale and the outer surface of the metal cause an interfacial failure as highlighted by the high Pilling and Bedworth ratio ($\text{PBR} = 1.71$). The delamination of the oxide scale will result in the exposure of the underlying metal, creating a new metal-oxygen interface. This re-exposure will cause an increase in the oxidation rate to a more linear rate of oxidation. Many studies have investigated the oxidation behaviour of titanium and found that the linear region is in-fact a series of successive parabolic steps resulting from film formation and delamination [132].

2.7.4.4 Mechanisms of Oxidation

The thermal oxidation of titanium is dominated by the diffusion of oxygen, in both the scale and the metal. The titanium dioxide scale growth is dependent on the oxygen gradient within the metal. Initially, oxygen is absorbed through the process known as physisorption, where oxygen enters the HCP lattice with very little change to the unit cell [125, 126]. The chemisorption process then takes over, with the dissociation of oxygen molecules to form oxygen ions, creating changes to the chemical structure [132]. This process will continue until a monolayer of oxide is formed. Depending on the oxygen

concentration gradient within the the titanium, oxygen will either continue to diffuse into the HCP lattice, by passing through the thin film or add to the oxide layer and produce fresh oxide [132]. The overall rate of diffusion is dependent on:

The rate of oxygen dissolution: This will occur if the chemical potential of oxygen within the film and metal-oxide interface are not in equilibrium, thus making oxygen dissolution the prevailing diffusion mechanism.

The diffusion of oxygen through the oxide scale: Once the metal-oxide interface becomes saturated with oxygen, the mode of diffusion will then change to one dominated by oxygen diffusion through the oxide layer. This process is dominated by the inward movement of oxygen, via anion-vacancy diffusion. The diffusion of Ti-ions outward through the oxide layer has been shown to be negligible, since Ti-ion diffusion has a much larger activation energy than oxygen ion diffusion through TiO_2 [131].

2.7.4.5 Optimisation of Thermal Oxidation

Thermal oxidation of titanium is a reaction that proceeds with great vigour at temperatures above 600 °C. Short duration oxidation at temperatures greater than 700 °C can result in large-scale titanium dioxide (rutile) formation [9, 119, 133]. It has been observed that an oxidation temperature between 600 °C and 650°C offers the best compromise between generating oxide layer thickness and adhesion [2, 10, 18]. Thus, numerous studies have focused on the optimisation of the thermal oxidation process, in order to create a sufficiently thick but tightly adherent TiO_2 (rutile) layer on a relatively thick hardened oxygen diffusion zone, with varying degrees of success, such as by controlled oxidation in air [18], glow discharge oxidation [134], diode plasma oxidation [135], and slow furnace cooling after thermal oxidation in air [77].

2.7.4.6 Tribological Response of Thermally Oxidised Titanium

The thermal oxidation of titanium produces a hard (1000HV) rutile oxide layer at the surface and a hardened oxygen diffusion zone in the subsurface of titanium and titanium

alloys [2, 135]. The oxide layer can have low friction ($\mu = 0.2$) and low wear rates [15], while the oxygen diffusion zone (ODZ) can be beneficial in enhancing the load bearing capacity, the lubrication ability and abrasive wear resistance of titanium [16].

The beneficial effects of thermal oxidation on the tribological properties of titanium have been demonstrated by many investigators [2, 70, 77, 116, 135]. However, the oxide layer generated has a tendency to delaminate from the substrate, causing sudden failure and removal of the layer, even at relatively low loads. This is especially true when thicker layers are generated during high temperature oxidation or prolonged oxidation [2, 10, 77].

2.7.4.7 Electrochemical Response of Thermally Oxidised Titanium

Several studies have also been conducted on the corrosion behaviour of thermally oxidised titanium. Various corrosive mediums have been investigated with thermal oxidation providing enhanced corrosion resistance in the following environments: Nitric acid (HNO_3) [119, 136], hydrochloric acid (HCl) [70, 136], saline solution (0.9 wt% NaCl) [8, 10, 137] and Ringer's solution made from distilled water and then prepared by adding (in g L^{-1}): NaCl - 9.0, KCl - 0.43, NaHCO_3 and CaCl_2 - 0.24 [118, 128]. It has been confirmed that the oxide layer provides additional protection against corrosion by serving as a barrier layer [61]. For the best corrosion resistance, the oxide film is required to be crack free and very adherent to the base metal [8]. Thermally oxidised titanium has also been demonstrated as having a very low hydrogen absorption rate. The diffusion coefficient of H in TiO_2 is $2.84 \times 10^{-16} \text{ cm s}^{-2}$ [138, 139]. Therefore, TiO_2 acts as a barrier layer preventing hydrogen embrittlement of the subsurface titanium.

Various studies have been carried out to optimise the corrosion protection of the rutile oxide film [137]. It was found that the duration, temperature and the rate of cooling after oxidation, have a substantial effect on the corrosion properties of TO-Ti.

Jamesh et al. [9] investigated the effect of cooling rate on the corrosion properties of titanium in a 0.9% NaCl solution. The authors found that slower cooling after the oxidation cycle resulted in a more adherent oxide film. The cooling rate was slowed down

by allowing the samples to furnace cool (FC). Faster cooling in air (AC) or water (WC), resulted in surface scales and spallation, especially true for thicker films. The corrosion resistance was shown to be much better for samples that were allowed to furnace cool. The authors proposed that the differences in thermal expansion of the rutile and the titanium substrate were the main causes for the observed spallation.

Kumar et al. [140] performed an investigation concerning oxidation time and temperature with regard to the corrosion resistance in Ringer's solution (pH = 7.8). This study showed that for longer duration oxidation or during high temperature oxidation when thicker films are formed, there is a marked reduction in corrosion current (I_{corr}) observed. This is true as long as descaling of the oxide film has not occurred as a result of the oxidation process. Therefore, a compromise between film growth and film adhesion needs to be met.

2.7.4.8 Tribocorrosion Response of Thermally Oxidised Titanium

A major consideration in the use of titanium is the interaction between wear and corrosion, i.e. tribocorrosion. There are various engineering applications where both corrosion and wear play an important role in component life: medical implants and valves are just two examples. In these scenarios, mechanical wear can cause the damage of a passive film. This can lead to accelerated corrosion, which in turn can cause accelerated wear [61, 141, 142]. The tribocorrosion behaviour of thermally oxidised titanium has been investigated by several investigators [117, 128, 143].

When TO-Ti was tribologically tested, there were two prevailing outcomes from the tests. When tested in a corrosive environment with a low surface contact pressure, the film demonstrated excellent frictional and corrosion response, reducing both chemical and mechanical wear [144]. However, once increased contact pressures are applied delamination of the oxide film has been observed [117, 145]. Delamination of the rutile film depends on both the thickness of the film (thicker films delaminate at lower loads) and the applied loads.

Under high load testing delamination of the rutile from the contact zone exposes the oxygen rich diffusion zone to the corrosive environment. The early removal of the oxide film during sliding contact negates the positive effects of the oxide film.

2.7.5 Carburising

Titanium carbide is a very important non-oxide ceramic, widely used in fields where high wear resistance is essential. There is also an increasing interest in biomedical applications [87]. Titanium carbide has attracted considerable attention due to its high melting point, low density, high hardness (2500-3000HV), superior chemical and thermal stability, and outstanding wear resistance [19]. Carburisation of titanium has been successfully demonstrated using various techniques, these include: Pack carburising [146], gas carburising [11, 21], plasma carburising [147], laser melting [13] and ion implantation [144].

One of the main issues associated with titanium carburisation is the high affinity between Ti and O₂, resulting in the formation of titanium dioxide (TiO₂) at elevated temperatures [7]. Therefore, carburisation must be undertaken within a vacuum to allow carbon absorption to occur rather than oxidation.

2.7.5.1 Dissolution of Carbon in Ti

Carbon has a maximum solubility of 3.3 at% in the α -phase Ti [148]. The limited solubility in alpha titanium results in the formation of a peritectoid system [149], as observed in Fig. 2.21. Between 3.3 and 40 at% carbon concentration there will be TiC accumulations within the titanium structure. Once the carbon content reaches 40 at% TiC will be the sole observable phase.

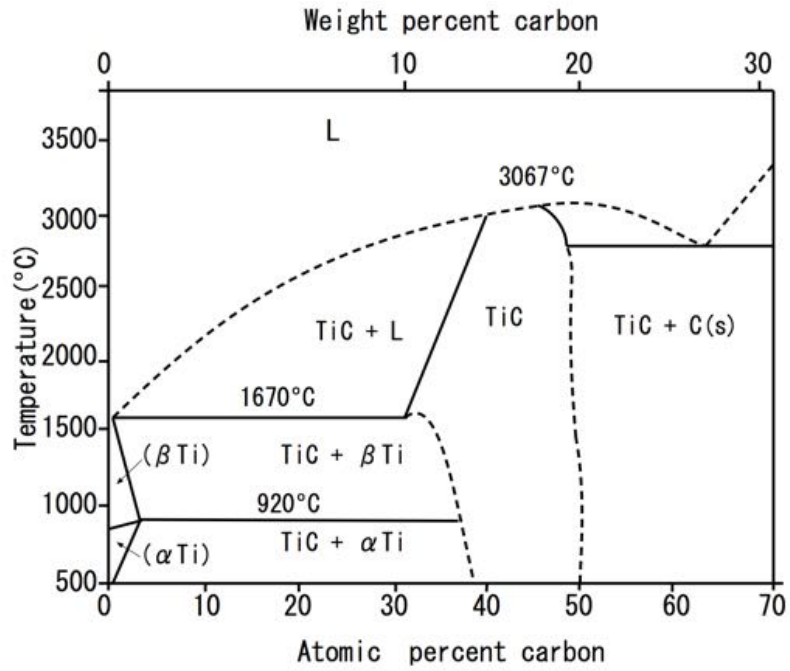


Fig. 2.21: Titanium-carbon phase diagram [150]

The effects of carbon dissolution in Ti is limited due to the low solubility however, there is a slight expansion of the lattice in the 'c' and 'a' direction. The lattice parameters expand linearly with increasing carbon content as depicted in Fig. 2.22 [149].

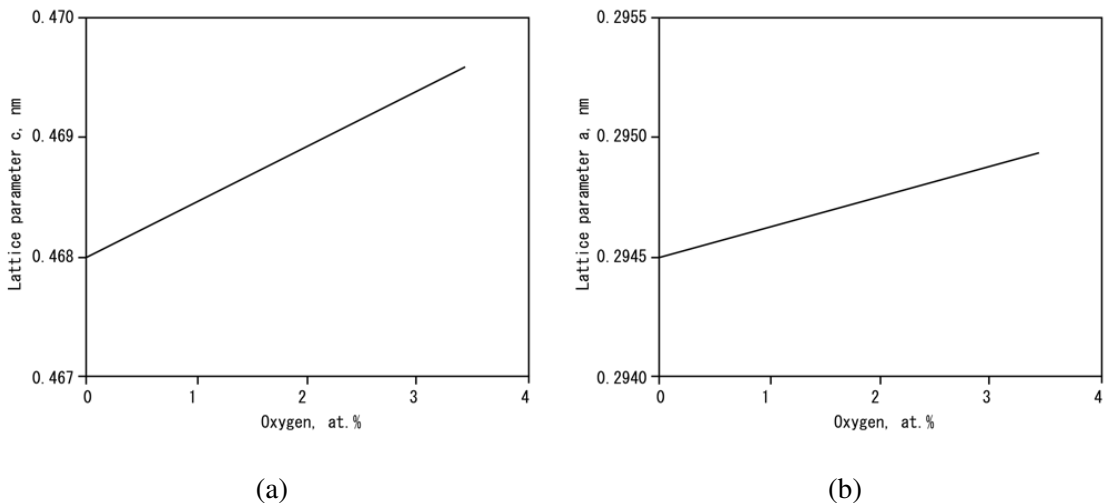
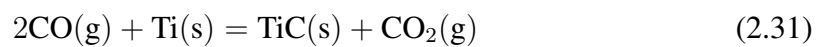


Fig. 2.22: The variation of lattice parameters with carbon content [149]

2.7.5.2 Mechanisms of Carburisation

Thermal techniques using gas or pack carburising methods are the most readily used, due to simplicity and cost-effectiveness [91]. Standard carburisation is usually divided into three stages: 1) absorption of active carbon 2) the diffusion of carbon 3) the rearrangement of carbon resulting in the creation of new phases. In order for carbon to diffuse in titanium, a constant supply of carbon monoxide (CO) is required. Once the production of CO is at the required level for carburisation to occur, the dominant reaction mechanism will be that of CO and Ti (Eq. 2.31).



The carburisation of titanium is dominated by the diffusion of carbon in both the TiC film and the metal. The titanium carbide growth is dependent on the carbon gradient within the metal. Initially, carbon is absorbed through the decomposition of carbon monoxide (CO) at the metal surface into carbon dioxide and atomic carbon in the metal (Eq. 2.31). Carbon will then diffuse into the HCP lattice with very little change to the unit cell [149]. Once the carbon content reaches the required level, there will then be TiC phase formation at the surface. This process will continue until a layer of TiC is formed at the surface. Depending on the carbon concentration gradient, carbon will either continue to diffuse into the HCP lattice by passing through the thin film or, add to the carbide layer and produce fresh carbide. The diffusion in the metal phase is so rapid compared the carbide that only the latter is considered rate determining [149].

2.7.5.3 Kinetics of Carburisation

The diffusion of carbon in titanium is very much dependent on crystal phase. Bucur and Wagner [148] found the frequency factors (D_0) and the activation energy (Q) for both alpha and beta phases of titanium (see Table. 2.7 on page 65). Thus, using the Arrhenius equation (see Eq. 2.30) the rate of carbon diffusion can be calculated. The diffusion of

carbon into titanium occurs at a much faster rate in the BCC structure of beta titanium. Therefore, temperatures above 883 °C are required for carburisation to take place at a substantial rate [148]. Film formation during carburisation has been shown to follow the parabolic rate law (Eq. 2.29, page 56) [149].

Table 2.7: The pre-exponential constants and activation energies for diffusion of carbon in alpha and beta titanium

	Alpha titanium	Beta titanium
D_0 (m s ⁻²)	8.63×10^{-4}	27.75×10^{-4}
Q (kJ mol ⁻¹)	186.6	186.6

2.7.5.4 Tribological Response of Carburised Titanium

Tribologically, it has been shown that TiC has the ability to produce very low wear rates [20, 21] and an extremely low coefficient of friction ($\mu = 0.2$) [11, 144]. However, the surface benefits are only present as long as the surface film remains intact.

The carburising duration is directly linked to the thickness of the TiC layer and the adhesion strength of the TiC film [151]. Longer duration carburising results in a larger and more tightly compact TiC protective film, which is much more resilient to wear.

2.7.5.5 Electrochemical Response of Carburised Titanium

Studies have been carried out showing the electrochemical response of carburised titanium in various mediums. Electrochemical corrosion measurements have been carried out in both HCl [146] and H₂SO₄ [39] solutions. In both corrosive mediums the response of carburised titanium is much improved over that of untreated titanium. During potential dynamic sweeps, it can be seen that the carburised titanium has a more noble corrosion potential and much larger passivation interval when compared with untreated titanium. These studies have shown that thicker film formation results in an improved corrosion resistance of the carburised titanium. Long term immersion testing carried out in HCl

also showed carburised titanium to be much more resistant to corrosion than untreated titanium [146].

TiC has also been investigated as a biocompatible material. TiC is very resistant to biological solutions. The TiC film prevents the dissolution of Ti-ions into surrounding tissue [87]. TiC has also been shown to stimulate osteoblast when used as a bone implant material [152].

2.7.5.6 Tribocorrosion Response of Carburised Titanium

There have been very few studies investigating the tribocorrosion response of carburised titanium. Luo et al. [11] conducted fretting wear tests of carburised titanium in bovine serum. This study demonstrated the effect of carburising on the friction and wear properties in a physiological medium. Untreated titanium was also tested in the same conditions and was found to have a friction coefficient of 0.33, while the carburised titanium's friction coefficient was observed as being < 0.2 . This investigation showed that once the TiC layer was removed, the friction coefficient reverted to that of the untreated titanium. While the TiC film was intact, there were marked reductions in both the friction and wear rate.

Chapter 3

Experimental Methods and Surface Analysis Techniques

This chapter highlights the experimental work carried out in terms of samples preparation, testing and analysis. All preparation and test details are provided. Analysis techniques used to investigate a materials surface and bulk characteristic are also reviewed.

3.1 Substrate Material and Preparation

For all tests conducted, commercially pure titanium (CP-Ti) grade 2 (99.4% purity see Table. 3.1) was used as the substrate material. Square samples of 20 mm x 20 mm x 2 mm were prepared by cutting an as-received CP-Ti plate. The samples were then manually ground using progressively finer SiC grinding papers down to the P1200 grade, resulting in a surface finish of $0.203\ \mu\text{m}$ (R_a). the samples were then ultrasonically cleaned in methanol for 15 minutes.

Table 3.1: Chemical composition of CP-Ti samples

Element	O	N	C	H	Fe	Residuals	Ti
Wt %	0.25	0.03	0.08	0.015	0.3	0.4	Rest

3.2 Surface Engineering Techniques

3.2.1 Thermal Oxidation

Thermal oxidation (TO) of CP-Ti was carried out in a muffle furnace, in air at a temperature of 625 °C for durations of 5, 20 and 72 hours. After the oxidation treatment, the specimens were allowed to cool in the furnace down to room temperature. This set of samples were designated as "furnace cooling" (FC). Under the present experimental conditions, furnace cooling from 625 °C to below 100 °C took approximately 6 hours. Samples reported in this thesis were FC unless otherwise stated.

In this study, initial efforts have been made to improve the adhesion/bonding of TiO₂ rutile film to the substrate material. This was achieved by:

Further Reducing the Cooling Rate of the Samples After Thermal Oxidation

The purpose was to reduce thermal stresses between the oxide layer and substrate, increasing the adhesion of the oxide layer [77]. This was achieved by programming the cooling scheme such that the cooling rate was controlled at half of the furnace-cooling (FC) rate, i.e. It took about 12 hours to cool the sample from 625 °C to below 100 °C. These samples were described as controlled slow cooling (CFC) and shown in Fig. 3.1.

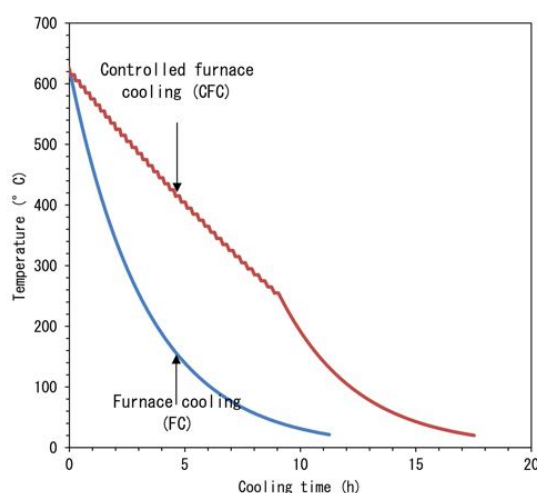


Fig. 3.1: The cooling rates employed during this study

Mechanically Treating the Surface of Titanium Before Thermal Oxidation

This was achieved by surface mechanical attrition treatment (SMAT), employing the technique reported in [59]. Briefly, SMAT was conducted using an electromagnetic shaker, the principle of which was similar to those reported elsewhere [153, 154] and was similar to conventional shot peening. During SMAT, the sample was secured to a cylindrical chamber, measuring 20 mm in diameter and 25 mm in length. This was then attached to the shaker. The 10 martensitic stainless steel balls (AISI 440) of 6 mm diameter inside the chamber vibrated with the shaker and impacted onto the specimen surface repeatedly at a frequency of 40 Hz and amplitude of 7 mm (see Fig. 3.2), causing indentation and plastic deformation on the impacting surface [59]. The total SMAT time was 180 min. After SMAT, the samples were ultrasonically cleaned in methanol for 15 min, and then were thermally oxidised at 625 °C for 20 h, followed by normal furnace cooling.

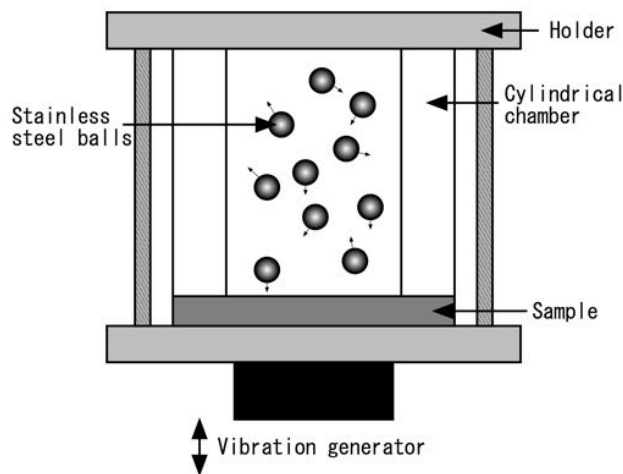


Fig. 3.2: Schematic diagram of the surface mechanical attrition treatment (SMAT) setup

Table 3.2 is a summary of all thermal oxidation conditions used during this study, highlighting post and prior treatments.

Table 3.2: Summary of thermal oxidation conditions used in this study

Temperature (°C)	Time (h)	Cooling Type	Prior SMAT (h)
625	5	FC	0
625	20	FC	0
625	72	FC	0
625	20	CFC	0
625	20	FC	3

3.2.2 Pack Carburisation

Pack carburisation (PC) was carried out in a steel container with an internal volume of 200 cm³. 140 cm³ of the container was filled with carburising compound, with the titanium samples fully emerged in the carburising compound as depicted in Fig. 3.3. In order to determine the most effective carburising conditions, various temperatures, durations and carburising compound compositions were investigated.

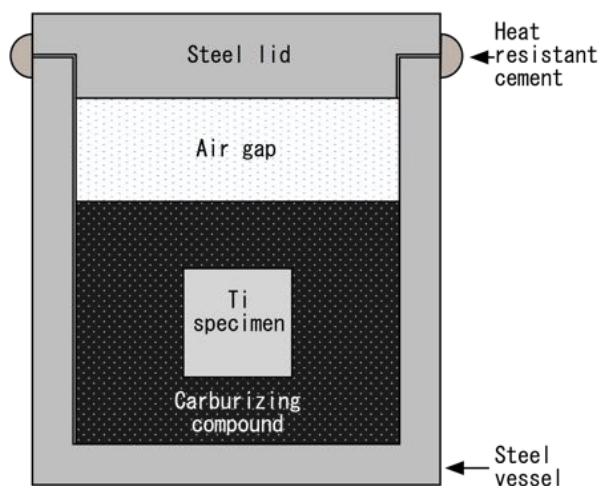


Fig. 3.3: Schematic diagram of the pack carburisation vessel

The initial composition of the carburising mixture was the same as that used for traditional steel carburisation. The composition of the pack was 70% carbon and 30% energiser. The carbon was in the form of finely ground hardwood charcoal and the energiser was made up of Barium-carbonate (BaCO_3), sodium-carbonate (Na_2CO_3) and

calcium carbonate (CaCO_3) in the ratio of 3:2:1 [155]. This pack was then used to determine the best temperature for the carburisation of titanium to take place. A duration of 20 h with furnace cooling (FC) was chosen and then temperatures of 625 °C, 725 °C, 825 °C and 925 °C were applied. These samples were then tribologically tested in order to determine the most effective temperature for producing a wear resistant coating.

Once the optimal temperature had been determined using the standard steel pack composition, the carburising compound composition was varied at the optimal temperature for a duration of 20 h. The composition of the energiser remained the same but the ratio of energiser to carbon was investigated with energiser percentage varied from 30-50%.

Once the most effective pack composition and temperature had been determined, the duration needed for optimal carburisation was then investigated. Times of 10, 20 and 40 h were investigated using a 1:1 pack composition. Wear testing was again used to determine the most effective carburisation duration for producing a wear resistant film. Using the optimal conditions the: tribological, corrosion and a tribocorrosive characteristics were investigated. Table 3.3 summarises the pack carburising conditions investigated.

Table 3.3: Summary of the pack carburising conditions used in this study

Optimisation Type	Temperature (°C)	Time	Pack Ratio			
			C	BaCO ₃	Na ₂ CO ₃	CaCO ₃
Temp Optimisation	625	20	14	3	2	1
	725	20	14	3	2	1
	825	20	14	3	2	1
	925	20	14	3	2	1
Pack Optimisation	925	20	14	3	2	1
	925	20	9	3	2	1
	925	20	6	3	2	1
Duration Optimisation	925	10	6	3	2	1
	925	20	6	3	2	1
	925	40	6	3	2	1

3.3 Chemical and Surface Analysis Techniques

3.3.1 X-Ray Diffraction (XRD)

X-ray diffraction is a non-destructive characterisation technique, allowing for rapid structural analysis. XRD allows for the identification of crystal structure, sample purity as well as unit cell dimensional information.

XRD, along with all techniques involving radiation diffraction by a crystalline material, depends upon Bragg's law. Bragg's law describes the relationship between atomic plane spacing and the position of maximum diffraction. By negating any atomic interaction between X-rays and crystalline substances, Bragg dealt with X-ray diffraction as if it was just a reflection from parallel planes, as depicted in Fig. 3.4 [156–158]. Using the parallel planes method, he devised Eq. 3.1.

$$\lambda = 2d_{hkl} \sin \theta \quad (3.1)$$

Where λ is the wavelength of X-ray radiation, θ is the incident angle with the hkl and planes d is the inter planar spacing between two hkl planes [156]. For hexagonal crystals, as those in titanium, Miller-Bravais notation ($nkil$) is used instead of the three axis Miller notation (nm) [159]. In Fig. 3.4, it can be seen that constructive interference will occur when the extra distance travelled by a parallel X-ray is equal to the wavelength of the X-ray. Therefore, if the wavelength of the radiation and the angle at which the beam is reflected are known, then the planar spacing can be calculated. This planar spacing can be used to identify crystal structure [156].

X-ray spectrometers have been developed to use Equation Bragg's law to identify Crystal phase. Fig. 3.5 shows the quintessential configuration of an X-ray spectrometer. The source radiation is usually developed from CuK or CoK. CuK radiation is most common, with a wave length of 1.5418 \AA [157], X-rays produced are filtered to produce monochromatic X-rays. X-rays are then directed towards the sample while the sample

and detector are rotated in order to change θ . The detector is always positioned at 2θ in order to detect the reflected beams. When the geometry of the incident X-rays satisfies the Bragg's Equation, constructive interference will occur at the detector, resulting in a peak intensity detection. The intensity and angle are recorded, with both being used for crystal identification. Intensity of the peaks can be related to the amount of phase present.

In the present study, XRD analysis was carried out using a Bruker D8 Advance X-ray Diffractometer with CuK α -radiation ($\lambda = 0.154 \text{ nm}$) at Birmingham University. CuK radiation was used between angles of 20° and 70° 2θ to determine the phases present in both thermally oxidised and pack carburised titanium.

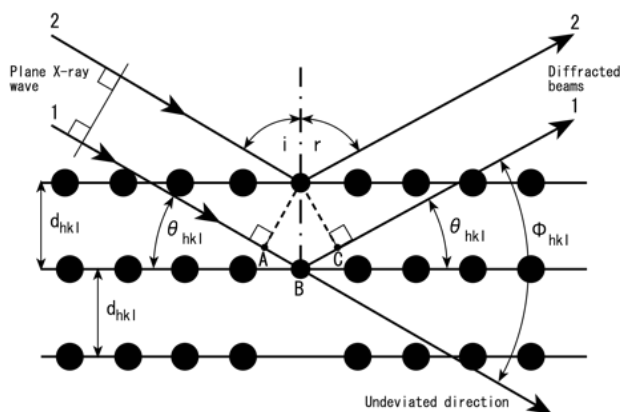


Fig. 3.4: The derivation of Bragg's law

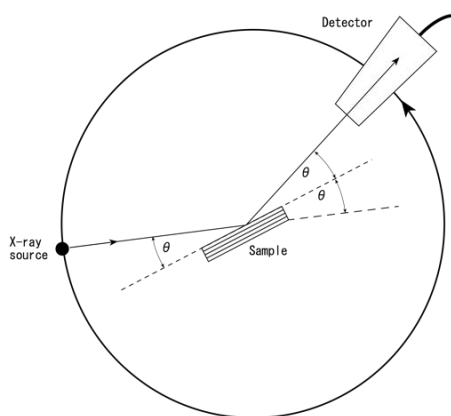


Fig. 3.5: Schematic diagram of the XRD apparatus

3.3.2 Glow Discharge Optical Spectroscopy (GDOS)

Glow discharge optical spectrometry allows for rapid chemical composition profiling of a solid material surface and subsurface. GDOS is able to analyse material composition to depths of several tens of μm [160]. A Grimm glow discharge lamp is used to provide a low pressure argon environment. Cathodic sputtering is carried out by applying a large voltage across two electrodes (one being the sample). Argon ions (Ar^+) are formed in the negative glow and bombarded upon the samples surface. This results in the release of atoms (M^0). The sputtered material is then excited in a low pressure plasma discharge, located away from the samples surface. Continued sputtering of the sample removes material layer by layer from the surface, without changing the materials chemistry [160]. Light emissions from the excited plasma is then analysed. The atomic line spectra generated is material specific and allows for elemental identification. There is a liner relationship between concentration and spectral intensity. Spectral databases allow for a qualitative profile across surface layers to be computed. This technique was conducted at the University of Birmingham (UK).

3.3.3 Metallographic Examination

In order to investigate the thermally oxidised and pack carburised titanium cross sections, the treated samples were cut using a desktop cutting machine. These samples were then nickel plated (if conductive) and set in a phenolic resin, using a Presi micro-press 3, to aid handling. The cross section were then manually ground using progressively finer SiC grinding papers down to the P1200 Grade. For structural characterisation a finer finish is required. Polishing of the cross section was carried out using Presi polishing pads embedded with initially $6\ \mu\text{m}$ diamond paste and then finally $1\ \mu\text{m}$ diamond paste. This generated a smooth and mirror like finish which can then be etched.

The polished samples were etched using a concentrated sulphuric acid (H_2SO_4) at a temperature of $100\ ^\circ\text{C}$. The titanium was left in the hot acid until a noticeable change in

surface colour occurred.

3.3.4 Light Microscope Analysis

A standard NIKON binocular metallurgical microscope was employed in this study. Optical microscopes can be used to visualise fine details within a larger structure through magnification, while simultaneously allowing the accruals of dimensional data. The image produced can be viewed directly through an eyepiece or recorded photographically.

3.3.5 Scanning Electron Microscopy (SEM)

With optical microscopes, the wavelength of light (λ) is a limiting factor in the resolution. In order to view objects at much higher resolutions, scanning electron microscopes (SEM) are used. These microscopes replace light with electrons which have a much reduced wavelength. SEMs are renowned for producing high resolution images with large depth of field, with the ability to show fine structural topography.

SEMs operate by generating a beam of electrons from a tungsten filament in a vacuumed environment. These electrons are then collected, condensed and accelerated away from the electron source to bombard the sample's surface. Fig. 3.6 shows a schematic diagram of the SEM and its basic components.

When the electron beam comes into contact with the specimens surface, electrons can scatter with a number of plausible outcomes. These outcomes have been characterised as being either elastic or inelastic and are depicted in Fig. 3.7.

Elastic scattering: When the electron beam passes close to a positively charged atomic nucleus charge, interactions can change the direction of the electrons with very little energy loss. Electron trajectory can be changed from almost 0° to 180° . This elastic scattering is much more likely to occur on specimens of high atomic number (Z) and if the incident electron is of low energy. Elastically scattered electrons are commonly used in SEM images. When electrons emerge from the specimen surface with a large deflection angle

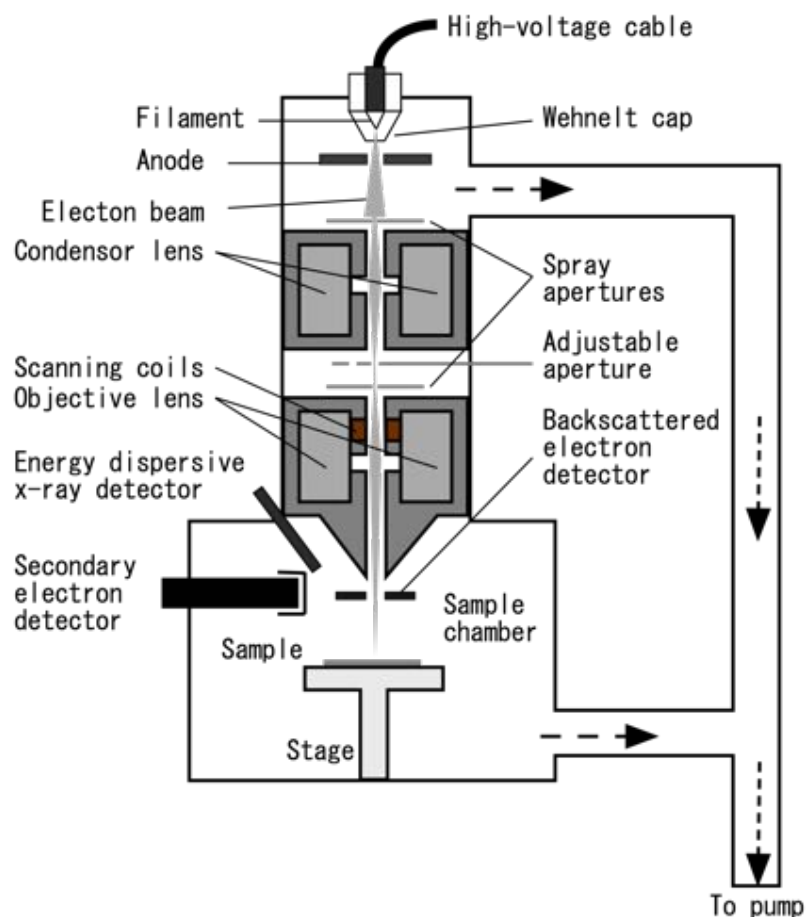


Fig. 3.6: Schematic diagram of the Scanning electron microscope (SEM)

(> 90°) the signal can be collected. This signal is known as backscattered electrons (BSE). BSE are dependent on atomic number. Therefore, BSE images can give contrast depending on atomic number. Heavier elements with larger atomic numbers (Z), show stronger signals (brighter) than those with a lower Z [161, 162].

Inelastic scattering: Some electrons will interact with the orbiting electrons and the atomic nuclei and in the process lose a considerable amount of energy. When this happens, there are numerous possible outcomes (see Fig. 3.7): Secondary electron emissions, X-rays production, Auger electrons production, phonons production and cathodoluminescence. Of these, the most commonly used is the secondary electrons. When incident electrons bombard a material's surface, loosely bound conduction electrons can be knocked out of the sample, the escaped secondary electrons (SE) can

be detected. Secondary electrons are widely used for generating topographical images [163].

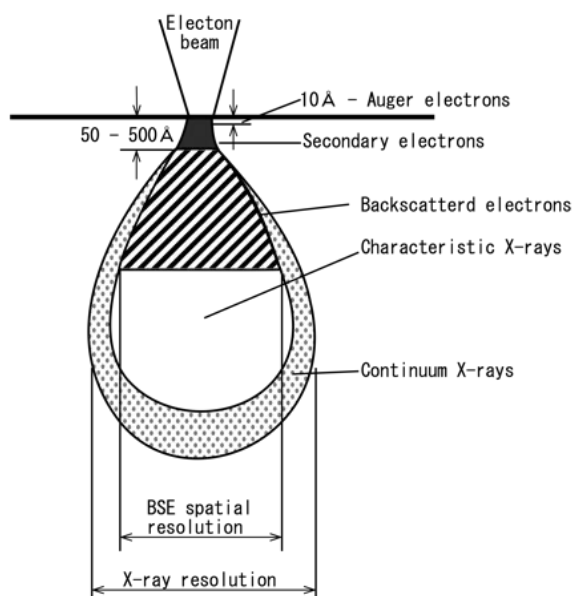


Fig. 3.7: Interactive volume of a material at the point of electron beam bombardment during SEM analysis

The emission of X-rays due to inelastic scattering has led to the development of some X-ray microanalysis techniques: WDS (wavelength dispersive spectroscopy) and EDX (Energy dispersive X-ray microanalysis).

When an electron is knocked out of a low energy orbital, a high level electron will then "fall" to the lower valance level. When this electron changes state, energy can be released in the form of an X-ray. When an electron transition occurs, the energy released will be specific to the atomic number of the element under investigation. WDS and EDX use these X-ray signals to identify elements. EDX is the most common form of X-ray analysis. EDX allows for the relative abundance of elements within the beam to be characterised and also, elemental maps of the surface showing element distribution can be generated [163].

Two different SEM models were used in this work; Carl-Zeiss EvoHD 15 and Leica S430. The specimens were investigated in secondary and backscattered electron modes.

EDX analysis was also performed for qualitative chemical analysis of the samples.

3.3.6 Ball Cratering

Ball cratering uses a large diameter steel ball in rotating contact with a test material to produce a taper section on a coated sample. This taper section enables coating thickness, interface sharpness and coating adhesion to be analysed.

During ball cratering a 25 mm diameter AISI 52100m steel ball is rotated upon the sample with diamond paste (1 μm). Rotation speed can be controlled between 3-12 rpm. Once the surface coating on the sample material has been penetrated, an optical microscope can be used to observe the tapered section. Total film thickness can be easily measured. Films that would not normally be observable can be observed due to the effective surface area increase of the tapered layer. Fig. 3.8 shows a schematic diagram of the ball cratering machine. The film thickness (t) can be calculated using Eq. 3.2 with x being the visible film thickness, y is the remaining crater width and D is the ball diameter in microns.

$$t = \frac{x \times y}{D} \quad (3.2)$$

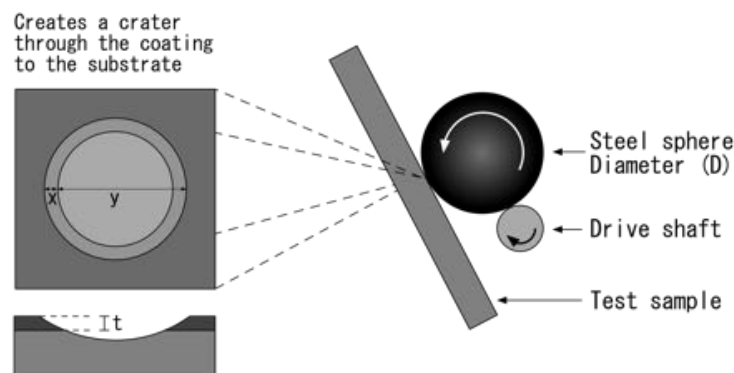


Fig. 3.8: Schematic diagram of the ball cratering technique and the resulting section taper

Ball cratering was used to determine the surface film thickness for both oxidised and carburised titanium. This technique was also used to examine wear tracks, allowing the depth of wear tracks to be visually related to surface layer structure.

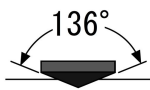
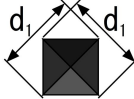
3.3.7 Micro-Hardness Test

The resistance of a material to indentation is known as hardness. Hardness is measured through the application of a hard indenter onto the surface of the test material. The indenter is applied with a constant load over a set amount of time. Measurements of the resulting depression are then used to calculate hardness [28].

Micro-hardness uses the exact same principles as standard hardness testing but micro indenters are used with the resulting deformation being viewed and measured under a high power microscope.

In the present study the Vickers hardness test method was employed using an Indentec ZHV micro-hardness tester. A diamond tipped square base pyramid indenter was used to create impressions on the samples surface. Loads of 0.025-0.5kg were applied via the indenter, depression marks were measured in accordance to Table. 3.4. Surface hardness measurements were taken along with cross sectional hardness profiles for both thermally oxidised and pack carburised titanium.

Table 3.4: Vickers hardness geometry [28]

Test	Indenter	Shape of Indentation		Load	Formula for hardness number
		Side view	Top view		
Vickers	Diamond Pyramid			P	$VHN = \frac{P \times 2 \sin\left(\frac{136}{2}\right)}{d_1^2}$

3.4 Tribological Measurements

3.4.1 Tribology Test

Tribological testing was conducted using a Teer Coatings pin-on-disk (POD) tribometer. This test method allows for the wear performance of the test specimen to be analysed through the determination of wear rate and the evaluation of friction forces generated during sliding contact. POD testing requires a contact couple with a counter face material (in this study a rigid ball) positioned perpendicular to the test sample (disk). The sample (disk) is then rotated about the pin as shown in Fig. 3.9. The resulting circular path wear track generated on the disk surface is also depicted.

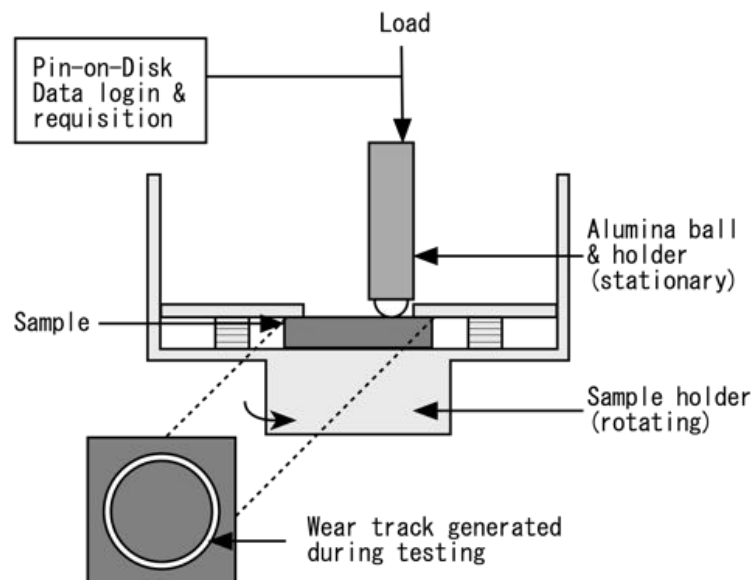


Fig. 3.9: Schematic diagram of the Teer Coatings pin on disk tribometer

Using the Teer Coatings POD tester, there are various test parameters that can be controlled, these include:

Load - The force applied to the sample is controlled via weights and is measured in Newtons (N).

Frequency - The relative speed between the two surfaces can be controlled and is measured in revolutions per minute (rpm).

Time - The sliding time is precisely controlled to the nearest second (s).

Distance - Sliding distance (d) can be controlled/calculated using the frequency (f), time (t) and the position of the ball, relative to the centre of the disk (wear track diameter, D) using the following equation:

$$d = f\pi Dt \quad (3.3)$$

Contact pressure - Depending on the size and material of the two contact materials, the contact pressure can be estimated using Herz theory (Eq. 2.7, page 12). Table 3.5 shows the calculated contact pressure between a titanium plate and a 8 mm alumina ball for contact loads between 1 N and 40 N.

During this study, various test parameters were used, Table. 3.5 is a summary of the values used during this study. All tribological tests were conducted using an 8 mm diameter Alumina ball (Al_2O_3 , Grade 5) manufactured by Trafalgar Bearings unless otherwise stated. Alumina was chosen due to its high hardness and inertness.

Table 3.5: Tribometer test parameters used during this study

Apparatus Parameter	Value
Load	1-40 N
Contact Pressure	448.3-1533.2 MPa
Track Diameter	6 - 12 mm
Frequency	60 rpm
Sliding time	1 -5 hours (1 hour most common)

When carrying out tribological wear testing, thorough prior and post cleaning is required. Initial cleaning stops any interaction between contaminates and the sliding contacts, which could affect the results. Post cleaning is also important to allow for accurate determination of the wear profile, by removing all wear debris generated during the sliding contact. Ultrasonic cleaning in ethanal was conducted for 20 min before and after the wear testing.

3.4.2 Wear Rate Measurements

In order to calculate the wear rate of the tested material, a Mitutoyo SJ-400 stylus type profilometer was used. Wear track profiles were recorded at 8 intervals around the wear

track. Using the mid ordinate form of integration, the cross sectional area (A) of wear track profile was calculated using numerical integration as shown in Fig. 3.10 and via Eq. 3.4 and 3.5.

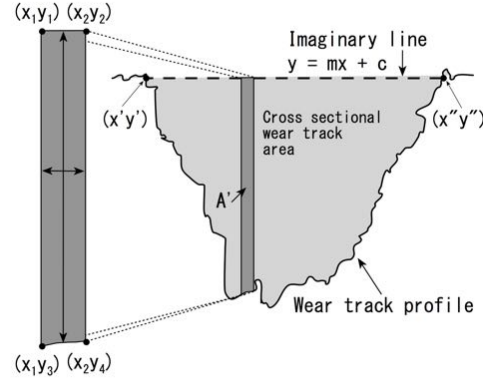


Fig. 3.10: Wear track cross sectional area calculation using numerical integration

$$A' = (x_2 - x_1) \times \left(\frac{(y_1 - y_3) + (y_3 - y_4)}{2} \right) \quad (3.4)$$

$$A = \Sigma A' \quad (3.5)$$

The cross sectional area was then averaged and multiplied by the wear track diameter (d_w) to generate the volume of material lost (V), as described by Eq. 3.6.

$$V = A \times d_w \quad (3.6)$$

The wear track volume was then used along with the sliding distance (d_s) and the applied load (L) to calculate the total material loss rate (TMLR), as described by Eq. 3.7.

$$TMLR = \frac{V}{d_s \times L} \quad (3.7)$$

3.5 Electrochemical Measurements

In this study various techniques were used to analyse the electrochemical corrosion properties of titanium and surface modified titanium. To do this, the following measurements were taken: free corrosion potential, anodic and cathodic polarisation both dynamically and statically and Mott-Stocky analysis.

Electrochemical tests were performed at various surface depths. This was to build a cross sectional profile for the surface modified titanium, to understand the electrochemical response of both the modified surface but also the modified subsurface. This was carried out by progressive grinding of the treated titanium using 1200P SiC Paper. This exposed the underlying layers at various depths from the surface. 2-3 μm of material was removed with each stage of grinding and was measured using a digital micrometer accurate to 1 μm . After cleaning ultrasonically in methanol for 5 min, each ground sample was then loaded into the electrochemical test cell and then cathodically charged at -500 mV for 3 min to create a uniformed starting point for all samples. Each exposed layer was then tested using the aforementioned electrochemical techniques.

All tests were performed using a Princeton applied research model K0235 three-electrode electrochemical flat cell connected to an ACM Gill AC potentiostat equipped with a data logger. Specimens were clamped to the cell, sealing against a PTFE (Polytetrafluoroethylene) knife edged gasket, which exposes 1.0 cm^2 of the specimen surface to the electrolyte. A schematic of this setup is shown in Fig. 3.11. The reference electrode was a saturated calomel electrode (SCE), with all potentials referring to the SCE scale. The electrolyte used for all tests was 0.9% NaCl solution, which was prepared from analytical grade chemicals and distilled water. All tests were performed at standard room temperature (20 °C) open to the air.

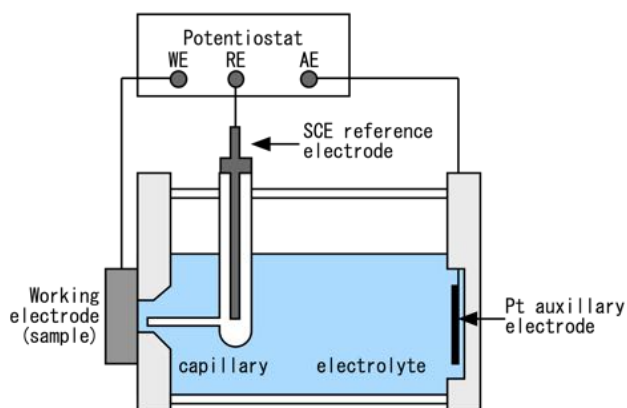


Fig. 3.11: The three-electrode cell setup diagram

3.5.1 Free Corrosion Potential Measurements

During this study, free corrosion potential (E_{corr}) was used to determine the effectiveness of surface modification on improving the in situ corrosion resistance of titanium. The value of E_{corr} is used in this study to determine whether titanium or treated titanium was in an active or passive state. Shifts in E_{corr} also highlight the effect of any surface modification applied to titanium giving an indication as to whether the corrosion resistance has been improved.

3.5.2 Potentiodynamic (PD) Measurements

Potentiodynamic polarisation measurement was performed using a sweep rate of 1 mV s^{-1} , starting from a cathodic potential of $-400 \text{ mV}_{\text{SCE}}$ to OCP (versus open circuit potential (OCP)), then to an anodic potential of $1500 \text{ mV}_{\text{SCE}}$ (verses OCP). The corrosion current densities were determined by the Tafel extrapolation method. OCP was determined during 30 min of stabilisation prior to the potential sweep.

3.5.3 Potentiostatic (PS) Measurements

During this study, current transient measurements were performed by potentiostatically polarising the specimens at a constant potential of $500 \text{ mV}_{\text{SCE}}$ for 3600 s. The variation in

current was recorded continuously throughout the test.

3.5.4 Mott-Stocky (M-S) Analysis

Mott-Stocky (M-S) analysis was performed by measuring the impedance against potentials of the passive film formed during potentiostatic polarisation at 500 mV_{SCE} for 3600 s. Potentials ranged from +1000 mV_{SCE} to -1000 mV_{SCE} with a step rate of 50 mV. An AC voltage signal of 1000 Hz and 10 mV peak-to-peak amplitude was applied to the system during the impedance measurements. The capacitance was then calculated using the imaginary part (Z'') of the measured impedance described in Eq. 2.24 on page 26. The dielectric constant of bulk rutile has been shown to be 80 [82], this was used to calculate dopant density.

3.6 Tribocorrosion Testing

Tribocorrosion tests were carried out using a pin-on-disk tribometer modified to incorporate electrochemical testing, as shown in Fig. 3.12. Before the test, a test area of 1.23 mm² was isolated using insulating lacquer. During the test, the sample rotated against a stationary alumina (Al₂O₃ Grade 25) ball, with a diameter of 8 mm manufactured by Trafalgar bearings. Alumina was chosen due to its hardness and inertness. The rotation speed of the sample was set to 60 rpm, with a wear track diameter of 9 mm. Thermally oxidised titanium was tested at a load of 2 N and pack carburised titanium was tested at a load of 20 N. The treated titanium was tested for a duration of 4 hours with 30 minutes stabilisation (cell rotation but no contact) time before and after sliding. This was to create a stable starting point for the samples and then to see the re-passivation response, once sliding had commenced. The tests were performed with a sliding speed of 2.8 cm s⁻¹ and a total sliding distance of 408 m. All tests were carried out in a 0.9% NaCl solution at room temperature (20 °C). Tribocorrosion tests were conducted in both OCP and potentiostatic conditions.

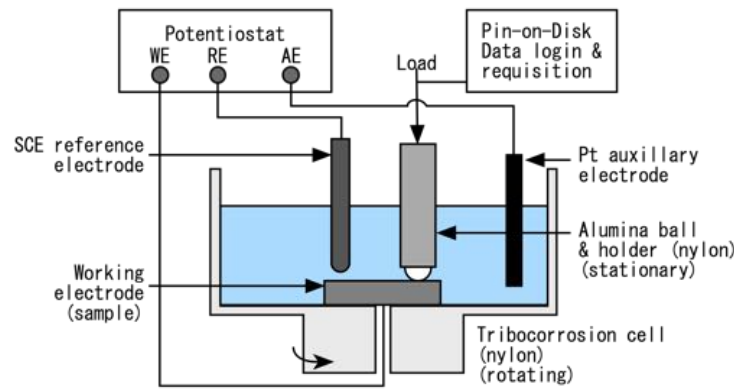


Fig. 3.12: Tribocorrosion test cell

3.6.1 Open Circuit Potential

During OCP testing all samples were stabilised for 30 minutes (cell rotation but no contact) before and after sliding. This was to create a stable starting point for the samples and then to see the repassivation response, once sliding had commenced. OCP readings were used to assess how the action of a sliding counter-face against titanium and surface treated titanium affects the passivity and for how long any protective film is present within the contact area.

3.6.2 Potentiostatic Testing

During this study, both oxidised and carburised titanium was tribologically tested at fixed anodic potentials of $+1000 \text{ mV}_{\text{SCE}}$, $+500 \text{ mV}_{\text{SCE}}$ and at cathodic potentials of $-900 \text{ mV}_{\text{SCE}}$ and $-1500 \text{ mV}_{\text{SCE}}$. The wear depth and total material loss (TML) in volume from each sample was then analysed using the method hi-lighted in section 3.4.2 at 8 different locations. The amount of material loss for the chemical (using Faradays' law (Eq. 2.28, page 36)) and mechanical aspects of wear were then evaluated. All tests were carried out multiple times and the mean results are presented.

Chapter 4

Results and Discussion

Tribological, Corrosion and Tribocorrosion Behaviour of Thermally Oxidised CP Titanium

In this chapter the results and discussion for all work carried out on thermally oxidised titanium (TO-Ti) were investigated. Characterisation of TO-Ti was undertaken, looking at the tribological, electrochemical and tribocorrosion behaviour of the multi-layered structure, produced from the thermal oxidation treatment.

Initial efforts have been made to enhance the tribological properties of the rutile film by improving adhesion to the substrate, through reducing the rate of furnace cooling and a prior mechanical surface treatment as explained in section 3.2.1.

As described in section 3.2.1, thermal oxidation of the CP-Ti samples was carried out in a muffle furnace, in air, at a temperature of 625 °C, for durations of 5 h, 20 h and 72 h. After the oxidation treatment, the specimens were allowed to cool down to room temperature in the furnace. This set of samples are designated as furnace cooling (FC). Under the present experimental conditions, FC from 625 °C to below 100 °C took approximately 6 h. Samples reported in this chapter were furnace-cooled unless otherwise stated.

4.1 Microstructural Characterisation

4.1.1 Layer Morphology

As observed by many investigators [18, 70, 116–118, 135, 164], and discussed in section 2.7.4, thermal oxidation of CP-Ti produced an oxide layer at the surface and an oxygen diffusion zone (ODZ) in the subsurface. Similar structural features have also been observed in this work. Fig. 4.1 shows typical ball-craters made on the oxidised surface, revealing the oxide layer, which has a dark grey appearance and can be easily distinguished from the underlying oxygen diffusion zone. Fig. 4.2 shows an SEM image of the cross section of an oxidised sample, revealing the uniformity of the oxide layer.

The thicknesses of the oxide layers were measured from the ball-craters and are listed in Table 4.1. It can be seen that the oxide layer thickened with increasing treatment time. After oxidation for 5 h, the oxide layer was 0.51 μm thick (Fig. 4.1a), which was increased to 0.98 μm after 20 h treatment (Fig. 4.1b). Prolonged oxidation for 72 h produced a 2.3 μm thick oxide layer (Fig. 4.1c). However, this became a scale and had poor adhesion with the underlying ODZ, as evidenced by the spallation of oxide layer at the edge of the ball crater shown in Fig. 4.1c, while the thinner oxide layers produced by 5 h and 20 h treatments adhered well with the diffusion zone.

Table 4.1: Summary of layer thickness and hardness results of thermally oxidised samples

TO time at 625 °C	Oxide layer thickness (μm)	OD layer thickness (μm)	Surface hardness			Surface roughness R_a (μm)
			HV0.05	HV0.1	HV0.2	
Untreated	0	0	298	298	282	0.203
5 h	0.51	4.5	453	390	343	0.205
20 h	0.98	8.5	766	563	431	0.211
72 h	2.3	15.5	1035	902	716	0.236

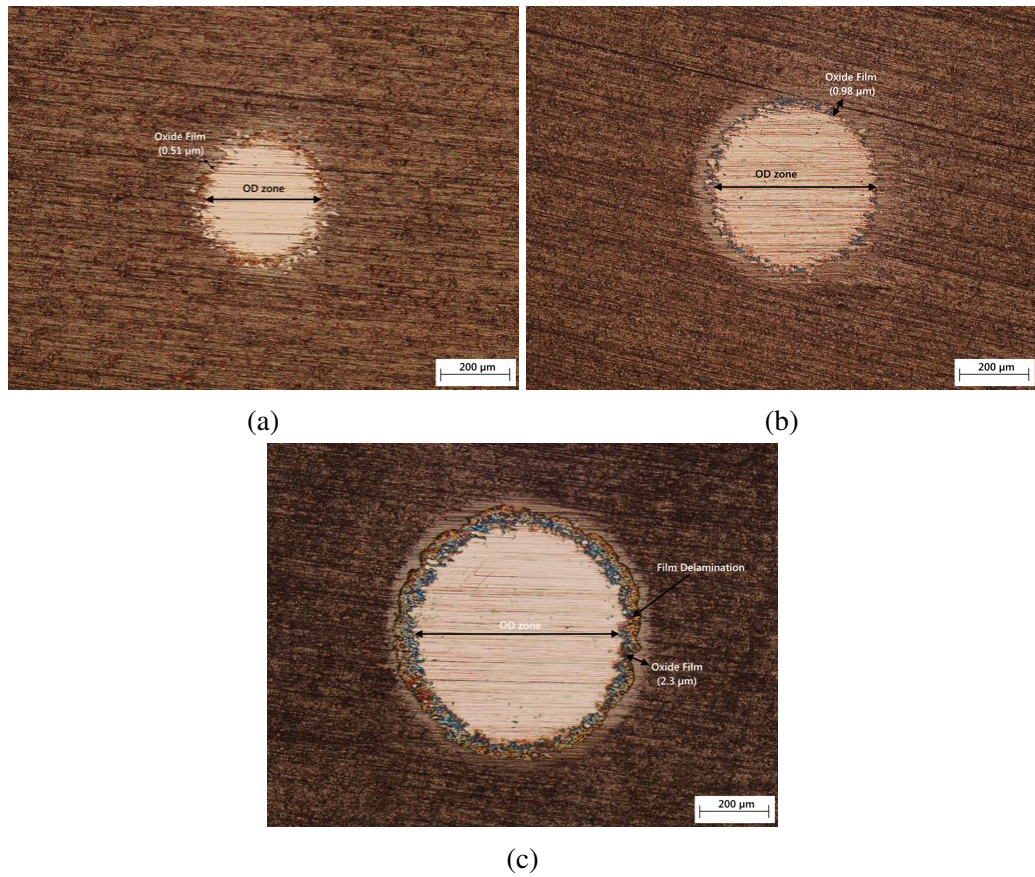


Fig. 4.1: Ball craters made on the surface of thermally oxidised CP-Ti at 625 °C for durations of: a) 5 h, b) 20 h and c) 72 h. These show the oxide layer formed on the surface

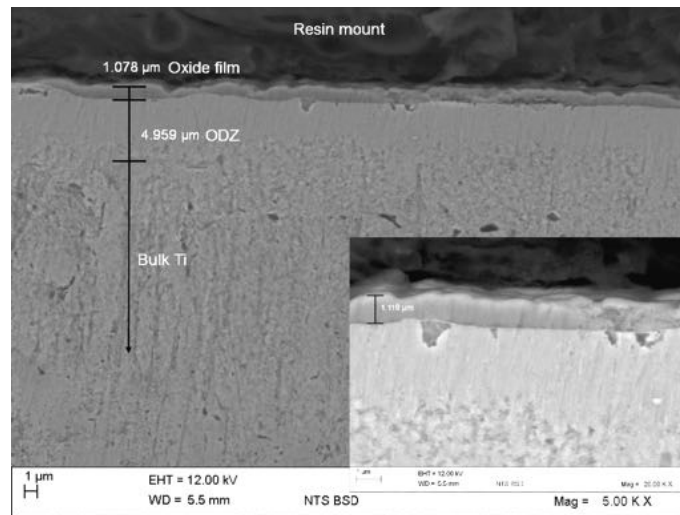


Fig. 4.2: SEM image showing the cross sectional profile of TO-Ti at 625 °C for, 20 h

4.1.2 Chemical Composition Analysis by GDOS

The incorporation of oxygen in the surface region to form an oxide layer and a diffusion zone was further confirmed by GDOS composition profile measurements, as shown in Fig. 4.3. The surface oxide layer had a high oxygen concentration close to TiO_2 stoichiometry. Below this oxide layer was an oxygen diffusion zone with gradually decreased oxygen concentration. The thicknesses of the diffusion zones were estimated from the GDOS composition profiles and are also listed in Table 4.1. As expected, the oxygen diffusion zone was only a few micrometers thick for treatment times up to 20 h. Even after 72 h treatment, the diffusion zone was approximately $16\ \mu\text{m}$ thick. This can be attributed to the slow diffusion of oxygen in $\alpha\text{-Ti}$ at the relatively low temperature of $625\ ^\circ\text{C}$ [18].

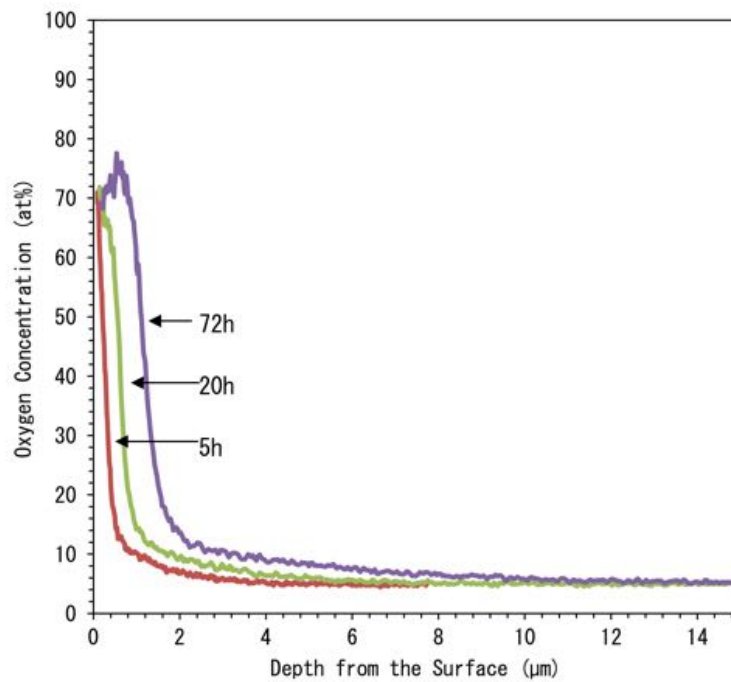


Fig. 4.3: Oxygen concentration profiles measured by GDOS across the oxide layers produced at $625\ ^\circ\text{C}$ for 5 h, 20 h and 72 h

4.1.3 Diffusion Layer Thickness

The amount of oxygen content within the titanium can be calculated as a function of depth from the oxidised surface using Flick's second law of semi-infinite non-steady state diffusion [130]:

$$\frac{C_x - C_0}{C_s - C_0} = 1 - \operatorname{erf} \left[\frac{x}{2\sqrt{Dt}} \right] \quad (4.1)$$

Where C_s is the constant surface concentration (34 at%), C_0 is bulk solute concentration (0.74 at% using the mass balance from Table 3.1), C_x is the solute concentration at any distance (x) from the surface, t is the diffusion time and D is the diffusion Coefficient. This is calculated using the Arrhenius equation (Eq. 2.30), with the following parameters: The pre exponential frequency factor ($D_0 = 4.08 \times 10^{-5} \text{ m s}^{-2}$ for O in α -Ti) [131], and the activation energy ($Q = 197 \text{ kJ mol}^{-1}$ for O in α -Ti) [131].

The calculated oxygen concentration against depth has been plotted (Fig. 4.4) for durations of 5 h, 20 h and 72 h at an oxidation temperature of 625 °C. The plots show a strong correlation to the data obtained via GDOS analysis (Fig. 4.3). Using Flick's law the ODZ thickness is estimated to be 4 μm , 9 μm and 15 μm for the 5 h, 20 h and 72 h samples respectively. This is inline with that evaluated using GDOS and cross sectional images highlighted in Table 4.1.

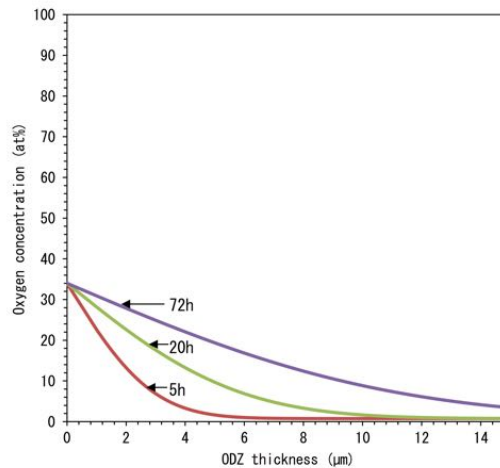


Fig. 4.4: Theoretical oxygen concentration profiles at 625 °C for 5 h, 20 h and 72 h

4.1.4 X-Ray Diffraction

X-ray diffraction (XRD) was undertaken using Cu-K α 1 radiation to identify phases present in the thermally oxidised samples.

X-ray diffraction analysis (see Fig. 4.5) confirmed that the surface oxide layer was rutile TiO₂ irrespective of treatment time. It has been reported that thermal oxidation of titanium at low temperatures and/or for short times favours the formation of anatase TiO₂, rather than rutile TiO₂ [128, 135]. The oxidation temperature and time employed in this work were sufficient for the formation of rutile oxide, which has been known to have better tribological properties than anatase oxide [77].

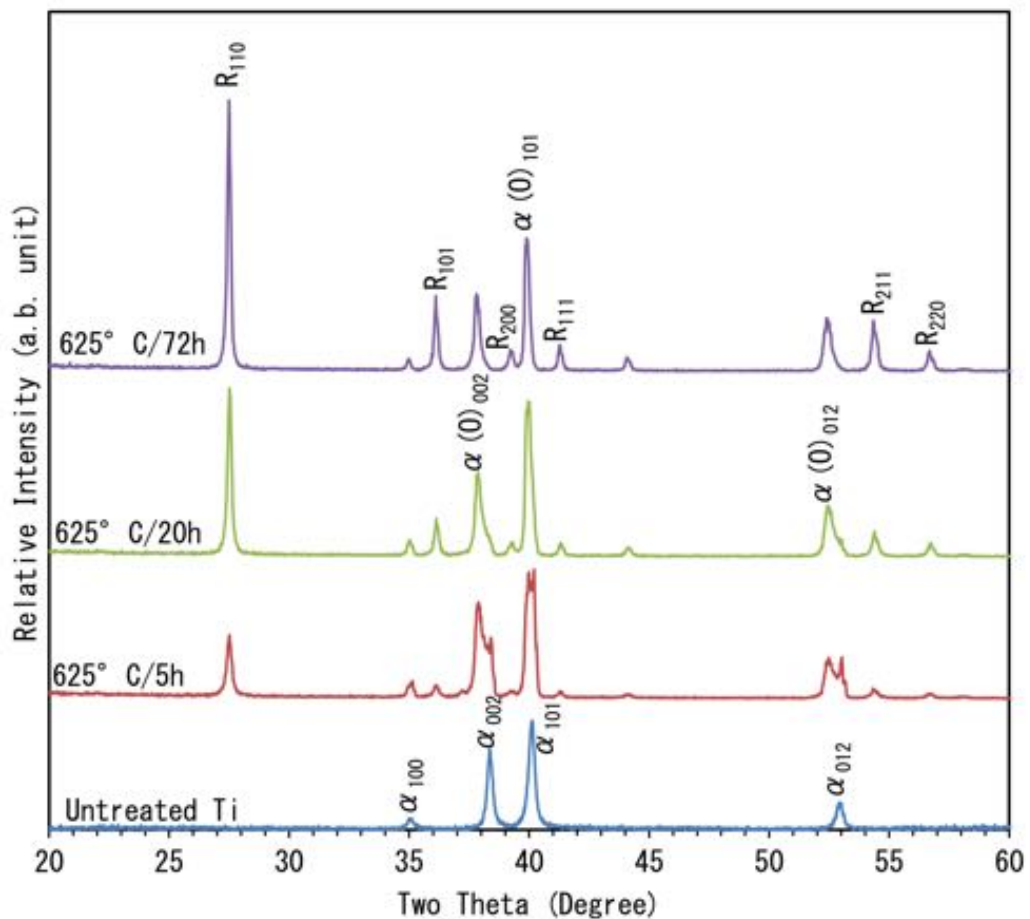


Fig. 4.5: X-ray diffraction patterns generated from untreated Ti and Ti thermally oxidised at 625 °C for 5 h, 20 h and 72 h

During thermal oxidation there is increased oxygen concentration within the HCP

crystal structure of Ti. This oxygen will cause small changes to the lattice parameters. The c/a ratio for titanium is 1.58, which is much less than ideal for a HCP crystal structure ($c/a=1.633$). The incorporation of oxygen within the ODZ should result in an expanded crystal structure with a c/a value closer to that of the ideal. Using the XRD data displayed in Fig. 4.5, the precise lattice parameters of the near surface ODZ can be calculated using Eq. 4.2 and for rutile using Eq. 4.3 [130].

$$\frac{1}{d_{(hkl)}^2} = \frac{4}{3} \left(\frac{h^2 + hk + k^2}{a^2} \right) + \frac{l^2}{c^2} \quad (4.2)$$

$$\frac{1}{d_{(hkl)}^2} = \frac{h^2}{a^2} + \frac{k^2}{b^2} + \frac{l^2}{c^2} \quad (4.3)$$

Where a , b and c are the lattice parameters of the crystal, (hkl) are the corresponding miller indices of the lattice planes and $d_{(hkl)}$ is calculated using Eq. 3.1, described in section 3.3.1.

Table 4.2 shows all the calculated lattice constants of α -Ti(O) and rutile, when oxidised at 625 °C, as a function of oxidation time. The standard lattice spacing for untreated titanium has also been shown for comparison purposes. The data in Table 4.2 clearly shows that as oxidation time is increased, more oxygen diffusion occurs, resulting in larger lattice expansion of α -Ti, while the lattice constants for rutile remains almost unchanged.

Table 4.2: Calculated lattice constants of α -Ti(O) and rutile as a function of oxidation time

Sample	α -Ti(O)			Rutile	
	a (Å)	c (Å)	c/a	a (Å)	c (Å)
Untreated	2.95	4.686	1.588		
5 h	2.951	4.755	1.6079	4.585	2.96
20 h	2.955	4.754	1.6088	4.587	2.96
72 h	2.965	4.771	1.6091	4.588	2.96

4.1.5 Surface Hardness

Surface hardness for 5 h, 20 h and 72 h oxidised samples were measured by increasing the contact load on the micro-hardness tester (Fig. 4.6). Hardness and oxygen content have previously been shown to correlate directly [165], increased oxygen content in the titanium lattice results in greater hardness. This method of measuring hardness was chosen as opposed to using cross sections, due to interfacial failure of the film when indentation occurs close to the film, resulting in immeasurable results.

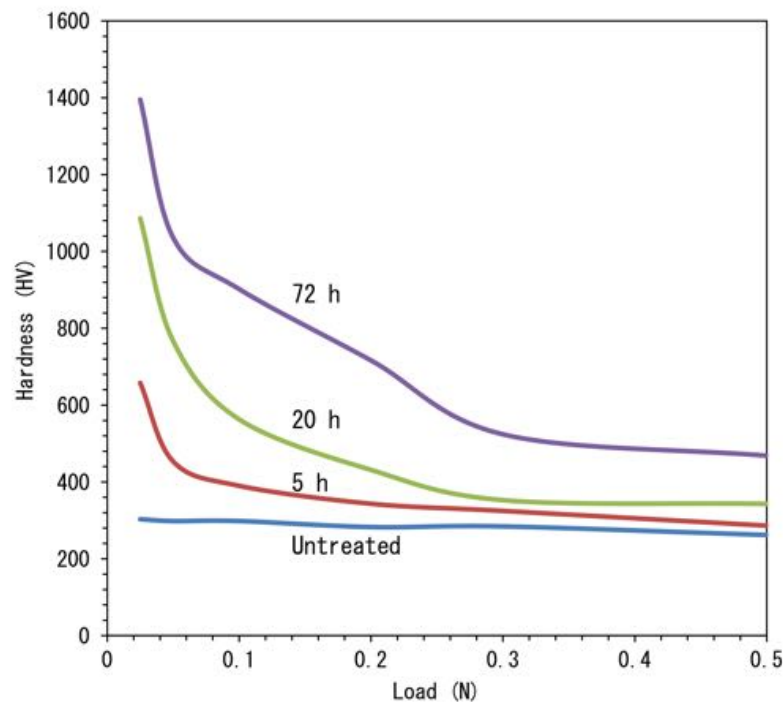


Fig. 4.6: Surface hardness, measured using an Indentec ZHV micro-hardness tester with increasing load applied to the thermally oxidised surface for samples oxidised at 625 °C for 5 h, 20 h and 72 h

From Fig. 4.6 it can be seen that thermal oxidation effectively hardened the surface of CP-Ti and such a hardening effect was more significant with increasing treatment time. This can be explained by the increased thickness of the oxide layer and the oxygen diffusion zone. Table 4.1 was produced to overview the key findings from hardness testing and characterisation. Surface roughness was also measured and included in the table. It is interesting to note that surface roughness also increased with increased oxidation time.

4.2 Unlubricated Sliding Friction and Wear Characteristics

4.2.1 Sliding Friction Behaviour

Fig. 4.7 shows the coefficient of friction (COF) curves recorded under a small contact load of 1 N for all the tested samples. Two important observations can be made from the figure. Firstly, all the oxidised samples exhibited much lower and smoother COF than the untreated sample. Secondly, COF was the lowest for the 5 h treated sample and was increased with increasing oxidation time. Thus, under such a small contact load, short time oxidation was more effective in reducing friction of CP-Ti. This is due to the reduced surface roughness generated after short duration oxidation (see Table 4.1). This also bears similarities to earlier work regarding the effect of oxidation temperature on the COF of magnetron sputtered titanium films on stainless steel [15]. Oxidation at lower temperatures (500-550°C) was more effective in achieving low friction than higher temperature oxidation.

Fig. 4.8 shows the ball-craters made on the wear tracks produced under 1 N load on the 5 h (Fig. 4.8a) and 72 h (Fig. 4.8b) treated samples. These images clearly show that in each wear track, the oxide layer maintained its integrity with the oxygen diffusion zone and wear only occurred in the oxide layer. Thus, the frictional behaviour of the oxidised samples shown in Fig. 4.7 was characteristic of the surface oxide layer. It was the oxide layer that was responsible for the observed low and smooth friction. Further examination of the wear tracks by SEM confirmed that no exfoliation of the oxide layers occurred during the sliding process under 1 N load. Material removal from the oxide layers were due to the micro-abrasion by the alumina slider, as can be seen from Fig. 4.9. This reveals that only the asperities in the wear track made real contact with the slider, and the asperities were smoothed by the polishing action of the alumina slider. The amount of material removed from the oxide layer was very small. After sliding for 3600 s, the 0.51 μm thick oxide layer produced by 5 h treatment was not worn through

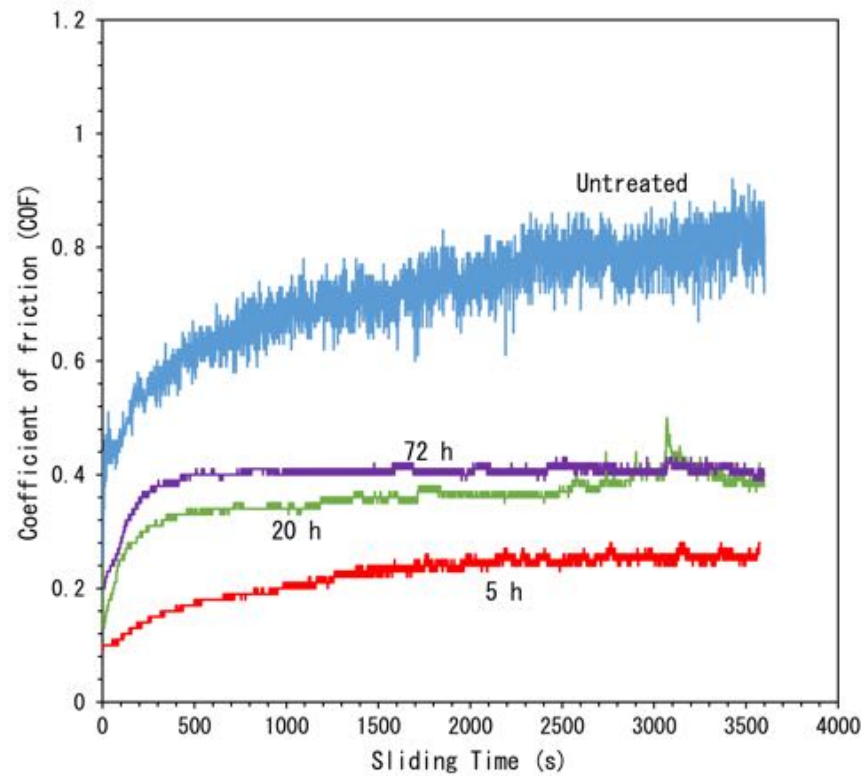


Fig. 4.7: Coefficient of friction (COF) curves recorded at a contact load of 1 N for the untreated and thermally oxidised samples produced at 625 °C for various times

(Fig. 4.8). This demonstrates the superior wear resistance of the oxide layer, in addition to its favourable friction characteristics.

It is also interesting to note that ball-cratering not only revealed the surface oxide layer and the wear depth, it also revealed the interfacial behaviour of the oxide layer. As can be seen from Fig. 4.8, the oxide layers produced by 5 h and 20 h treatments were worn through gradually during ball-cratering without interfacial failure. On the other hand, the ball-crater made on the 72 h treated sample (Fig. 4.8b) revealed that the oxide layer was a scale and poorly adhered to the ODZ. Clearly interfacial failure occurred in the inner part of the oxide layer, leaving behind a clear gap between the inner part of the oxide layer and the diffusion zone. Although such an oxide scale had poor adhesion with the underlying diffusion zone, it can still resist the small load of 1 N during sliding wear, resulting in the observed low friction and low wear. But under higher contact loads, the situation became quite different, as discussed below.

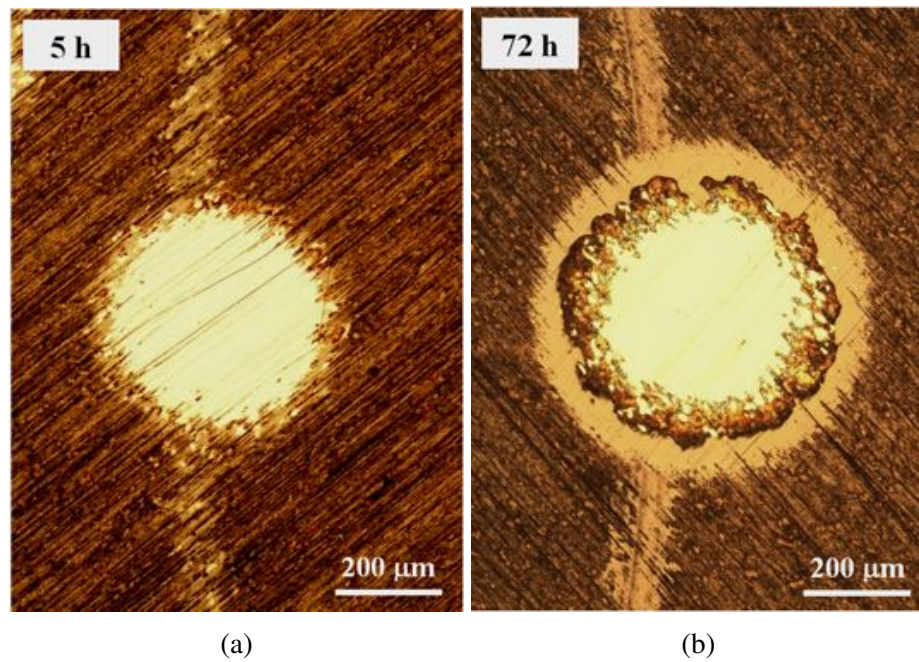


Fig. 4.8: Morphology of wear tracks produced at 1 N load and ball craters made across the wear tracks, showing the wear track depth within the surface oxide layers produced by 5 h and 72 h oxidation at 625 °C

When the contact load was increased to 2 N, the friction behaviour of the oxidised samples was different from that observed under the load of 1 N. As can be seen from Fig. 4.10, only the 20 h treated sample exhibited the low and smooth COF characteristics of the oxide layer throughout the test duration of 3600 s. Indeed, ball-cratering made on the wear track (Fig. 4.11a) confirmed that wear occurred in the oxide layer which maintained its integrity with the underlying diffusion zone during the sliding process. On the other hand, for the 5 h treated sample, the COF was initially lower than the 20 h treated sample, but it increased quickly after about 1200 s to reach a value of 0.76. The COF remained at this level for roughly 400 s (between 1700 s and 2100 s), the COF then decreased quickly and became similar to that of the untreated sample (0.6). As further discussed in Section 4.2.4, such a peculiar frictional behaviour is associated with the surface oxide layer, the oxygen diffusion zone and the substrate. For the 72 h treated sample, the COF was initially smooth and lower than that of the untreated sample, but it increased abruptly after 800 s sliding to reach a value higher than that of the untreated sample and maintained at such high values throughout the rest of the test duration. Ball-cratering made on the wear track

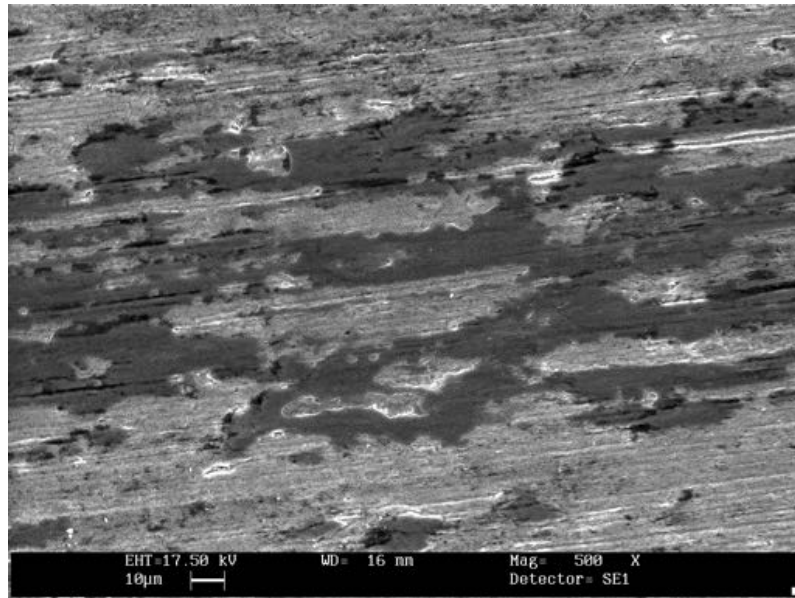


Fig. 4.9: SEM image showing the morphology of the wear track produced at 1 N load on the 625 °C/20 h oxidised sample

(Fig. 4.11b) revealed that the oxide scale was completely removed from the wear track and wear occurred in the diffusion zone. If the initial smooth and low friction region was attributed to the oxide layer and the quick or sudden increase in COF was due to wearing through or failure of the oxide layer, it can be seen that the COF of the oxide layer decreased with decreasing oxidation time, confirming the results in Fig. 4.7 obtained under the smaller load of 1 N. However, under 2 N load, only the oxide layer produced by 20 h treatment survived the test duration, while the very thin oxide layer produced by 5 h treatment and the thick scale by 72 h treatment could only last a limited period of time.

When the contact load was further increased to 5 N, none of the oxide layers survived the test duration, see Fig. 4.12. All the oxidised samples experienced a short initial low friction region, after which the COF increased quickly. For the 5 h treated sample, the COF increased above the value for the untreated sample and then decreased quickly to become similar to that of the untreated sample. For the 20 h treated sample, similar behaviour was observed, but its COF was maintained at high values for a significant period of time before it decreased to the value for the untreated sample. For the 72 h treated sample, after the initial low friction region, the COF was maintained at the high values

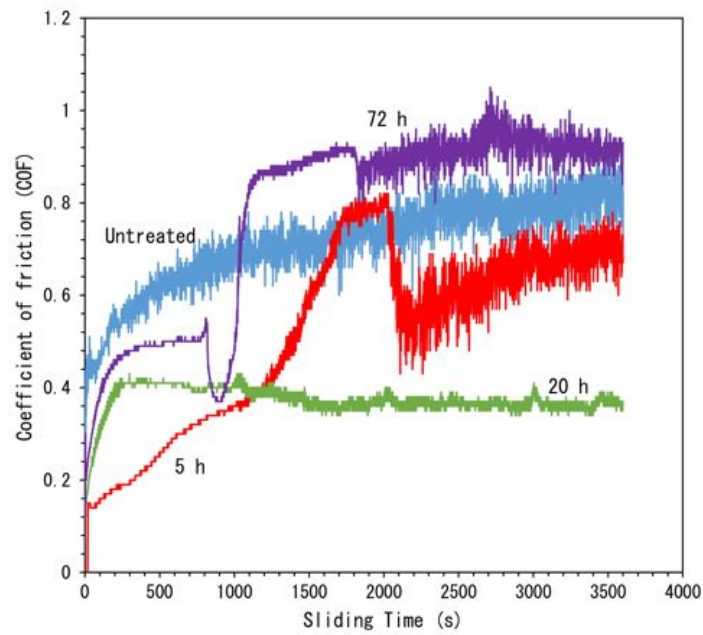


Fig. 4.10: Coefficient of friction (COF) curves recorded at a contact load of 2 N for the untreated and thermally oxidised samples produced at 625 °C for various times

throughout the rest of the test duration. Microscopic examination showed that the oxide layers were completely removed from the wear tracks, which were wide, deep and rough with obvious signs of abrasion, adhesion and delamination, as can be seen from Fig. 4.13 for the 20 h treated sample.

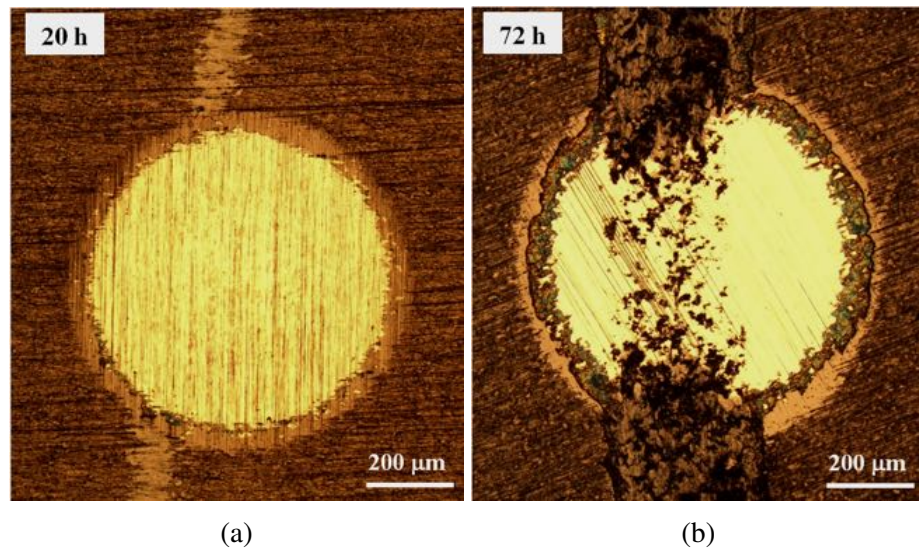


Fig. 4.11: Morphology of wear tracks produced at 2 N load and ball craters made across the wear tracks on samples oxidised at 625 °C for 20 h and 72 h

4.2.2 Wear Rate

The measured wear rates as a function of contact load for the test samples are shown in Fig. 4.14. Several observations can be made from the figure. Firstly, for each test sample, the wear rate increased with increasing load. For the untreated sample, such an increase was gradual, but for the oxidised samples there existed an abrupt rise in wear rate by more than two orders of magnitude when the contact load was above a certain critical value, corresponding to the wearing through of the surface oxide layer and the increase in COF. Secondly, as long as wear occurred only in the oxide layer, e.g. at the small load of 1 N for all the oxidised samples and at 2 N for the 20 h treated sample, not only was the COF smooth and low (Fig. 4.7 and Fig. 4.10), the wear rate was also very low, 3 to 4 orders of magnitude lower than that of the untreated sample. Finally, when the oxide layer was worn through and wear occurred mainly in the diffusion zone and/or the substrate, e.g. at 2 N load for the 5 h and 72 h treated samples and at 5 N load for the 20 h treated sample, the wear rate was increased abruptly by more than 2 orders of magnitude. Similar observations have also been made by Banfield et al. [135] regarding the superior wear resistance of the oxide layer and the abrupt increase in wear rate when

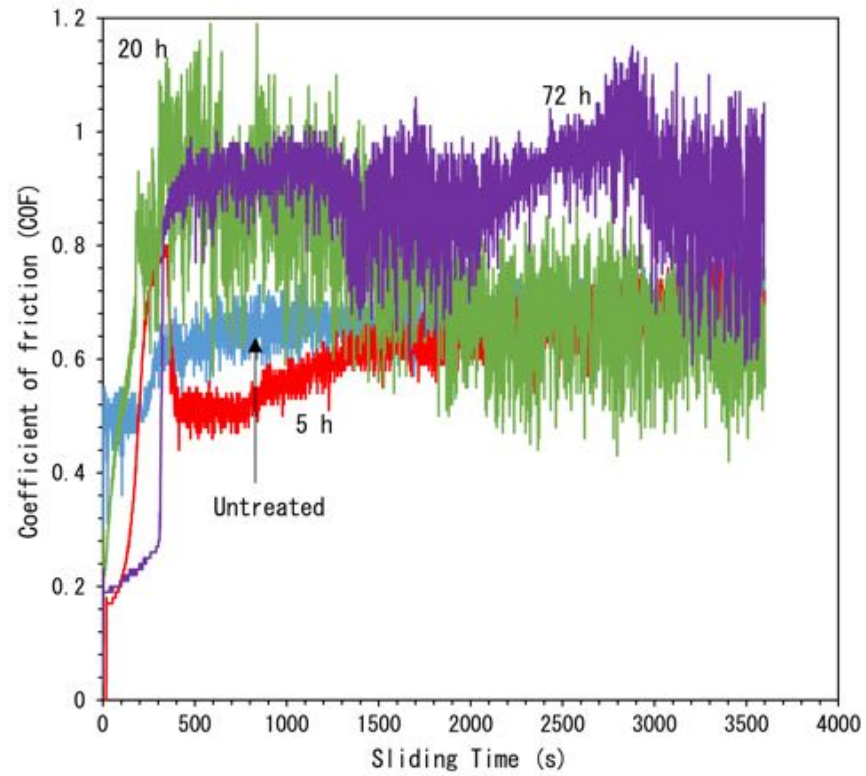


Fig. 4.12: Coefficient of friction (COF) curves recorded at a contact load of 5 N for the untreated and thermally oxidised samples produced at 625 °C for various times

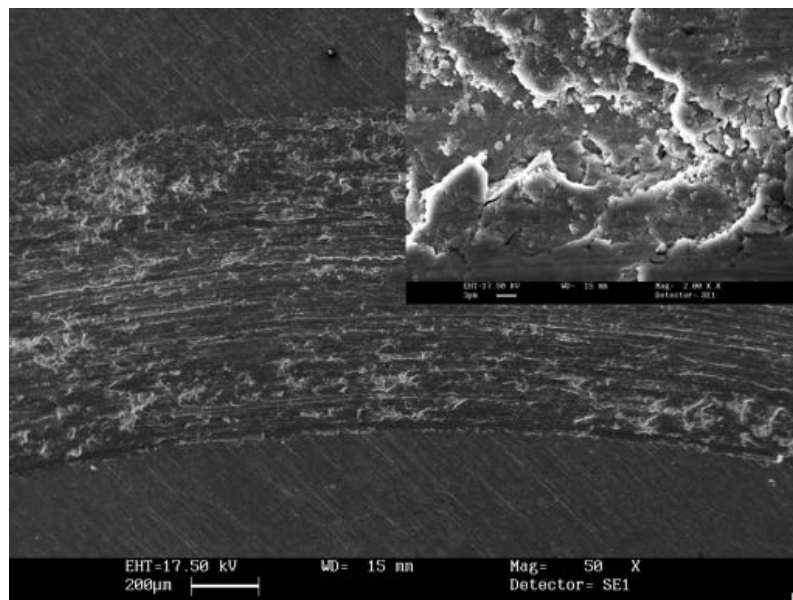


Fig. 4.13: Morphology of wear track produced at 5 N load on 625 °C/20 h oxidised sample. The inset is the higher magnification view showing cracking, delamination and fracture in the wear track

the oxide layer was worn through. However, as compared to the untreated sample, all the oxidised samples exhibited lower wear rates, even when the oxide layer was completely removed at high loads. The hardened oxygen diffusion zone, although experienced very high and unstable friction, reduced the wear rate of CP-Ti by 1.2 to 9.5 times, depending on oxidation time and contact load. The diffusion zone produced by 72 h treatment was the most effective at a contact load of 2 N. With decreasing oxidation time and increasing contact load, the effectiveness of the diffusion zone in reducing wear was diminished due to the decreased diffusion zone thickness and the easier wearing through of the zone during sliding.

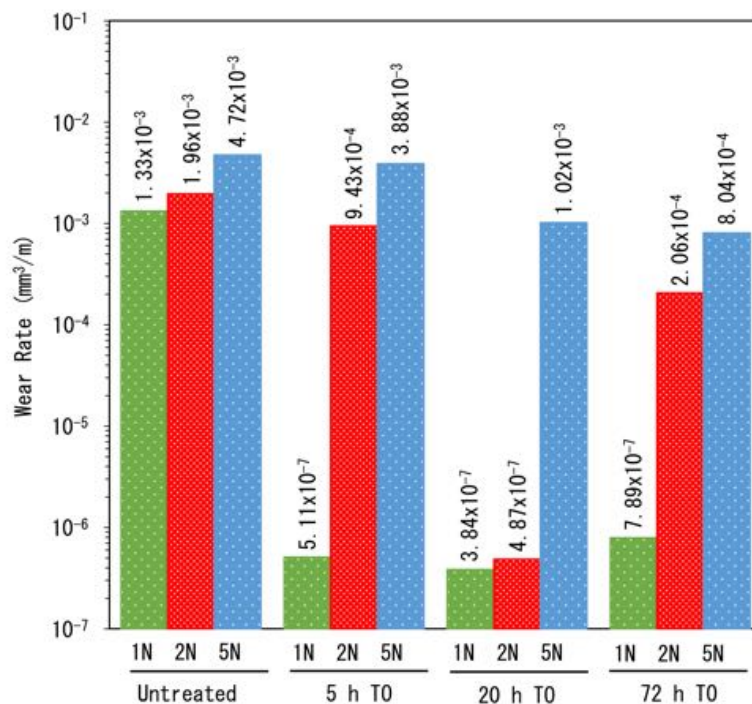


Fig. 4.14: Measured wear rate as a function of applied load for various samples

4.2.3 Initial Attempts to Improve Oxide Layer Performance

Clearly, it was the oxide layer that offered improvements to both frictional behaviour and wear resistance. TO Ti wear resistance was 3 orders of magnitude greater than that of the untreated CP-Ti and 2 orders of magnitude better than the ODZ. Unfortunately, the oxide layer was quite thin and can only resist a contact load of 1 N or 2 N when treated for 20 h

at 625 °C. Under higher contact loads, the oxide layer was worn through easily, as shown in the COF curves in Fig. 4.10 and Fig. 4.12. The present effort to increase the oxide layer thickness by increasing oxidation time to 72 h did not result in improved tribological performance of the oxide layer because the thicker oxide layer became a scale and had poor adhesion with the ODZ. Earlier efforts by other investigators to increase oxide layer thickness, by increasing oxidation temperature, also resulted in the formation of a crumbly oxide layer with no practical use [8, 15, 18]. It is thus imperative to find an alternative means to improve the tribological performance of the oxide layer such that it can last longer and resist higher contact loads.

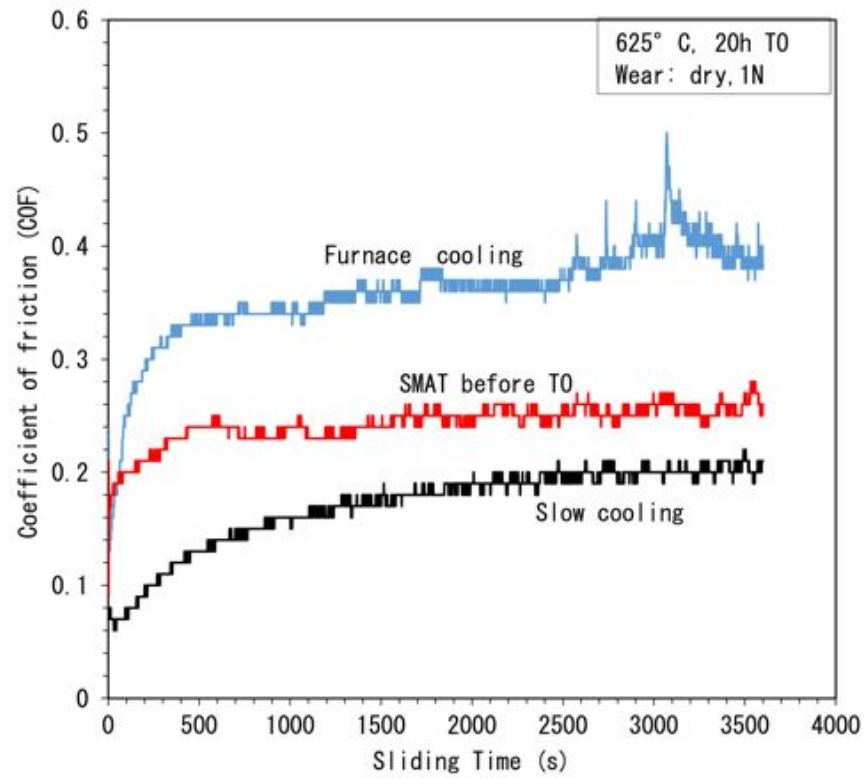
In the present work, initial efforts have been made to improve the sliding friction performance of the oxide layer formed on CP-Ti by thermal oxidation at 625 °C for 20 h. These include:

Modification of the CP-Ti surface by SMAT, before thermal oxidation: The surface of the CP-Ti is mechanically treated before thermal oxidation. This was achieved by surface mechanical attrition treatment (SMAT), employing the same technique described in section 3.2.1. The total SMAT time was 180 min. After SMAT, the samples were ultrasonically cleaned in methanol for 15 min, and were then thermally oxidised at 625 °C for 20 h, followed by normal furnace cooling.

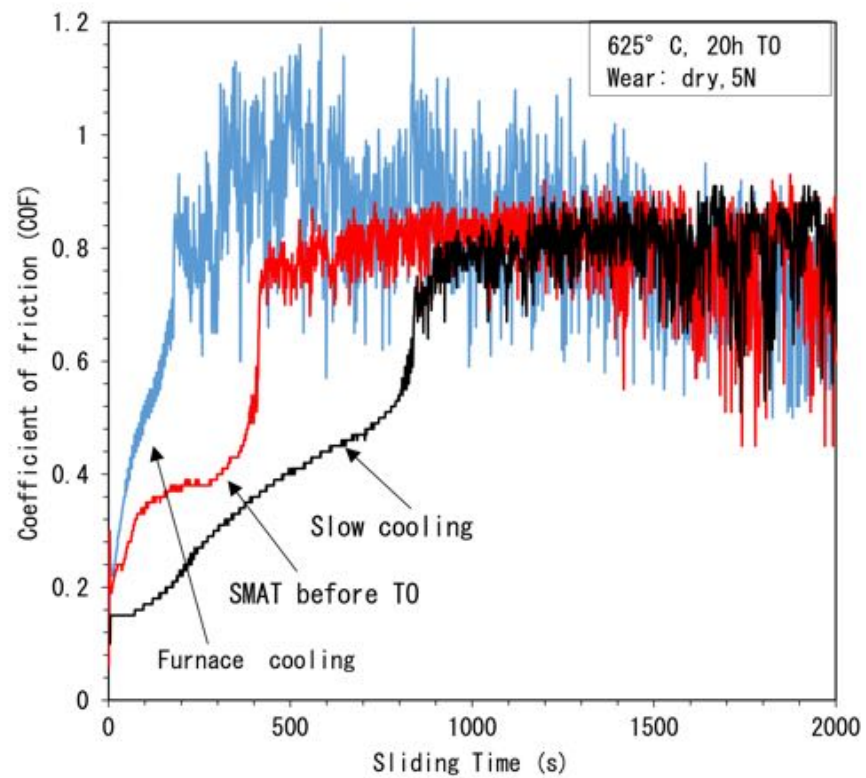
Controlled slow cooling after thermal oxidation: Reducing the cooling rate of the samples after thermal oxidation, is designed to reduce thermal stresses in the oxide layer and thus, enhance the tribological performance of the oxide layer [77]. This was achieved by programming the cooling scheme such that the cooling rate was controlled at half of the furnace-cooling rate, i.e. it took about 12 h to cool the sample from 625 °C to below 100 °C. These samples are designated as controlled furnace cooling (CFC). the cooling scheme is described in section 3.2.1.

Fig. 4.15 shows the recorded COF curves under 1 N and 5 N. Under the small load of 1 N, when the oxide layer still maintained its integrity with the diffusion zone, both

prior SMAT and controlled slow cooling were effective in reducing the COF of the oxide layer (Fig. 4.15a). Under the high contact load of 5 N, these two techniques enhance the durability of the oxide layer, under the present unlubricated sliding condition (Fig. 4.15b). Wear track images also show how the pre and post oxidation treatments have a dramatic effect on increasing oxide adhesion and reducing overall wear (Fig. 4.16). In all cases, the failure mechanism of the oxide layer was similar in the form of oxide delamination, but for the SMAT and the controlled cooling samples the oxide layer lasts longer, resulting in reduced wear.

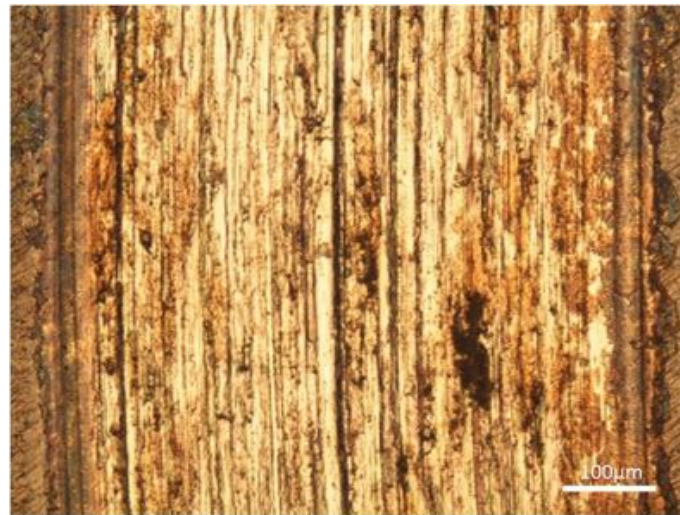


(a)

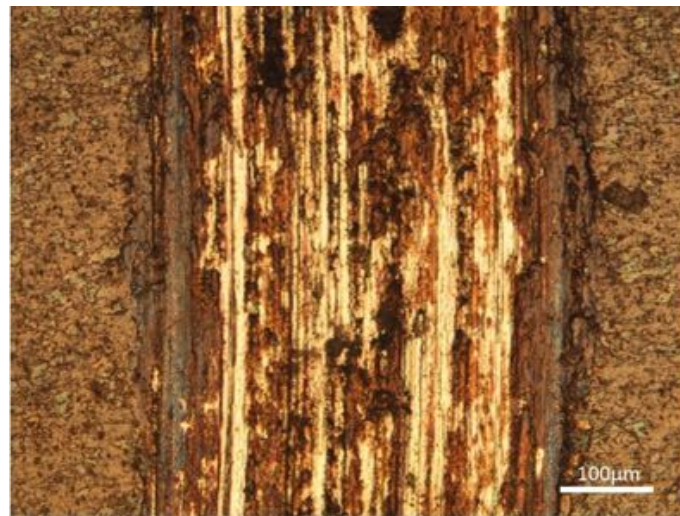


(b)

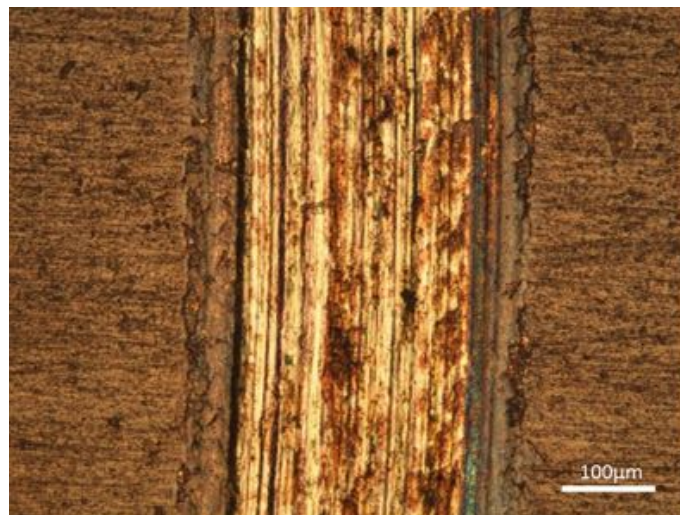
Fig. 4.15: Coefficient of friction curves recorded during dry sliding wear tests at (a) 1 N and (b) 5 N loads, showing the beneficial effects of prior SMAT treatment and controlled slow cooling on the frictional behaviour of the 625 °C/20 h oxidised samples



(a)



(b)



(c)

Fig. 4.16: Optical wear track images displayed for (a) furnace cooling (b) SMAT before TO and (c) slow cooling, showing the differing wear tracks after a contact load of 5 N for 3600 s

4.2.4 Identification of Four Frictional Zones

The results presented in the previous section demonstrate that although the oxygen diffusion zone could improve the sliding wear resistance of CP-Ti by up to 9.5 times under the present thermal oxidation and unlubricated sliding conditions, it experienced high and unstable friction. On the other hand, the surface oxide layer, so long as it maintained its integrity with the oxygen diffusion zone, offered both low friction and superior wear resistance. Thus, an ideal tribological system of thermally oxidised titanium should comprise an adherent and long lasting oxide layer supported by a hardened oxygen diffusion zone beneath [2]. Unfortunately, the oxide layer produced was either too thin (5 h treatment) or too crumbly (72 h treatment) such that it only lasted a short period of time under slightly higher contact loads, leading to the peculiar frictional behaviour (Fig. 4.10 and Fig. 4.12) and much increased wear rates (Fig. 4.14).

To further illustrate the peculiar friction behaviour of the oxidised samples, the COF curve for the 5 h treated sample at a contact load of 2 N is reproduced in Fig. 4.17a. In conjunction with microscopic examination and the wear depth measurements (Fig. 4.17b), four friction zones can be identified, each with its own characteristics, as illustrated in the figure and elaborated in more details below.

Zone I is the low and smooth friction region characteristic of the surface oxide layer. The wear track has a typical morphology similar to that shown in Fig. 4.8 and Fig. 4.9. Under small contact loads, e.g. 1 N for all the oxidised samples and 2 N for the 20 h treated sample, Zone I prevailed throughout the test duration because wear only occurred in the oxide layer. The principle wear mechanism involved is micro-polishing of the oxide layer by the alumina slider (Fig. 4.9).

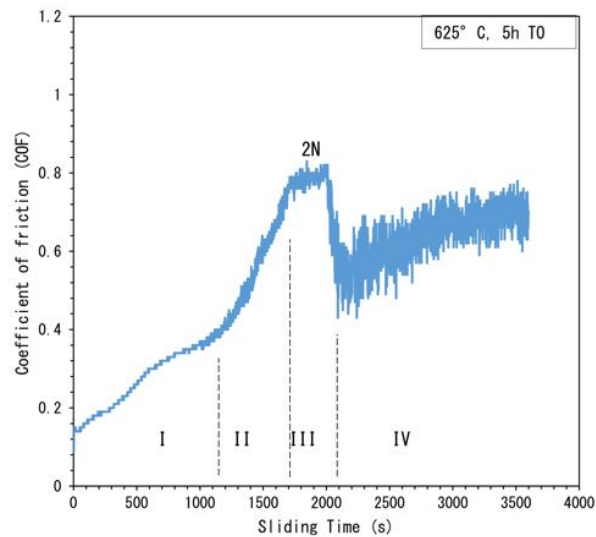
Zone II is the transition zone arising from the partial wearing through or partial failure of the oxide layer. Fig. 4.18a is an SEM image showing the wear track morphology produced in Zone II on the 5 h treated sample. It can be seen that the oxide layer was partially worn through or delaminated from the diffusion zone, with many cracks at the

centre of the wear track. It seems that failure of the oxide layer was mainly caused by interfacial fatigue due to the repeated sliding action, as earlier identified by Dong and Bell [2], under oil lubricated conditions and by Dearnley et al. [10] and Dahm [166] in a corrosive solution. It is noted that under 2 N contact load, Zone II is quite gradual for the 5 h treated sample, but it is very abrupt for the 72 h treated sample (Fig. 4.10). This suggests that the oxide layer on the 5 h treated sample was worn through gradually, while that on the 72 h treated sample failed suddenly due to its poor adhesion with the diffusion zone. The thinner and adherent oxide layer on the 5 h treated specimen actually lasted longer than the thicker oxide layer on the 72 h treated sample.

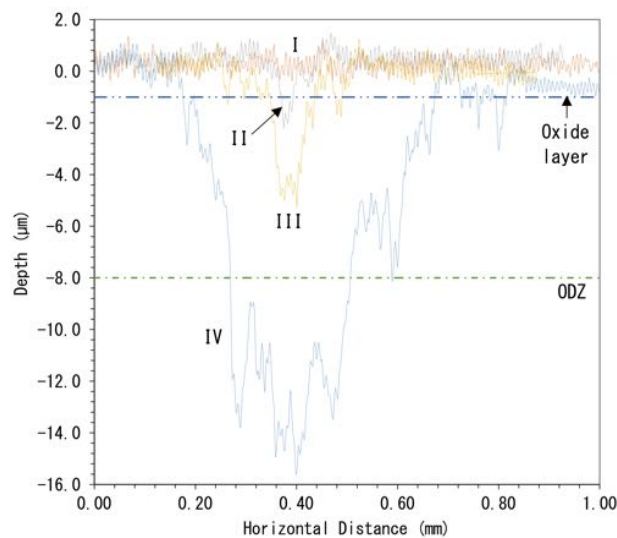
Zone III arises from the contact between the slider and the oxygen diffusion zone, characterised by COF values even higher than that of the untreated sample. In this zone, the oxide layer was removed completely from the wear track and wear occurred in the diffusion zone. The duration of this zone depended on diffusion zone thickness and contact load. The shorter the oxidation time and the higher the contact load, the shorter the duration of Zone III, as can be seen from Figs. 4.10 and 4.12. In particular, for the 72 h treated sample, due to its larger diffusion zone thickness, Zone III lasted the rest of the test duration under 2 N and 5 N loads. In this zone, the wear track has a dark appearance with many craters as can be seen from Fig. 4.11 for the 72 h sample. Indeed, SEM examination revealed that the wear track was covered with many patches of dark oxide films, formed presumably during sliding due to the high frictional heating (Fig. 4.18b). The oxide films made real contact with the slider and then were delaminated to form wear debris, as can be more clearly seen in Fig. 4.18c. SEM examination of the collected wear debris (Fig. 4.18d) revealed agglomerates of fine particles and some thin platelets, typical of oxidative wear and delamination wear. The accumulation of trapped wear debris, together with the higher hardness within the oxygen diffusion zone could be responsible for the higher COF observed.

Zone IV denotes the wearing through of the diffusion zone and the contact between the

slider and the substrate CP-Ti, such that the COF becomes similar to that of the untreated sample. For the 72 h treated sample, the diffusion zone was not worn through at the end of the tests under 2 N and 5 N loads, thus Zone IV was not detected in the COF curves. The wear track produced in Zone IV has a typical morphology shown in Fig. 4.13, which has a rough metallic appearance typical of metallic wear dominated by severe abrasion, adhesion and delamination.



(a)



(b)

Fig. 4.17: The four zones observed in a typical friction curve of thermally oxidised samples. I: oxide layer; II: partial removal of oxide layer; III: oxygen diffusion zone; IV: substrate. (b) Wear profiles associated with each frictional zone

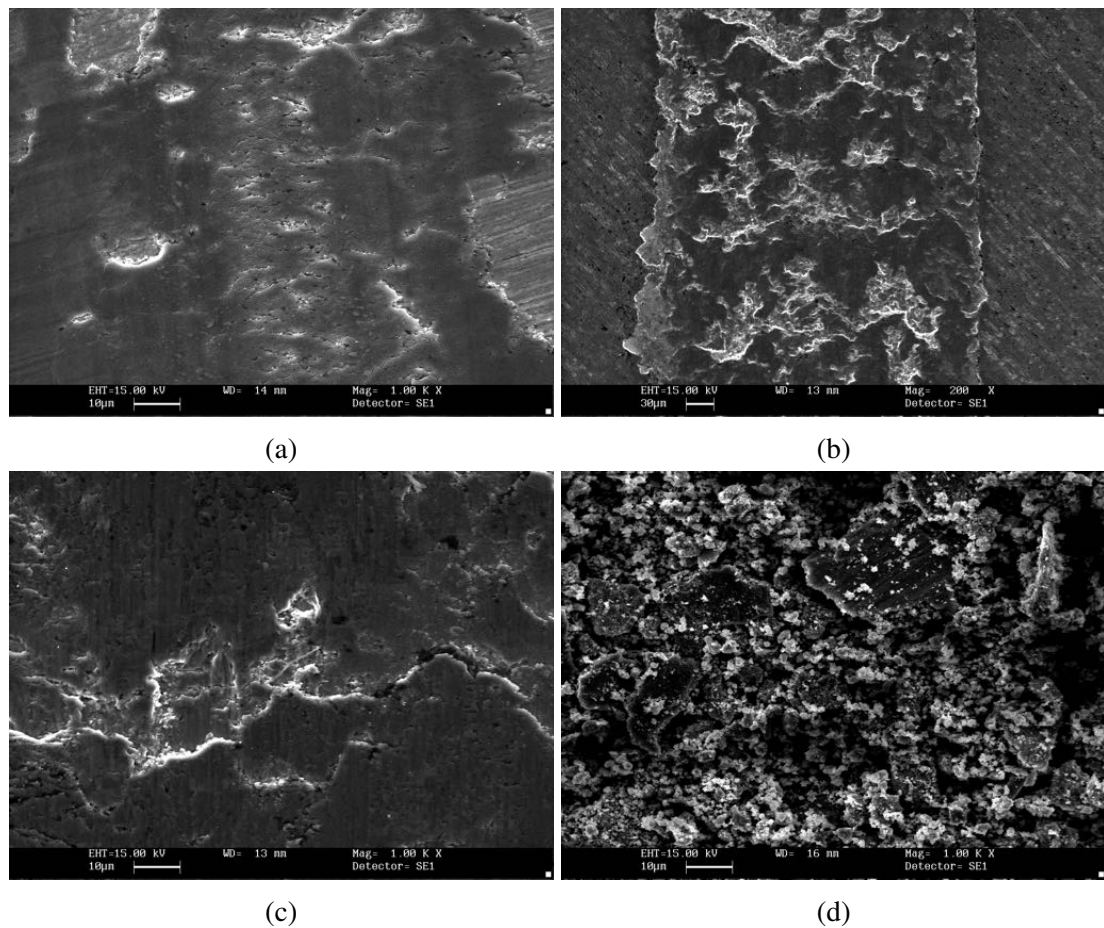


Fig. 4.18: SEM images showing (a) morphology of the wear track produced on the 625 °C/5 h oxidised sample, under a contact load of 2 N for 1200 s corresponding to Zone II in Fig.4.17; (b) morphology of the wear track produced on the 625 °C/72 h oxidised sample, under a contact load of 2 N for 3600 s corresponding to Zone III in Fig.4.17; (c) a higher magnification view of (b); and (d) wear debris particles produced from the sample shown in (b)

Surface roughness must also be considered when investigating the frictional response of a surface treatment. Table 4.1 shows the effect of the various oxidation durations on surface roughness. It can be clearly seen that as the oxidation duration is increased, as too is the surface roughness. The surface roughness for both the controlled cooling and the SMAT samples are 0.212 µm and 0.261 µm respectively, which are higher than the furnace cooled 20 h sample. This indicates that the surface roughness is not the prevailing factor causing the variation in friction coefficient of the oxide layer.

4.2.5 The Role of Rutile in Reducing Friction

Theoretically, rutile titanium dioxide with TiO_2 stoichiometry has a primitive tetragonal unit cell and does not have easy shear planes to offer low friction [120, 121]. However, according to Gardos et al. [122], rutile-like oxides, slightly deficient in oxygen (TiO_{2-x} , $0.02 < x < 0.07$), known as Magneli phases with the formulas TiO_{2n-1} , should have a lower friction than titanium dioxide and behave as a lubricious material. Magneli phase exhibits contact mechanics different from that of rutile phase, explained to be due to the lamellar crystal structure arising from the lamellar organisation of oxygen vacancies to form easy shear crystallographic planes [121, 122]. Although the XRD patterns shown in Fig. 4.5, and those reported in other publications [10, 15, 18, 164], did not show any evidence of Magneli phase formation in thermally oxidised samples, it has been discussed in many publications that Magneli phases can be induced tribologically in titanium-based ceramics and coatings such as TiN and TiC, leading to effective reduction in wear rate and COF [167, 168]. It is thus suggested that the observed low COF, as low as 0.2, of some of the oxide layers observed in the present work could be due to the stress-induced Magneli phase formation, during the tribological process. The ease of formation of the Magneli phase during tribological processes can vary with microstructure and degree of oxygen deficiency of the oxide layer, which in turn can vary with oxidation conditions [15]. Thus, the lowest friction observed for the 5 h treated sample (Fig. 4.7) could be attributed to the influence of microstructure most favourable to the stress-induced Magneli phase formation. The effectiveness of prior SMAT treatment and controlled slow cooling in further reducing friction of the oxide layer (see Fig. 4.15) could also be explained similarly.

The PillingBedworth ratio between rutile TiO_2 and Ti is about 1.73, i.e. $1 \mu\text{m Ti}$ gives rise to $1.73 \mu\text{m TiO}_2$. Thus, the formation of TiO_2 on a titanium surface leads to significant volume expansion in the oxide layer. This results in very high compressive residual stresses and thus easy debonding of the oxide layer. It has been explained

by Ashrafizadeh and Ashrafizadeh [8] that during thermal oxidation of titanium in air, particularly at relatively high temperatures, a large number of vacancies are progressively generated in the oxide lattice. This may cause the growth of oxide scale by anion migration rather than cation migration. The inwards migration of oxygen (anion) from the gas-metal interface to the scale-metal interface leads to scale growth at the scale-metal interface. Thus, growth stresses are developed at the interface, which, when coupled with the thermal stresses arising from the large difference in coefficient of thermal expansion between TiO_2 and Ti, can become sufficiently high to produce micro-cracks at the metal-oxide interface, deteriorating the adhesion of the oxide layer to the diffusion zone or even causing spallation of the oxide layer.

It is therefore difficult to obtain an adherent oxide layer in combination with an inner hardened oxygen diffusion zone of sufficient thicknesses, unless well controlled parameters are used to minimise the thickness of the oxide layer, but at the expense of the thickness of the diffusion zone [18]. However, the initial attempts in this work demonstrated that it is possible to improve the tribological performance of the oxide layers by modifying the surface structure and stress conditions before or after thermal oxidation, i.e. by prior SMAT treatment and by controlled slow cooling (Fig. 4.15). It is conceivable that prior SMAT treatment may modify the growth kinetics of the oxide layer and the diffusion zone due to the structural defects and grain refinements in the near surface region of CP-Ti. The compressive residual stresses induced by SMAT may also modify the stress state in the oxide layer formed subsequently. In the case of controlled slow cooling, it is beneficial in minimising thermal stresses and providing an annealing effect to relieve part of the growth stresses in the oxide layer.

4.3 Electrochemical Behaviour as a Function of Depth from the Oxidised Surface

The electrochemical behaviour of thermally oxidised Ti was investigated as a function of depth from the surface by mechanically removing successive layers from the oxidised materials surface. Before electrochemical testing, progressive grinding of the TO-Ti was carried out using 1200 SiC paper. This was to expose the underlying layers at various depths from the surface. 2-3 μm of material was removed with each stage of grinding.

In order to accurately measure the thickness of the material, the following measurements before and after surface grinding were used: Weighing the specimen using a balance accurate to 0.1 mg, measuring the size of the diagonals of a Vickers hardness indent made on the surface just outside the corrosion test area, and measuring the thickness of the specimen using a digital micrometer accurate to 1 μm .

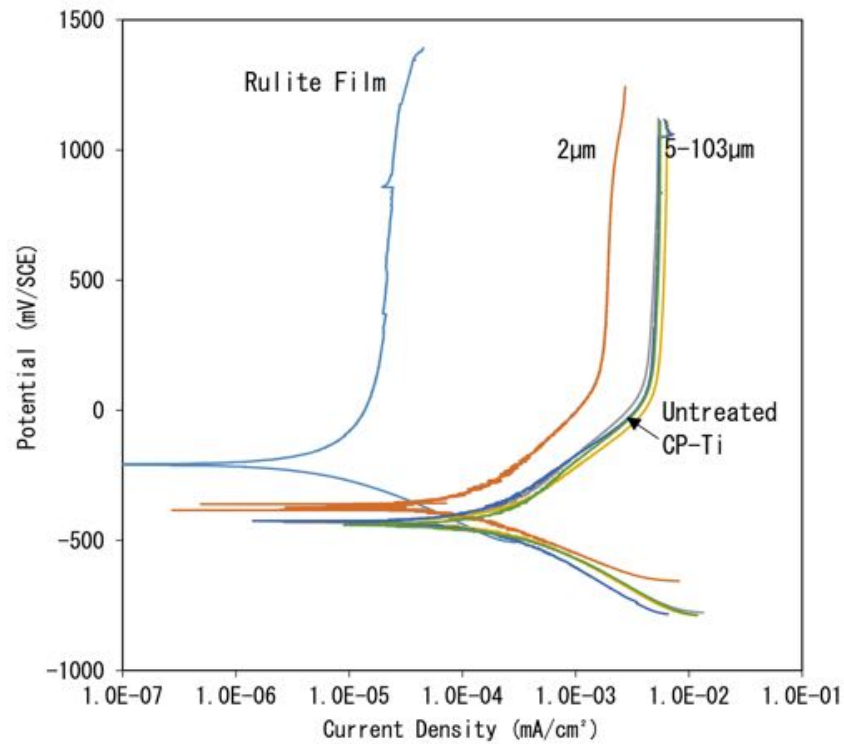
In this study, electrochemical and tribocorrosion investigations were carried out using CP-Ti thermally oxidised at 625 °C for 20 h. These conditions were chosen due to the relatively good film adhesion experienced during dry sliding tests. The 20 h duration also allows for a sufficient build up of both the oxide film and oxygen diffusion zone, such that it can be investigated.

4.3.1 Potentiodynamic Behaviour

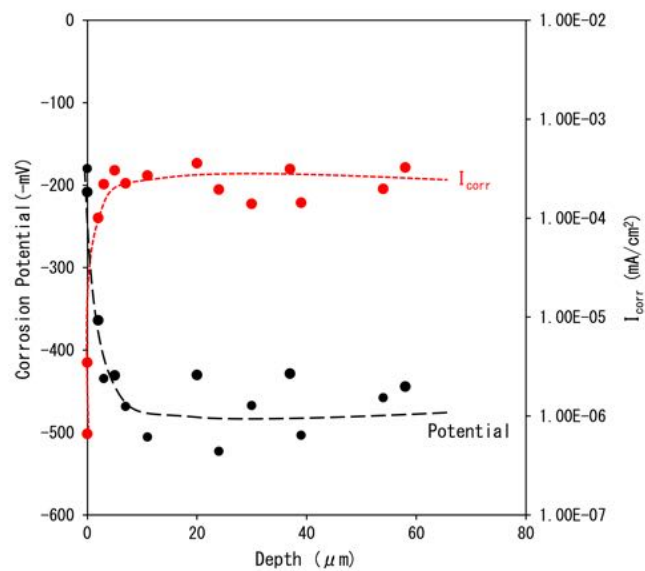
Fig. 4.19a shows anodic polarisation curves for the 20 h thermally oxidised titanium at various depths from the as-oxidised surface, correlating to different amounts of oxygen within the subsurface. The polarisation curves show that the thermally-formed oxide layer offers much enhanced corrosion resistance over untreated CP-Ti. The oxide layer offers an anodic shift in the free corrosion potential to $-200 \text{ mV}_{\text{SCE}}$, from approximately $-450 \text{ mV}_{\text{SCE}}$ for untreated CP-Ti. Along with the shift in corrosion potential, the oxide layer also shows very low current densities throughout the potential sweep. Both the anodic shift and low current densities have been reported previously [8, 55, 118]. At $2 \mu\text{m}$ below the surface, the $1 \mu\text{m}$ thick oxide layer has been fully removed and the ODZ is then exposed. The free corrosion potential and the corrosion current density of the ODZ are slightly shifted from that of the bulk material. Oxygen in the diffusion zone seems to have a slight positive effect on the corrosion properties of titanium, through reduced current densities and higher corrosion potential ($-350 \text{ mV}_{\text{SCE}}$). At further depths ($5 \mu\text{m}$ and deeper) from the surface, the oxygen content is much reduced (Fig. 4.3) and the materials electrochemical response shows a very reproducible and consistent polarisation curve, with a stable passive region between $200 \text{ mV}_{\text{SCE}}$ and $1000 \text{ mV}_{\text{SCE}}$. The current density is stable at around 0.005 mA cm^{-2} , which is similar to that of untreated CP-Ti. The main benefit of thermal oxidation comes from the oxide layer and to a lesser extent, from the upper part of the ODZ, with the bulk titanium retaining its corrosion properties.

Fig. 4.19b shows the evolution of both corrosion current and corrosion potential with depth. Both the corrosion potential and current are highly variable depending on the structure exposed to the corrosive medium. The rutile oxide surface layer is the most effective at reducing the rate of corrosion this is demonstrated by the low corrosion currents and higher corrosion potential. When there is a high oxygen concentration within the subsurface layers the corrosion current and corrosion potential are improved over that experienced at further depths from the surface. Once the depth is below $10 \mu\text{m}$, the surface

corrosion potential and corrosion current become much more consistent and inline with that of untreated Ti.



(a)



(b)

Fig. 4.19: a) Anodic Polarisation curves and b) the corrosion potential and corrosion current density (I_{corr}) measured for thermally oxidised titanium at various depths from the treated surface, using a sweep rate of 1mV/s in a 0.9% NaCl solution

4.3.2 Current Transient Behaviour

Potentiostatic testing was carried out at various sample depths by applying a potential of 500 mV_{SCE} for 3600 s. According to Fig. 4.19a, at this potential all samples are within the passive region. Fig. 4.20 shows the current transient response for the samples in the Log (*I*) vs. Log (*t*) scale. The Point Defect Model (PDM) and the High Field Theory (HFT) are well-used models to describe the change in ion flux at the sample surface [43, 44, 55].

As the surface passive film thickens, the ion flux is reduced, leading to lower conduction and therefore lower current densities. This current response over time is described by Eq. 4.4 [44–46]:

$$I = 10^{[-A+k \log(t)]} \quad (4.4)$$

Using Eq. 4.4, a plot of Log (*I*) against Log (*t*) should produce a straight line, where the gradient = $-k$ and intercept at *A* when *t* = 1. If *k* = 1, this would be characteristic of a thick (greater than 0.5 nm) dense film. Thinner, more porous films would have a $k < 1$ [44, 45].

In Fig. 4.20, the curves generated for the ground samples clearly conform to Eq. 4.4. There exists an initial stage in all the tested samples where there are lower curve gradients ($k \approx 0.5$). This low value of *k* is attributed to small film thickness in the initial stage of polarisation, a phenomenon that has been reported in previous studies [44, 45]. As polarisation time increases the passive film thickens and the *k* value approaches 1. Once again, it can be observed that there is a variation between the current densities just below the thermally-formed oxide layer (2 μm) and then deeper (5 μm-inwards). At a depth of 2 μm the curve reaches linearity sooner (after 50 s), than at deeper depths (approx. 200 s). There is also a difference in the linear slope gradients. The 2 μm depth sample never reaches $k = 1$. Whereas, the further ground samples all achieve this ideal value. This variation in the time to reach the linear stage and final slope value shows that when there is a high oxygen content within the titanium lattice, a stable passive film can be built up more quickly to result in the lower passivity current density (Fig. 4.20). This faster

response at the 2 μm depth could be attributed to the higher free corrosion potential and lower current densities observed in Fig. 4.19. However, the data in Fig. 4.20 suggest that the film generated is less dense and slightly more porous than that produced when lower oxygen concentrations are present within the titanium substructure. It can clearly be seen from Fig. 4.20, that the oxide layer on the as-oxidised surface is a barrier layer which results in very low current densities. The current transient behaviour of the as-oxidised surface does not comply with Eq. 4.4 because a thick (1 μm) oxide layer already exists before the polarisation test.

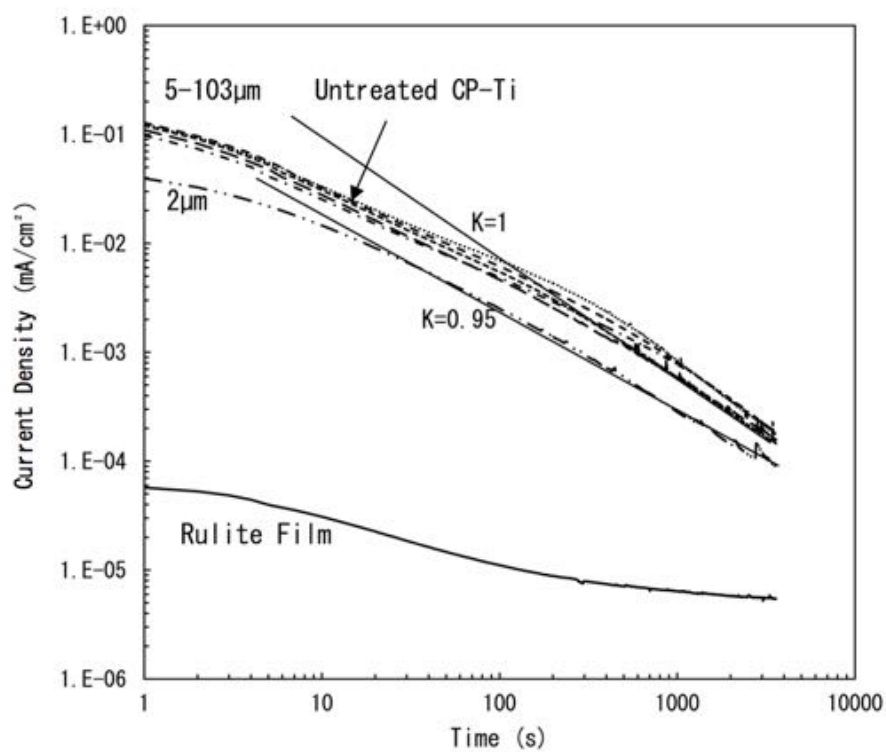


Fig. 4.20: Current transient curves in the log (I) vs log (t) scale measured during film formation at various depths from the surface of thermally oxidised titanium. All tests were conducted at a potential of 500 mV for a duration of 3600 s in a 0.9% NaCl solution

4.3.3 Mott-Stocky Behaviour

In the work presented, M-S analysis was carried out using the technique highlighted in section 3.5.4 on page 85. M-S analysis was used to determine the dopant density at various depths from the surface of oxidised titanium. Passive films were formed at various sample depths from the surface. Films were generated at a potential of 500 mV_{SCE} for 3600 s. Fig. 4.21a shows the initial response of the sample at the surface (rutile film).

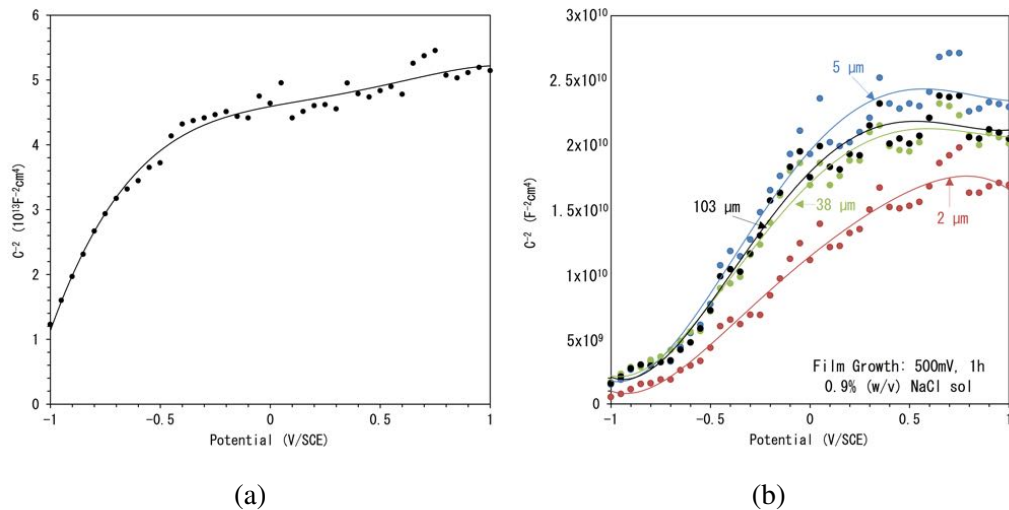


Fig. 4.21: M-S plots (C^2 vs E) generated for the passive film at (a) the surface of thermally oxidised titanium and (b) at various depths from the surface of the thermally oxidised titanium. The passive film was grown potentiostatically at 500 mV for 3600 s in a 0.9% NaCl solution

Fig. 4.21b shows the M-S plots at various ground depths from the rutile film. Using the slopes presented in Fig. 4.21a and Fig. 4.21b, a plot of dopant density as a function of sample depth was generated and is shown in Fig. 4.22. The dopant density was calculated using Eq. 2.25.

M-S analysis clearly shows that the surface and subsurface of the thermally oxidised samples have very different semiconducting properties. The surface rutile film shows an extremely low dopant density of $2.99 \times 10^{17} \text{ cm}^{-3}$. This is in direct correlation to that expected for passive metals [169–172]. The rutile surface clearly has a much lower dopant density than the passive film on the subsurface (4.21b). The low defect density means there is less ion transportation and hence a lower rate of corrosion. At lower

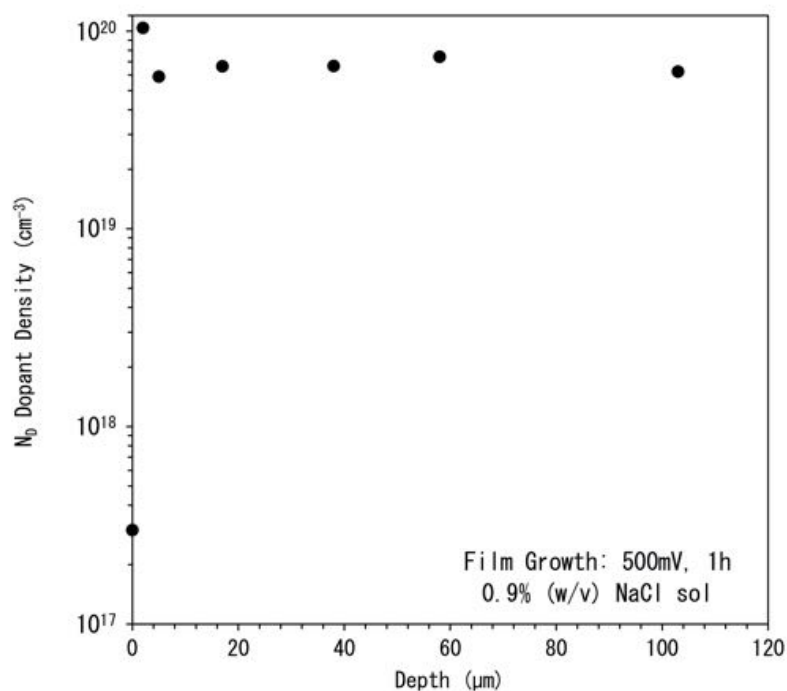


Fig. 4.22: Variation of the charge carrier density in the semiconducting passive film with the depth from the sample surface. The passive films generated only showed n-type semiconducting characteristics. These were calculated from M-S plots and the linear region between -0.6 and -0.05V

depths from the surface, it can be seen that the samples dopant levels are all around the $10^{19} - 10^{20} \text{ cm}^{-3}$. This is the same as seen in previous titanium corrosion studies [62]. This figure suggests that the film formed during the polarisation is oxygen deficient compared with bulk rutile [62, 172]. In Fig. 4.22 there is a clear spike in dopant density at a depth of $2 \mu\text{m}$ below the sample surface. This increase in dopant density is of interest when looking at the transient current curves presented in Fig. 4.20. It is seen that for the $2 \mu\text{m}$ ground sample $k \neq 1$. This shows a less dense film that is more susceptible to corrosion. However, the passive film was, formed at a faster rate than that of the lower depth samples. This shows that increased oxygen content allows for a faster film growth but the film generated has a higher defect density than that of bulk titanium.

4.4 Tribocorrosion Behaviour

A major consideration in the use of titanium is the interaction between wear and corrosion, this is also known as tribocorrosion. This is observed in medical implants, valves and marine applications, where wear can cause damage to a passive film in the contact zone. This can lead to accelerated corrosion, which in turn can cause accelerated wear [60, 61, 141, 142, 145, 173]. Although the tribocorrosion behaviour of thermally oxidised titanium has been investigated by several authors [117, 143, 145], none of these studies have identified the relative contribution of the oxide layer and the ODZ to the tribocorrosion process. Thus, another objective of the present investigation is to clarify the effect of each substructure of the oxidised Ti on tribocorrosion. Therefore, in the present work, experiments were conducted to investigate the tribocorrosive behaviour of thermally oxidised titanium in a 0.9% NaCl solution. Tribocorrosion tests were conducted under combined sliding wear and electrochemical conditions, at various applied potentials.

4.4.1 Open Circuit Tribocorrosion Behaviour

Initial tribocorrosion tests were carried out at open circuit without externally applied potentials. The samples were tested for a duration of 5 hours, with 4 hour sliding and 30 minutes stabilisation before and after sliding. Fig. 4.23 shows the evolution of potential and friction coefficient over time for the thermally oxidised sample. During tribocorrosion testing, four distinct frictional zones are observed. These friction zones have been observed during dry sliding of thermally oxidised CP-Ti in section 4.2.3. It is proposed that each zone observed is related to the material composition and structure. Thermal oxidation generates a layered structure and the friction behaviour is a response to each structure and the transition between these layers as wear progresses. The frictional zones relate to the following structural transitions: I) oxide layer; II) removal of the oxide layer; III) oxygen diffusion zone and IV) bulk titanium. With the identification of these

four frictional zones from the friction curves, it can be clearly seen that the open circuit potential (OCP) data shows these corresponding zones. OCP gives insight into the surface condition of the sample in real time during the sliding wear process. Each zone exhibits a unique friction and OCP response with differing levels of material activity, friction and wear, as described below with reference to Fig. 4.23.

Zone I Sliding contact between the Al_2O_3 ball and the oxide layer results in low friction. Upon sliding, the OCP experiences a cathodic shift from $-200 \text{ mV}_{\text{SCE}}$ to $-500 \text{ mV}_{\text{SCE}}$ and remains at $-500 \text{ mV}_{\text{SCE}}$ for around 700 s. During this phase, wear occurs within the oxide layer, resulting in the observed low friction coefficient (< 0.6) [10, 100] and a relatively small drop in OCP. Fig. 4.24a shows the wear track produced after sliding wear test at OCP for 500 s. It can be seen that the oxide layer is not worn through and maintains its integrity with the substructure. The dominant wear mechanism is micro-polishing of the oxide layer.

Zone II As sliding wear continues, the oxide layer is gradually removed or damaged, exposing areas of the ODZ from below. During this transitional zone, the OCP is gradually dropped from $-500 \text{ mV}_{\text{SCE}}$ to $-900 \text{ mV}_{\text{SCE}}$. Along with this cathodic shift of OCP, the friction coefficient is gradually increased from 0.6 to 1.2. The wear mechanism changes from micro-polishing of the oxide layer in Zone I to delamination of the oxide layer and abrasive wear of the exposed ODZ, as can be clearly seen in Fig. 4.24b.

Zone III Full exposure of the ODZ to sliding contact results in a large cathodic shift of OCP. The exposure of the ODZ coincides with a period of increased friction ($\mu = 1.2$). While sliding occurs in the ODZ, the OCP is gradually shifted from -920 mV to -750 mV over a time period of approximately 3000 s. This is due to passive film formation within the wear track. With each successive pass of the alumina ball, the passive film is only partially removed. There becomes a point when the film generated within the wear track is removed at the same or slower rate than the passive oxide film is formed. This is shown by the stabilisation of the OCP at the later stage of Zone III. This removal and formation

of the passive film can also explain the smooth nature of the wear track observed during this period of the test [10, 100, 117], shown in Fig. 4.24c.

Zone IV Removal of the ODZ from the wear track allows for the exposure of the underlying bulk material. There is a reduction in friction coefficient, as previously seen when in contact with untreated CP-Ti [77, 100]. The OCP data shows another cathodic shift as the ODZ is removed. The OCP shows a recovery over 4000 s. Microscopic examination of the wear track shown in Fig. 4.24d indicates a joint mechanical and chemical tribocorrosion response. At the outer edges there is a smooth area in the wear track. This is associated with the fast passivation of the ODZ. This fast passivation results in a smooth polished surface. In the centre of the wear track, typical wear morphology expected of titanium is observed with wear regimes dominated by severe adhesion and delamination [10, 100].

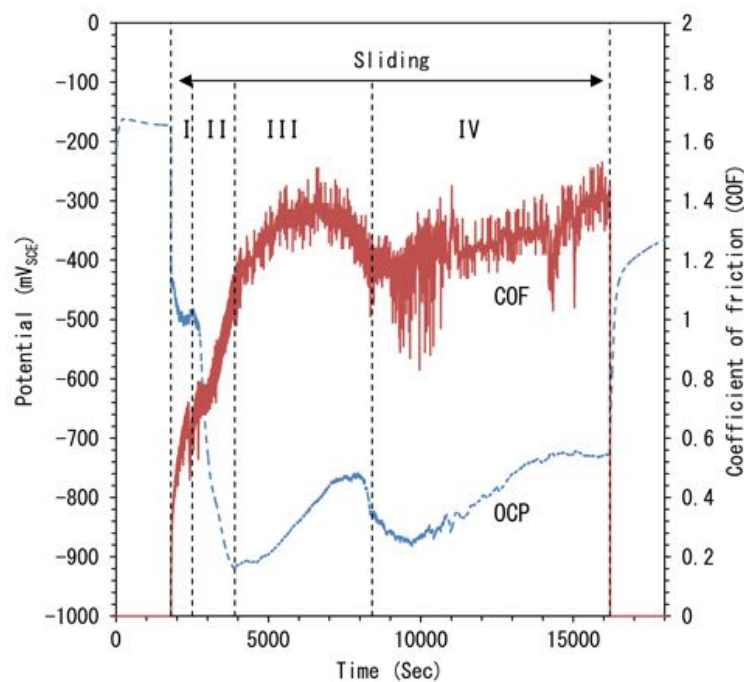


Fig. 4.23: Open circuit potential and Coefficient of friction curves recorded for a contact load of 2 N in a 0.9% NaCl solution for thermally oxidised CP-Ti. The onset of sliding is indicated after 30 minutes stabilisation. Four distinct frictional zones can be observed: I) Oxide layer, II) Partial removal of the oxide layer, III) Oxygen diffusion zone and IV) Substrate

When considering the tribocorrosion response of thermally oxidised titanium at OCP, it is clear that the oxide layer offers the most effective protection against both corrosion and tribocorrosion, with the layer thickness being a restraining factor as to the duration of protection. Once the oxide layer has been removed, the diffusion zone and bulk titanium have similar OCP response. However, the time taken for repassivation is significantly less for the ODZ than for the bulk titanium. When relating this to the corrosion depth profiling analysis undertaken in Section 4.3, it is clear that the passivation of the ODZ happens at a faster rate than that of bulk titanium. The ODZ offers improved passivation kinetics and reduced wear as compared to bulk titanium, with the drawback of having increased friction.

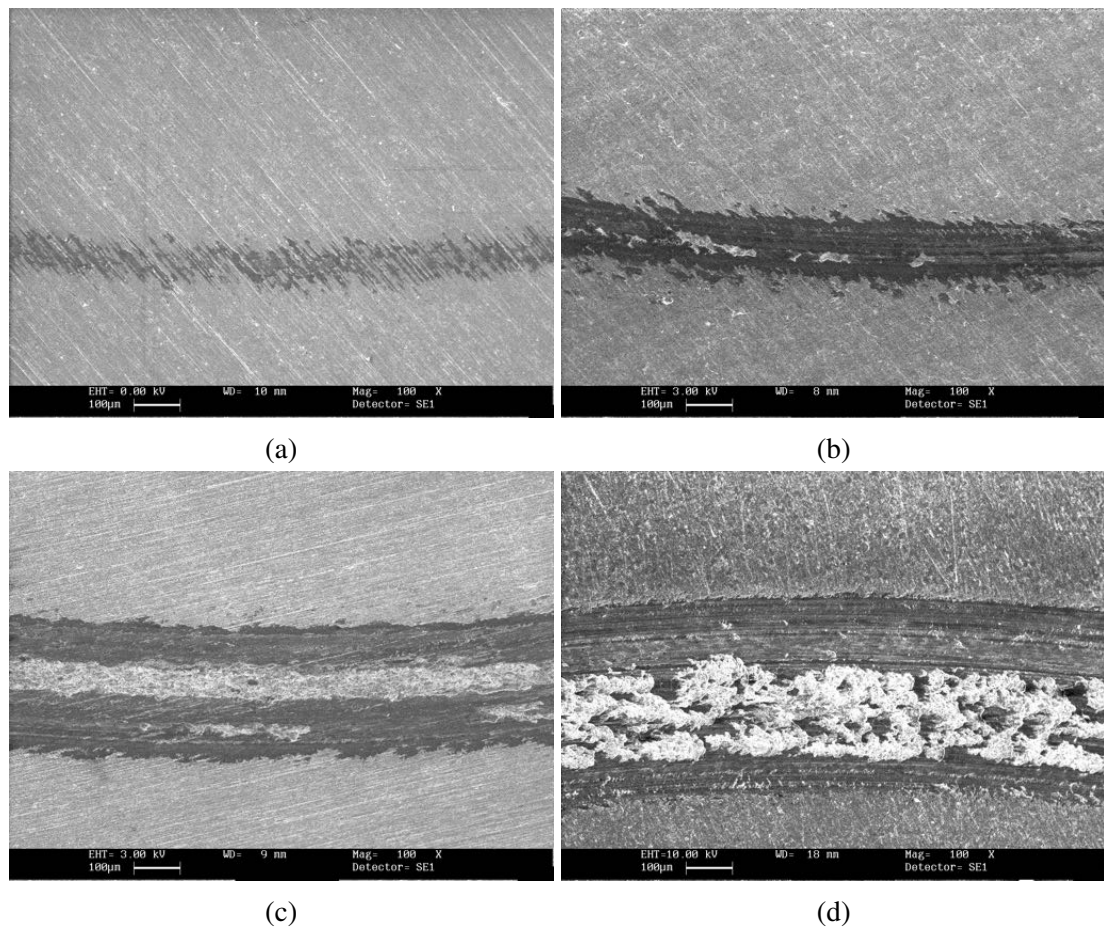


Fig. 4.24: SEM images showing wear track morphology of the OCP tribocorrosion tests after sliding durations of (a) 500 s, (b) 1700 s, (c) 4700 s and (d) 14400 s. The times selected represent the four frictional zones observed in Fig. 4.23. All tests were subjected to a 2 N sliding load

4.4.2 Effect of Applied Potential on Tribocorrosion Behaviour

In order to understand the contributing factor of corrosion on the overall tribocorrosion behaviour of thermally oxidised titanium, potentiostatic sliding wear tests were carried out at both anodic and cathodic potentials. Fig. 4.25 shows the friction and current responses of the test sample, at potentials of $+1000 \text{ mV}_{\text{SCE}}$, $+500 \text{ mV}_{\text{SCE}}$, $-900 \text{ mV}_{\text{SCE}}$ and $-1500 \text{ mV}_{\text{SCE}}$. Clearly, applied potential has a large impact on the friction behaviour of the thermally oxidised titanium.

Applying an anodic potential on a sample allows the anodic forward reactions to take place. For passive materials this is normally associated with increased current at higher potentials. However, it can be seen in Fig. 4.25a ($1000 \text{ mV}_{\text{SCE}}$) and Fig. 4.25b ($500 \text{ mV}_{\text{SCE}}$) that sliding only leads to a small increase in current during the course of Zone I, and such an increase is even smaller at the higher potential. This lower current is in tandem with reduced friction coefficients observed throughout the test. As the reduced friction is associated with the thermally-formed oxide layer (Zone I), it can be assumed that during these tests, this oxide layer stays in place longer and is removed at a more gradual rate than that observed under OCP conditions. As discussed earlier, Zone I (the oxide layer) lasts about 700 s at OCP (Fig. 4.23). At the anodic potential of $500 \text{ mV}_{\text{SCE}}$, Zone I lasts much longer, about 4000 s (Fig. 4.25b). When the anodic potential is increased to $1000 \text{ mV}_{\text{SCE}}$, Zone I is further extended to nearly 10 000 s. Clearly, increasing anodic potential helps to increase the durability of the thermally-formed oxide layer on CP-Ti and thus, to reduce friction and chemical wear. The wear track morphologies shown in Fig. 4.26a and 4.26b for the $1000 \text{ mV}_{\text{SCE}}$ and $500 \text{ mV}_{\text{SCE}}$ wear tracks are also substantially different from those observed after the OCP tests (Fig. 4.24d). At the potential of $1000 \text{ mV}_{\text{SCE}}$ (Fig. 4.26a), the wear track exhibits wear mechanisms dominated by micro-polishing of the thermally-formed oxide layer (Zone I) with some slight delamination of the layer and exposure of the underlying ODZ (Zone II), indicating that Zone I dominates the sliding wear process. At $500 \text{ mV}_{\text{SCE}}$, the wear track morphology

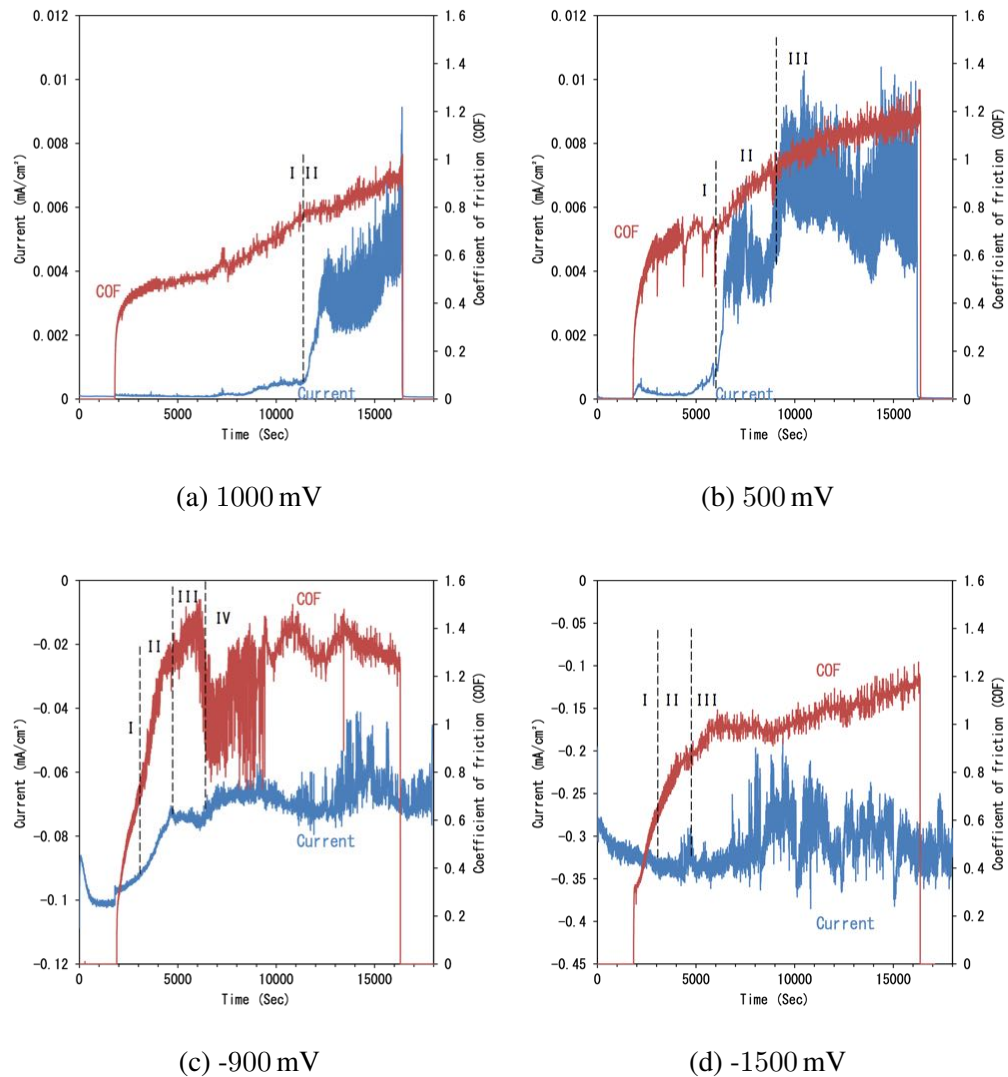


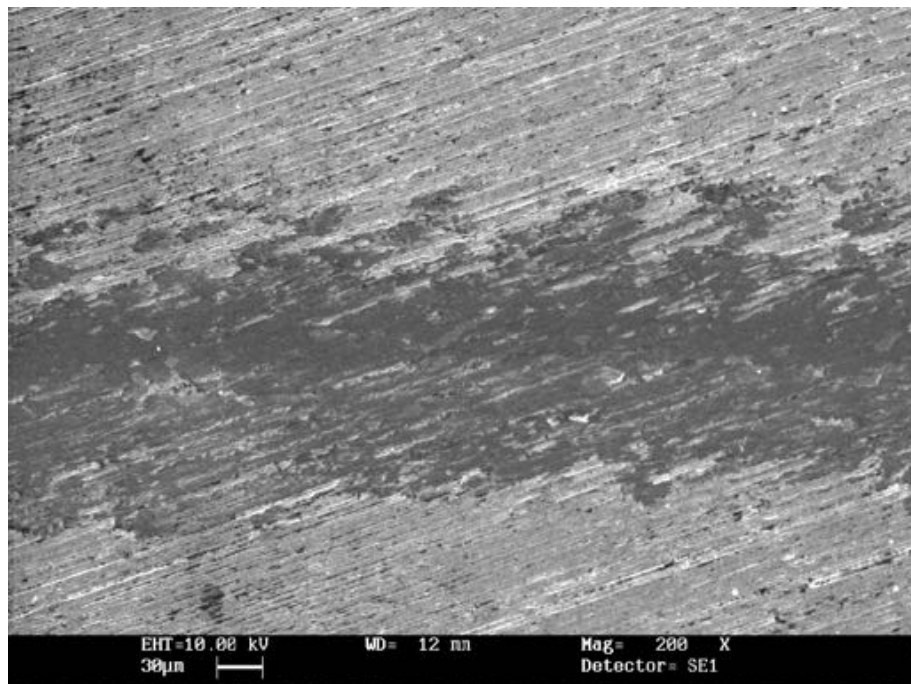
Fig. 4.25: Friction coefficient (μ) and current density (I) against time for tribocorrosion testing at potentials of: a) 1000 mV, b) 500 mV, c)-900 mV and d) -1500 mV. Frictional zones identified: I) Oxide layer, II) Partial removal of the oxide layer, III) Oxygen diffusion zone and IV) Substrate. Sliding contact was initiated for 4 hours, with a 30 minute settling period before and after sliding

shows large scale delamination of the oxide layer and large exposure of the ODZ (Zone III) (Fig. 4.25b). No exposure of the bulk Ti (Zone IV) is observed at these two anodic potentials.

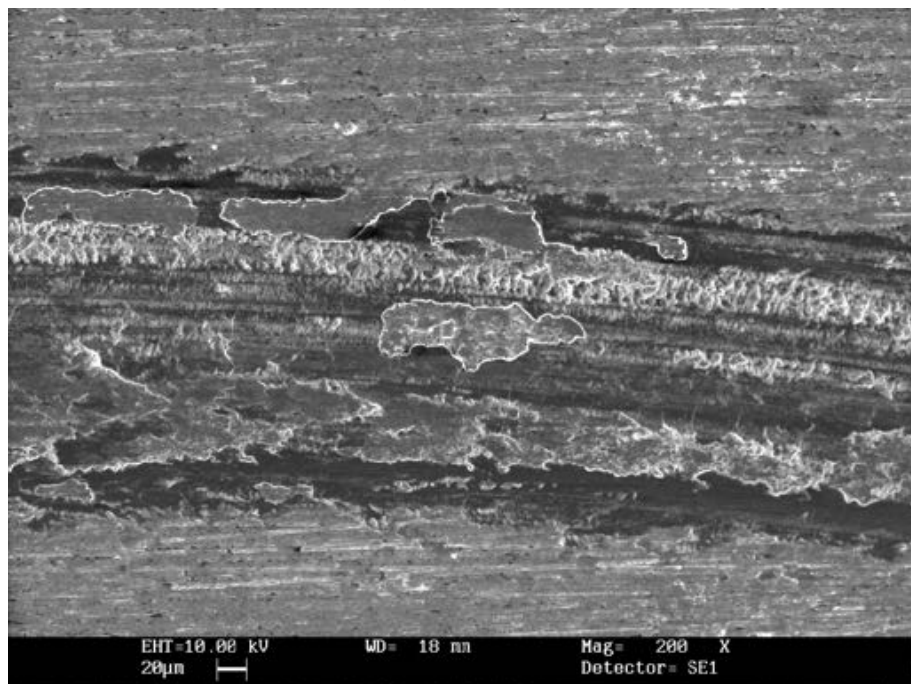
It is usually expected that when the potential of the system is moved to a value in a cathodic direction from OCP, material loss is solely due to the mechanical wear process, as the negative charge removes the ability for the formation of positive metal ions. This

is shown through the flow of a negative current [41]. Fig. 4.25c shows the friction and current response when a cathodic potential of $-900 \text{ mV}_{\text{SCE}}$ is applied to the sample. The friction curve observed is very similar to that at OCP in Fig. 4.23, characterised by the four-zone mechanism described previously. The thermally-formed oxide layer, which lasts for only 600 s (Zone I) is damaged quickly by the mechanical action. Wear track morphology, as shown in Fig. 4.26c, is seen to be dominated by severe abrasion and adhesive wear. When looking at how this wear track differs from that at OCP shown in Fig. 4.24d, there are no longer the smooth sides associated with passivation of the ODZ. This is as expected due to lack of anodic oxidation at cathodic potentials.

Tribocorrosion tests were conducted at a further cathodic potential of $-1500 \text{ mV}_{\text{SCE}}$. At such a potential, the evolution of hydrogen is predicted [75, 174–177]. Hydrogen is able to penetrate into titanium, causing the formation of titanium hydride (TiH_2). The friction and current responses shown in Fig. 4.25d indicates that initial removal of the thermally-formed oxide layer occurs at the same rate as at $-900 \text{ mV}_{\text{SCE}}$ (Fig. 4.25c). Once the oxide layer has been removed, there is a stabilisation of the frictional response, rather than the peak and drop associated with the wear of the ODZ (Zone III to Zone IV in Fig. 4.23). This indicates that the ODZ has not been worn through during the test (no Zone IV). When looking at the wear track morphology shown in Fig. 4.26d, there is a substantial difference in wear mechanisms involved. The wear track is now littered with cracks and dominated by abrasive wear, with the polishing of the peaks. This has been observed in a previous tribocorrosion study of a titanium alloy, when hydride was formed under cathodic conditions [178]. It is interesting to note that once the load has been removed, there is no reduction in cathodic current flowing in the sample, indicating that the evolution of hydrogen continues after sliding.

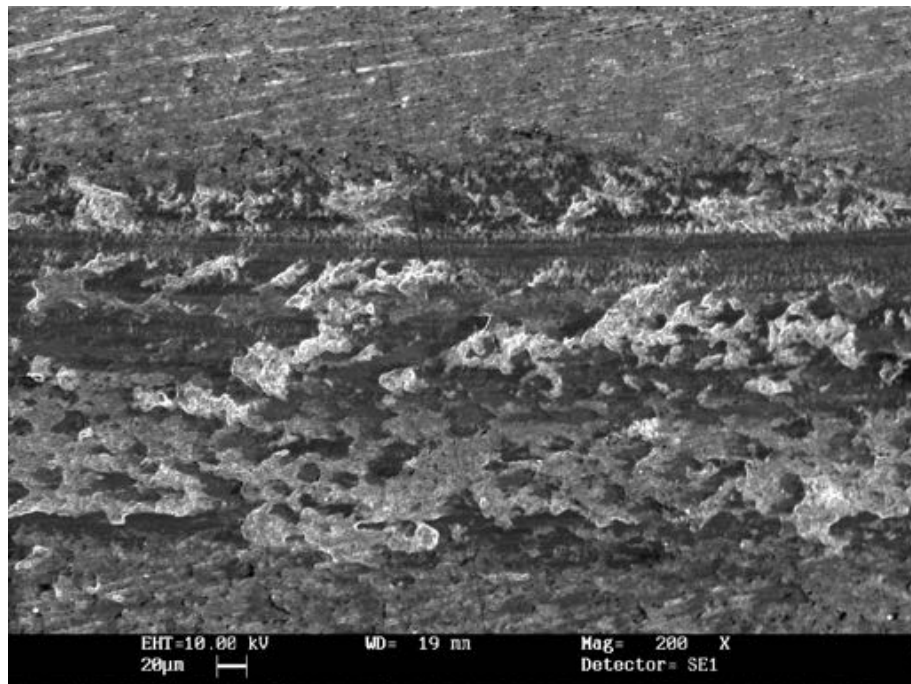


(a) +1000 mV

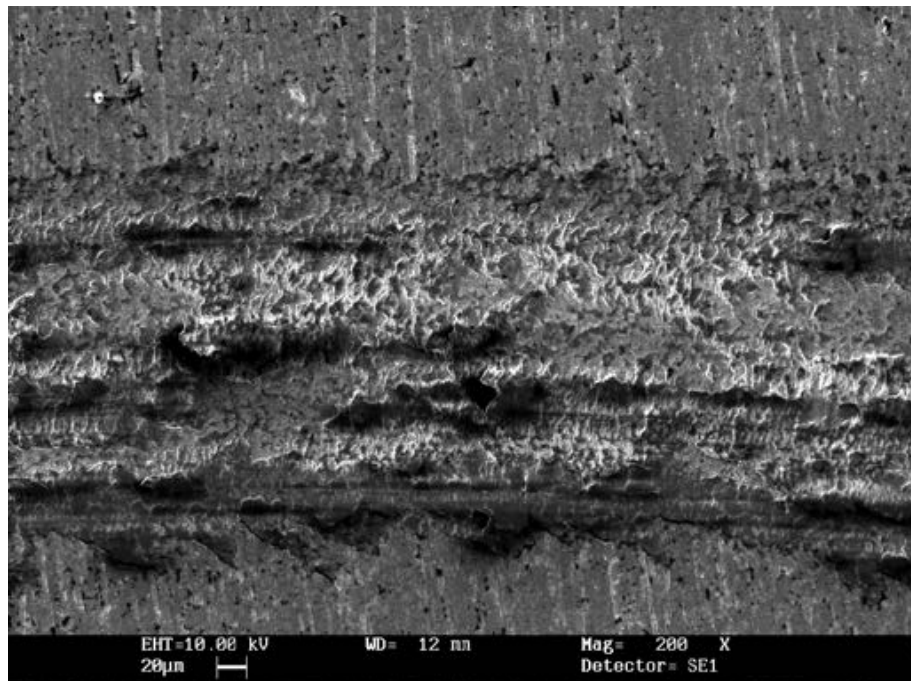


(b) +500 mV

Fig. 4.26: SEM images showing the wear track morphology produced on the thermally oxidised titanium, after tribocorrosion testing at potentials of: a) 1000 mV, b) 500 mV, c)-900 mV and d) -1500 mV. All tests were conducted using a load of 2 N for 14 400 s



(c) -900 mV



(d) -1500 mV

Fig. 4.26: SEM images showing the wear track morphology produced on the thermally oxidised titanium, after tribocorrosion testing at potentials of: a) 1000 mV, b) 500 mV, c)-900 mV and d) -1500 mV. All tests were conducted using a load of 2 N for 14 400 s

4.4.3 Total Material Loss Rate

Total material loss (TML) from the wear track was measured using a profilometer, which was then normalised with total sliding distance and applied load to obtain specific total material loss rate (TMLR). The results are shown in Fig. 4.27 as a function of applied potential, for the thermally oxidised and untreated CP-Ti samples. TML in volume (V_{total}) is a sum of both mechanical (V_{mech}) and chemical (V_{chem}) volume loss, described by Eq. 2.27.

Faraday's law can be used to determine the contribution of chemical wear in the tribocorrosion process. The anodic current detected during tribocorrosion testing is related to the amount of material lost, due to anodic oxidation and/or dissolution through Faraday's law [41, 55, 56, 179]:

$$V_{chem} = \frac{ItM}{nF\rho} \quad (4.5)$$

where I is the average current (A) developed during sliding contact, t is the time (s) of sliding contact, F is Faraday's constant ($964858.34 \text{ A s mol}^{-1}$), M is the atomic mass of the metal ($47.767 \text{ g mol}^{-1}$ for Ti), n is the charge number for the oxidation reaction (valance = +4 for Ti [62]) and ρ is the density of the metal (4.11 g cm^{-3}).

From Fig. 4.27, several observations can be made regarding the effects of thermal oxidation on the tribocorrosion response of titanium and the effect of potential on TMLR.

Firstly, thermal oxidation reduces the TMLR across the spectrum as compared to untreated CP-Ti by one order of magnitude at OCP and cathodic potentials, when mechanical wear is predominant. Such a beneficial effect of thermal oxidation is more significant at the anodic potentials, where a reduction in TMLR by nearly two orders of magnitude is seen due to the reduction in both mechanical and chemical wear.

Secondly, the effect of potential on TMLR of the oxidised CP-Ti is different from that of the untreated CP-Ti and many other materials reported [56, 180]. For the untreated CP-Ti, as expected, the TMLR increases with increasing potential due to increased

chemical wear. But at the cathodic potential of $-1500 \text{ mV}_{\text{SCE}}$, the TMLR is much reduced, presumably due to the formation of titanium hydride. On the other hand, for the thermally oxidised CP-Ti, as the potential is increased from OCP, the TMLR is reduced, by nearly an order of magnitude at $1000 \text{ mV}_{\text{SCE}}$, which is not usually expected. This is due to the prolonged durability of the thermally-formed oxide layer (Fig. 4.25a and 4.25b) relative to the tests at OCP (Fig. 4.23) and at cathodic potentials (Fig. 4.25c and 4.25d). This prolonged oxide layer coverage offers beneficial protection from both mechanical and chemical wear. Such an anodic protection of the thermally-formed oxide layer has not been reported previously. The reasons behind such an anodic protection are not clear at this stage. It is believed that applying an anodic potential to the samples increases the rate at which the exposed ODZ forms a passive film. When the thermally-formed oxide layer begins to breakdown, rapid passivation of the exposed ODZ would reduce the internal stresses on any oxide layer remaining in place by filling cracks or gaps produced in the layer. This shows that if the adhesion between the thermally-formed oxide layer and the underlying substructure can be addressed, thermal oxidation can offer a viable method to reduce wear and corrosion of CP-Ti.

Finally, for the oxidised sample, when the potential is shifted cathodically from OCP to $-900 \text{ mV}_{\text{SCE}}$, the difference in TMLR is associated with the chemical wear induced at OCP. This is as expected due to the absence of chemical wear at the cathodic potential. A further higher cathodic potential of $-1500 \text{ mV}_{\text{SCE}}$ allows for the hydrolysis of water and the production of hydrogen. Absorption and diffusion of hydrogen into titanium at this potential is expected and the creation of a small hydrogen diffusion zone (HDZ) cannot be ruled out. However, the solubility limit of hydrogen in α -Ti is as low as 20-150 ppm [174, 181], excess hydrogen that is adsorbed above the solubility limit will form various hydride phase precipitates in the wear tracks. This formation of titanium hydride is known to induce hydrogen embrittlement and is usually associated with reduced mechanical properties of titanium [182, 183]. However, the formation of hydride also induces real-time hardening within the wear track and could be accountable for the reduced TMLR

measured for both the thermally oxidised and untreated CP-Ti, under the relatively small contact load of 2 N employed in this work.

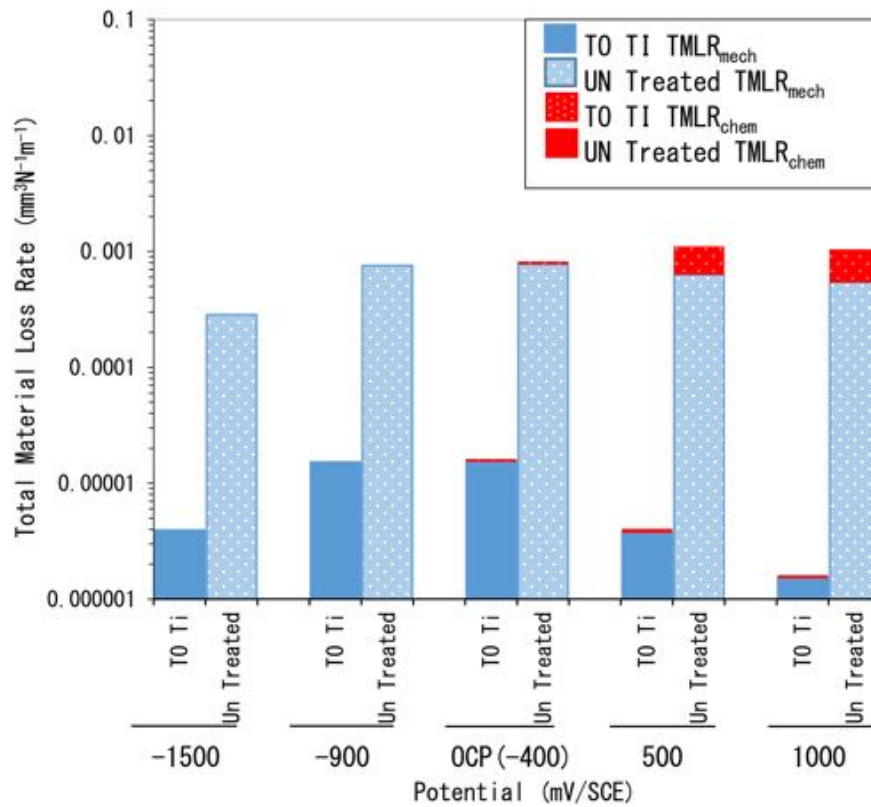


Fig. 4.27: Contribution of mechanical wear and corrosion to total material loss rate volume of thermally oxidised titanium and untreated titanium. All tests were conducted in a 0.9% NaCl solution

Chapter 5

Results and Discussion

Optimisation of Pack Carburised CP-Ti with Oxygen Diffusion for Improved Tribological Performance

In the present study, a new pack carburisation technique for titanium was investigated. The aim of the process has been to produce a titanium carbide/oxycarbide layer atop of an extended oxygen diffusion zone (α -Ti(O)).

The effect of temperature, pack composition and time, on the resulting structural features has been investigated. The carbon and oxygen concentrations across the carburised layers were studied, with a particular focus on the tribological response of carburised Ti. The process was optimised to give the most effective resilience to wear.

5.1 The Effect of Temperature on the Carburisation Process

The initial composition of the carburising mixture was the same as that used for traditional steel carburisation. The composition of the pack was 70% carbon and 30% energiser. The carbon was in the form of finely ground hardwood charcoal and the energiser was made up of Barium-carbonate (BaCO_3), sodium-carbonate (Na_2CO_3) and calcium carbonate (CaCO_3) in the ratio of 3:2:1 [155]. This pack was then used to determine the best temperature for the carburisation of titanium to take place. A duration of 20 h with furnace cooling (FC) was chosen and then temperatures of 625 °C, 725 °C, 825 °C and 925 °C were used. These samples were then tribologically tested in order to determine the most effective temperature for producing a wear resistant structure.

5.1.1 Layer Morphology

Using a pack carburising method with oxygen within the container, it is expected that the oxygen will diffuse into titanium. This is due to the extremely high affinity between titanium and oxygen [67, 74, 75]. The pack carburised samples were then cut to produce cross sections. The cross sections were then nickel plated and mounted in resin. The nickel plate helps to show dark surface films against the resin mount. The samples were then etched using a concentrated sulphuric acid (H_2SO_4) solution. SEM images, reveal the resulting structure (Fig. 5.1) produced by the carburising process.

The SEM cross section images for the samples treated at temperatures of 625 °C, 725 °C and 825 °C are all very similar in appearance. There is a thick pack residue at the surface and what appears to be some cracking of the surface layer, which is followed by a uniformed subsurface. In contrast, when carburised at a temperature of 925 °C, there is a new structural feature present upon the surface below the pack residue. This new structure has a network like appearance, and shows a uniformity to a depth of $\approx 4.5 \mu\text{m}$,

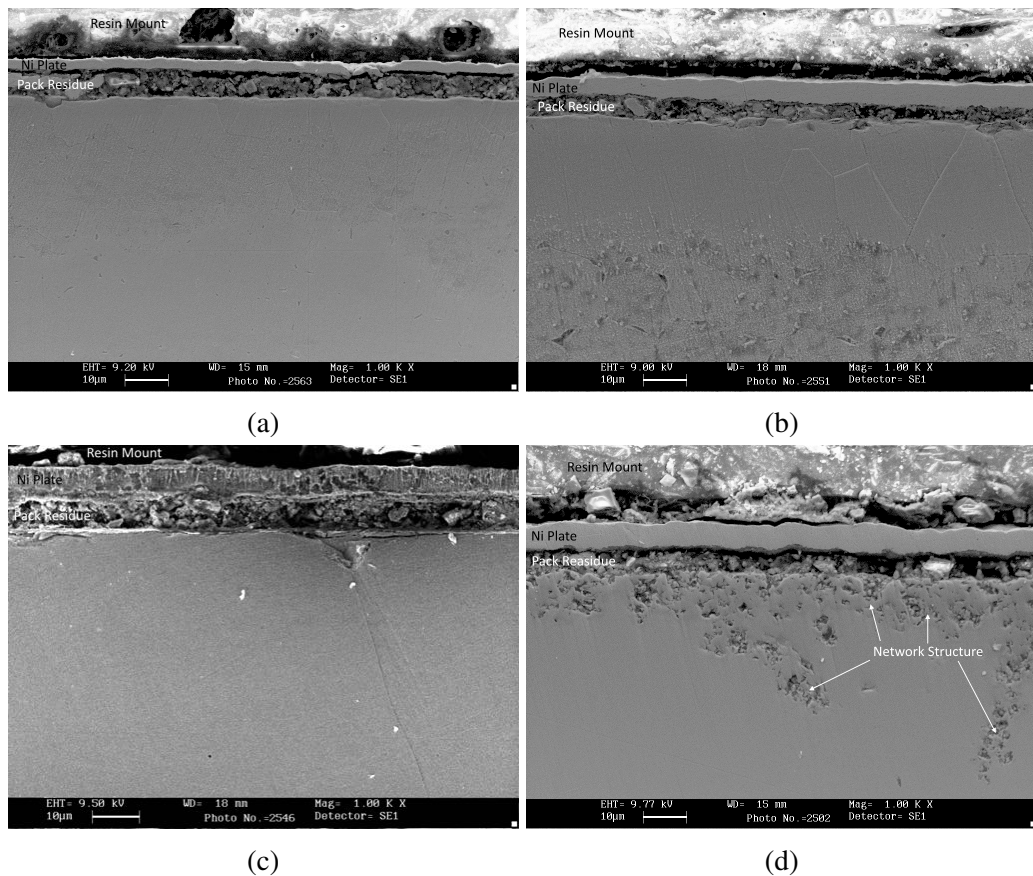


Fig. 5.1: SEM images showing the cross sectional structure after pack carburisation for 20 h at temperatures of: (a) 625 °C, (b) 725 °C, (c) 825 °C and (d) 925 °C

but in places can reach depths of $\approx 16 \mu\text{m}$. The network has no clear defining edge and thus, no obvious place for delamination of this structure to occur, suggesting good adhesion to the subsurface.

5.1.2 Glow Discharge Optical Spectroscopy (GDOS)

The incorporation of oxygen and carbon into the surface region of the treated titanium, was investigated via GDOS composition profile measurements. The carbon profile shown in Fig. 5.2a shows clearly that carbon diffusion was most effective at a temperature of 925 °C, with an extended region of carbon rich titanium clearly present. For the samples treated below 925 °C, there is a very limited amount of carbon diffusion. From the GDOS profile, it is estimated that carbon penetrated just 1-2 μm , compared with over 20 μm for the 925 °C samples.

When considering the oxygen diffusion within the treated samples (Fig. 5.2b), the amount of oxygen is constant throughout the depths of the samples. This indicates that large scale oxygen diffusion has occurred. It can be seen that when carburising was undertaken at 625 °C, the oxygen concentration starts to drop much sooner than that of the samples treated at a higher temperature. This can be attributed to the slow diffusion of oxygen in α -Ti, at the relatively low temperature of 625 °C [18].

GDOS demonstrates that the network structure identified in Fig. 5.1d is linked to the increased carbon concentration within the subsurface. The depth of this network structure was measured from cross sections (Fig. 5.1) and was shown to reach a depth of $\approx 16 \mu\text{m}$. Carbon has a maximum solubility of 3.3 at% within the α -Ti substructure [148]. The GDOS data suggests that titanium carbide (TiC) formation could be occurring at depths of up to ≈ 16 -17 μm from the surface, this is in direct correlation to the cross sectional images. The nature of the network structure would be that of the TiC.

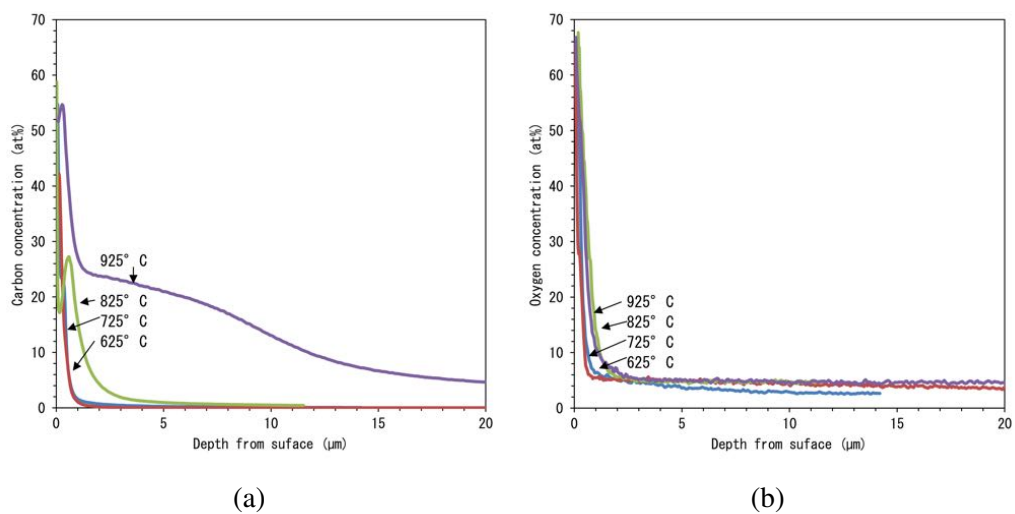


Fig. 5.2: Carbon (a) and oxygen (b) concentration profiles measured by GDOS produced by carburisation at temperatures of : 625, 725, 825 and 925 °C for 20 h

5.1.3 X-ray Diffraction (XRD)

X-ray diffraction analysis (see Fig. 5.3) of the samples treated at 925 °C and 825 °C shows that TiC has been formed. Therefore, the network like structure must mainly consist of

TiC. It is clearly demonstrated via the diffraction data that the samples treated at 925 °C has much more TiC than that treated at 825 °C. Thus, confirming that carbon diffusion happens at a much faster rate when treated at 925 °C. XRD also demonstrates the presence of oxygen within the titanium subsurface. The α -Ti peaks of the untreated samples are shifted to a smaller 2θ angle, showing that lattice expansion has occurred due to oxygen dissolution. This lattice expansion has been observed by numerous authors [100, 134, 165].

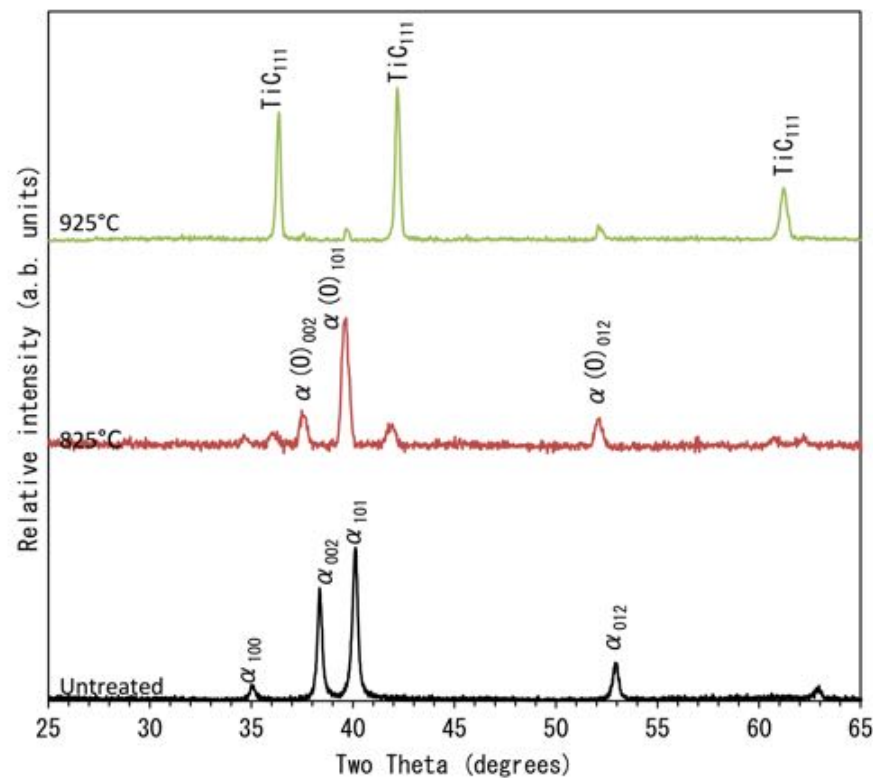


Fig. 5.3: X-ray diffraction patterns generated from samples carburised at temperatures of 825 °C and 925 °C for 20 h against untreated titanium

5.1.4 Tribological Response

5.1.4.1 Friction Behaviour

One of the aims of this study is to improve the tribological response of titanium. Therefore, when characterising a new technique, the tribological performance is of great

importance. All the pack carburised samples were tribologically tested for 1 h under loads of 5 N, 10 N, 20 N and 40 N, until film failure was observed. The coefficient of friction (COF) was recorded and the resulting wear rates were measured. Fig. 5.4 shows the frictional response for the various treatment temperatures at the highest load tested.

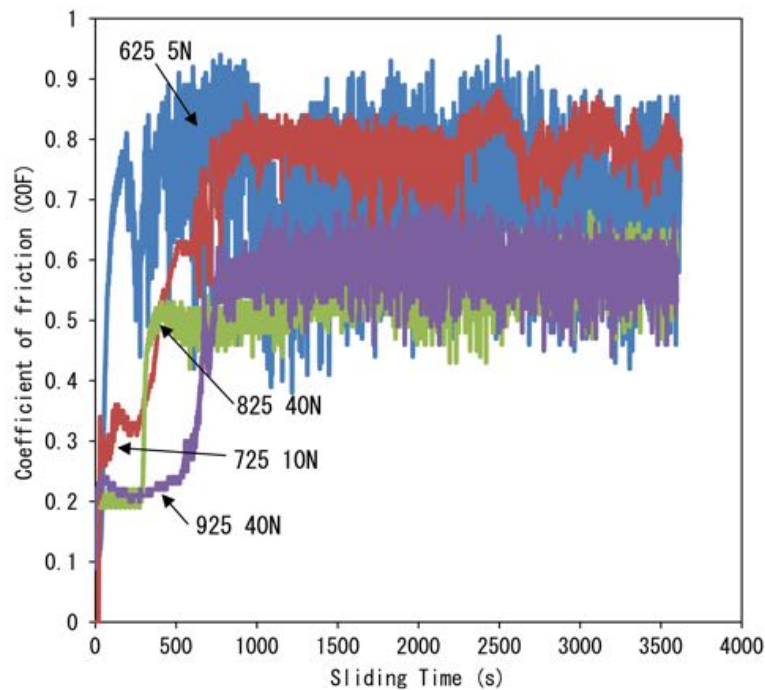


Fig. 5.4: Coefficient of friction (COF) curves recorded for samples pack carburised at 625 °C, 725 °C, 825 °C and 925 °C for 20 h under various loads

Fig. 5.4 shows that titanium treated at 625 °C was not able to withstand a load of 5 N. The COF observed is higher than 0.6 associated with pure titanium and more in-line with that of oxygen rich titanium [100, 184]. Ti treated at 725 °C was able to withstand a load of 10 N for ≈ 600 s, with a low COF ($\mu < 0.4$). There is then a period of ever increasing friction, as the film is removed until the COF reaches 0.8. Again, this COF is consistent with that of oxygen rich Ti. When the temperature was increased to 825 °C the Ti was able to withstand loads of 5 N, 10 N and 20 N. However, when the load was increased to 40 N, the carburised Ti initially responded with a low COF ($\mu \approx 0.3$), but then subsequent film breakdown and removal resulted in the COF increasing to 0.5. The titanium treated at 925 °C was able to withstand a load of 5 N, 10 N and 20 N. When tested under a load

of 40 N, the sample produced low friction ($\mu = 0.2$) for a longer duration than any of the other samples. Both the 825 °C and 925 °C samples had a sudden rise in friction, although they did not reach the same level of COF, as that experienced by samples treated at 625 °C and 725 °C. This could be due to the rate of oxygen diffusion within the titanium substrate. There is a limited oxygen source within the carburising container. Therefore, if the temperature is increased, the rate of oxygen diffusion will be increased, creating a more even distribution of oxygen within its structure.

The low COF observed can be related to the amount of carbon within the titanium (see Fig. 5.2). It is clear that the samples with more carbon diffusion are able to withstand higher loads for longer periods of time. It is interesting to note that the titanium treated using 925 °C has a network like structure (Fig. 5.1d). This feature resulted in the best tribological response of all the samples, with low friction and good adhesion.

5.1.4.2 Wear Rates

The measured wear rates ($\text{mm}^3 \text{m}^{-1}$) as a function of contact load for all the test samples, are shown in Fig. 5.5. Several observations can be made: Firstly, for each test sample, the wear rate increased with increasing load. There is an abrupt rise in the wear rate for all the carburised samples when a critical load was tested. This corresponds with the increased COF observed by the removal of the surface carbide layer film within the wear track. Secondly, as long as wear occurred only in the TiC layer, the COF and wear rate remain very low, 3 to 4 orders of magnitude lower than that of the untreated sample. Finally, when the carbide layer was worn through and wear occurred mainly in the diffusion zone, for example: 5 N, 625 °C; 10 N, 725 °C; 40 N, 825 °C; 40 N, 925 °C, an abrupt increase in both friction and wear occurred.

When carburised Ti is compared to untreated Ti, all carburised samples exhibited lower wear rates, even when the carbide network layer was completely removed at high loads. The hardened oxygen diffusion zone experienced very high and unstable friction in both the 625 °C sample and the 725 °C sample. However, both experienced a reduced

wear rate when compared to CP-Ti. The diffusion zone is effective at reducing wear, this is more pronounced under lower contact loads.

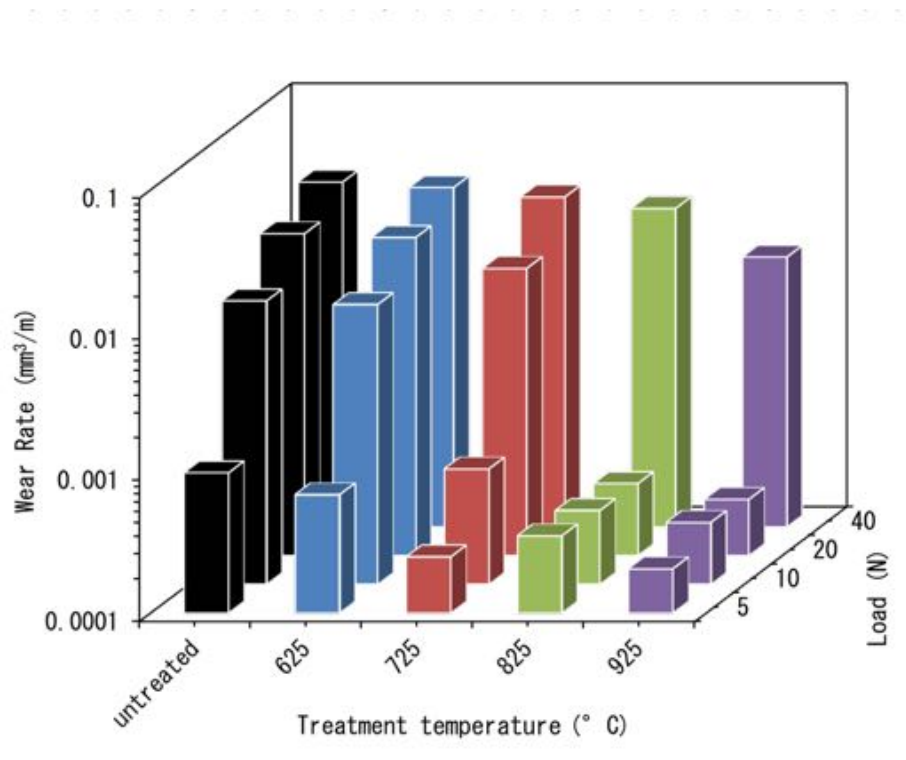
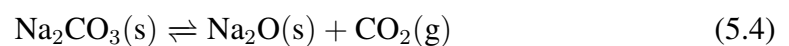
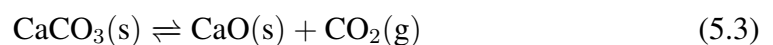
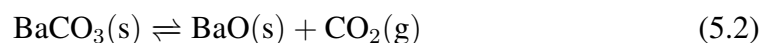


Fig. 5.5: Wear rate of carburised titanium produced at various temperatures and loads

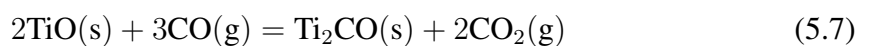
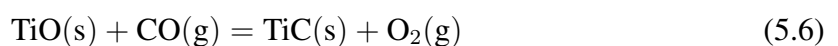
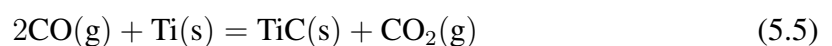
5.1.5 Mechanisms Involved in Producing Optimal Film Performance

During pack carburisation, carbon absorption is not through a solid-solid reaction [146], but through the reaction of carbon monoxide (CO) and the titanium surface. Carbon monoxide is produced through the reduction of carbon dioxide, as shown in the following reactions:



In order for carbon to diffuse in titanium, a constant supply of CO is required. During pack carburising, CO₂ is generated through the thermal decomposition of the carbonates (Eq. 5.2, 5.3 and 5.4). This allows for the constant supply of the CO₂ required for Eq. 5.1 to take place. The decomposition of BaCO₃, CaCO₃ and Na₂CO₃ occurs at temperatures >800 °C [185–188]. The reaction described by Eq. 5.1 will only begin to occur once the temperature exceeds 800 °C. Until a constant supply of CO₂ is created, it would be reasonable to assume that any oxygen within the pack container will react with Ti at the elevated temperatures. Thermal oxidation of titanium is a reaction that proceeds with great vigour at temperatures above 600 °C. Oxidation for a short duration, at temperatures greater than 700 °C can result in large-scale titanium dioxide (rutile) formation [9, 119, 133]. Once all the available oxygen has been exhausted, oxygen diffusion into the subsurface can continuously occur. It has been previously shown by Dong and Li [16] that prolonged heating (in a vacuum furnace) after initial oxidation allows for the creation of a large oxygen diffusion zone, through the reduction of TiO₂. GDOS (Fig. 5.2b) and XRD (Fig. 5.3) analysis, confirms that oxygen diffusion has occurred to form a diffusion zone with a thickness of 200 μm.

The initial oxidation of titanium can impede the rate of carburisation, however TiO₂ itself can be converted into TiC during the carburisation process. This occurs initially through the reduction of the dioxide into suboxides: (Ti₆O₁₁, Ti₅O₉, Ti₄O₇ and Ti₃O₅), then an intermediate oxycarbide (Ti₂OC) phase is observed and then finally the formation of TiC [189]. Thus, once the production of CO is at the required level for carburisation to occur, there are multiple reactions that could take place in order for carbon to react with and to diffuse in the substrate material (Eq. 5.5, 5.6 and 5.7).



The formation of TiC has been shown by XRD analysis (Fig. 5.3). The diffusion of carbon within titanium is dependent on crystal phase, with β -Ti being faster than α -Ti. β -Ti has a pre exponential diffusion coefficient (D_0) of $27.27 \times 10^{-4} \text{ m s}^{-2}$ compared with that of α -Ti of $8.63 \times 10^{-4} \text{ m s}^{-2}$. Clearly, this shows that carbon diffuses much faster into β -Ti. When titanium is carburised at a temperature of 925°C , the β phase would normally be expected. However, using a pack carburisation technique that allows limited oxygen diffusion, would result in stabilisation of the alpha phase, thus, causing an increase in the transition temperature to the β phase. This increase will be dependent on the amount of oxygen present within the titanium substructure. Using the data obtained via GDOS (5.2b) the average amount of oxygen present within the sub structure is 6 at%. Using the Ti-O phase diagram (Fig. 2.19) it can be seen that the transition temperature is $\approx 960^\circ\text{C}$. Therefore, the transition temperature can be discounted as to the reason why increased carbon diffusion occurs at a temperature of 925°C .

Taking into account the decomposition temperatures of the carbonates and the phase transition temperatures of titanium, it is believed that the decomposition of carbonates and the generation of carbon monoxide is the dominating factor in determining the rate of carbon diffusion. When the temperature is below 925°C the rate of carbonate decomposition happens at a slow rate, inhibiting the dissolution of carbon into titanium. Therefore, a temperature around 925°C is required for a fast and effective treatment. Accordingly, further treatments were conducted at 925°C .

5.2 The Effect of Pack Composition on Film Growth

In the previous section it was demonstrated that 925 °C was the most effective temperature for inducing carbon and oxygen diffusion within titanium. It was also shown that the decomposition of the carbonates allowed for the formation of carbon monoxide. This was one of the major contributing factors leading to the the formation of the TiC network structure. The tests in the previous section were carried out using a pack composition of 70 wt% carbon and 30 wt% carbonates. It was shown that the amount of TiC produced was directly related to the wear rate of the treated titanium.

Without increasing the temperature, the only way to increase the rate of carburisation is to increase the amount of carbonates that can decompose to form carbon monoxide (CO). Using the same 20 h duration, the effect of pack composition was investigated. Carbonate percentages of 30%, 40% and 50% were investigated, in the ratio of Barium-carbonate (BaCO_3) 3 part, sodium-carbonate (Na_2CO_3) 2 part and calcium carbonate (CaCO_3) 1 part, as highlighted in Table 5.1.

Table 5.1: Variation in carbon and carbonate percentage used within the pack

Carbon (wt%)	Carbonates (wt%)	Ratio (C: BaCO_3 : Na_2CO_3 : CaCO_3)
70	30	14:3:2:1
60	40	9:3:2:1
50	50	6:3:2:1

5.2.1 Structural Investigation

Cross sectional images of the carburised samples were produced. These images can be seen in Figs. 5.6a, 5.6c and 5.6e for 30%, 40% and 50% carbonate concentration respectively. The etched cross sections show the extent of both oxygen diffusion and creation of TiC. The images indicate that the carburising compound has little, if any,

effect on the rate of oxygen diffusion. Measurements of the ODZ show it has a depth of $\approx 220\ \mu\text{m}$ for all samples. Therefore, the ODZ is independent of and unaffected by the percent of carbonates in the carburising compound.

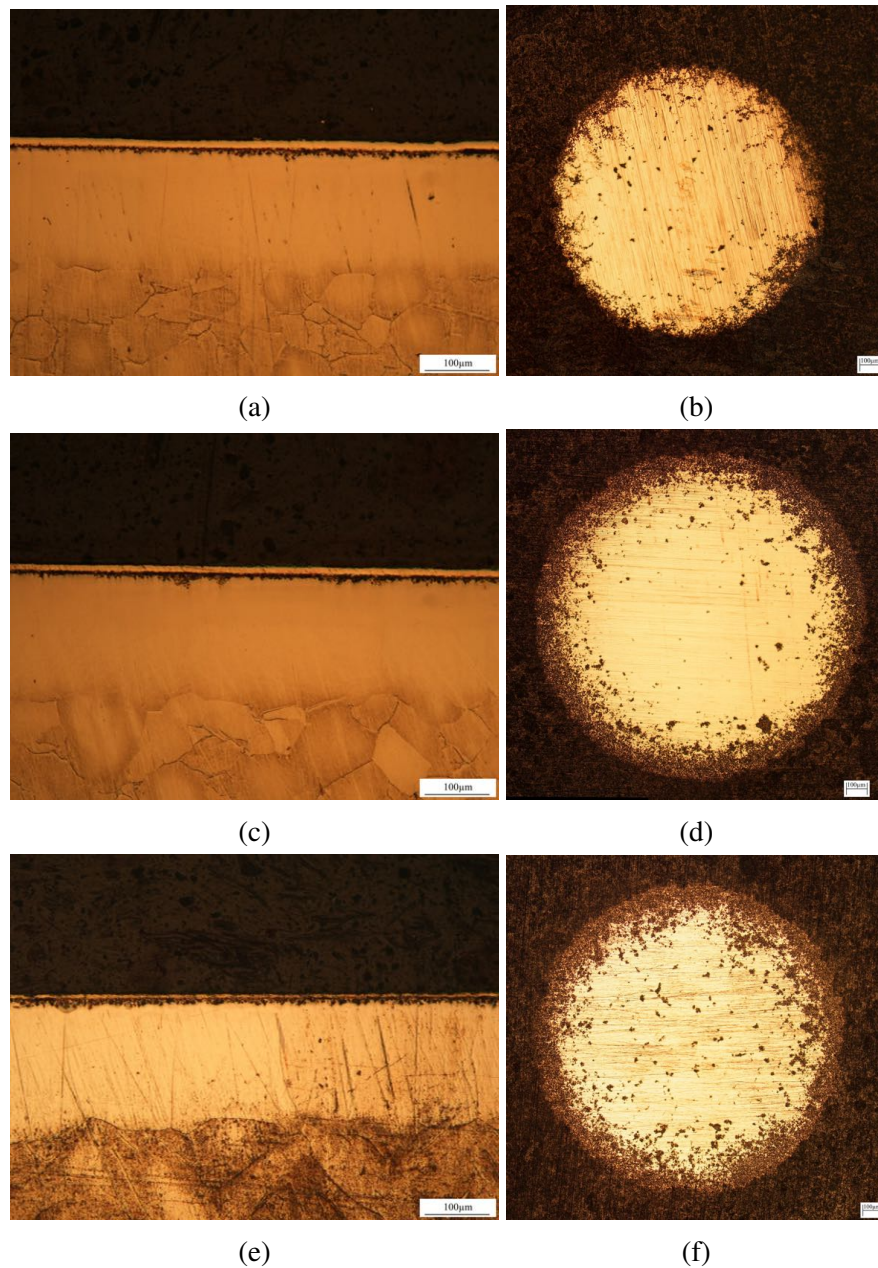


Fig. 5.6: Optical micrographs showing the etched cross sectional morphology and surface ball craters for pack carburised titanium treated at 925 °C for durations of 20 h with pack composition of: 30% (a and b), 40% (c and d) and 50% (e and f)

The ball cratering technique was also carried out to measure the uniformed thickness of the TiC network structure (Figs. 5.6b, 5.6d and 5.6f). Measurements of the TiC

structure taken via ball cratering are displayed graphically in Fig. 5.7. The ODZ measurements from the samples cross sections are also displayed. Fig. 5.7 shows that increasing the carbonate percentage, increases the thickness of the TiC layer. The titanium treated with 1:1 ratio of carbon to energiser produced a TiC layer that was almost twice the thickness ($8.2\ \mu\text{m}$) of that created at using a pack ratio of 7:3 ($4.2\ \mu\text{m}$).

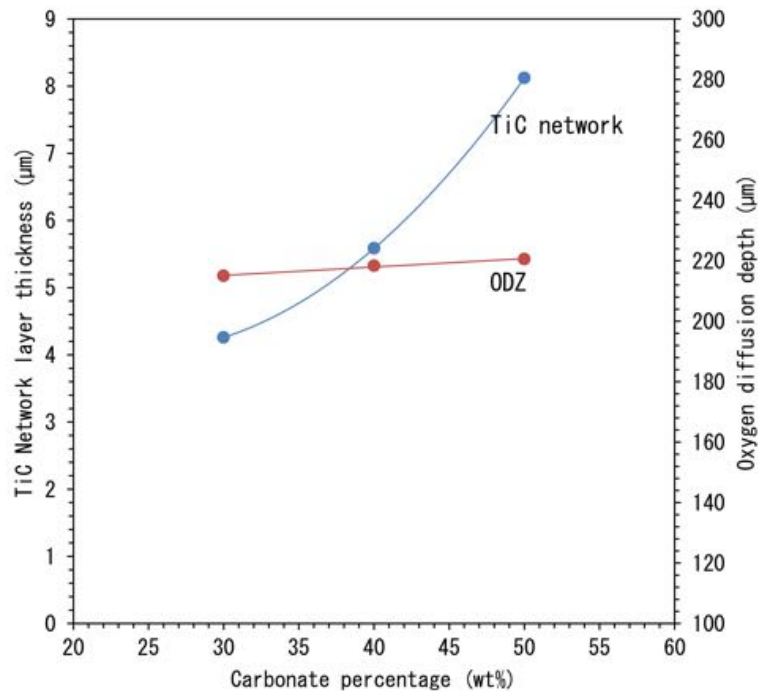


Fig. 5.7: Film thickness of the TiC network and ODZ with regard to the carbonate concentration, at a temperature of $925\ ^\circ\text{C}$ for durations of 20 h

5.2.2 Tribological Response

The samples were then tribologically tested using loads of: 5 N, 10 N, 20 N and 40 N. When the carburised titanium samples were tested using a contact load of 20 N (Fig. 5.8a), the COF for all samples remained low ($\mu < 0.3$). When tested at 40 N (see Fig. 5.8b) it can be seen that the initial friction is very low. However, When Ti is carburised in a pack using a 30% concentration of carbonates, the initial low friction lasts for just 500 s. After the initial low friction zone, breakdown of the TiC network structure occurred, exposing the underlying ODZ and resulting in a high COF. When the concentration of carbonates

is increased to 40% the low COF period is extended and lasts for 1500 s. This is again followed by the high friction of the ODZ. Once the carbonate percentage is increased to 50% the COF remains low for the duration of the test.

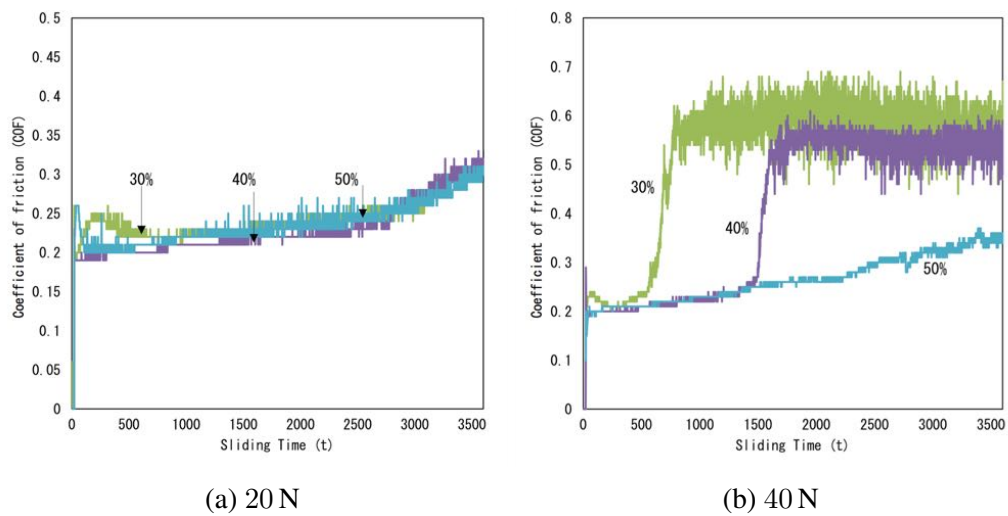
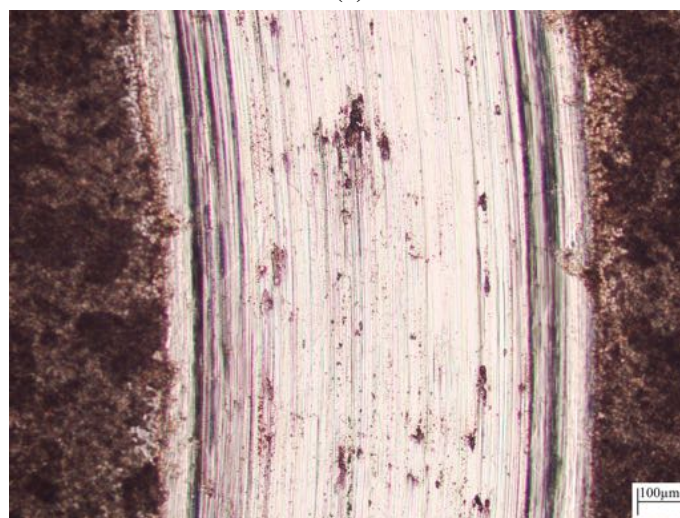


Fig. 5.8: COF curves for the response of PC-Ti (925 °C, 20 h) produced under loads of 20 N (a) and 40 N (b) for various pack compositions

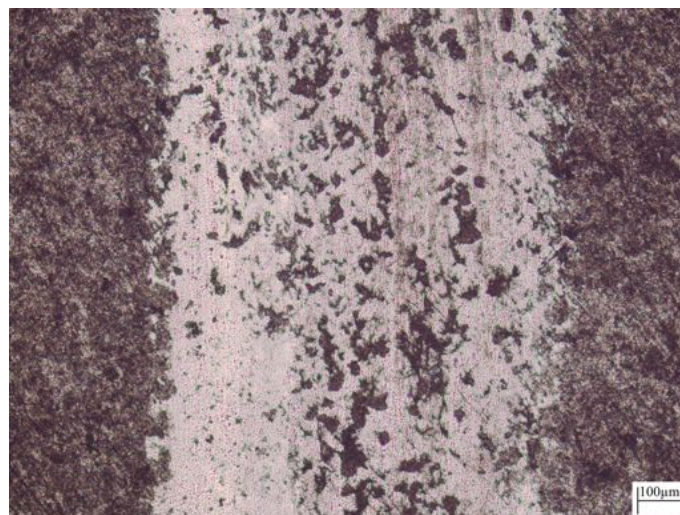
Wear track morphology (See Fig. 5.19) again demonstrates the exposure of the ODZ within the wear track for the samples treated using 30% and 40% pack. Wear within the ODZ has been previously discussed in section 4.2.4. Analysis of the wear track images (Fig. 5.9a and 5.9b) showed wear occurred through oxidative wear and delamination. The ODZ of the pack carburised titanium showed a relatively smooth wear track. This feature is very similar to that of thermally oxidised titanium (Fig. 4.18b). The samples treated in a 50% energised pack (Fig. 5.9c) showed no sign of ODZ exposure. The dominating wear mechanism is that of abrasive polishing.



(a)



(b)



(c)

Fig. 5.9: Optical images showing wear track morphology of titanium carburised at 925 °C for a duration of 20 h with carbonate percentages of (a) 30%, (b) 40% and (c) 50%. All tests were conducted using a 40N load for 3600 s

5.2.2.1 Wear Rates

Fig. 5.10 displays the wear rates recorded when the samples were tested under the different contact loads. It can be seen that all the samples were able to produce extremely low wear rates when tested at loads ≤ 20 N. The data also clearly shows that the samples treated with 50% carbonates were the only samples capable of producing a low wear rate for the duration of the 40 N test. The wear rate backs up what was observed from the frictional traces (Fig. 5.8).

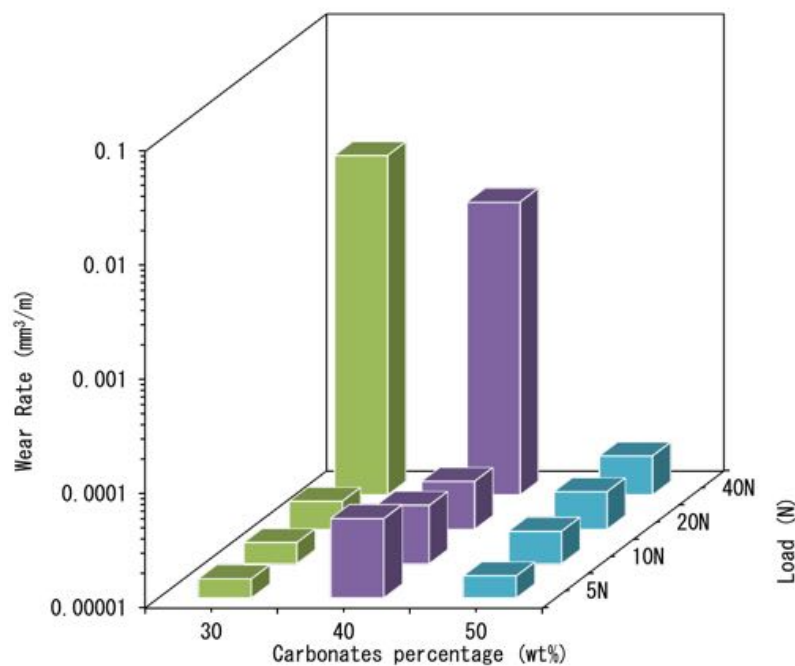


Fig. 5.10: Wear rate of pack carburised titanium (925 °C, 20 h) produced under various loads and after using pack compositions of: 30%, 40% and 50%

When considering the frictional response with regard to the depth of the TiC layer (Fig. 5.7), there is a clear correlation between low friction/wear and the thickness of the TiC network layer. The thicker the TiC network layer, the longer the sample is able to exhibit low friction and wear resistance. Therefore, the extent of the TiC network layer is the determining factor in the generation of low friction and wear.

5.2.3 Optimal Pack Composition

The rate of carburisation is dependent on the amount of CO produced in the carburising vessel, as described in section 5.1.5. The amount of CO produced is dependent on the rate of carbonate decomposition. The decomposition starts to occur readily when temperatures exceeds 800 °C [185–188]. When carburisation was undertaken at a temperature of 925 °C, the decomposition was great enough for substantial CO production, and ultimately resulting in carbon diffusion.

Increasing the amount of carbonates in the pack will increase the amount of CO₂ produced by the carbonates decomposition. Increasing the amount of CO, will result in an increased carbon potential at the surface, as more CO is available to react with the titanium at any one time. Increasing the source concentration will result in increased carbon diffusion (Flick's 2nd law (Eq. 4.1) [130]). Increasing the carbonates concentrations would also allow for the CO supply to be maintained for a longer period of time.

This study demonstrated that by increasing the carbonate concentrations within the pack, allowed for a thicker TiC network layer structure to be produced. When treated at a temperature of 925 °C and for a duration of 20 h, the optimal pack composition was that of: 6 part C, 3 part BaCO₃, 2 part Na₂CO₃ and 1 part CaCO₃. The low COF observed is attributed to the TiC network layer. Therefore, all further tests were conducted using the 1:1 carbon to carbonate ratio.

5.3 The Effect of Carburisation Time on Film Growth

From the previous sections, it has been demonstrated that using a carburisation temperature of 925 °C was the most effective at generating both oxygen and carbon diffusion. Investigation into the carburising compound has also shown that using a pack mixture of 50% carbon and 50% carbonates, in the ratio of: 3 part BaCO₃, 2 part Na₂CO₃ and 1 part CaCO₃ was most effective at producing the TiC network. All tests to this point have been conducted using a duration of 20 h. A full micro-structural characterisation will

now be undertaken, with the effect of carburising duration investigated.

5.3.1 Structural Characterisation

After the carburising treatment, the surface appearance of the CP-Ti samples was changed from polished silver to black. This black surface was due to pack residue and was removed through slight polishing. This cleaned surface was then characterised and tribologically tested.

Fig. 5.11, shows ball-craters made on the surface of the cleaned samples. Ball cratering reveals a network-like structure in the near surface region, which appears dark under an optical microscope.

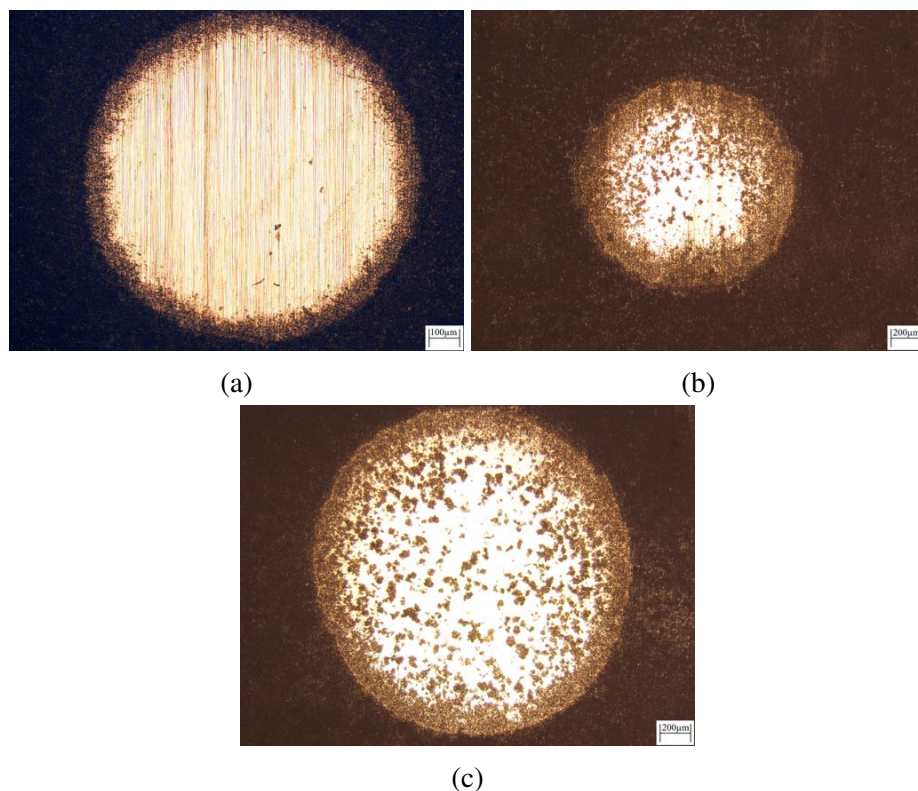


Fig. 5.11: Ball craters made on the surface of pack carburised CP-Ti at 925 °C for: (a) 10 h, (b) 20 h and (c) 40 h, showing the resulting network layer formed on the surface

Etched cross sections were also produced and these are shown in Fig. 5.12, for the 10 h (a), 20 h (c) and 40 h (e) samples. Higher magnification SEM images of the network structures were also taken for the 10 h (b), 20 h (d) and 40 h (f) samples. Using both the ball

craters (Fig. 5.11) and cross sectional data (Fig. 5.12), Table 5.2 was produced showing, network structure depth and oxygen diffusion depth, relative to carburisation time.

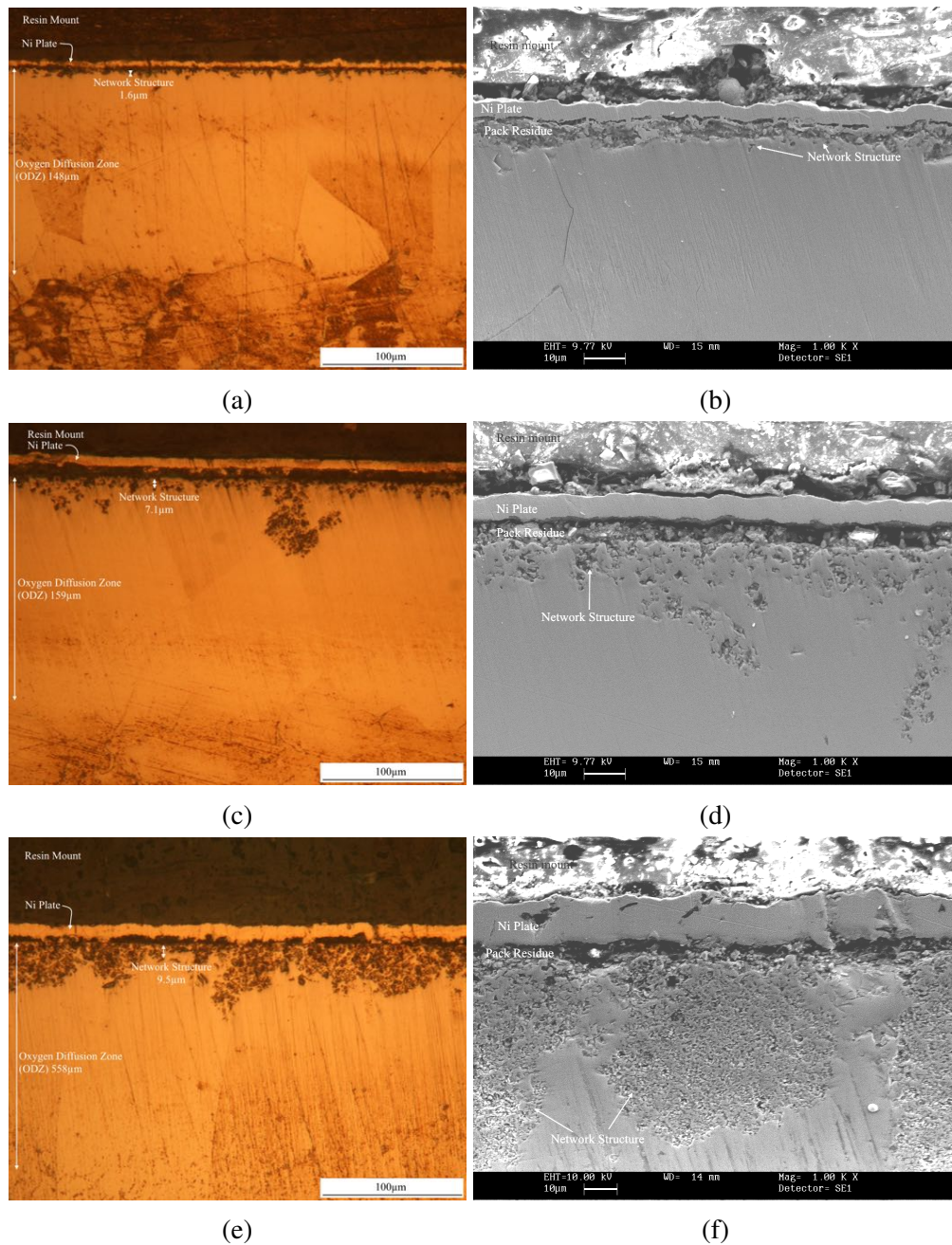


Fig. 5.12: Optical and SEM micrographs showing the cross sectional morphology of pack carburised titanium treated at 925 °C for durations of 10 h (a and b), 20 h (c and d) and 40 h (e and f). Optical images were taken at a magnification of 400X, with SEM images taken at magnification of 1000X

Table 5.2: Summary of the layer thickness developed during pack carburisation

Carburisation duration (h)	TiC network layer depth (μm)	Oxygen diffusion depth (μm)
10	1.6	148.1
20	7.1	159.8
40	9.5	162.7

The TiC network structure measurements displayed in Table 5.2 show the depth at which the network structure offers uniform coverage to the surface. In all the samples, smaller accumulations can be seen extending to further subsurface depths. The density of the network structure decreases with increasing depth from the surface. Below the network layer, there is an oxygen diffusion zone characterised by the stabilised α -Ti. This is due to the dissolution of interstitial elements (O and C), as can be clearly seen in the etched cross-sectional micrographs in Figs. 5.12a, 5.12c and 5.12e. There is no clearly defined boundary between the surface network layer and the underlying diffusion zone for all treated samples. More detailed examination under SEM (Figs. 5.12b, 5.12d and 5.12f) reveals that the network layer contains many dark phases with a crystalline appearance embedded in a metallic matrix connected with the ODZ.

5.3.1.1 EDX and GDOS Composition Analysis

EDX analysis in Fig. 5.13 shows the distribution of Ti (d), C (b) and O (c) for the samples treated for 20 h. These images show that the network structure is carbon-rich and oxygen is distributed evenly throughout the network layer and the adjacent diffusion zone.

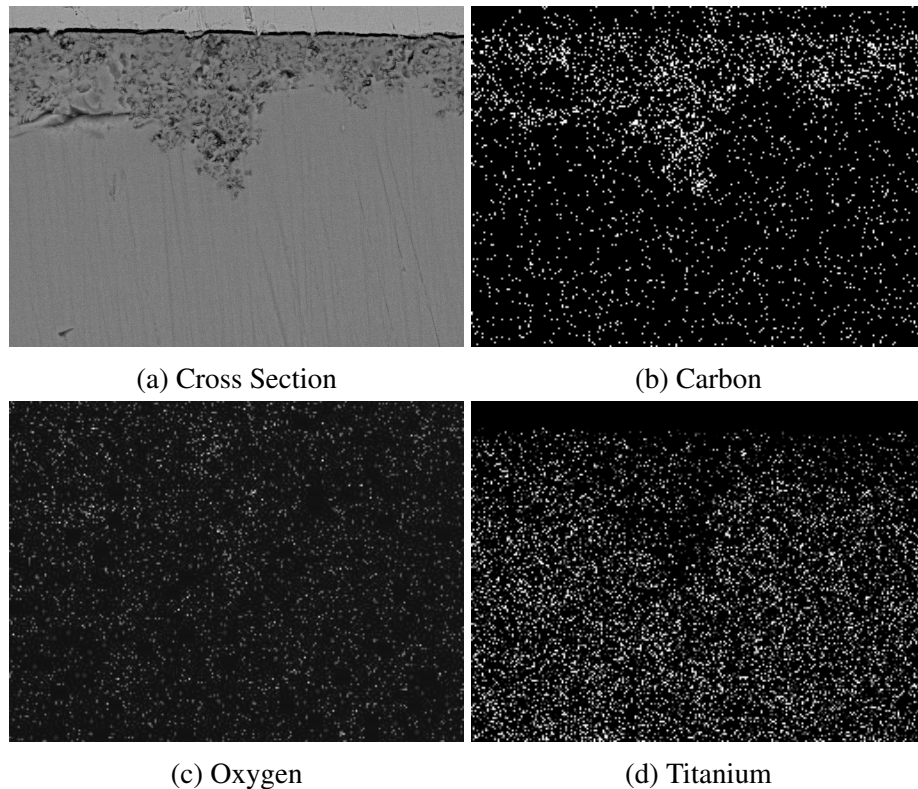


Fig. 5.13: EDX map showing element composition of the carburised cross section (a) with the following elements identified: (b) carbon, (c) oxygen and (d) titanium

This is in direct correlation to the composition profiles measured by GDOS analysis (Fig. 5.14), which shows that carbon concentration is very high at the sample surface and in the subsurface layer. The GDOS data, shows the longer the duration of carburisation, the further the carbon diffuses into the titanium subsurface. Carburisation can continue for prolonged periods as long as there is a sufficient amount of energiser remaining within the pack. Therefore, using a 1:1 ratio of carbon to carbonates allows for the carburisation process to carry on for the duration of 40 h, as demonstrated by the increased diffusion of carbon. The oxygen content is rather uniform throughout the network layer and the upper part of the diffusion zone that can be measured by GDOS profiling. It is interesting to

note that the diffusion zone contains more oxygen than carbon. The diffusion zone is rich in oxygen and this is true for all treatment times.

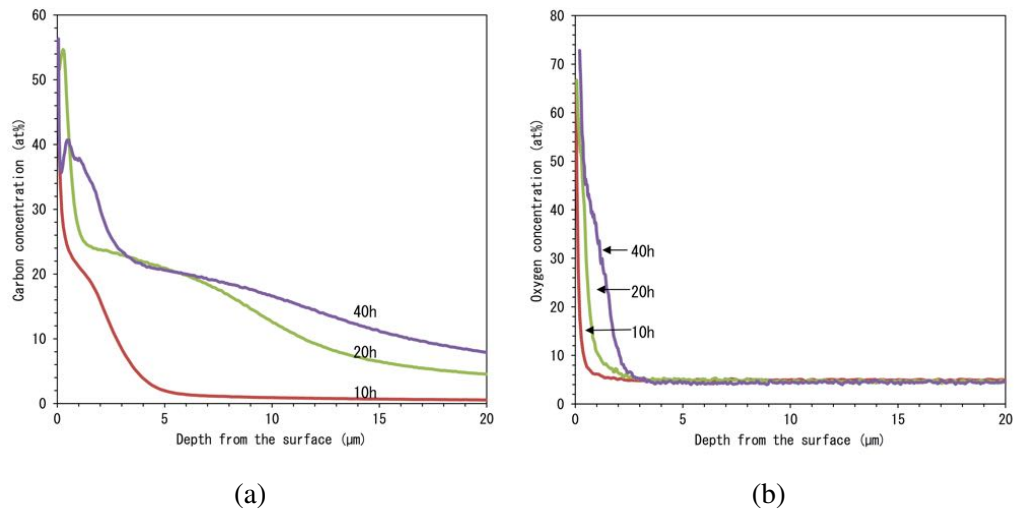


Fig. 5.14: Carbon (a) and oxygen (b) concentration profiles measured by GDOS produced by carburisation at 925 °C for 10, 20 and 40 h

5.3.1.2 X-Ray Diffraction (XRD)

X-ray diffraction (XRD) was undertaken using Cu-K radiation to identify phases present in the carburised samples. Fig. 5.15, shows the X-ray diffraction data for untreated titanium, 10 h, 20 h and 40 h carburised titanium. The diffraction patterns show that the network layer consisted of titanium carbide (TiC). The XRD data also shows the presence of the α -Ti(O), with shifts in the Ti peaks as a result of the lattice expansion from the dissolved oxygen. As carburisation duration is increased, the thickness of the TiC network layer is increased. For the 40 h samples, the X-ray radiation could not penetrate the sample to a sufficient depth to detect the ODZ. This also explains why the peaks for the α -Ti(O) are reduce from 10 h to 20 h.

5.3.1.2.1 Determination of Lattice Constants

The pack carburisation process resulted in the production of a network structure, this network has been shown to be rich in carbon (Fig. 5.14), with XRD confirming the presence of TiC (Fig. 5.15). By calculating the precise lattice parameters, it is possible

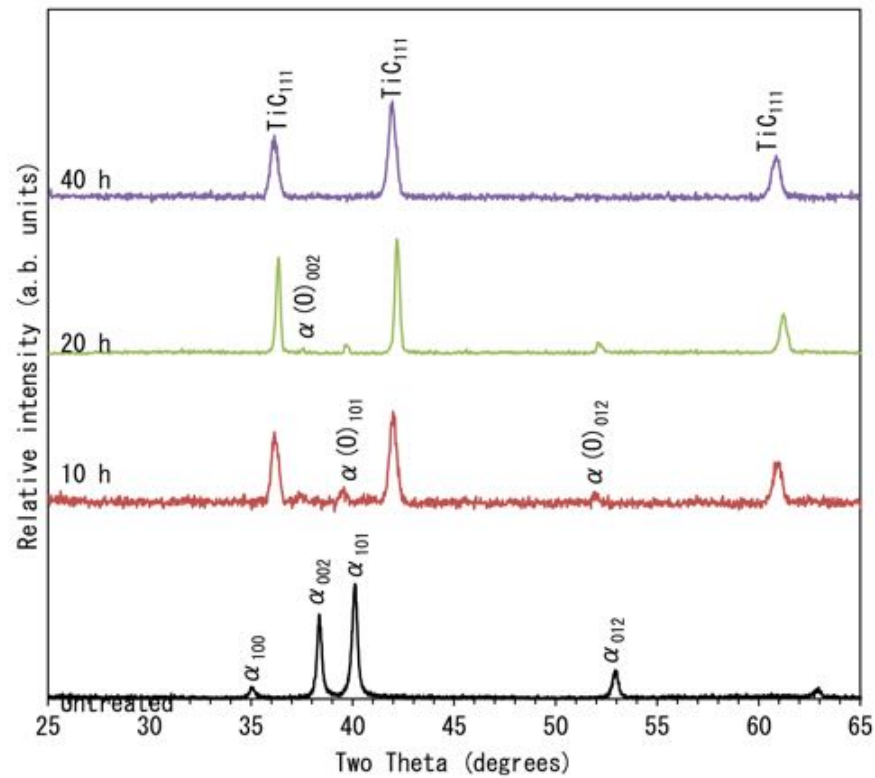


Fig. 5.15: X-ray diffraction patterns generated from the carburised samples produced at 925 °C for 10 h, 20 h and 40 h

determine whether the TiC phases present are stoichiometric. Deviation from standard lattice parameters ($a = 4.38 \text{ \AA}$) would suggest the presence of carbon vacancies or the incorporation of oxygen within the TiC structure. This would result in the formation of binary and tertiary solid solutions over a wide range of homogeneity. The solid solutions can be considered as Ti(CO) mixed crystals [89].

Along with the carburised surface layer, oxygen diffusion has also been demonstrated. This increased oxygen concentration within the HCP crystal structure will cause small changes to the lattice parameters. The c/a ratio for titanium is 1.58, this is much less than ideal for an HCP crystal structure ($c/a = 1.633$). The incorporation of oxygen in the ODZ should result in an expanded crystal structure with a c/a closer to that of ideal.

Using the XRD data displayed in Fig. 5.15, the lattice parameters of TiC phase can be evaluated using Eq. 5.8. The precise lattice parameters of the near surface ODZ can be

calculated using Eq. 4.2 (page 93) [130].

$$d_{hkl} = \frac{a}{h^2 + k^2 + l^2} \quad (5.8)$$

Where a , b and c are the lattice parameters of the crystal, (hkl) are the corresponding miller indices of the lattice planes and $d_{(hkl)}$ is calculated by Eq. 3.1 on page 72.

Table 5.3, shows all the calculated lattice constants of α -Ti(O) and TiC produced during carburisation at 925 °C as a function of time. The standard lattice spacing for untreated titanium and titanium carbide has also been shown for comparison purposes. The data in Table 5.3 shows that the TiC phases present are very close to that of pure titanium carbide and is consistent for all durations of carburisation. The slight deviation from the standard, suggest some incorporation of oxygen into the TiC lattice. The atomic radius of oxygen (60 pm [190]) is smaller than that of carbon (70 pm [190]), thus any oxygen substitution within the TiC lattice would reduce the lattice spacing.

Table 5.3: Calculated lattice constants of α -Ti(O) and titanium carbide as a function of carburisation time compared to JCPDS standards. All carburisation was undertaken at a temperature of 925 °C with a pack composition of 6:3:2:1

Carburisation time (hour)	Lattice Parameters			TiC a (Å)
	a (Å)	$\alpha / \alpha(\text{O})\text{-Ti}$ c (Å)	c/a	
Standard	2.95	4.69	1.588	4.38
10	3.01	4.81	1.59	4.30
20	3.00	4.79	1.59	4.30
40	-	-	-	4.30

Oxygen diffusion within the carburised samples, resulted in expansion in the HCP crystal structure. α -Ti could not be identified in the 40 h sample as the TiC layer was much thicker and the X-ray radiation could not penetrate far enough into the samples. The observed expansion is slightly lowered as the temperature increases. This is due to the migration of oxygen through the titanium as the time increases, and the oxygen will be more evenly distributed through the structure. This is due to the non-infinite source of

oxygen within the carburising container.

5.3.1.3 Cross-sectional Hardness Profiles

Micro-hardness testing (Fig. 5.16) shows that the surface region with network TiC structure is very hard, with hardness in the region of 2100 HV, which is as expected for TiC [11, 19].

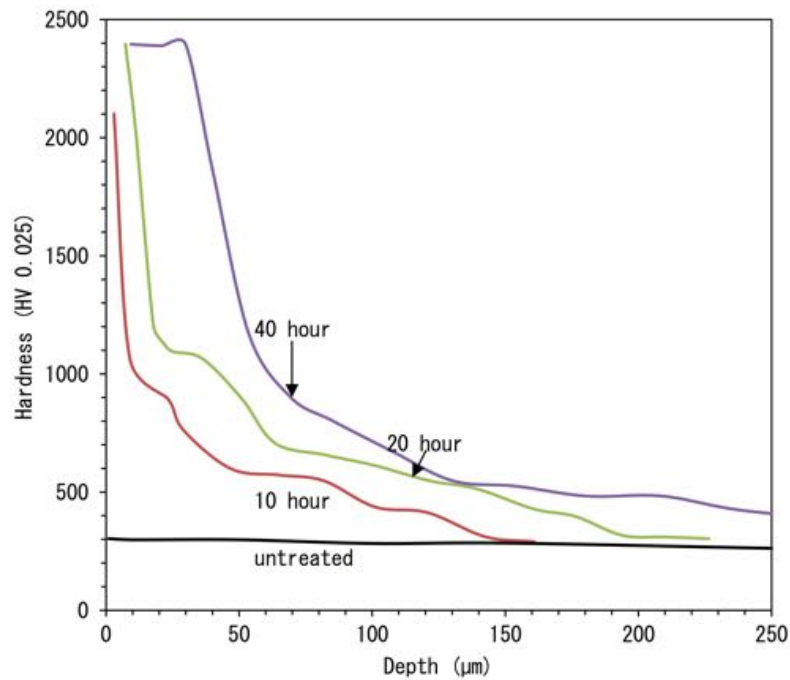


Fig. 5.16: Cross sectional hardness profiles for the carburised samples produced at 925 °C for 10 h, 20 h and 40 h

The surface hardness is dependent on the thickness of the TiC layer as for longer durations the higher hardness is present until much further depths. The TiC network accumulations also contribute towards the much higher subsurface hardness. This is demonstrated by the 40h sample. Fig. 5.12f shows the increased carbide accumulation in the subsurface. These accumulations allow the hardness to remain very high until a depth of $\approx 30\mu\text{m}$. There is then a sharp reduction in hardness from 2100 HV to 1000 HV across the network layer, obviously, due to the reduction in the amount of TiC phase with depth. This is followed by a gradual decline in hardness across the

oxygen diffusion zone from 1000 HV to that of untreated titanium (300 HV). Hardness profiles successfully demonstrate that a thick, oxygen diffusion zone of about 200 μm was successfully produced. Increasing the carburisation time allowed for deeper oxygen diffusion into the titanium substructure. The large ODZ is beneficial for increased load bearing capacity. The carburised structure identified for all durations is multi-layered, with a TiC network structure and $\alpha\text{-Ti(O)}$ diffusion zone. The duration of the process affects the thickness of each structural zone with both the ODZ and TiC network structure increasing in thickness, with increasing duration.

5.3.2 Tribological Response

The carburised samples were tribologically tested under dry conditions against an Al_2O_3 counter-face. All samples were able to last for 1 h under loads up to 20 N, with very little wear (Fig. 5.17) and a constant low COF of 0.2 (Fig. 5.18).

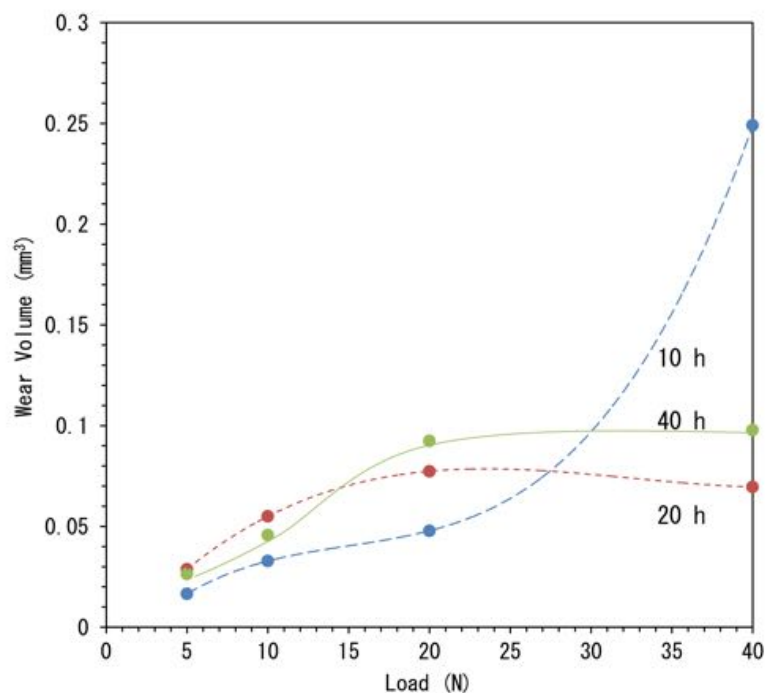


Fig. 5.17: Wear volume data for PC-Ti produced at 925 °C for 10 h, 20 h and 40 h under various loads

Fig. 5.18 displays the coefficient of friction (COF) curves recorded under a contact

load of 40 N. The results again demonstrate that the carburisation process creates a low and stable COF. The duration of carburisation has little effect on the initial frictional response of the treated samples. However, after 3000 s the samples treated for 10 h starts to show increased friction. This can be attributed to breakdown of the TiC network structure. For both the 20 h and 40 h samples there was no such obvious breakdown of the TiC network layer, with both lasting the duration of the test. When comparing the tribological response with the structural characterisation of treated samples, we can see that there is a direct correlation between the thickness of the TiC network layer and the low friction observed during wear testing.

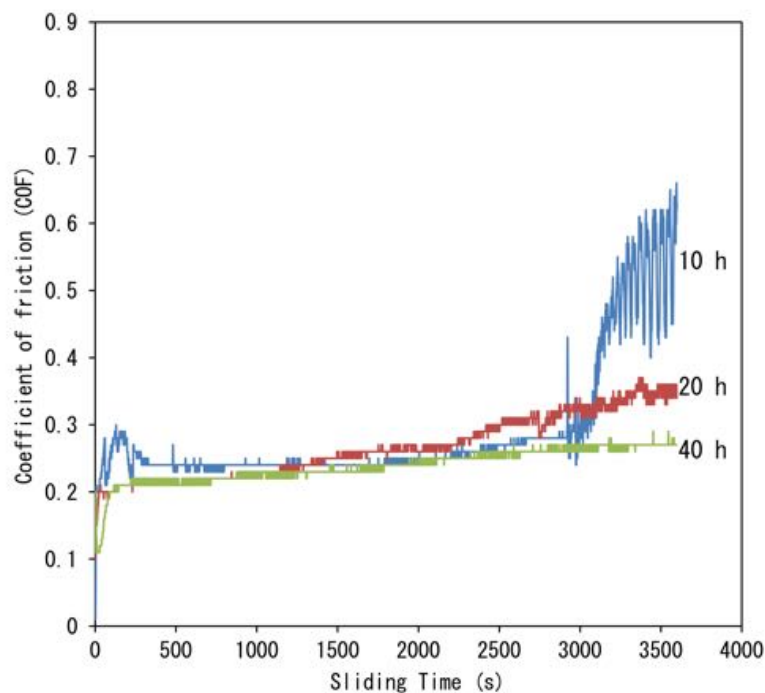


Fig. 5.18: COF curves for PC-Ti produced at 925 °C for 10 h, 20 h and 40 h under a contact load of 40 N

Wear track morphology shown in Fig. 5.19 again demonstrates the effect of the carburising process. The samples treated for 20 h and 40 h have very little wear, with the dominating mechanism being that of simple polishing abrasion. This is highlighted by the smooth finish in the wear track of the 20 h and 40 h samples. When comparing the wear track morphology of the 10 h (Fig. 5.19a) sample with that of the 20 h (Fig. 5.19b)

and 40 h (Fig. 5.19c) samples, it can be seen that the breakdown of the TiC structure within the wear track allows for the exposure of the ODZ to become the dominating factor determining the COF and wear rate. The mechanisms change from polishing of the TiC film to delamination of TiC and abrasive wear of the exposed ODZ.

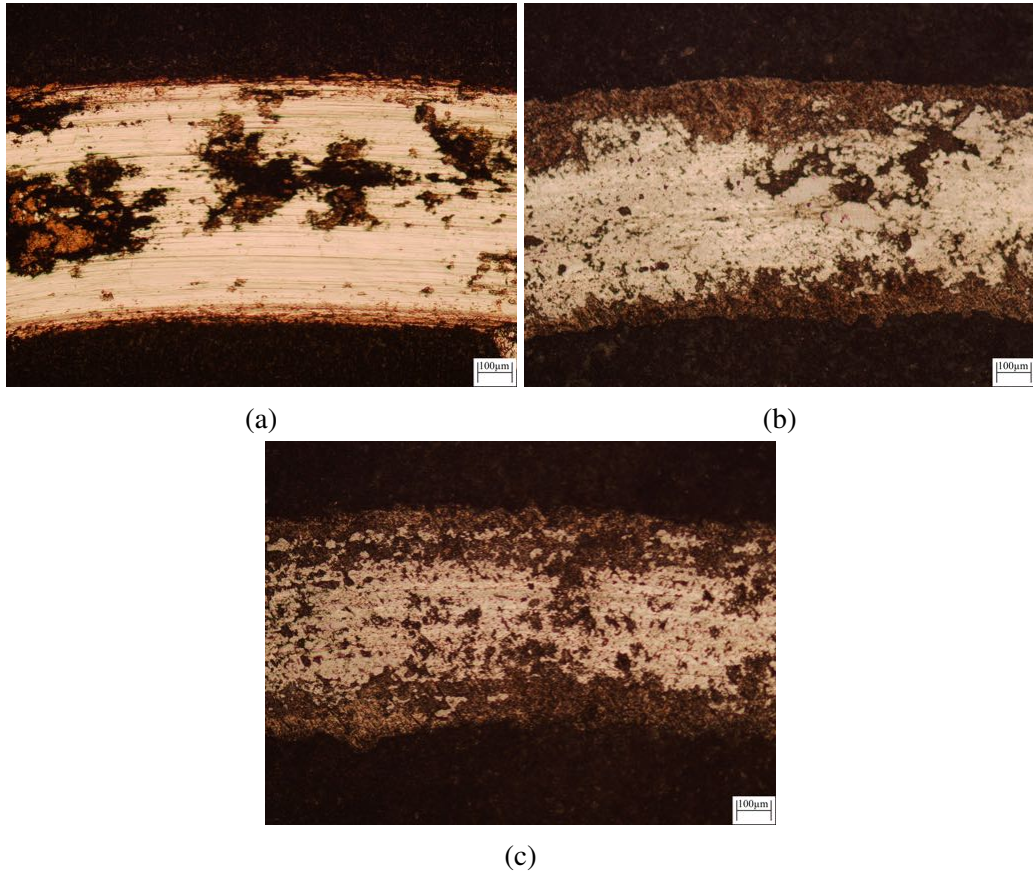


Fig. 5.19: Optical micrograph images showing wear track morphology of titanium carburised at 925 °C for durations of (a) 10 h (b) 20 h and (c) 40 h and tested under a 40N load for 3600 s

Increased carburising time produced a thicker TiC network layer. The longer the layer remains present with the contact zone, the longer the low friction will be observed. Thus, increased carburising time allows or increased carbon diffusion into the titanium subsurface, as demonstrated via GDOS (Fig. 5.14). Increased carbon diffusion allows for a thicker layer of TiC to form. This is demonstrated by the the cross sectional images (Fig. 5.12). The TiC is responsible for the low COF observed during the wear test.

5.3.3 Duration Optimisation

The amount of CO produced within the carburising vessel has a drastic effect on the amount of TiC produced. The duration of the process is also a key parameter in determining the depth and uniformity of TiC network layer. The amount of TiC directly correlates to the duration of the carburising process. Longer duration carburisation resulted in greater carbon diffusion and thus, a thicker more uniformed TiC network layer.

All tribological tests carried out on the treated titanium showed that frictional response is directly related to the amount of TiC at the surface of the samples. The TiC network layer is responsible for producing a low COF ($\mu = 0.2$) when sliding against Alumina. When titanium was treated for a duration of 10 h, the film thickness was not sufficient to withstand 40 N for 1 h without breakdown. However, the samples treated for 20 h and 40 h were able to withstand a 40 N load for 1 h with no film breakdown. The TiC network layer was worn via simple abrasion. Therefore, the low friction will last as long as the TiC network remains uniformed and in-tacked.

Using pack carburisation with oxygen diffusion, the duration of the treatment must be tailored to the application. Using a pack composition of: 6 part C, 3 part BaCO₃, 2 part Na₂CO₃ and 1 part CaCO₃ at a temperature of 925 °C the duration affects the thickness of the TiC network layer. Therefore, depending on application, the carburisation duration must be controlled to generate the desired protection in the most efficient and economical way.

Chapter 6

Results and Discussion

Tribological, Corrosion and Tribocorrosion Behaviour of Pack Carburised CP-Ti with Oxygen Diffusion

Chapter 5 demonstrated the optimal conditions to successfully pack carburise Ti with oxygen diffusion (PC-Ti). The duration of this process determines the effective thickness of a wear reducing TiC network structure when using a temperature of 925 °C and a pack consisting of: 6 part C, 3 part BaCO₃, 2 part Na₂CO₃ and 1 part CaCO₃.

Pack carburisation with oxygen diffusion produces a multilayered structure, consisting of a TiC network, with an extended α -Ti(O) diffusion zone. In this chapter, this multilayered structure was generated using the optimised parameters, i.e. 925 °C for 20 h. This allowed for the substantial carbon diffusion to occur. The tribological, electrochemical and tribocorrosion characteristics of the pack carburised Ti were then investigated.

6.1 Tribological Response

6.1.1 Unlubricated Sliding friction

When PC-Ti is tribologically tested in dry conditions for extended durations, there is a peculiar friction behaviour. The COF curves for the carburised Ti tested for 10 h under a contact load of 20 N is displayed in Fig. 6.1a. Four frictional zones can be identified, each with its own characteristics as illustrated in the figure and elaborated in more details below. These frictional zones are very similar to those observed when titanium was thermally oxidised (see Section 4.2.1).

Fig. 6.1b shows wear volume recorded using a Mitutoyo SJ-400 stylus profilometer. These correspond to each frictional zone observed in Fig. 6.1a. SEM images of each wear track zone are observable in Fig. 6.2, which shows the wear mechanisms involved in each zone identified.

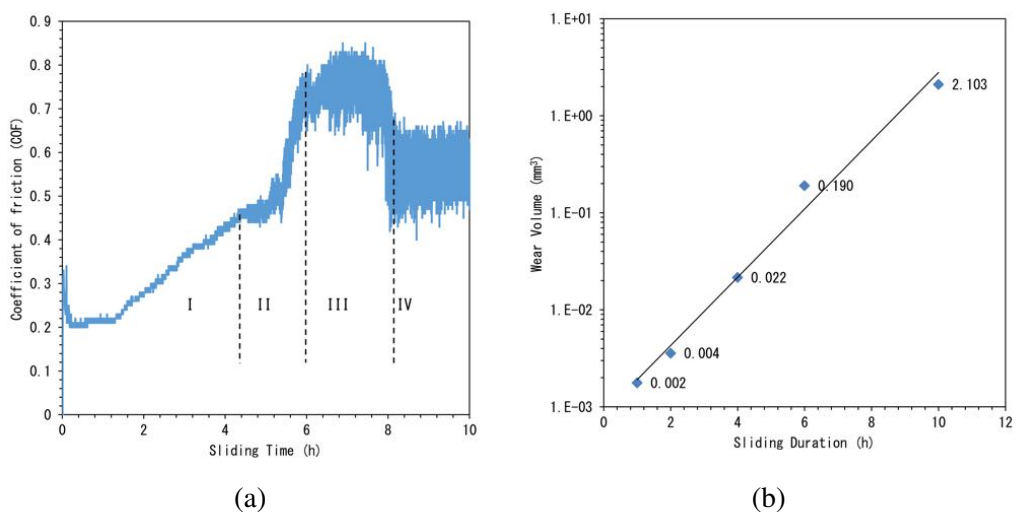


Fig. 6.1: (a) The four zones observed in a typical friction curve of pack carburised titanium. I: Titanium carbide layer; II: partial removal of carbide layer; III: oxygen diffusion zone; IV: substrate. (b) Wear profiles associated with each frictional

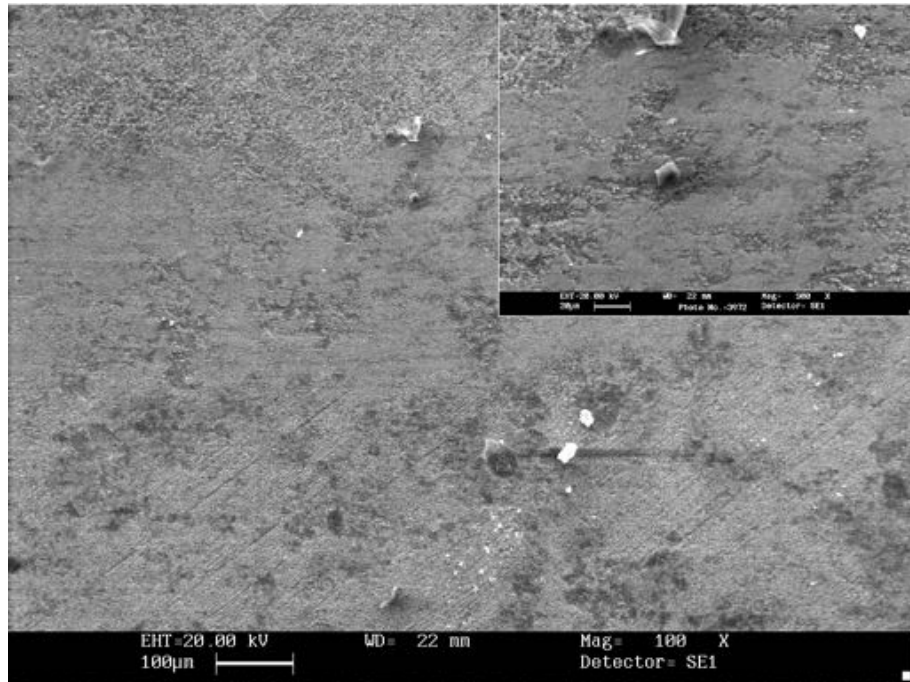
Zone I is characterised by a low and smooth COF and is associated with the TiC network layer in contact with the alumina slider. When tested for short durations, e.g. 1 h, zone I is observed throughout the test duration because wear only occurred in the TiC network

layer. The principle wear mechanism involved is micro-polishing of the TiC network layer by the alumina slider (Fig. 6.2a).

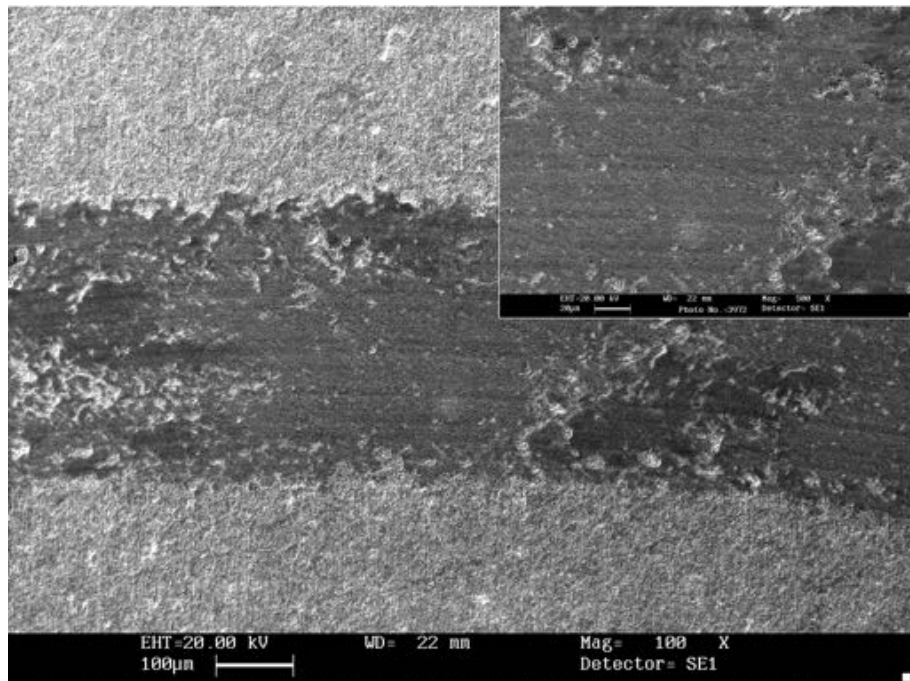
Zone II is the transition zone arising from the partial wearing through or partial failure of the TiC network. Fig. 6.2b is an SEM image showing the wear track morphology produced in Zone II. It can be seen that the TiC network was partially worn through exposing the ODZ. This suggests that the COF increase is due to the gradual wearing through of the TiC network, indicating excellent adhesion with the diffusion zone.

Zone III arises from the contact between the slider and the ODZ. This is characterised by COF values even higher than that of the untreated sample. In this zone, the TiC network layer was removed completely from the wear track. The duration of this zone depends on the ODZ thickness and contact load. SEM images reveal that the wear track has a dark appearance with many craters, as seen in Fig. 6.2c. The wear track image shows large amounts of oxidative wear, with many patches of dark oxide films, presumably formed during sliding due to the high frictional heating. The oxide film made real contact with the slider and was then delaminated to form wear debris. This is the same mechanism observed for TO-Ti (Section 4.2.1).

Zone IV denotes the wearing through of the ODZ and the contact between the slider and the substrate CP-Ti, such that the COF becomes similar to that of the untreated Ti. The wear track produced in zone IV has a typical worn Ti morphology, shown in Fig. 6.2d. This has a rough metallic appearance typical of metallic wear, dominated by abrasion, with patches of adhesion and delamination (see inset).

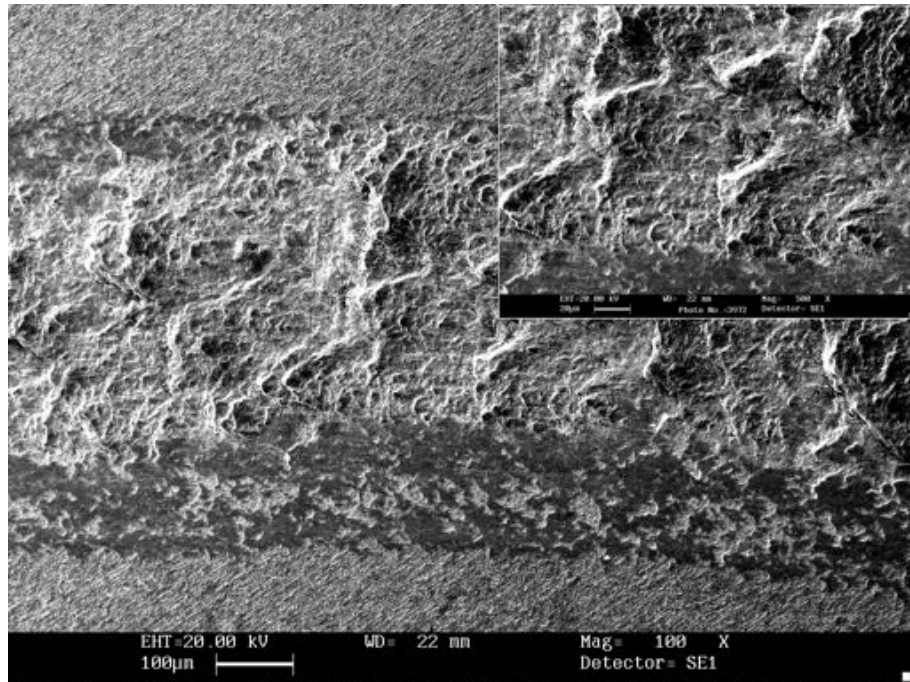


(a)

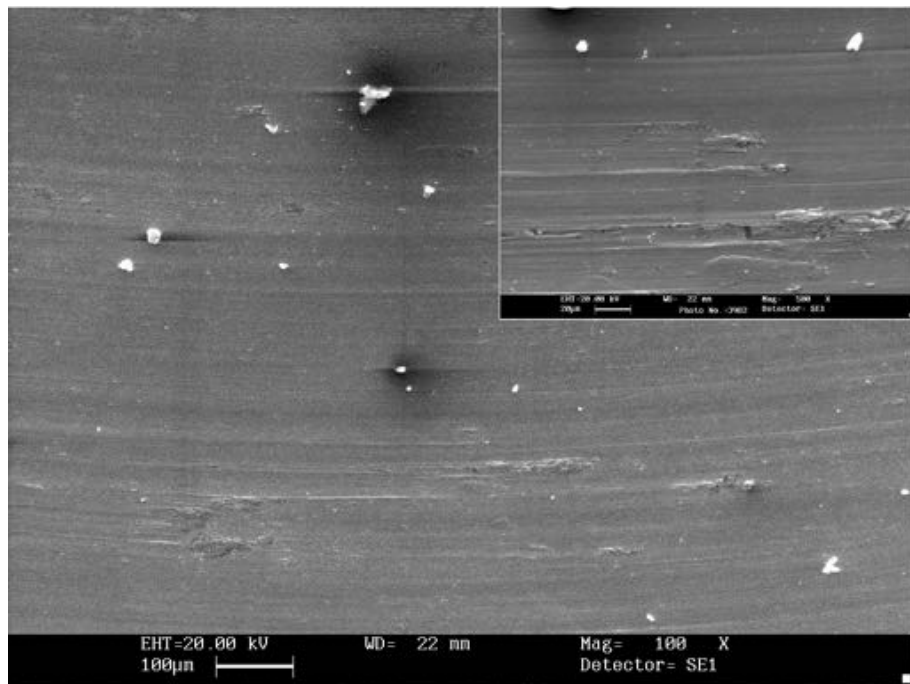


(b)

Fig. 6.2: SEM images showing morphology of the wear track produced on the 925 °C/20 h carburised sample, under a contact load of 20 N for (a) 3600 s corresponding to Zone I in Fig. 6.1a; (b) 14 400 s corresponding to Zone II in Fig. 6.1a; (c) 21 600 s corresponding to Zone III in Fig. 6.1a; and (d) 36 000 s corresponding to Zone IV in Fig. 6.1a



(c)



(d)

Fig. 6.2: SEM images showing morphology of the wear track produced on the 925 °C/20 h carburised sample, under a contact load of 20 N for (a) 3600 s corresponding to Zone I in Fig. 6.1a; (b) 14 400 s corresponding to Zone II in Fig. 6.1a; (c) 21 600 s corresponding to Zone III in Fig. 6.1a; and (d) 36 000 s corresponding to Zone IV in Fig. 6.1a

6.1.2 Lubricated Sliding Friction

Titanium is known for its poor response to lubrication. Generally lubricants are ineffective at reducing friction and wear. However, by changing the surface characteristics, it is possible to use lubrication to prolong the life of treated components. The effectiveness of lubrication on the PC-Ti was investigated. Fig. 6.3 shows the frictional response of PC-Ti in Mineral oil (10W40) for 30 h, under a load of 20 N.

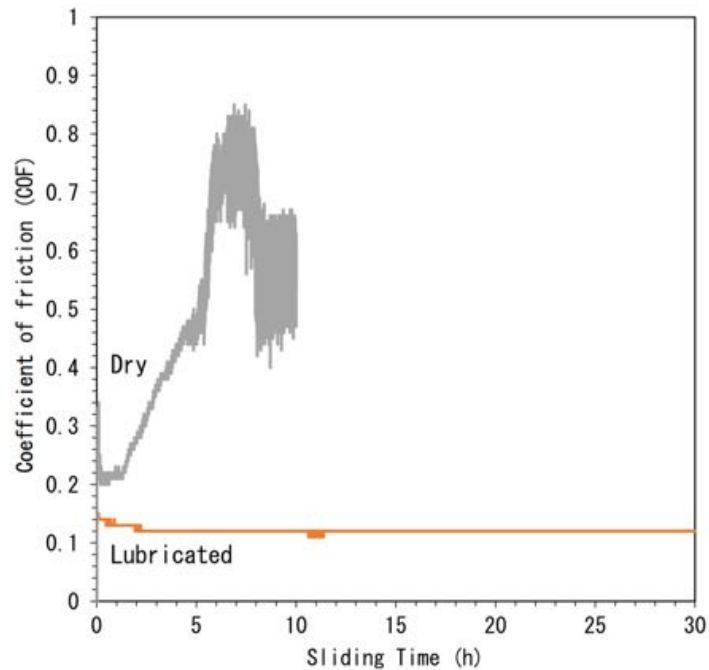


Fig. 6.3: Coefficient of friction (COF) curves recorded at a contact load of 20 N for the PC-Ti in lubricated and un-lubricated conditions

Fig. 6.3 shows that under lubrication, the COF remains fixed at 0.12 with very little variation. The COF is significantly lower than the 0.2 observed during dry sliding. Under dry conditions, the TiC network layer is fully removed from the wear track within 4 h. Lubrication allows for the TiC network layer to be preserved within the wear track for a much greater duration. The wear track ball crater image, shown in Fig. 6.4, shows no sign of significant wear. The wear track morphology is of a smooth, polished surface.

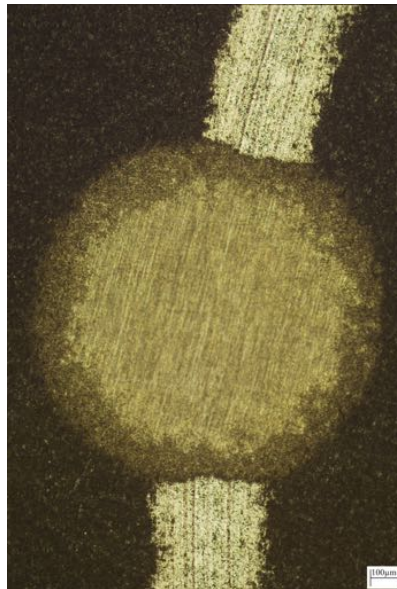


Fig. 6.4: Ball crater and wear track morphology produced at a load of 20 N under lubricated conditions on PC-Ti

6.1.3 Tribological Comparison Between Pack Carburised Ti, Thermally Oxidised Ti and AISIS 440C Stainless Steel

6.1.3.1 Frictional Response

In order to understand the benefits of the carburising treatment, further dry sliding tests were conducted, using various comparable materials. Fig. 6.5 shows the frictional response of: untreated CP-Ti, carburised CP-Ti (CP-Ti), thermally oxidised CP-Ti (TO-Ti) and bearing steel (AISI 440C), all under a 20 N load against an Al_2O_3 counter-face. Bearing steel was chosen, as it is a martensitic steel with a very high carbon concentration and is therefore, a good comparison to case hardened steel. This allows the carburised titanium to be compared with a common engineering material used in high load bearing tribological situations [191–194]. It is clear from Fig. 6.5 that the new carburising treatment offers much improved frictional behaviour over the other samples tested. The carburised sample exhibits low and stable friction unseen in any of the other samples tested.

The low friction and high load bearing capacity of the carburised sample can be

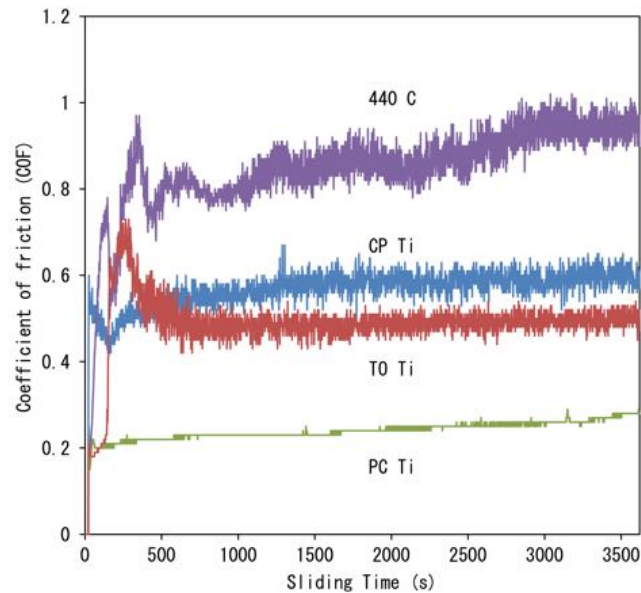


Fig. 6.5: Coefficient of friction (COF) curves recorded at a contact load of 20 N for: Untreated Ti, thermally oxidised Ti (625 °C for 72 h), carburised (925 °C for 20 h) and AISI 440C stainless steel

attributed to the layered structure, comprising a network TiC layer and a thick ODZ, with no clearly defined boundary between the two zones. The resulting structure offers some very positive tribological characteristics, with friction coefficients of around 0.2, compared with those of untreated (COF = 0.6) and thermally oxidised titanium (COF = 0.2-0.5). It is observed in Fig. 6.5 that the carburised sample is able to withstand loads that would cause total film spallation in TO-Ti. This issue of oxide film spallation in TO-Ti is well documented [9, 10, 100, 195]. Clearly, the carburised samples suffer no such film failure.

6.1.3.2 Wear Rate

The material loss from the wear track was measured using a Mitutoyo SJ-400 stylus profilometer, which was then normalised with the total sliding distance to obtain specific wear rate (in $\text{mm}^3 \text{m}^{-1}$). The results are displayed in Fig. 6.6 as a function of applied load for all the materials tested.

From Fig. 6.6, it can be seen that wear rates of the carburised sample are much lower

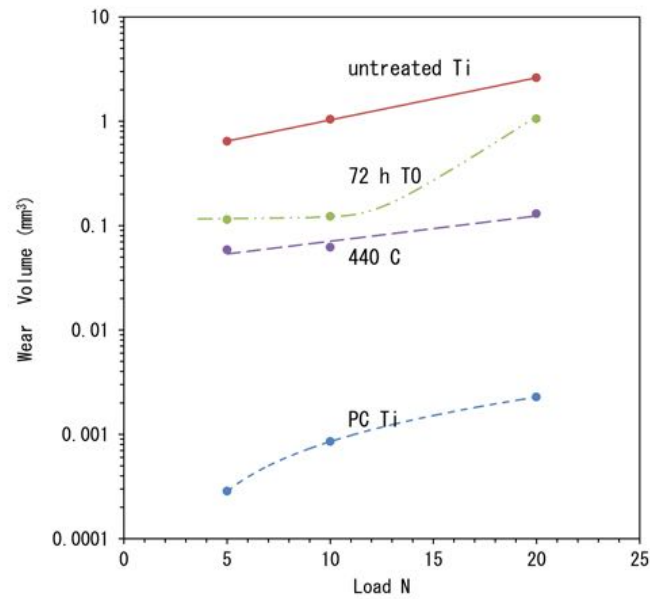


Fig. 6.6: Measured wear rate as a function of applied load for: Untreated Ti, thermally oxidised Ti (625 °C for 72 h), carburised (925 °C for 20 h) and AISI 440C stainless steel

than those of untreated and thermally oxidised titanium (by an order of 3). This is a significant reduction in wear and correlates with the reduced friction shown in Fig. 6.5 and coincides with the smooth wear track morphology displayed in Fig. 6.2a. The wear rate of the carburised sample increases gradually as the load is increased, demonstrating a controlled and predictable material loss rate depending on the applied load. This is in contrast to TO-Ti, which shows decreasing effectiveness as the load is increased. This is a symptom of oxide film spallation and the wearing-through of the relatively thin (15.5 μm) ODZ [100].

Another key point shown in Fig. 6.6 is the comparison between the PC-Ti sample and the AISI 440C sample. It is seen that the wear rates of the carburised titanium are two orders of magnitude lower than those of the hardened bearing steel. Under dry sliding conditions, it is clear that this pack carburising treatment with oxygen diffusion offers a surface, which performs even better than hardened steel under high load bearing sliding conditions. This again can be attributed to the favourable combination of the network TiC layer with a thick oxygen diffusion zone.

6.2 Electrochemical Behaviour as a Function of Depth from the Carburised Surface

6.2.1 Potentiodynamic Behaviour

Fig. 6.7 shows anodic polarisation curves for the PC-Ti at various depths from the as-carburised surface. This correlates to different amounts of carbon and oxygen within the subsurface. The polarisation curves show that the TiC network layer (surface - 10 μm) results in an anodic shift in the free corrosion potential to $-200 \text{ mV}_{\text{SCE}}$ from $\approx -500 \text{ mV}_{\text{SCE}}$ for the untreated CP-Ti. However, the welcomed shift in corrosion potential comes with higher current densities throughout the potential sweep. Both the anodic shift and the increased current densities have been reported previously [196]. Olah et al. [196] found that TiC coatings have an improved corrosion potential, but suffer from a greater rate of corrosion. The density of the TiC film was given as the attributing factor towards the increased corrosion rate. Thinner, less dense TiC films, would have a greater porosity and a higher defect density.

Using the pack carburisation technique incorporating oxygen, allows for the surface film generated to consist of multiple titanium, carbon and oxygen species. These phases include: TiC, TiO_2 , TiO, $\text{TiC}_x\text{O}_{1-x}$ and α -Ti. XRD (Fig. 5.15) demonstrated that TiC is mostly formed at the surface but other stoichiometry cannot be ruled out. The Pourbaix diagram of TiC (Fig. 6.8), shows that when exposed to a neutral solution (0.9% NaCl, $\text{pH} \approx 7$), a titanium dioxide (TiO_2) boundary layer will be formed along with methane (CH_4), which was also demonstrated by Avgustinik et al. [197]. Considering this, the overall rate of TiO_2 formation during corrosion will vary depending on the film composition at any one point. This will lead to a film of varying density and porosity, resulting in an increased rate of dissolution, as seen during the anodic sweep. The TiC network layer persists with consistent polarisation sweeps to a depth of around 10 μm , which is consistent with the carbon concentration profile produced via GDOS (Fig. 5.14a).

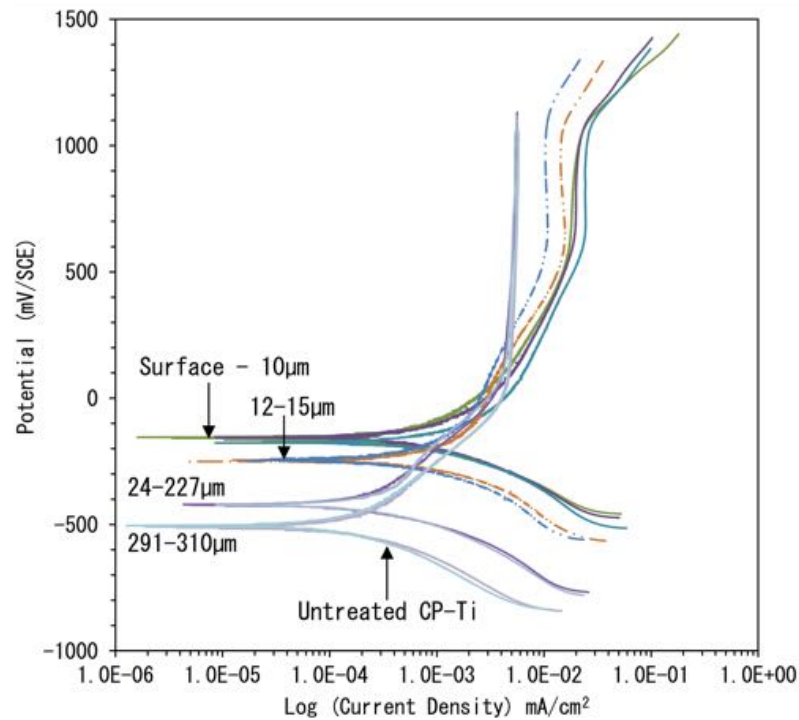


Fig. 6.7: Anodic polarisation curves measured for PC-Ti at various depths for the treated surface, using a sweep rate of 1 mV s^{-1} in a 0.9% NaCl solution

There is then a transitional period where the anodic shift in corrosion potential is less pronounced and the anodic corrosion currents are reduced. This coincides with the reduced carbon content, at depths of 12-15 μm . Once the surface was ground to a depth of 24 μm , the polarisation curves became consistent to a depth of $\approx 230 \mu\text{m}$. This zone is within the observed oxygen diffusion zone. There is a slight anodic shift in the free corrosion potential (-400 mV), compared with that of untreated titanium (-500 mV). At these depths, there is a reduced current density compared to the surface in the anodic region, and the current density is similar to those of untreated titanium. This response of oxygen rich titanium has been observed in the thermal oxidation section of this work (Section 3.5). Oxygen in the diffusion zone seems to have a slight positive effect on the corrosion properties of titanium, by creating a higher corrosion potential (-400 mV_{SCE}). At further depths (290 μm and deeper) from the surface, the oxygen content is much reduced and the materials electrochemical response shows a very reproducible and consistent polarisation curve. There is an extended passive region between 200 mV_{SCE}

and $1000 \text{ mV}_{\text{SCE}}$, where the current density is stable at around 0.005 mA cm^{-2} , similar to that of untreated CP-Ti.

It seems that the pack carburisation process allows for a large anodic shift in the corrosion potential, meaning that initially it will be quite resistant to corrosion. However, when corrosion starts, the carburised titanium will dissociate at a faster rate than untreated Ti.

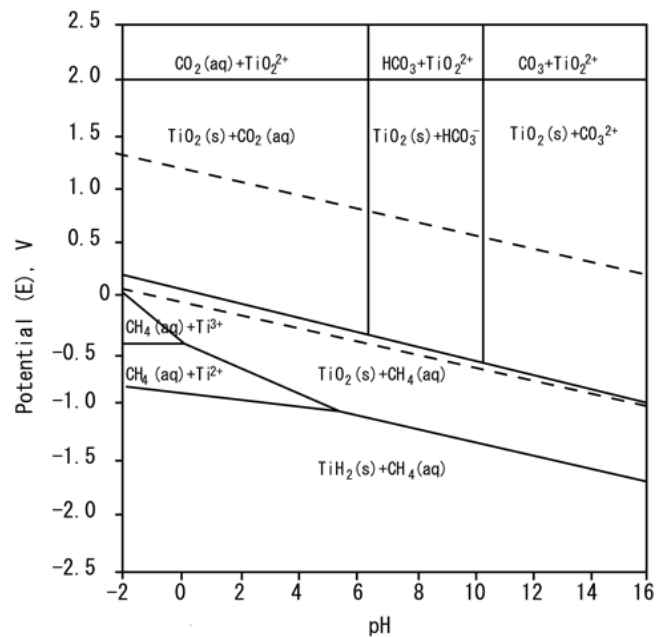


Fig. 6.8: Pourbaix diagram for titanium carbide (E/pH) [198]

6.2.2 Current Transient Behaviour

Potentiostatic testing was carried out at various surface depths, by applying a potential of $500 \text{ mV}_{\text{SCE}}$ for 3600 s. According to Fig. 6.7, at this potential all samples are within the passive region. The Pourbaix diagram for TiC (Fig. 6.8) also shows that when polarised at $500 \text{ mV}_{\text{SCE}}$ in a neutral pH solution, a TiO_2 surface film should be generated. Fig. 6.9 shows the current transient response for the samples in the $\log(I)$ vs. $\log(t)$ scale. It was described in section 4.3.2 how the Point Defect Model (PDM) and the High Field Theory (HFT) are used to describe the change in ion flux at the sample surface. This current response over time is described by Eq. 4.4 (page 116).

In Fig. 6.9, the curves generated for the ground samples clearly conform to Eq. 4.4. There exists an initial stage in all the tested samples, where there are low curve gradients ($k \approx 0.5$). This low value of k is attributed to small film thickness in the initial stage of polarisation, a phenomenon that has been reported in previous studies [44, 45]. As polarisation time increases, the passive film thickens and the k value approaches 1. Once again, it can be observed that there is a variation between the current densities observed in the carbon rich region and the oxygen rich region below.

From the surface, until a depth of 10 μm , the curve (Fig. 6.9a) reaches linearity quickly after around 10 s. This is much faster than at deeper depths (Fig. 6.9b and 6.9c). This carbon rich zone never reaches $k = 1$. The upper diffusion zone with high oxygen content also never achieves this ideal value for k (Fig. 6.9b). Whereas, the further ground samples (Fig. 6.9c) all achieve this ideal value, as expected for titanium [184]. This variation in the time to reach the linear stage and final slope value shows that when there is a high carbon and oxygen content present within the titanium subsurface, a passive film can be formed very quickly, this results initially in lower current density. This faster response could be attributed to the higher free corrosion potential observed in Fig. 6.7. However, with larger carbon and oxygen content present, the data in Fig. 6.9 suggest that the film generated is less dense and more porous than that produced when lower carbon and oxygen concentrations are present.

The ODZ reaches linearity in around 100 s and initially, there is higher current density when compared with the carbon rich zone. Section 4.3.2 showed how the ODZ of TO-Ti had similar characteristics. The film was fast forming but, had a lower than ideal k value. Using M-S analysis (Section 3.5.4), it was demonstrated that the passive film formed on the ODZ had a higher defect density than that of untreated Ti or Ti with a lower oxygen content. Therefore, the passive film on the pack carburised titanium with oxygen diffusion will undoubtedly have a high defect density in the close to medium sub surface (0-100 μm). Increased levels of carbon and oxygen results in the formation of various titanium phases. These phases include: TiC, TiO₂, TiO, TiC_xO_{1-x} and α -Ti etc. Galvanic

corrosion can occur, as the multiple phases can cause local cells to develop on the surface, resulting in a faster dissociation [199]. The incorporation of carbon within TiO_2 will also generate extra interstitial sites, this will allow for greater ion transportation. This would explain the increases corrosion current observed during anodic potentials in the carbon rich near surface regions (as seen in Fig. 6.7).

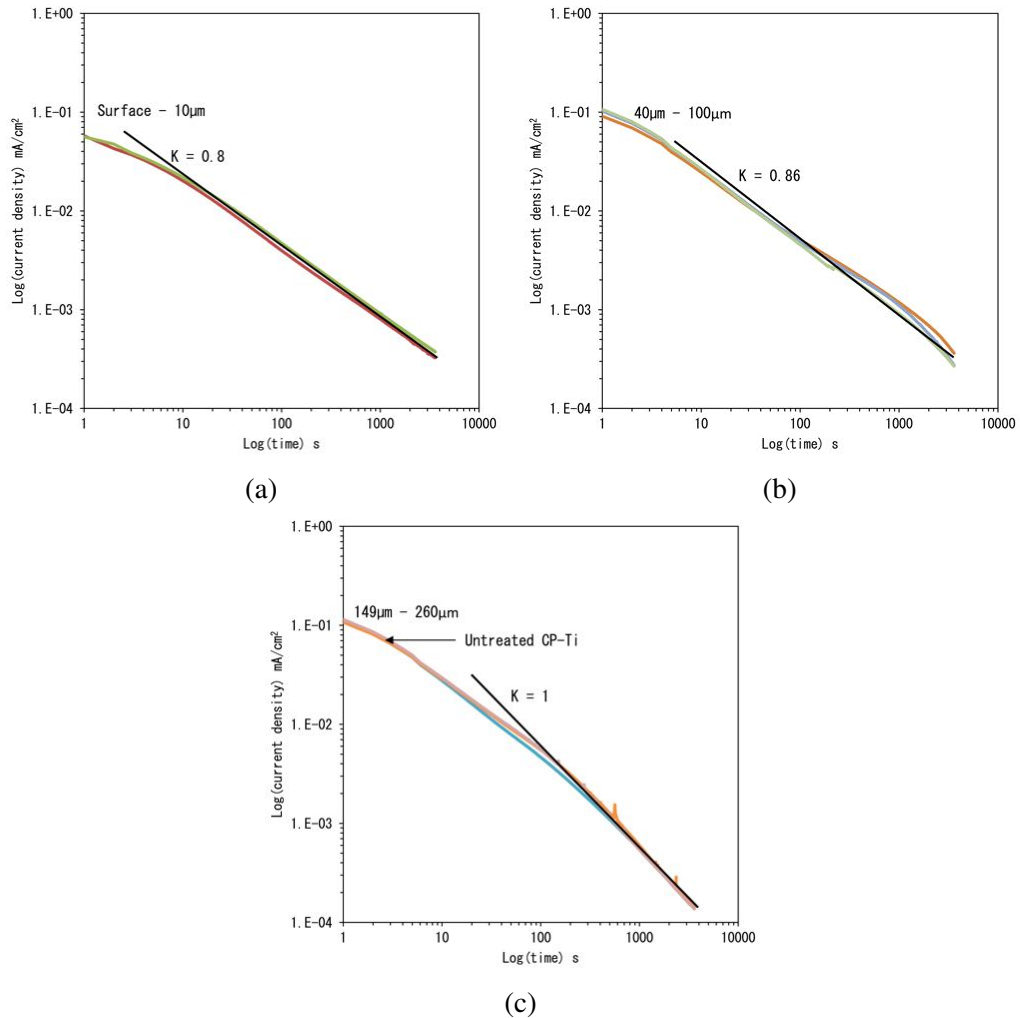


Fig. 6.9: Current transient curves in the $\log(I)$ vs. $\log(t)$ scale measured during film formation at various depths from the surface of pack carburised titanium with (a) showing the carbon rich surface layers, (b) shows the oxygen rich diffusion zone and (c) shows the lower ODZ and untreated titanium. All tests were conducted at a potential of 500 mV for a duration of 3600 s in a 0.9% NaCl solution

6.3 Tribocorrosion Behaviour

6.3.1 Open Circuit Tribocorrosion Behaviour

Initial tribocorrosion tests were carried out under open circuit conditions without any externally applied potential. The samples were tested for a duration of 3 h, with 2 h sliding and 30 min stabilisation before and after under a load of 20 N. Fig. 6.10 shows the evolution of potential and friction coefficient over time for the pack carburised samples. During tribocorrosion testing, three distinct frictional zones are observed, which were also seen during dry sliding (see Fig. 6.1a).

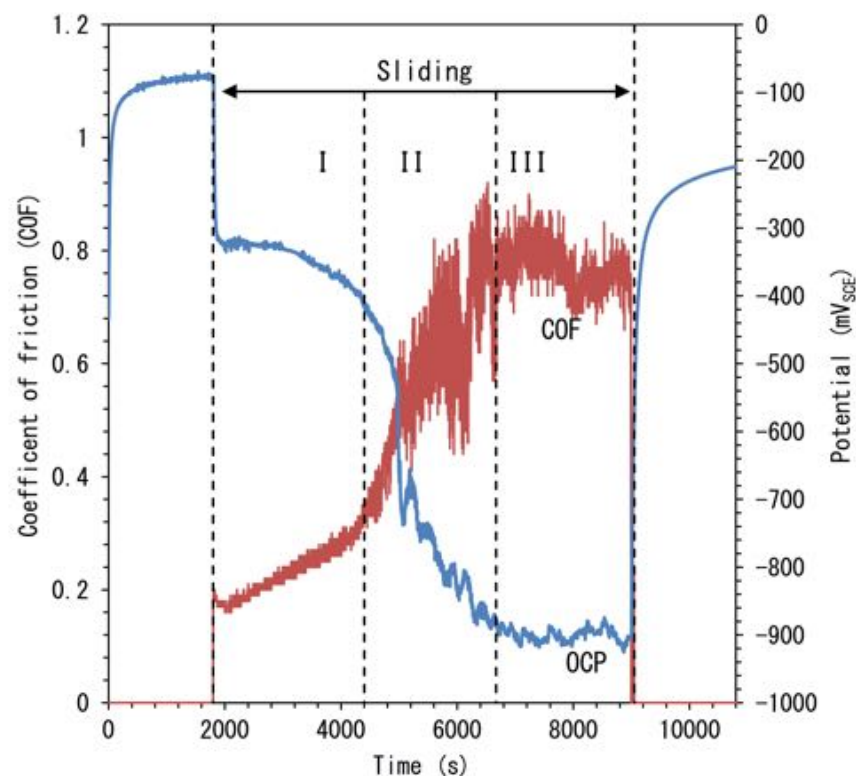


Fig. 6.10: Open circuit potential and coefficient of friction curves recorded for a contact load of 20 N in a 0.9%NaCl solution for pack carburised CP-Ti. The onset of sliding is indicated after 30 minutes stabilisation. Three distinct frictional zones can be observed: I) Oxide layer, II) Partial removal of the oxide layer and III) Oxygen diffusion zone

It is proposed that each zone is related to the materials composition and substructure. Pack carburisation with oxygen diffusion generates a multilayer structure. The frictional

response over time is dependant on the exposed layer and the transition between each layer. The friction zones observed in Fig. 6.10 relate to the following structural transitions: (I) carbide network layer, (II) the removal of the carbide network and (III) the ODZ. Zone IV (exposure of Ti substrate), identified in Fig. 6.1b, would have been observed had the test run for a longer duration. With the identification of the three frictional zones, it can be clearly seen that the OCP data also correlates to the frictional zones. Fig. 6.12c shows the wear track morphology, revealing the removal of the TiC network layer and exposure of the underlying ODZ.

OCP gives insight into the surface condition of the samples in real time during the sliding wear process. Each zone exhibits a unique friction and OCP response, correlating to the varying levels of material activity:

Zone I Sliding contact between the Al₂O₃ ball and the carbide network layer results in low friction. The OCP experiences an initial cathodic shift from -100 mV to -300 mV. As the carbide layer is worn, the potential gradually drops from -300 mV to -400 mV. During this time, the COF gradually rises from 0.2-0.3 over a period of 3200 s.

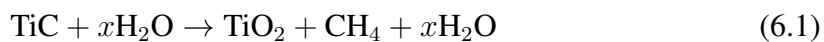
Zone II As the sliding continues, the carbide network layer is gradually removed or damaged, exposing the ODZ. This transitional period results in a cathodic shift in potential from -400 mV to -900 mV. This shift in OCP coincides with a dramatic increase in COF from 0.3 to 0.8 in just 2100 s.

Zone III Full exposure of the ODZ to the contact zone, results in a stabilisation of the OCP (≈ -900 mV) and COF ($\mu \approx 0.8$).

When considering the tribocorrosion response of carburised titanium, it is interesting to compare the frictional response in both the corrosive medium (0.9% NaCl in Fig. 6.10) and in a dry un-lubricated medium (Fig. 6.1a). During dry sliding, the TiC network layer was able to withstand a load of 20 N for 10 800 s (3 h), all while producing a low COF. However, when subjected to the same load in a 0.9% NaCl solution, the low friction was

observed for just 3200 s (< 1 h). This reduced level of protection is clearly generated by the interaction between the surface carbide and the corrosive medium.

Avgustinik et al. [197] showed that TiC is decomposed by water at room temperature to form TiO₂ to a depth of 150 Å from the surface by the reaction described in Eq. 6.1.



Therefore, during wear the sliding contact will be between TiO₂ and the Al₂O₃ slider. The subsequent removal and reformation of the TiO₂ layer can be accredited to the increased wear rate observed when in a corrosive medium.

6.3.2 Effect of Applied Potential on Tribocorrosion Behaviour

In order to understand the contributing factor of corrosion on the overall tribocorrosion behaviour of PC-Ti, potentiostatic sliding wear tests were performed at both anodic (+1000 mV and +500 mV) and cathodic potentials (−900 mV and −1500 mV). Fig. 6.11 shows both the COF and current traces recorded at each potential. It is clear that the applied potential has a significant impact on the frictional response of the pack carburised titanium.

At anodic potentials accelerated corrosion is usually expected as this favours the anodic forward reaction. Fig. 6.11a and 6.11b show the friction and the current for the samples polarised at 1000 mV and 500 mV respectively. The frictional response of both samples is very similar, with low friction (COF < 0.4) observed throughout the test. The current flow is clearly affected by the onset of sliding. When sliding is initiated there is a sharp jump in the measured current density, showing an activation of the sample surface. As expected, the amount of current flow is proportional to the applied potential, the higher the potential the higher the current. Polarisation in the anodic region actively encourages corrosion to take place. The higher the potential, the greater the rate of dissociation.

When we consider the frictional response of these samples, it is important to make

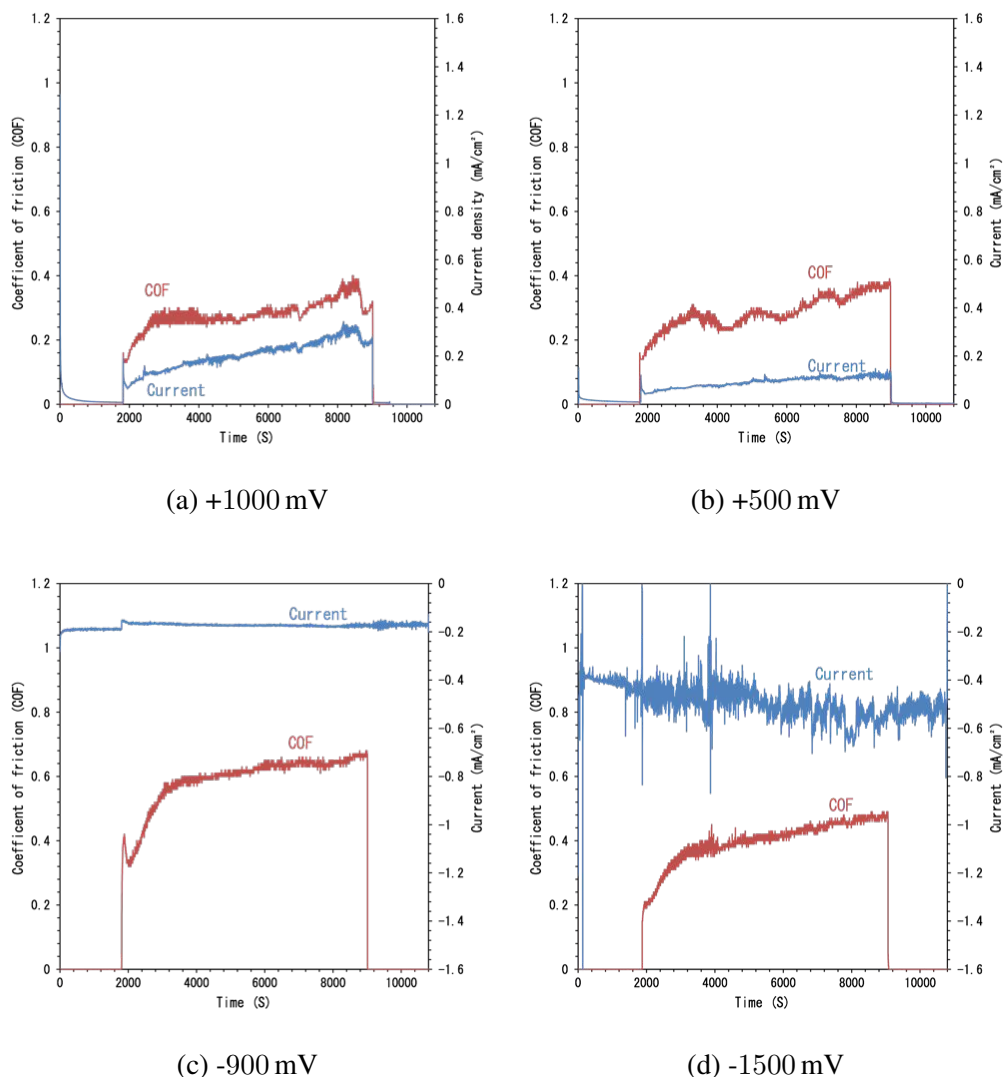


Fig. 6.11: Friction coefficient (μ) and current density (I) against time for tribocorrosion testing at potentials of: a) 1000 mV, b) 500 mV, c) -900 mV and d) -1500 mV. Contact was initiated for 3 hours, with a 30 minute settling period before and after sliding under a 20 N load

comparisons to that of the samples tested at OCP (Fig. 6.10). This is to understand how corrosion affects the wear mechanisms. When PC-Ti is anodically charged, the samples no longer display the three frictional zones highlighted under OCP conditions. These differences are also evident when looking at the wear track morphology produced after sliding at 1000 mV (Fig. 6.12a), 500 mV (Fig. 6.12b) and the OCP sample (Fig. 6.12c). There is a clear shift in the wear mechanism from that at OCP and at anodic potentials. Wear track morphology of the samples tested at OCP shows exposure of the underlying

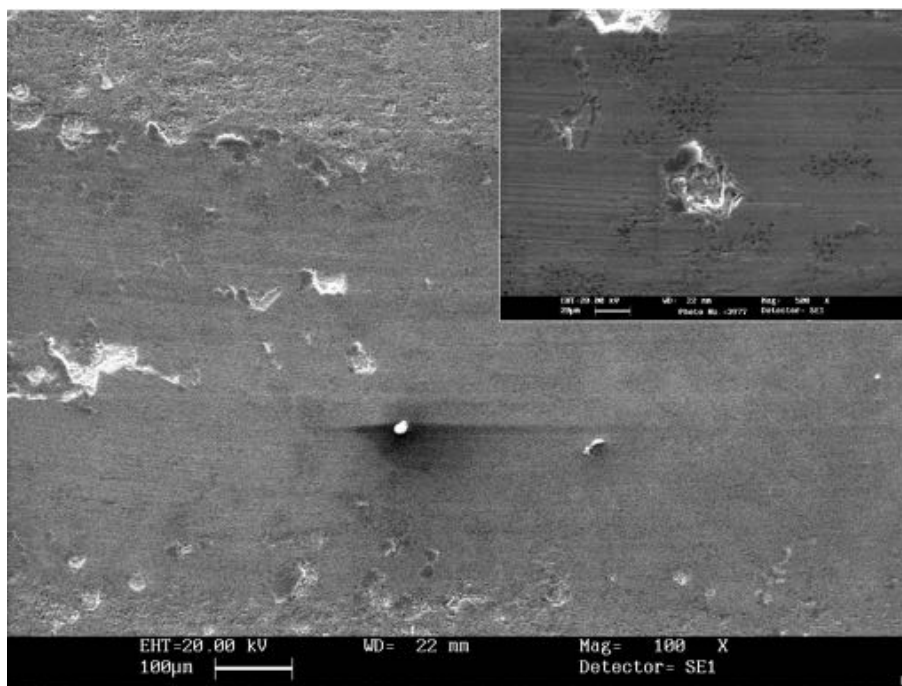
ODZ within the centre of the wear track, with large amounts of adhesive wear observable. This is also highlighted by the large COF recorded in Fig. 6.10. The anodically charged samples were tested under the same contact load and for the same duration as the OCP samples. However, throughout the duration of the test, the COF never surpassed 0.4. When looking at the wear track morphology (Fig. 6.12a and 6.12b) of these samples, the dominating wear mechanism is that of simple abrasion, with a very smooth wear track and no large scale de-lamination. On closer inspection there are areas where some delamination has occurred through the creation and propagation of micro cracks within the wear track. This is more evident in the 500 mV (Fig. 6.12b) sample.

This change in wear mechanism can be attributed to the formation of a TiO_2 layer at the samples surface, via the decomposition of TiC [197]. At anodic potentials the decomposition of TiC (Eq. 6.1) can proceed to depths much greater than 150 Å. This produces a protective layer that will not be fully removed with each subsequent pass of the slider. This constant film removal and formation within the wear track would result in the smooth polished like surface observed. This would also account for the low COF observed, due to the enhanced tribological properties of TiO_2 .

When a metal is cathodically charged, it is possible to remove the corrosive element of wear during the tribocorrosion process. By applying a negative charge to the sample, it is no longer possible to generate the metal anions (M^+) required for corrosion. However, when polarisation is taken to the extreme negative potentials, hydrogen production can occur at the samples surface via the electrolysis of water. This can result in hydrogen uptake by the cathode material, known as hydrogen embitterment [75, 174–177]. When PC-Ti was cathodically charged to -900 mV and -1500 mV, the frictional response was very different from that encountered at OCP (see Fig. 6.11c and 6.11d respectively). Again, the frictional response was no longer characterised by three distinct zones. When polarised to -900 mV the friction gradually reached 0.6, at which point it then stabilised. The -1500 mV sample reached a stable friction coefficient of 0.4. This strange frictional response has to be attributed to hydrogen embitterment and the formation of TiH_2 . At

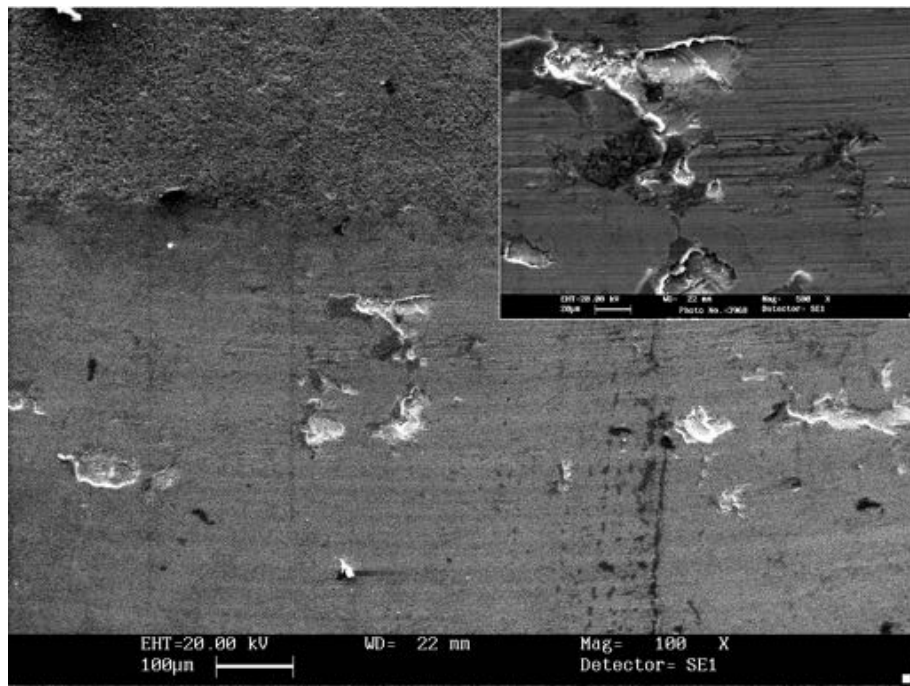
these potentials, TiH_2 formation is predicted (see Pourbaix diagram, Fig. 6.8).

SEM wear track images for the -1500 mV (Fig. 6.12e) and -900 mV (Fig. 6.12d) samples show the formation of a surface layer within the wear track. This shows a smooth, polished wear track, with large scale cracking and delamination. The amount of hydrogen present within the wear track is directly related to the frictional response of the samples. The sample treated at -1500 mV will have a greater hydrogen uptake than that treated at -900 mV. This should explain the difference in frictional response between the two samples. The sample treated at -1500 mV will have a much more uniform covering of TiH_2 , compared with -900 mV which is much more likely to have a mixed phase surface consisting of TiH_2 , TiH , TiC , TiO_2 , TiO , Ti , and any intermediate phases. This can result in increased friction due to the uneven wear of each phase.

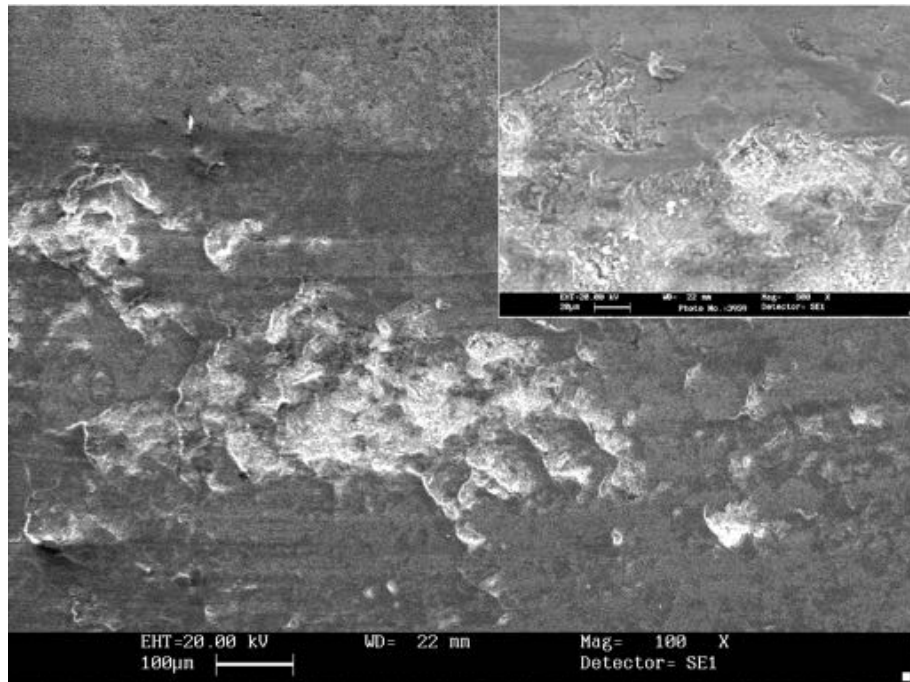


(a) +1000 mV

Fig. 6.12: SEM images showing the wear track morphology produced on the pack carburised titanium, after tribocorrosion testing at potentials of: a) 1000 mV, b) 500 mV, c) -900 mV and d) -1500 mV. All tests were conducted using a load of 20 N for 10 800 s

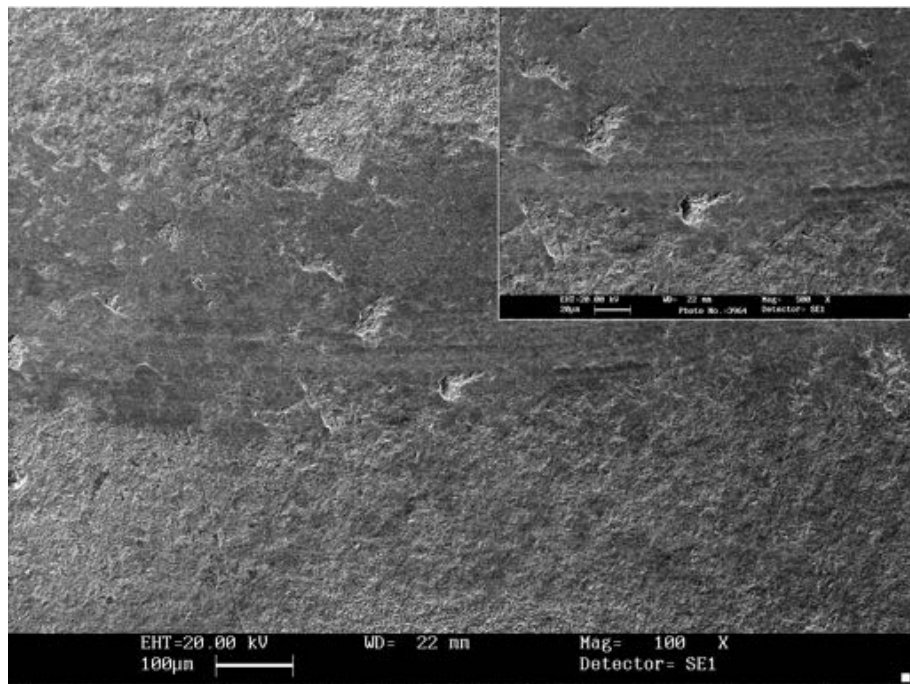


(b) +500 mV

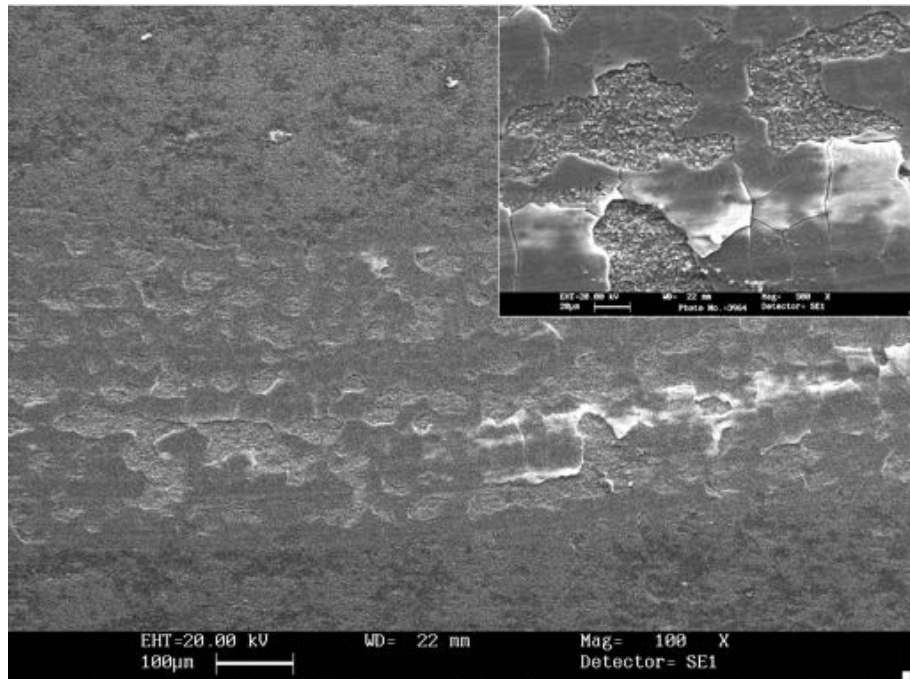


(c) OCP

Fig. 6.12: SEM images showing the wear track morphology produced on the pack carburised titanium, after tribocorrosion testing at potentials of: a) 1000 mV, b) 500 mV, c)-900 mV and d) -1500 mV. All tests were conducted using a load of 20 N for 10 800 s



(d) -900 mV



(e) -1500 mV

Fig. 6.12: SEM images showing the wear track morphology produced on the pack carburised titanium, after tribocorrosion testing at potentials of: a) 1000 mV, b) 500 mV, c)-900 mV and d) -1500 mV. All tests were conducted using a load of 20 N for 10 800 s

6.3.3 Total Material Loss Rate

Using a Mitutoyo SJ-400 stylus profilometer the total material loss (TML) from the wear track was measured. This was then normalised with the sliding distance and applied load. This generates a value known as the total material loss rate (TMLR). The results are shown in Fig. 6.13 as a function of applied potential for the pack carburised, thermally oxidised and untreated CP-Ti samples.

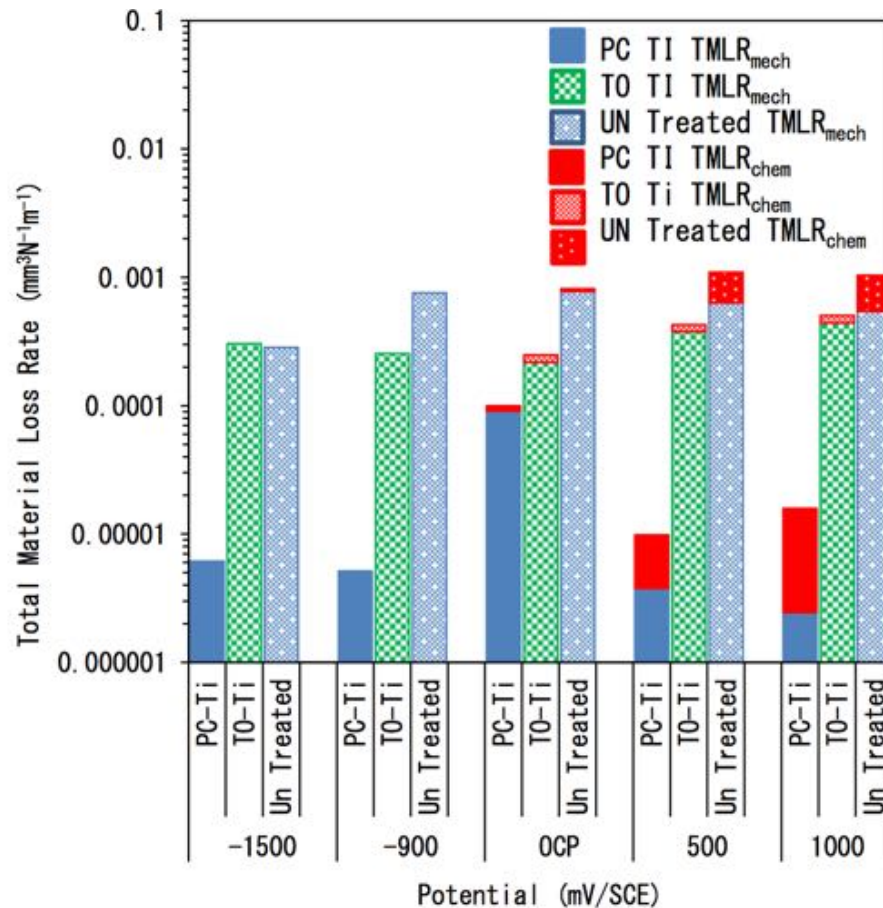


Fig. 6.13: Contribution of mechanical wear and corrosion to total material loss rate volume of pack carburised titanium, thermally oxidised titanium and untreated titanium. All tests were conducted in a 0.9% NaCl solution under a 20 N load

In section 4.4.3 the contribution of both mechanical and chemical wear on the overall wear rate was discussed and expressed via Eq. 2.27. The chemical contribution of wear can be determined using the currents measured during anodic polarisation, via Faraday's law (Eq. 4.5).

In order to calculate the amount of material lost due to corrosion at OCP, both Vieira et al. [200] and Pina et al. [201] used the Buller Volmer equation to calculate anodic current passing through the wear track (i_a). Once the current has been calculated, Faraday's law can then be used to calculate the volume lost due to the chemical interaction (V_{chem}). The Buller Volmer equation takes into account the cathodic kinetics and the corrosion potential of the alloy, the potential present during sliding contact and the anode to cathode area ratio. From this model, the anodic current passing through the wear track (i_a) was calculated using Eq. 6.2 [200, 201].

$$\log I_a = \frac{E_{\text{corr}} - E_c + a_c}{b_c} - \log \left(\frac{A_a}{A_c} \right) \quad (6.2)$$

where E_c is the potential measured during rubbing (OCP sliding Fig. 6.10), E_{corr} is the corrosion potential (-204 mV from Fig. 6.7), a_c and b_c are the Tafel constants extracted from the cathodic polarisation curves ($a_c = -825$ mV, $b_c = 274$ mV from Fig. 6.7). A_a corresponds to the wear track area after sliding (0.3 cm²), A_c corresponds to the cathode area which can be approximated by the sample area (1.23 cm²).

Fig. 6.13 clearly demonstrates the effective wear reducing properties of PC-Ti, when compared with that of untreated titanium. Pack carburisation reduced the TMLR across the spectrum by at least one order of magnitude.

The effect of potential on the tribocorrosion properties of titanium has been discussed previously in section 4.4.3. Ti follows that of a traditional passive material, whereby under anodic potentials, the contribution of corrosion on the TMLR is increased. When charged cathodically, the chemical wear is all removed altogether. When the charge is reduced further, hydrogen embitterment occurs. This does have an effect of reducing the TMLR of untreated Ti.

When evaluating the effect of potential on the tribocorrosion performance of PC-Ti, it is clear to see that potential has a dramatic effect on the TMLR recorded. When an anodic potential is applied (500 mV and 1000 mV in this case), the TMLR is much reduced over that of the samples tested at OCP. However, the amount of wear attributed to corrosion

(V_{chem}) is dramatically increased, as indicated by the larger currents developed during sliding (Fig. 6.11). It is believed that at anodic potentials the decomposition of TiC to TiO₂ (Eq. 6.1) is greatly increased, resulting in the formation of a TiO₂ barrier film. TiO₂ has good tribological properties and helps to keep mechanical wear to a minimum. During the course of the test, the TiO₂ film is removed. As a result, more TiC would be converted to TiO₂, thus generating the anodic currents, low friction and the low TMLR.

When the PC-Ti was tested under cathodic potentials of (−900 mV and −1500 mV) there was a much reduced TMLR recorded. This reduction is more than simply due to the removal of the anodic current/corrosion. At such cathodic potentials the hydrolysis of water is predicted. The low solubility of H in Ti results in the formation of titanium hydride (Fig. 6.8). The formation of titanium hydride has been shown to decrease the rate of material loss, under tribocorrosive conditions for both oxidised and untreated titanium [184]. When polarised to −900 mV, there will be less hydrogen embitterment than that of the sample polarised to −1500 mV. This will result in slightly less cracking and delamination of the hard hydride film, clearly observable in the SEM wear track images in Fig. 6.12 and is accountable for the change in TMLR between the two voltages.

When the PC-Ti is compared with that of TO-Ti (625 °C, 20 h), it can be seen that the wear rate is significantly improved (Fig. 6.13). Under the high load of 20 N the rutile titanium dioxide film was immediately delaminated from the contact zone. This wear occurred predominantly in the limited ODZ (effective to a depth of 8.5 μm) and then the substrate titanium. The TO-Ti was only marginally better at preventing material loss than untreated Ti. The ODZ is attributed to the reduction in wear and corrosion. Under such high load, the ODZ is quickly removed and most of the wear is carried out in the substrate material, hence the similar wear to untreated Ti. The PC-Ti demonstrated much improved wear at all the potentials tested, proving itself to be much more effective at reducing the material loss rate than thermally oxidised titanium.

Chapter 7

Conclusions and Recommendations

The primary aim of this work was to develop a surface treatment technique capable of improving the tribological, electrochemical and tribo-electrochemical performance of commercially pure titanium. Two different approaches were taken:

1. Thermal oxidation.
2. Pack carburisation with oxygen diffusion.

7.1 Conclusions

The following findings are summarised from the experiments carried out during this course of the study and the results and discussion presented in chapter four, five and six.

Thermal Oxidation of CP-Ti

Titanium was thermally oxidised at a temperature of 625 °C for durations of 5, 20 and 72 h. These samples were then structurally characterised with the following results:

- The thermal oxidation treatment produced a multilayered structure comprising of a titanium dioxide layer (rutile) atop of an α -titanium oxygen diffusion zone (α -Ti(O)).

- Increasing the oxidation time increased the amount of titanium dioxide produced and the degree of α -titanium oxygen diffusion.
- The film produced for a duration of 72 h was more prone to delamination during tribological testing than those treated for shorter durations.

Unlubricated Sliding Friction and Wear Characteristics

Tribological characterisation of thermally oxidised titanium treated at 625 °C for 20 h was conducted using a pin-on-disk tribometer and an alumina (Al_2O_3) counter-face. Initial attempts were made to improve film adhesion when tested at higher loads using a prior surface mechanical attrition treatment (SMAT) and controlled slow cooling after oxidation

- Thermally oxidised CP-Ti exhibits peculiar frictional behaviour during unlubricated sliding with alumina. Four frictional zones can be identified in a typical friction curve, each having its own characteristics corresponding to the oxide layer, the gradual or partial removal of the oxide layer, the diffusion zone and the substrate.
- The oxide layer offers both low friction and superior wear resistance. The oxide layer formed by short time oxidation is more beneficial in achieving low friction.
- The oxygen diffusion zone can offer improved wear resistance by up to 10 times over the untreated CP-Ti, but it experiences very high and unstable friction.
- An ideal tribological system in titanium should comprise of an adherent and long lasting oxide layer supported by an oxygen diffusion zone. But in reality, the oxide layer produced is either too thin or too crumbly to resist high contact loads under unlubricated conditions.
- It is possible to improve the tribological performance of the oxide layer by prior SMAT treatment or by controlled slow cooling.

Electrochemical Behaviour as a Function of Depth from the Surface

Experiments were conducted to investigate the corrosion behaviour of thermally oxidised titanium in 0.9% NaCl solution as a function of depth from the surface. This was achieved by mechanically removing successive layers across the oxidised sample.

- The oxide layer produced by thermal oxidation serves as a barrier layer to improve the corrosion resistance of CP-Ti by reducing anodic currents and increasing corrosion potential.
- The high oxygen content in titanium subsurface (upper part of the ODZ) helps to accelerate passive film formation and thus to reduce corrosion of titanium.

Tribo-electrochemical Behaviour

Tribo-electrochemical characterisation was carried out in a 0.9% NaCl solution, against an alumina counter face. Investigations were conducted under both OCP and at potentials of 1000 mV_{SCE}, 500 mV_{SCE}, -900 mV_{SCE} and -1500 mV_{SCE}.

- During sliding wear at open circuit in a 0.9% NaCl solution, four frictional zones can be identified in a typical friction curve. Each zone has its own characteristics corresponding to the oxide layer, the gradual or partial removal of the oxide layer, the diffusion zone and the substrate.
- The thermally-formed oxide layer offers both low friction and better resistance to material removal during tribocorrosion than untreated CP-Ti.
- The thermally formed oxide layer exhibits unusual anodic protection behaviour. When the thermally oxidised titanium is polarised anodically during sliding, the durability of the oxide layer is prolonged, resulting in low friction and a much reduced TMLR. This is in contrast to the results obtained from the untreated CP-Ti and is believed to be due to the fast passivation of the exposed ODZ.

- Both the thermally oxidised and untreated CP-Ti experience a reduction in TMLR when cathodically charged to $-1500 \text{ mV}_{\text{SCE}}$ during sliding. This is believed to be related to hydrogen evolution and titanium hydride formation.

Pack Carburisation With Oxygen Diffusion

A new pack carburising surface treatment method has been developed, whereby oxygen diffusion and carburisation of CP-Ti were undertaken concurrently. The treatment was optimised then structurally characterised. The carburised titanium was then tested for its tribological, electrochemical and tribo-electrochemical characteristics.

Optimisation

- The pack carburising technique resulted in a multilayer structure comprising of a titanium carbide (TiC) network layer atop of a relatively thick α -Ti(O) diffusion zone.
- By increasing the carbonate concentrations within the pack, thicker TiC network layer structures were produced. When treated at a temperature of $925 \text{ }^\circ\text{C}$ and a duration of 20 h. The optimal pack composition was that of: 6 part C, 3 part BaCO_3 , 2 part Na_2CO_3 and 1 part CaCO_3 . The low COF is attributed to the TiC network layer.
- The carburisation duration affects the thickness of the TiC network layer. Therefore, depending on application, the carburisation duration must be controlled to generate the desired protection in the most efficient and economical way.
- When treated for 20 h at $925 \text{ }^\circ\text{C}$ using a pack composition ratio of 1:1. The resulting multilayered structure was that of a surface TiC network layer ($7.6 \text{ }\mu\text{m}$) connected to a thick subsurface oxygen diffusion zone ($200 \text{ }\mu\text{m}$).

Tribological, Electrochemical and Tribo-electrochemical Properties

All characterisation tests were conducted using a carburisation duration of 20 h at a temperature of 925 °C with pack composition ratio of 1:1.

- The carburised samples have a low friction coefficient ($\mu \approx 0.2$) when in sliding contact with Al_2O_3 , it is also able to withstand loads of up to 40 N.
- When tested for prolonged periods a peculiar frictional behaviour is observed. Four frictional zones can be identified in a typical friction curve, each has its own characteristics corresponding to the TiC network layer, gradual/partial removal of the network layer, the oxygen diffusion zone and the substrate.
- The surface treatment allows for a greatly improved friction and wear response when compared to untreated CP-Ti, TO-Ti and AISI 440C stainless steel.
- The pack carburising process has a limited impact on the corrosion resistance of titanium. Carburisation resulted in an anodic shift in OCP, this suggests, it will initially be less likely to corrode. However, when polarised anodically higher current densities were observed than those recorded for untreated CP-Ti.
- During tribocorrosion testing at OCP three frictional zones were observed. However, in the 0.9% NaCl solution the TiC film was worn through at a much faster rate than that observed under dry conditions. This is explained by the hydrolysis of water and the formation of TiO_2 at the surface of the TiC layer. The subsequent removal and reformation of this film results in accelerated wear of the TiC network, reducing its wear reducing properties.
- When anodically charged to 1000 mV_{SCE} and 500 mV_{SCE} the TiC surface layer produces TiO_2 at a fast rate. The TiO_2 film then acts as a barrier layer providing low friction and reduced wear.

- At a cathodic potential of $-1500 \text{ mV}_{\text{SCE}}$ the formation of titanium hydride created a hardened zone within the wear track. This reduces the rate of wear, but also increased the COF.

7.2 Recommendations

- In the current work, methods to improve film adhesion during the thermal oxidation process have been investigated. Both, prior surface mechanical attritional treatment (SMAT) via shot peening and extended cooling showed promising results. Prior SMAT has been shown to have a positive effect on both the frictional response and adhesion of the oxide film. Future work should focus on finding the optimal conditions for the most efficient shot peening parameters to induce positive effects on film formation. Controlling the cooling rate further, could allow for the formation of thicker titanium dioxide (TiO_2) films with increased adhesion. Therefore, work should focus on producing thicker films and then use extended slow cooling in order to reduce the rate of thermal contraction between the rutile film and the substrate.
- An investigation should be carried out whereby a combined prior surface mechanical attritional treatment (SMAT) is conducted along with extended cooling.
- A comprehensive analytical study should look into the anodic protection of thermally oxidised titanium, with a focus on describing this unusual response. Full characterisation of the tribo-film developed during sliding through the use of X-ray photoelectron spectroscopy (XPS) and secondary ion mass spectrometry (SIMS). These were both unavailable during this study.
- In this study the carburising method was achieved using the most primitive method available (pack carburising). Further study should focus on developing a more controllable multistage process using a vacuum furnace. Whereby, the sample

is first thermally oxidised resulting in oxygen diffusion and then subsequent carburisation. This would allow for much more controlled and designer surface that can be tailored to need.

- A scientific investigation should look at the interaction between carbon and oxygen at the titanium surface. This would allow for a more complete understanding of the process and result in a standard model, whereby the process results can be predicted rather than generated through trial and error.
- Characterisation of the PC-Ti using TEM would allow for the identification of the TiC networks crystal structure and the true nature of this film.
- An investigation into the fatigue properties of the pack carburised titanium with oxygen diffusion should be undertaken. This would be beneficial in the determination of a practical application, to which the PC-Ti treatment would be beneficial.
- An investigation to determine the activation energy and the pre exponential diffusion coefficient for carbon in α -TiO.
- Future work should also look at the tribocorrosive response of both TO-Ti and PC-Ti when cathodically charged, to detect the formation of titanium hydride. This could be achieved using XPS and SIMS.

References

- [1] A. Bloyce. Surface engineering of titanium alloys for wear protection. *Proceedings of the Institution of Mechanical Engineers, Part J: Journal of Engineering Tribology*, 212(6):467–476, 1998.
- [2] H. Dong and T. Bell. Enhanced wear resistance of titanium surfaces by a new thermal oxidation treatment. *Wear*, 238(2):131–137, 2000.
- [3] H. Dong and T. Bell. Designer surfaces for titanium components. *Ind Lubrication and Tribology*, 50(6):282–289, 1998.
- [4] C. Lee, A. Sanders, N. Tikekar, and K. S. Ravi Chandran. Tribology of titanium boride-coated titanium balls against alumina ceramic: Wear, friction, and micromechanisms. *Wear*, 265(34):375–386, 2008.
- [5] B. Sarma, N. M. Tikekar, and K. S. Ravi Chandran. Kinetics of growth of superhard boride layers during solid state diffusion of boron into titanium. *Ceramics International*, 38(8):6795–6805, 2012.
- [6] S. Barril, S. Mischler, and D. Landolt. Triboelectrochemical investigation of the friction and wear behaviour of TiN coatings in a neutral solution. *Tribology International*, 34(9):599–608, 2001.
- [7] A. Zhecheva, W. Sha, S. Malinov, and A. Long. Enhancing the microstructure and properties of titanium alloys through nitriding and other surface engineering methods. *Surface and Coatings Technology*, 200(7):2192–2207, 2005.
- [8] A. Ashrafizadeh and F. Ashrafizadeh. Structural features and corrosion analysis of thermally oxidized titanium. *Journal of Alloys and Compounds*, 480(2):849–852, 2009.
- [9] M. Jamesh, T. S. N. Sankara Narayanan, and P. K. Chu. Thermal oxidation of titanium: Evaluation of corrosion resistance as a function of cooling rate. *Materials Chemistry and Physics*, 138(23):565–572, 2013.
- [10] P. A. Dearnley, K. L. Dahm, and H. Çimenoglu. The corrosion-wear behaviour of thermally oxidised CP-Ti and Ti-6Al-4V. *Wear*, 256(5):469–479, 2004.
- [11] Y. Luo, S. Ge, D. Zhang, Q. Wang, and H. Liu. Fretting wear of carburized titanium alloy against ZrO₂ under serum lubrication. *Tribology International*, 44(11):1471–1475, 2011.

- [12] S. Bradbury. *An introduction to the optical microscope*. Oxford University Press, 1989.
- [13] A. F. Saleh, J. H. Abboud, and K. Y. Benyounis. Surface carburizing of Ti-6Al-4V alloy by laser melting. *Optics and Lasers in Engineering*, 48(3):257–267, 2010.
- [14] N. Makuch, M. Kulka, P. Dziarski, and D. Przystacki. Laser surface alloying of commercially pure titanium with boron and carbon. *Optics and Lasers in Engineering*, 57(0):64–81, 2014.
- [15] D. Siva Rama Krishna and Y. Sun. Effect of thermal oxidation conditions on tribological behaviour of titanium films on 316L stainless steel. *Surface and Coatings Technology*, 198(13):447–453, 2005.
- [16] H. Dong and X. Y. Li. Oxygen boost diffusion for the deep-case hardening of titanium alloys. *Materials Science and Engineering: A*, 280(2):303–310, 2000.
- [17] J. Qu, P. J. Blau, J. Y. Howe, and H. M. Meyer III. Oxygen diffusion enables anti-wear boundary film formation on titanium surfaces in zinc-dialkyl-dithiophosphate (ZDDP)-containing lubricants. *Scripta Materialia*, 60(10):886–889, 2009.
- [18] H. Dong, A. Bloyce, P. H. Morton, and T. Bell. Surface engineering to improve tribological performance of Ti-6Al-4V. *Surface engineering*, 13(5):402–406, 1997.
- [19] Y. Luo, H. Jiang, G. Cheng, and H. Liu. Effect of carburization on the mechanical properties of biomedical grade titanium alloys. *Journal of Bionic Engineering*, 8(1):86–89, 2011.
- [20] N. Tsuji, S. Tanaka, and T. Takasugi. Effects of combined plasma-carburizing and shot-peening on fatigue and wear properties of Ti-6Al-4V alloy. *Surface and Coatings Technology*, 203(1011):1400–1405, 2009.
- [21] Y. Luo, S. Ge, H. Liu, and Z. Jin. Microstructure analysis and wear behavior of titanium cermet femoral head with hard TiC layer. *Journal of Biomechanics*, 42(16):2708–2711, 2009.
- [22] J. A. Williams. *Engineering tribology*. Cambridge University Press, 2005. ISBN 9780521609883.
- [23] C. Kajdas, S. S. K. Harvey, and E. Wilusz. *Encyclopedia of tribology*. Elsevier, 1990. ISBN 9780444884015.
- [24] J. Takadoum. *Materials and Surface Engineering in Tribology*. ISTE, 2008. ISBN 9781848210677.
- [25] I. M. Hutchings. *Tribology: friction and wear of engineering materials*. CRC Press, 1992. ISBN 9780340561843.
- [26] J. R. Davis. *Surface engineering for corrosion and wear resistance*. ASM International, 2001. ISBN 9780871707000.

- [27] K. R. Trethewey and J. Chamberlain. *Corrosion for science and engineering*. Longman, 1995. ISBN 9780582238695.
- [28] J. F. Shackelford. *Introduction to materials science for engineers*. Pearson/Prentice Hall, 2005. ISBN 9780131424869.
- [29] K. G. Budinski. *Surface engineering for wear resistance*. Prentice Hall, 1988. ISBN 9780138779375.
- [30] G. W. Stachowiak and A. W. Batchelor. *Engineering tribology*. Boston: Butterworth-Heinemann, 3rd revised edition edition edition, 2001.
- [31] A. C. Goncalves, D. F. Lago, and M. C. F. Albuquerque. *Maintenance of Reducers with an Unbalanced Load Through Vibration and Oil Analysis Predictive Techniques*, pages 81–102. Recent Advances in Vibrations Analysis. InTech, on line, 2011.
- [32] A. C. Fischer-Cripps. *Introduction to Contact Mechanics*. Mechanical Engineering Series. Springer, 2007.
- [33] T. J. Joyce. Theoretical calculation of lubrication regimes in a metal-on metal first metatarsophalangeal prosthesis evaluated against an ex vivo sample. In R. Magjarevic and J. H. Nagel, editors, *World Congress on Medical Physics and Biomedical Engineering 2006*, volume 14 of *IFMBE Proceedings*, pages 3315–3318. Springer Berlin Heidelberg, 2007.
- [34] L. L. Shreir, R. A. Jarman, and G. T. Burstein. *Corrosion (3rd Edition) Volumes 1-2*. Elsevier, 1994. ISBN 978-0-7506-1077-3.
- [35] J. R. Davis. *Corrosion: Understanding the Basics*. A S M International, 2000. ISBN 9781615030682.
- [36] M. J. Donachie. *Titanium: a technical guide*. ASM International, 2000. ISBN 9780871706867.
- [37] S. Mischler. Triboelectrochemical techniques and interpretation methods in tribocorrosion: A comparative evaluation. *Tribology International*, 41(7):573–583, 2008.
- [38] R. G. Kelly. *Electrochemical techniques in corrosion science and engineering*. Marcel Dekker, 2003. ISBN 9780824799175.
- [39] C. Liao, J. Yang, Y. He, and X. Ming. Electrochemical corrosion behavior of the carburized porous TiAl alloy. *Journal of Alloys and Compounds*, 619(0):221–227, 2015.
- [40] P. Ponthiaux, F. Wenger, D. Drees, and J. P. Celis. Electrochemical techniques for studying tribocorrosion processes. *Wear*, 256(5):459–468, 2004.
- [41] D. Landolt, S. Mischler, and M. Stemp. Electrochemical methods in tribocorrosion: a critical appraisal. *Electrochimica Acta*, 46(24-25):3913–3929, 2001.

- [42] P. R. Roberge. *Handbook of corrosion engineering*. McGraw-Hill, 2000. ISBN 9780070765160.
- [43] Y. Zhang, D. D. Macdonald, M. Urquidi-Macdonald, G. R. Engelhardt, and R. B. Dooley. Passivity breakdown on AISI type 403 stainless steel in chloride-containing borate buffer solution. *Corrosion Science*, 48(11):3812–3823, 2006.
- [44] K. S. Raja and D. A. Jones. Effects of dissolved oxygen on passive behavior of stainless alloys. *Corrosion Science*, 48(7):1623–1638, 2006.
- [45] Y. Sun. Depth-profiling electrochemical measurements of low temperature plasma carburised 316L stainless steel in 1M H₂SO₄ solution. *Surface and Coatings Technology*, 204(16-17):2789–2796, 2010.
- [46] Y. X. Qiao, Y. G. Zheng, W. Ke, and P. C. Okafor. Electrochemical behaviour of high nitrogen stainless steel in acidic solutions. *Corrosion Science*, 51(5):979–986, 2009.
- [47] D. D. Macdonald. Passivity - the key to our metals-based civilization. *Pure and Applied Chemistry*, 71(6):951–978, 1999.
- [48] D. D. Macdonald, S. R. Biaggio, and H. Song. Steady-state passive films. interfacial kinetic effects and diagnostic criteria. *Journal of the Electrochemical Society*, 139(1):170–177, 1992.
- [49] Y. F. Cheng and J. L. Luo. Electronic structure and pitting susceptibility of passive film on carbon steel. *Electrochimica Acta*, 44(17):2947–2957, 1999.
- [50] S. Ahn, D. Kim, and H. Kwon. Analysis of repassivation kinetics of Ti based on the point defect model. *Journal of the Electrochemical Society*, 153(9):B370–B374, 2006.
- [51] A. Shahryari, S. Omanovic, and J. A. Szpunar. Electrochemical formation of highly pitting resistant passive films on a biomedical grade 316LVM stainless steel surface. *Materials Science and Engineering: C*, 28(1):94–106, 2008.
- [52] S. Watson. Methods of measuring wear-corrosion synergism. *Wear*, 181-183(0):476–484, 1995.
- [53] N. Diomidis, S. Mischler, N. S. More, M. Roy, and S. N. Paul. Fretting-corrosion behavior of β titanium alloys in simulated synovial fluid. *Wear*, 271(7-8):1093–1102, 2011.
- [54] N. S. More, N. Diomidis, S. N. Paul, M. Roy, and S. Mischler. Tribocorrosion behavior of β titanium alloys in physiological solutions containing synovial components. *Materials Science and Engineering: C*, 31(2):400–408, 2011.
- [55] Y. Sun and E. Haruman. Effect of electrochemical potential on tribocorrosion behavior of low temperature plasma carburized 316L stainless steel in 1M H₂SO₄ solution. *Surface and Coatings Technology*, 205(17-18):4280–4290, 2011.

- [56] Y. Sun and E. Haruman. Tribocorrosion behaviour of low temperature plasma carburised 316L stainless steel in 0.5M NaCl solution. *Corrosion Science*, 53(12): 4131–4140, 2011.
- [57] S. Mischler, A. Spiegel, M. Stemp, and D. Landolt. Influence of passivity on the tribocorrosion of carbon steel in aqueous solutions. *Wear*, 251(1-12):1295–1307, 2001.
- [58] A. A. Sagues and E. I. Meletis. *Wear Corrosion Interactions in Liquid Media*, volume 3. The Society, illustrated edition, 1991.
- [59] Y. Sun. Sliding wear behaviour of surface mechanical attrition treated AISI 304 stainless steel. *Tribology International*, 57(0):67–75, 2013.
- [60] A. C. Vieira, A. R. Ribeiro, L. A. Rocha, and J. P. Celis. Influence of pH and corrosion inhibitors on the tribocorrosion of titanium in artificial saliva. *Wear*, 261(9):994–1001, 2006.
- [61] C. Albayrak, L. Hacisalihoglu, S. Yenil vangolu, and A. Alsaran. Tribocorrosion behavior of duplex treated pure titanium in simulated body fluid. *Wear*, 302(12): 1642–1648, 2013.
- [62] Z. Jiang, X. Dai, and H. Middleton. Investigation on passivity of titanium under steady-state conditions in acidic solutions. *Materials Chemistry and Physics*, 126(3):859–865, 2011.
- [63] C. Leyens and M. Peters. *Titanium and Titanium Alloys: Fundamentals and Applications*. John Wiley and Sons, 2006. ISBN 9783527605200.
- [64] G. M. Bedinger. Minerals commodity summaries 2014: U.S geological survey, 2014.
- [65] D. Banerjee and JC Williams. Microstructure and slip character in titanium alloys. *Defence Science Journal*, 36(2):191–206, 2014.
- [66] H. Numakura, Y. Minonishi, and M. Koiwa. $\langle 1123 \rangle \{1011\}$ slip in titanium polycrystals at room temperature. *Scripta metallurgica*, 20(11):1581–1586, 1986.
- [67] G. Lutjering, J. C. Williams, and A. Gysler. Microstructure and mechanical properties of titanium alloys. *Microstructure and Properties of Materials*, 2:1–74, 2000.
- [68] F. Bridier, P. Villechaise, and J. Mendez. Analysis of the different slip systems activated by tension in a α/β titanium alloy in relation with local crystallographic orientation. *Acta Materialia*, 53(3):555–567, 2005.
- [69] G. E. Dieter. *Mechanical metallurgy*. McGraw-Hill, 1986. ISBN 9780070168930.
- [70] A. Bloyce, P. Y. Qi, H. Dong, and T. Bell. Surface modification of titanium alloys for combined improvements in corrosion and wear resistance. *Surface and Coatings Technology*, 107(2-3):125–132, 1998.

- [71] D. H. Buckley. *Surface effects in adhesion, friction, wear, and lubrication*, volume 5. Elsevier, 1981.
- [72] D. H. Buckley, T. J. Kuczkowski, and R. L. Johnson. Influence of crystal structure on the friction and wear of titanium and titanium alloys in vacuum. Technical Report 16, National Aeronautics and space administration, 1965.
- [73] R. W. Roberts and R. S. Owens. Boundary lubrication of titanium-titanium and titanium-steel. *Wear*, 6(6):444–456, 1963.
- [74] W. Wilhelmsen and A. P. Grande. Electrochemical and SIMS studies of cathodically formed hydride layers on titanium. *Electrochimica Acta*, 35(1112):1913–1917, 1990.
- [75] W. Tsai, C. Ju, Y. Wen, and J. Lee. Hydride formation during the cathodic polarization of titanium in artificial sea water. *Surface and Coatings Technology*, 31(4):401–408, 1987.
- [76] M. Liu, Y. He, W. Lv, C. Zhang, H. Du, B. Li, Q. Yang, and F. Kang. High catalytic activity of anatase titanium dioxide for decomposition of electrolyte solution in lithium ion battery. *Journal of Power Sources*, 268(0):882–886, 2014.
- [77] D. Siva Rama Krishna, Y. L. Brama, and Y. Sun. Thick rutile layer on titanium for tribological applications. *Tribology International*, 40(2):329–334, 2007.
- [78] Y. X. Leng, J. Y. Chen, P. Yang, H. Sun, and N. Huang. The microstructure and properties of titanium dioxide films synthesized by unbalanced magnetron sputtering. *Nuclear Instruments and Methods in Physics Research Section B: Beam Interactions with Materials and Atoms*, 257(12):451–454, 2007.
- [79] S. Mo and W. Ching. Electronic and optical properties of three phases of titanium dioxide: Rutile, anatase, and brookite. *Physical Review B*, 51(19):13023–13032, 1995.
- [80] M. D. Wiggins, M. C. Nelson, and C. R. Aita. Phase development in sputter deposited titanium dioxide. *Journal of Vacuum Science & Technology A*, 14(3):772–776, 1996.
- [81] K. H. G. Ashbee and R. E. Smallman. The plastic deformation of titanium dioxide single crystals. *Proceedings of the Royal Society of London. Series A. Mathematical and Physical Sciences*, 274(1357):195–205, 1963.
- [82] U. Diebold. The surface science of titanium dioxide. *Surface Science Reports*, 48(58):53–229, 2003.
- [83] Y. Sun. Tribological rutile-TiO₂ coating on aluminium alloy. *Applied Surface Science*, 233(14):328–335, 2004.
- [84] X. Liu, P. K. Chu, and C. Ding. Surface modification of titanium, titanium alloys, and related materials for biomedical applications. *Materials Science and Engineering: R: Reports*, 47(34):49–121, 2004.

- [85] Y. X. Leng, N. Huang, P. Yang, J. Y. Chen, H. Sun, J. Wang, G. J. Wan, X. B. Tian, R. K. Y. Fu, L. P. Wang, and P. K. Chu. Structure and properties of biomedical TiO₂ films synthesized by dual plasma deposition. *Surface and Coatings Technology*, 156(13):295–300, 2002.
- [86] F. R. Chien, X. J. Ning, and A. H. Heuer. Slip systems and dislocation emission from crack tips in single crystal TiC at low temperatures. *Acta Materialia*, 44(6):2265–2283, 1996.
- [87] Y. Luo, S. Ge, and Z. Jin. Wettability modification for biosurface of titanium alloy by means of sequential carburization. *Journal of Bionic Engineering*, 6(3):219–223, 2009.
- [88] W. S. Williams. Influence of temperature, strain rate, surface condition, and composition on the plasticity of transition-metal carbide crystals. *Journal of Applied Physics*, 35(4):1329–1338, 1964.
- [89] H. O. Pierson. *Carbides of Group IV: Titanium, Zirconium, and Hafnium Carbides*, pages 55–80. Handbook of Refractory Carbides and Nitrides. William Andrew Publishing, Westwood, NJ, 1996. ISBN 9780815513926.
- [90] P. D. Miller and J. W. Holladay. Friction and wear properties of titanium. *Wear*, 2(2):133–140, 1958.
- [91] S. Izman, R. A. Mohammed, M. Anwar, E. M. Nazim, R. Rosliza, A. Shah, and M. A. Hassan. *Surface Modification Techniques for Biomedical Grade of Titanium Alloys: Oxidation, Carburization and Ion Implantation Processes*, page 201. Titanium Alloys - Towards Achieving Enhanced Properties for Diversified Applications. InTech, online, 2012.
- [92] U. Wiklund and M. Larsson. Low friction PVD titanium-carbon coatings. *Wear*, 241(2):234–238, 2000.
- [93] E. Atar, E. S. Kayali, and H. Cimenoglu. Characteristics and wear performance of borided Ti-6Al-4V alloy. *Surface and Coatings Technology*, 202(19):4583–4590, 2008.
- [94] K. G. Anthymidis, N. Maragoudakis, G. Stergioudis, O. Haidar, and D. N. Tsipas. A comparative study of boride coatings obtained by pack cementation method and by fluidized bed technology. *Materials Letters*, 57(1617):2399–2403, 2003.
- [95] C. Guo, J. Zhou, J. Zhao, B. Guo, Y. Yu, H. Zhou, and J. Chen. Microstructure and friction and wear behavior of laser boronizing composite coatings on titanium substrate. *Applied Surface Science*, 257(9):4398–4405, 2011.
- [96] N. M. Tikekar, K. S. Ravi Chandran, and A. Sanders. Nature of growth of dual titanium boride layers with nanostructured titanium boride whiskers on the surface of titanium. *Scripta Materialia*, 57(3):273–276, 2007.

- [97] L. Qin, C. Liu, K. Yang, and B. Tang. Characteristics and wear performance of borided Ti-6Al-4V alloy prepared by double glow plasma surface alloying. *Surface and Coatings Technology*, 225(0):92–96, 2013.
- [98] B. Sarma and K. S. Ravi Chandran. Recent advances in surface hardening of titanium. *JOM*, 63(2):85–92, 2011.
- [99] K. S. R. Chandran and S. Aich. Titanium boride coatings on titanium surfaces and associated methods, 2007. URL <http://www.google.com/patents/US7264682>. US Patent 7,264,682.
- [100] R. Bailey and Y. Sun. Unlubricated sliding friction and wear characteristics of thermally oxidized commercially pure titanium. *Wear*, 308(12):61–70, 2013.
- [101] J. L. Murray, P. K. Liao, and K. E. Spear. The B-Ti (boron-titanium) system. *Bulletin of Alloy Phase Diagrams*, 7(6):550–555, 1986.
- [102] H. Li, Z. Cui, Z. Li, S. Zhu, and X. Yang. Surface modification by gas nitriding for improving cavitation erosion resistance of CP-Ti. *Applied Surface Science*, 298(0):164–170, 2014.
- [103] A. Molinari, G. Straffelini, B. Tesi, T. Bacci, and G. Pradelli. Effects of load and sliding speed on the tribological behaviour of Ti-6Al-4V plasma nitrided different temperatures. *Wear*, 203204(0):447–454, 1997.
- [104] T. M. Manhabosco, S. M. Tamborim, C. B. dos Santos, and I. L. Muller. Tribological, electrochemical and tribo-electrochemical characterization of bare and nitrided Ti-6Al-4V in simulated body fluid solution. *Corrosion Science*, 53(5):1786–1793, 2011.
- [105] M. Rinner, K. Volz, W. Ensinger, W. Assmann, and B. Rauschenbach. Composition and microstructure of titanium nitride formed on Ti-6Al-4V by nitrogen plasma immersion ion implantation. *Surface and Coatings Technology*, 100101(0):366–371, 1998.
- [106] A. R. Hamad, J. H. Abboud, F. M. Shuaeib, and K. Y. Benyounis. Surface hardening of commercially pure titanium by laser nitriding: Response surface analysis. *Advances in Engineering Software*, 41(4):674–679, 2010.
- [107] H. Shibata, K. Tokaji, T. Ogawa, and C. Hori. The effect of gas nitriding on fatigue behaviour in titanium alloys. *International Journal of Fatigue*, 16(6):370–376, 1994.
- [108] F. Galliano, E. Galvanetto, S. Mischler, and D. Landolt. Tribocorrosion behavior of plasma nitrided Ti-6Al-4V alloy in neutral NaCl solution. *Surface and Coatings Technology*, 145(1-3):121–131, 2001.
- [109] W. Osterle, D. Klaffke, M. Griepentrog, U. Gross, I. Kranz, and Ch Knabe. Potential of wear resistant coatings on Ti-6Al-4V for artificial hip joint bearing surfaces. *Wear*, 264(78):505–517, 2008.

- [110] X. Chen, G. Wu, R. Wang, W. Guo, J. Yang, S. Cao, Y. Wang, and W. Han. Laser nitriding of titanium alloy in the atmosphere environment. *Surface and Coatings Technology*, 201(911):4843–4846, 2007.
- [111] Y. Sul, C. B. Johansson, Y. Jeong, and T. Albrektsson. The electrochemical oxide growth behaviour on titanium in acid and alkaline electrolytes. *Medical engineering & physics*, 23(5):329–346, 2001.
- [112] A. F. Yetim. Investigation of wear behavior of titanium oxide films, produced by anodic oxidation, on commercially pure titanium in vacuum conditions. *Surface and Coatings Technology*, 205(6):1757–1763, 2010.
- [113] B. Bacroix, M. Lahmari, G. Inglebert, and I. L. Caron. A modified oxygen boost diffusion treatment for Ti alloys and associated tribological properties with respect to biological environment. *Wear*, 271(1112):2720–2727, 2011.
- [114] A. F. Yetim, F. Yildiz, Y. Vangolu, A. Alsaran, and A. Celik. Several plasma diffusion processes for improving wear properties of Ti-6Al-4V alloy. *Wear*, 267(12):2179–2185, 2009.
- [115] A. L. Yerokhin, X. Nie, A. Leyland, and A. Matthews. Characterisation of oxide films produced by plasma electrolytic oxidation of a Ti-6Al-4V alloy. *Surface and Coatings Technology*, 130(23):195–206, 2000.
- [116] F. Borgioli, E. Galvanetto, F. Iozzelli, and G. Pradelli. Improvement of wear resistance of Ti-6Al-4V alloy by means of thermal oxidation. *Materials Letters*, 59(17):2159–2162, 2005.
- [117] H. Guleryuz and H. Cimenoglu. Effect of thermal oxidation on corrosion and corrosion-wear behaviour of a Ti-6Al-4V alloy. *Biomaterials*, 25(16):3325–33, 2004.
- [118] S. Kumar, T. S. N. Sankara Narayanan, S. Ganesh Sundara Raman, and S. K. Seshadri. Thermal oxidation of CP-Ti: an electrochemical and structural characterization. *Materials Characterization*, 61(6):589–597, 2010.
- [119] A. Ravi Shankar, N. S. Karthiselva, and U. Kamachi Mudali. Thermal oxidation of titanium to improve corrosion resistance in boiling nitric acid medium. *Surface and Coatings Technology*, 235(0):45–53, 2013.
- [120] C. Langlade, B. Vannes, T. Sarnet, and M. Autric. Characterization of titanium oxide films with Magnéli structure elaborated by a solgel route. *Applied Surface Science*, 186(14):145–149, 2002.
- [121] M. Woydt, A. Skopp, I. Dorfel, and K. Witke. Wear engineering oxides/anti-wear oxides. *Wear*, 218(1):84–95, 1998.
- [122] M. N. Gardos, H. Hong, and W. O. Winer. The effect of anion vacancies on the tribological properties of rutile (TiO_{2-x}), part II: Experimental evidence. *Tribology Transactions*, 33(2):209–220, 1990.

- [123] D. M. Brunette. *Titanium in medicine: material science, surface science, engineering, biological responses, and medical applications*. Springer, 2001.
- [124] A. Seeber, A. N. Aloisio, C. V. Speller, P. Egert, F. A. Weber, and A. Lago. Sintering unalloyed titanium in dc electrical abnormal glow discharge. *Materials Research*, 13:99–106, 2010.
- [125] C. Leyens. *Oxidation and Protection of Titanium Alloys and Titanium Aluminides*, pages 187–230. Titanium and Titanium Alloys. Wiley-VCH Verlag GmbH and Co. KGaA, 2003; 2005. ISBN 9783527602117.
- [126] G. Welsch, R. Boyer, and E. W. Collings. *Materials Properties Handbook: Titanium Alloys*. ASM International, 1993. ISBN 9780871704818.
- [127] S. Andersson, B. Collen, U. Kuylenstierna, and A. Magneli. Phase analysis studies on the titanium-oxygen system. *Acta chem.scand*, 11(10):1641–1652, 1957.
- [128] S. Kumar, T. S. N. Sankara Narayanan, S. Ganesh Sundara Raman, and S. K. Seshadri. Surface modification of CP-Ti to improve the fretting-corrosion resistance: Thermal oxidation vs. anodizing. *Materials Science and Engineering: C*, 30(6):921–927, 2010.
- [129] M. D. Bui, C. Jardin, J. P. Gauthier, G. Thollet, and P. Michel. Oxidation mechanism, oxide decomposition and phase transition in industrial titanium studied by high-resolution low-energy electron spectrometry. In *Titanium'80*, volume 4, pages 2819–2827, 1980.
- [130] L. H. Van Vlack. *Materials science for engineers*. Addison-Wesley Pub. Co, 1970.
- [131] Z. Liu and G. Welsch. Literature survey on diffusivities of oxygen, aluminum, and vanadium in alpha titanium, beta titanium, and in rutile. *Metallurgical Transactions A*, 19(4):1121–1125, 1988.
- [132] P. K. Imbrie and D. C. Lagoudas. Morphological evolution of TiO₂ scale formed on various 1D and 2D geometries of titanium. *Oxidation of Metals*, 55(3-4):359–399, 04/01 2001.
- [133] S. Kumar, T. S. N. Sankara Narayanan, S. Ganesh Sundara Raman, and S. K. Seshadri. Evaluation of fretting corrosion behaviour of CP-Ti for orthopaedic implant applications. *Tribology International*, 43(7):1245–1252, 2010.
- [134] F. Borgioli, E. Galvanetto, F. P. Galliano, and T. Bacci. Air treatment of pure titanium by furnace and glow-discharge processes. *Surface and Coatings Technology*, 141(1):103–107, 2001.
- [135] S. Banfield, J. C. Avelar-Batista Wilson, G. Cassar, A. Leyland, A. Matthews, and J. Housden. An investigation into the effect of triode plasma oxidation (TPO) on the tribological properties of Ti-6Al-4V. *Surface and Coatings Technology*, 206(7):1955–1962, 2011.

- [136] M. Jamesh, S. Kumar, and T. S. N. Sankara Narayanan. Effect of thermal oxidation on corrosion resistance of commercially pure titanium in acid medium. *Journal of Materials Engineering and Performance*, 21(6):900–906, 2012.
- [137] E. Arslan, Y. Totik, E. Demirci, and A. Alsaran. Influence of surface roughness on corrosion and tribological behavior of CP-Ti after thermal oxidation treatment. *Journal of Materials Engineering and Performance*, 19(3):428–433, 2010.
- [138] Z. Qin, Y. Zeng, and D. W. Shoesmith. Modeling hydrogen permeation through a thin titanium oxide film and palladium. *Thin Solid Films*, 534(0):673–679, 2013.
- [139] S. K. Yen. Retardation effects of thermally grown oxide films on the hydrogen embrittlement of commercial pure titanium. *Corrosion Science*, 41(10):2031–2051, 1999.
- [140] S. Kumar, T. S. N. Sankara Narayanan, S. Ganesh Sundara Raman, and S. K. Seshadri. Thermal oxidation of CP-Ti: Evaluation of characteristics and corrosion resistance as a function of treatment time. *Materials Science and Engineering: C*, 29(6):1942–1949, 2009.
- [141] T. Kosec, P. Mocnik, and A. Legat. The tribocorrosion behaviour of NiTi alloy. *Applied Surface Science*, 288(0):727–735, 2014.
- [142] B. Li, Y. Li, J. Li, X. Fu, C. Li, H. Wang, S. Liu, L. Guo, S. Xin, C. Liang, and H. Li. Improvement of biological properties of titanium by anodic oxidation and ultraviolet irradiation. *Applied Surface Science*, 307(0):202–208, 2014.
- [143] A. C. Fernandes, F. Vaz, E. Ariza, L. A. Rocha, A. R. L. Ribeiro, A. C. Vieira, J. P. Rivière, and L. Pichon. Tribocorrosion behaviour of plasma nitrided and plasma nitrided + oxidised Ti-6Al-4V alloy. *Surface and Coatings Technology*, 200(2223):6218–6224, 2006.
- [144] C. Pierret, L. Maunoury, I. Monnet, S. Bouffard, A. Benyagoub, C. Grygiel, D. Busardo, D. Muller, and D. Höche. Friction and wear properties modification of Ti-6Al-4V alloy surfaces by implantation of multi-charged carbon ions. *Wear*, 319(12):19–26, 2014.
- [145] S. Kumar, T. S. N. Sankara Narayanan, S. Ganesh Sundara Raman, and S. K. Seshadri. Fretting corrosion behaviour of thermally oxidized CP-Ti in ringers solution. *Corrosion Science*, 52(3):711–721, 2010.
- [146] C. Liao, Y. He, J. Yang, B. Nan, and X. Liu. Effect of carburization on electrochemical corrosion behaviours of TiAl alloy. *Materials Science and Engineering: B*, 178(7):449–456, 2013.
- [147] T. Kim, Y. Park, and M. Wey. Characterization of Ti-6Al-4V alloy modified by plasma carburizing process. *Materials Science and Engineering: A*, 361(12):275–280, 2003.

- [148] E. Bucur and F. C. Wagner. *Rate of Diffusion of Carbon in Alpha and in Beta Titanium as a Function of the Temperature and Concentration*. Defense Technical Information Center, 1954.
- [149] W. L. Finlay and J. A. Snyder. Effects of three interstitial solutes (nitrogen, oxygen, and carbon) on the mechanical properties of high-purity, alpha titanium. *J.Metals*, 188, 1950.
- [150] A. Emamian, S. F. Corbin, and A. Khajepour. *In-Situ Deposition of Metal Matrix Composite in Fe-Ti-C Systems Using Laser Cladding Process*. Metal, ceramic and polymeric composites for various uses. inTech, online 20, July, 2011, 2011. ISBN 978-953-307-353-8.
- [151] S. Izman, M. R. A. Kadir, M. Anwar, E. M. Nazim, A. Nalisa, and M. Konneh. Effect of carburization process on adhesion strength of Ti carbide layer on titanium alloy substrate. *Advanced Materials Research*, 197:219–224, 2011.
- [152] M. Brama, N. Rhodes, J. Hunt, A. Ricci, R. Teghil, S. Migliaccio, S. D. Rocca, S. Leccisotti, A. Lioi, M. Scandurra, G. De Maria, D. Ferro, F. Pu, G. Panzini, L. Politi, and R. Scandurra. Effect of titanium carbide coating on the osseointegration response in vitro and in vivo. *Biomaterials*, 28(4):595–608, 2007.
- [153] K. Lu and J. Lu. Nanostructured surface layer on metallic materials induced by surface mechanical attrition treatment. *Materials Science and Engineering: A*, 375377(0):38–45, 2004.
- [154] B. Arifvianto, Suyitno, M. Mahardika, P. Dewo, P. T. Iswanto, and U. A. Salim. Effect of surface mechanical attrition treatment (SMAT) on microhardness, surface roughness and wettability of AISI 316L. *Materials Chemistry and Physics*, 125(3): 418–426, 2011.
- [155] R. C. Sharma. *Principles of heat treatment of steels*, pages 214–216. New Age International, New Delhi, 2003. ISBN 8122408699.
- [156] T. F. J. Quinn. *X-rays, electrons and crystalline materials*. Butterworths, 1970. ISBN 9780408700511.
- [157] E. W. Nuffield. *X-ray diffraction methods*. Wiley, 1966.
- [158] B. D. Cullity and S. R. Stock. *Elements of X-ray Diffraction: Pearson New International Edition*. Pearson Education, Limited, 2013. ISBN 9781292040547.
- [159] W. D. Callister and D. G. Rethwisch. *Materials Science and Engineering: An Introduction*. John Wiley and Sons, 2010. ISBN 9780470419977.
- [160] T. Bell and Y. Sun. Glow discharge depth profiling - a powerful analytical technique in surface engineering. In *paper presented at 5th IFHT Seminar*, 1995.
- [161] T. G. Rochow and E. G. Rochow. *An introduction to microscopy by means of light, electrons, X-rays, or ultrasound*. Plenum Press, 1978. ISBN 9780306311116.

- [162] E. M. Slayter and H. S. Slayter. *Light and Electron Microscopy*. Cambridge University Press, 1992. ISBN 9780521339483.
- [163] G. Lawes, A. M. James, and (Project) ACOL. *Scanning Electron Microscopy and X-ray Microanalysis*. ACOL, Thames Polytechnic, London, by Wiley, 1987. ISBN 9780471913900.
- [164] H. Guleryuz and H. Cimenoglu. Surface modification of a Ti-6Al-4V alloy by thermal oxidation. *Surface and Coatings Technology*, 192(23):164–170, 2005.
- [165] C. J. Rosa. Oxygen diffusion in alpha and beta titanium in the temperature range of 932°C to 1142°C. *Metallurgical Transactions*, 1(9):2517–2522, 1970.
- [166] K. L. Dahm. Fatigue-like failure of thermally oxidised titanium in reciprocating pin-on-plate wear tests. *Wear*, 267(14):409–416, 2009.
- [167] T. Akhadejdamrong, T. Aizawa, M. Yoshitake, A. Mitsuo, T. Yamamoto, and Y. Ikuhara. Self-lubrication mechanism of chlorine implanted TiN coatings. *Wear*, 254(78):668–679, 2003.
- [168] T. Aizawa, A. Mitsuo, S. Yamamoto, T. Sumitomo, and S. Muraishi. Self-lubrication mechanism via the in situ formed lubricious oxide tribofilm. *Wear*, 259(16):708–718, 2005.
- [169] S. Ahn, H. Kwon, and D. D. Macdonald. Role of chloride ion in passivity breakdown on iron and nickel. *Journal of the Electrochemical Society*, 152(11):B482–B490, 2005.
- [170] E. Sikora and D. D. Macdonald. Passivity of iron in the presence of ethylenediaminetetraacetic acid. I. general electrochemical behavior. *Journal of the Electrochemical Society*, 147(11):4087–4092, 2000.
- [171] J. Liu and D. D. Macdonald. The passivity of iron in the presence of ethylenediaminetetraacetic acid: II. the defect and electronic structures of the barrier layer. *Journal of the Electrochemical Society*, 148(11):B425–B430, 2001.
- [172] T. Bak, J. Nowotny, M. Rekas, and C. C. Sorrell. Defect chemistry and semiconducting properties of titanium dioxide: II. defect diagrams. *Journal of Physics and Chemistry of Solids*, 64(7):1057–1067, 2003.
- [173] M. J. Runa, M. T. Mathew, and L. A. Rocha. Tribocorrosion response of the Ti-6Al-4V alloys commonly used in femoral stems. *Tribology International*, 68(0):85–93, 2013.
- [174] I. M. Bernstein and A. W. Thompson. *Hydrogen in metals*. American Society for Metals, Michigan, 1974.
- [175] P. Millenbach and M. Givon. The electrochemical formation of titanium hydride. *Journal of the Less Common Metals*, 87(2):179–184, 1982.

- [176] D. S. Shih, I. M. Robertson, and H. K. Birnbaum. Hydrogen embrittlement of α titanium: In situ TEM studies. *Acta Metallurgica*, 36(1):111–124, 1988.
- [177] S. C. Lee, W. Y. Ho, and T. M. Chen. Prevention of hydrogen degradation in titanium by deposition of TiN thin film. *Journal of Materials Engineering and Performance*, 3(6):740–743, 1994.
- [178] X. Jiang, S. Li, C. Duan, and M. Li. A study of the corrosive wear of Ti-6Al-4V in acidic medium. *Wear*, 129(2):293–301, 1989.
- [179] Y. Sun and V. Rana. Tribocorrosion behaviour of AISI 304 stainless steel in 0.5 M NaCl solution. *Materials Chemistry and Physics*, 129(12):138–147, 2011.
- [180] A. Igual Munoz and L. Casaban Julian. Influence of electrochemical potential on the tribocorrosion behaviour of high carbon cocrmo biomedical alloy in simulated body fluids by electrochemical impedance spectroscopy. *Electrochimica Acta*, 55(19):5428–5439, 2010.
- [181] G. Nakayama, Y. Sakakibara, Y. Taniyama, H. Cho, T. Jintoku, S. Kawakami, and M. Takemoto. The long term behaviors of passivation and hydride layer of commercial grade pure titanium in tru waste disposal environments. *Journal of Nuclear Materials*, 379(13):174–180, 2008.
- [182] C. L. Briant, Z. F. Wang, and N. Chollocoop. Hydrogen embrittlement of commercial purity titanium. *Corrosion Science*, 44(8):1875–1888, 2002.
- [183] M. J. Frank, M. S. Walter, M. M. Bucko, E. Pamula, S. P. Lyngstadaas, and H. J. Haugen. Polarization of modified titanium and titanium-zirconium creates nanostructures while hydride formation is modulated. *Applied Surface Science*, 282(0):7–16, 2013.
- [184] R. Bailey and Y. Sun. Corrosion and tribocorrosion performance of thermally oxidized commercially pure titanium in a 0.9% NaCl solution. *Journal of Materials Engineering and Performance*, 24(4):1669–1678, 2015.
- [185] I. Arvanitidis, Du Siche, and S. Seetharaman. A study of the thermal decomposition of BaCO₃. *Metallurgical and Materials Transactions B*, 27(3):409–416, 1996.
- [186] A. K. Galwey and E. Brown. *Thermal Decomposition of Ionic Solids: Chemical Properties and Reactivities of Ionic Crystalline Phases*. Elsevier Science, 1999. ISBN 9780080542799.
- [187] J. Kim and H. Lee. Thermal and carbothermic decomposition of Na₂CO₃ and Li₂CO₃. *Metallurgical and Materials Transactions B*, 32(1):17–24, 2001.
- [188] B. V. L'vov. *Thermal Decomposition of Solids and Melts: New Thermochemical Approach to the Mechanism, Kinetics and Methodology*. Springer, 2007. ISBN 9781402056727.

- [189] A. Maitre, D. Tetard, and P. Lefort. Role of some technological parameters during carburizing titanium dioxide. *Journal of the European Ceramic Society*, 20(1): 15–22, 2000.
- [190] J. C. Slater. Atomic radii in crystals. *The Journal of Chemical Physics*, 41(10): 3199–3204, 1964.
- [191] M. Albertini, M. Herrero-Climent, P. Lázaro, J. V. Rios, and F. J. Gil. Comparative study on AISI 440 and AISI 420B stainless steel for dental drill performance. *Materials Letters*, 79(0):163–165, 2012.
- [192] K. H. Lo, F. T. Cheng, and H. C. Man. Laser transformation hardening of AISI 440C martensitic stainless steel for higher cavitation erosion resistance. *Surface and Coatings Technology*, 173(1):96–104, 2003.
- [193] R. Puli and G. D. Janaki Ram. Microstructures and properties of friction surfaced coatings in AISI 440C martensitic stainless steel. *Surface and Coatings Technology*, 207(0):310–318, 2012.
- [194] J. R. Yang, T. H. Yu, and C. H. Wang. Martensitic transformations in AISI 440C stainless steel. *Materials Science and Engineering: A*, 438440(0):276–280, 2006.
- [195] M. Wen, C. Wen, P. Hodgson, and Y. Li. Improvement of the biomedical properties of titanium using SMAT and thermal oxidation. *Colloids and Surfaces B: Biointerfaces*, 116(0):658–665, 2014.
- [196] N. Olah, Z. Fogarassy, M. Furko, C. Balazsi, and K. Balazsi. Sputtered nanocrystalline ceramic TiC/amorphous C thin films as potential materials for medical applications. *Ceramics International*, 41(4):5863–5871, 2015.
- [197] A. I. Avgustinik, G. V. Drozdetskaya, and S. S. Ordan'yan. Reaction of titanium carbide with water. *Soviet Powder Metallurgy and Metal Ceramics*, 6(6):470–473, 1967.
- [198] A. Jain, S. P. Ong, G. Hautier, W. Chen, W. D. Richards, S. Dacek, S. Cholia, D. Gunter, D. Skinner, G. Ceder, and K. A. Persson. The materials project: A materials genome approach to accelerating materials innovation. *APL Materials*, 1(1):1, 2013.
- [199] M. Schneider, K. Kremmer, C. Lämmel, K. Sempf, and M. Herrmann. Galvanic corrosion of metal/ceramic coupling. *Corrosion Science*, 80(0):191–196, 2014.
- [200] A. C. Vieira, L. A. Rocha, N. Papageorgiou, and S. Mischler. Mechanical and electrochemical deterioration mechanisms in the tribocorrosion of Al alloys in NaCl and in NaNO₃ solutions. *Corrosion Science*, 54(0):26–35, 2012.
- [201] V. G. Pina, A. Dalmau, F. Devesa, V. Amigó, and A. I. Munoz. Tribocorrosion behavior of beta titanium biomedical alloys in phosphate buffer saline solution. *Journal of the Mechanical Behavior of Biomedical Materials*, 46(0):59–68, 2015.